amU
Aix Marseille Université

NNT : 2024AIXM0001

THÈSE DE DOCTORAT

Soutenue à AMU — Aix-Marseille Université
le 19 Décembre 2024 par

Virginia QUADRI

Impact of neutrals and density regimes on turbulence in the edge plasma of tokamaks

Discipline
Physics and Material Sciences

Spécialité
Energy, Radiation, and Plasma Physics

École doctorale
ED 352 PHYSIQUE ET SCIENCES DE LA MATIÈRE

Laboratoire/Partenaires de recherche
Institut pour la Recherche sur la Fusion par Confinement Magnétique (IRFM) - CEA Saint-Paul-lez-Durance, France

Laboratoire de la Physique des Interactions Ioniques et Moléculaires (PIIM) - AMU Marseille, France

Composition du jury

Anders Henry NIELSEN DTU	Rapporteur
Christian Gabriel THEILER EPFL/SPC	Rapporteur
Livia CASALI UTK	Examinatrice
Wouter DEKEYSER KU Leuven	Examinateur
Nicolas FEDORCZAK CEA/IRFM	Examinateur
Peter Beyer AMU/PIIM	Président du Jury
Yannick MARANDET CNRS/PIIM	Directeur de thèse
Patrick TAMAIN CEA/IRFM	Co-directeur de thèse
Philippe GHENDRIH CEA/IRFM	Membre invité
Oliver SCHMITZ UW-Madison	Membre invité

cea irfm PIIM NUMERICS EUROfusion

Affidavit

I, undersigned, Virginia Quadri, hereby declare that the work presented in this manuscript is my own work, carried out under the scientific supervision of Yannick Marandet and Patrick Tamain, in accordance with the principles of honesty, integrity and responsibility inherent to the research mission. The research work and the writing of this manuscript have been carried out in compliance with both the french national charter for Research Integrity and AMU charter on the fight against plagiarism.

This work has not been submitted previously either in this country or in another country in the same or in a similar version to any other examination body.

Aix en Provence, 14 mars 2025.



This work is licensed under Creative Commons Attribution-NonCommercial-NoDerivatives 4.0 International Public License

Liste de publications et participation aux conférences

Liste des publications réalisées dans le cadre du projet de thèse :

1. "Self-organization of plasma edge turbulence in interaction with recycling neutrals", **V. Quadri**, P. Tamain, Y. Marandet, H. Bufferand, N. Rivals, G. Ciraolo, G. Falchetto, R. Düll, H. Yang, Contributions to Plasma Physics 2024, 64, (7-8), https ://doi.org/10.1002/ctpp.202300146
2. "Edge plasma turbulence simulations in detached regimes with the SOLEDGE3X code", **V. Quadri**, P. Tamain, Y. Marandet, H. Bufferand, N. Rivals, G. Ciraolo, G. Falchetto, R. Düll, H. Yang, S. Sureshkumar, N. Varadarajan, H. Reimerdes, D. S de Oliveira, D. Mancini, Nuclear Materials and Energy 2024, 101756, https ://doi.org/10.1016/j.nme.2024.101756
3. "Introducing electromagnetic effects in Soledge3X", R. Düll, H. Bufferand, E. Serre, G. Ciraolo, **V. Quadri**, N. Rivals, P. Tamain, Contributions to Plasma Physics 2024, 64, (7-8), https ://doi.org/10.1002/ctpp.202300147.
4. "First full-scale TCV L-mode edge turbulent simulation including neutral recycling with the SOLEDGE3X code", H. Bufferand, G. Ciraolo, R. Düll, G. L. Falchetto, N. Fedorczak, K. Galazka, Ph. Ghendrih, Y. Marandet, **V. Quadri**, M. Raghunathan, N. Rivals, F. Schwander, E. Serre, P. Tamain, H. Yang, EPS 2023-49th Plasma Physics Conference, 2023, https ://cea.hal.science/cea-04203326v1
5. "Core and edge modeling of JT-60SA H-mode highly radiative scenarios using SOLEDGE3X–EIRENE and METIS codes", L. de Gianni, G. Ciraolo, G. Giruzzi, G. L. Falchetto, N. Rivals, L. Balbinot, N. Varadarajan, S. Sureshkumar, F. Artaud, H. Bufferand , R. Düll, A. Gallo, Ph. Ghendrih, **V. Quadri**, G. Rubino, P. Tamain, Frontiers Physics, Sec. Fusion Plasma Physics, Vol. 12, 2024, https ://doi.org/10.3389/fphy.2024.1422286.

Participation aux conférences et écoles d'été au cours de la période de thèse :

1. **Invited Talk :**
   — 19th International Workshop on Plasma Edge Theory in Fusion Devices, September 18-21, 2023, ASIPP, Hefei, China,
   http ://www.ipp.ac.cn/xwdt/kydt/202309/t20230928_757780.html
2. **Talks :**
   — TSVV3 Eurofusion Workshop, June 2023, Garching, Germany (online).
   — Workshop SOL modeling and PWI, February 2024, Tervaniemi, Finland.
   — TSVV3 Eurofusion Workshop, May 2024, Leuven, Belgium (online).
   — WPTE RT-05 Analysis, 9th-13th September 2024, Culham, UK (online).
3. **Poster :**
   — 26th International Conference on Plasma Surface Interaction in Controlled Fusion Devices (PSI-26), May 12-17, Marseille, France,
   https ://www.psi26.com/home
4. **Summer School :**
   — Culham Plasma Physics Summer School, July 2023, CCFE, UK.

Résumé et mots clés

Mots-clés : Fusion nucléaire, plasma du bord, turbulence, neutres, tokamaks, simulations.

Les régimes de divertor dissipatifs sont essentiels à la gestion de l'évacuation de la chaleur dans les réacteurs de fusion magnétique à grande échelle tels qu'ITER et DEMO. Ces régimes aident à atténuer les interactions plasma-paroi en exploitant les interactions plasma-neutres à proximité de la paroi du vaisseau. La largeur de la SOL, un facteur clé pour accéder à ces régimes, est largement déterminée par les mécanismes de transport perpendiculaires, où le transport turbulent joue un rôle significatif.les efforts de modélisation reposent sur des codes de transport qui fournissent une description très fidèle des interactions plasma-neutres, mais reposent sur des coefficients de diffusion arbitraires pour le transport turbulent, ajustés à partir de lois expérimentales, adaptées uniquement aux plasmas attachés. Cependant, les expériences montrent que le transport turbulent est affecté par le régime d'évacuation du divertor.

Cette thèse étudie l'impact des interactions plasma-neutres et des régimes de divertor sur le transport turbulent et l'équilibre du plasma de bord, à travers des simulations numériques avec le code SOLEDGE3X et un modèle de neutres fluides intégré.

Après avoir décrit les améliorations du code, nous comparons l'effet du recyclage dans une configuration limitée circulaire entre une simulation sans neutres et une avec recyclage neutre. De nouvelles asymétries poloïdales apparaissent en raison du recyclage localisé autour du limiteur. Alors que les neutres n'impactent que peu les longueurs de décroissance dans la SOL proche, la SOL lointaine s'élargit d'un facteur de 2,4 en présence de neutres, en raison de l'aplatissement des profils de densité. Les coefficients de transport en champ moyen reconstruits à partir des données de turbulence conservent la même distribution spatiale, que les neutres soient inclus ou non, mais leur amplitude augmente jusqu'à 100

Ensuite, l'impact des régimes de densité dans une géométrie de divertor réaliste de TCV est étudié. Nous démontrons que notre modèle de neutres fluides fournit une approximation suffisante des régimes de densité. Deux simulations 3D de turbulence sont analysées, l'une à basse densité avec un divertor extérieur attaché, l'autre à haute densité avec un divertor extérieur détaché. La transition entre les régimes attaché et détaché révèle des changements substantiels dans les propriétés globales et locales du plasma et de la turbulence. En conséquence, il apparaît que le détachement entraîne une augmentation des longueurs de décroissance des flux de chaleur dans la SOL proche et lointaine d'un facteur de 1,6 et 2,7 respectivement, en accord avec les tendances expérimentales. Nous reconstruisons enfin les coefficients de transport en

champ moyen à partir de nos simulations de turbulence. Le détachement entraîne une augmentation importante du coefficient de diffusion des particules allant jusqu'à un facteur de 5, tandis que la conductivité thermique devient négative dans le divertor extérieur, soulevant des questions fondamentales sur la validité de la description ad-hoc du transport anormal dans les codes de champ moyen. Nous proposons plusieurs pistes pour résoudre cette incohérence, aboutissant à des coefficients de transport ayant un comportement plus physique.

Enfin, notre travail fournit un premier retour concernant la méthodologie pour exécuter des simulations de turbulence avec des neutres. Les longues échelles de temps physiques liées à la physique des neutres rendent difficile l'obtention d'un état stationnaire significatif, même en appliquant des stratégies dédiées pour raccourcir le temps de convergence. Ce point critique devra être abordé à l'avenir si les simulations de turbulence avec des neutres auto-cohérents doivent être utilisées pour les études d'évacuation de chaleur.

Abstract and keywords

Key-words: Nuclear Fusion, edge plasma, turbulence, neutrals, tokamaks, simulations.

Dissipative divertor regimes are the key stones of the strategy to manage heat exhaust issues in large-scale magnetic fusion reactors like ITER and DEMO. These regimes help mitigate plasma-wall interactions by exploiting plasma-neutrals interactions in the vicinity of the vessel wall. The width of the SOL, a key factor accessing these regimes, is largely determined by perpendicular transport mechanisms, where turbulent transport plays a significant role. For the last decades the modeling effort has relied on transport codes which provide a high fidelity description of plasma-neutrals interactions, at the expense of adopting an ad-hoc model for turbulent transport. Transverse transport in these codes is described by arbitrary diffusion coefficients that are usually tuned from experimental scaling laws, which have been derived for attached plasmas only. However, experimental findings indicate that transverse turbulent transport is impacted by the divertor exhaust regime. This thesis presents an investigation into the impact of plasma-neutral interactions and divertor regimes on edge plasma turbulent transport and equilibrium. The problem is addressed through numerical simulations with the SOLEDGE3X code. A fluid neutrals model has been implemented in the code to treat self-consistently plasma-neutrals interactions and turbulent transport. After describing the changes made to the code to handle neutrals physics, we first investigate the impact of recycling in circular limited configuration by comparing a simulation without neutrals, driven by a core particle flux, to a simulation driven by a gas puff and including neutrals recycling. The main outcome is that the inclusion of recycling in the model affects deeply both the plasma equilibrium and turbulence characteristics even in the considered low-recycling condition. New poloidal asymmetries emerge due to the localized recycling around the limiter. While neutrals barely impact the near SOL decay lengths, the far SOL widens by a factor of 2.4 in the presence of neutrals due to a flattening of density profiles. Mean-field transport coefficients reconstructed from turbulence data keep the same spatial distribution whether neutrals are included or not, but their amplitude increases by up to 100%. These effects are showed to be due solely to the localization of the recycling source. Then, the impact of density regimes in a realistic TCV divertor geometry is studied. We demonstrate that our fluid neutrals model provides a sufficient approximation of density regimes. Two 3D turbulence simulations are analyzed, one at low density with an attached outer divertor, one at high density with a detached outer divertor. The transition from attached to detached regimes reveals substantial changes in both

global and local properties of plasma and turbulence. As a consequence, one finds that detachment leads to an increase of both the near SOL and far SOL heat flux decay lengths by a factor of 1.6 and 2.7 respectively, in line with experimental trends. We finally reconstruct mean-field transport coefficients from our turbulence simulations. Detachment leads to a large increase of the particle diffusion coefficient by up to a factor of 5, but not in the heat conductivity becoming negative in the outer divertor, raising fundamental questions about the validity of the ad-hoc anomalous transport description in mean-field codes. We propose several routes to solve this inconsistency, resulting in transport coefficients with a more physical behavior. Finally our work provides a first feedback concerning the methodology to run turbulence simulations with neutrals. Long physical time scales related to neutrals physics make it difficult to achieve a meaningful steady-state, even when applying dedicated strategies to shorten the convergence time. This critical point will need to be addressed in the future if turbulence simulations with self-consistent neutrals are to be used for heat exhaust studies.

Résumé étendu et mots clés

Mots-clés : Fusion nucléaire, plasma du bord, turbulence, neutres, tokamaks, simulations.

Les régimes de divertor dissipatifs, en particulier le détachement, sont à la base de la stratégie de gestion des problèmes d'extractio, de chaleur et de particules dans les réacteurs de fusion magnétique tels qu'ITER et DEMO. Ces régimes aident à atténuer les interactions plasma-paroi au niveau du plasma de bord, en favorisant des interactions fortes entre le plasma et les neutres (atomes, molécules) à proximité de la paroi de la machine pour réduire ainsi les flux de particules, de quantité de mouvement et d'énergie avant qu'ils n'atteignent la paroi. Une compréhension approfondie du transport transverse au champ magnétique dans le plasma de bord, en particulier dans la région de ligne de champ connectées à la paroi, la Scrape-Off Layer (SOL), est essentielle pour la préparer l'opération de ces futures machines. La largeur de la SOL, un facteur clé pour accéder à ces régimes, est déterminée par des mécanismes de transport parallèles et perpendiculaires, où le transport turbulent — résultant de fluctuations et d'instabilités — joue un rôle important en augmentant le transport de particules et de chaleur à travers les surfaces de flux magnétiques. Depuis quelques décennies, l'effort de modélisation numérique des problèmes d'extraction de chaleur repose entièrement sur les codes de transport, qui fournissent une description très fidèle des interactions plasma-neutres, au détriment de l'adoption d'un modèle auto-cohérent pour le transport turbulent. Dans ces codes qui résolvent un modèle de champ moyen, le transport transverse est entièrement décrit par des coefficients de diffusion qui sont des paramètres libres du modèle à ajuster en fonction des conditions de transport attendues. Actuellement, ces ajustements se font sur la base de lois d'échelle expérimentales pour les largeurs de la SOL, qui ont été dérivées uniquement pour des plasmas attachés de faible densité. Cependant, des résultats expérimentaux indiquent que le transport turbulent transverse est influencé par le régime d'évacuation de chaleur dans le divertor. En particulier, des observations révèlent que des conditions de plus haute densité sont associées à une augmentation de la largeur de la SOL et à un transport anormal accru. Ainsi, l'étude du lien entre les régimes du divertor et le transport turbulent transverse est un enjeu clé pour réduire les incertitudes dans la modélisation des régimes d'évacuation de chaleur.

Cette thèse présente une étude de l'impact des interactions entre le plasma et les neutres et des régimes de divertor sur le transport turbulent et l'équilibre du plasma de bord. Le problème est abordé à l'aide de simulations numériques traitant de manière auto-cohérente les interactions plasma-neutres et le transport turbulent.

Les résultats détaillés dans ce manuscrit représentent une avancée significative dans cette direction, en fournissant les premières simulations incluant les interactions entre la turbulence et les neutres dans les régimes détachés, dans une géométrie réaliste et à grande échelle de tokamak. Le code multi-fluide de bord SOLEDGE3X a été utilisé. Dans le cadre des études présentées ici, plusieurs modèles de neutres ont été implémentés dans le code et exploités dans diverses géométries.

Les principales questions de recherche abordées lors de ce projet sont les suivantes :

1. comment la localisation de la source de particules due à l'injection de particules externes et au recyclage affecte-t-elle le transport turbulent dans le plasma de bord ?
2. les simulations peuvent-elles reproduire un changement dans le transport turbulent entre des régimes de faible et haute densité ?
   — peut-on reproduire et expliquer l'apparition d'épaulements dans les profils dans la SOL ?
   — comment la largeur de la SOL réagit-elle aux régimes de densité ?
3. quelles recommandations peuvent être faites aux codes de champ moyen pour modéliser cette phénoménologie ?
4. est-il nécessaire d'adopter une méthodologie spécifique pour converger des simulations de turbulence avec des neutres auto-cohérents ?

Après un chapitre introductif, présentant le contexte et définissant les objectifs du travail, le Chapitre 2 discute de la méthodologie employée pour modéliser la turbulence et les interactions neutres dans SOLEDGE3X, en fournissant des détails sur la géométrie et les modèles de simulation. Ce chapitre souligne comment la turbulence est représentée dans SOLEDGE3X et présente une section dédiée aux neutres. Les efforts entrepris dans ce travail pour permettre des simulations auto-cohérentes intégrant à la fois la turbulence et les neutres sont détaillés. Des développements dédiés ont été réalisés dans le code pour permettre une description auto-cohérente du recyclage des neutres dans des simulations 3D de turbulence. Deux approches ont été suivies : une extension en 3D du couplage au code de neutres cinétiques Monte-Carlo EIRENE et la mise en œuvre d'une hiérarchie intégrée de modèles de neutres fluides. En raison de limitations techniques liées à l'utilisation de la mémoire lors du couplage au code EIRENE, la première approche n'a finalement pas pu être appliquée dans les simulations de production en 3D à haute résolution, malgré sa mise en œuvre technique. Les modèles de neutres fluides ont cependant permis de capturer qualitativement la physique d'ordre zéro intervenant dans le recyclage des particules et les régimes de densité du divertor.

La première question mentionnée ci-dessus a été abordée dans le Chapitre 3 à travers l'analyse de simulations turbulentes 3D dans une configuration circulaire limitée. Le choix de cette géométrie académique idéalisée a été fait afin d'isoler les effets d'ordre zéro liés au recyclage des neutres sans la complexité d'un point-X. Même dans les machines à divertor, une telle géométrie correspond à la configuration

magnétique utilisée durant la phase de démarrage du plasma, avant que le courant ne soit monté dans les bobines du divertor pour produire le point-X, donc les conclusions tirées de cette étude s'appliquent en réalité à cette phase de la décharge plasma. L'étude a été réalisée en comparant une simulation sans neutres, dans laquelle le flux de particules était injecté depuis le centre du plasma, à une simulation alimentée par une injection de gaz au niveau de la paroi et incluant un recyclage auto-cohérent des neutres. La première simulation est représentative d'une manière largement utilisée de forcer les simulations de turbulence lorsque le recyclage des neutres n'est pas inclus dans le modèle. La seconde simulation se rapproche davantage de la situation expérimentale où la décharge est alimentée par injection de gaz à la périphérie du plasma.

Avant d'analyser l'impact du recyclage, nous avons d'abord démontré que la présence d'une injection de gaz périphérique localisée toroïdalement peut avoir un impact significatif sur la symétrie toroïdale du plasma et des propriétés de la turbulence, comme illustré sur la Fig. 1. La perturbation induite par l'injection de neutres est principalement localisée à proximité du point d'injection du gaz mais se propage également le long des tubes de flux connectés. La distance de propagation dépend du champ considéré, étant bien plus grande pour la température que pour la densité en raison de la différence des mécanismes de transport parallèle. Les propriétés des fluctuations turbulentes et du transport associé sont également perturbées par l'injection de gaz. Ces résultats montrent la capacité du modèle à répondre quantitativement à des questions de longue date concernant l'analyse des diagnostics d'imagerie qui reposent sur l'injection locale de gaz pour augmenter leur contraste. Y répondre est cependant hors du champ de ce manuscrit et nécessiterait des simulations et analyses dédiées. Pour ce qui concerne ce manuscrit, nous avons également démontré que cette perte de symétrie n'entrave pas l'agrégation dans la direction toroïdale pour l'analyse statistique des propriétés des fluctuations, car les perturbations locales n'ont qu'un impact limité sur les moyennes toroïdales.

Le principal résultat de notre étude est que l'inclusion du recyclage auto-cohérent des neutres dans le modèle affecte profondément à la fois l'équilibre du plasma et les caractéristiques de la turbulence, même dans les conditions de faible recyclage considérées dans le chapitre 3. En particulier, on observe une inversion des pentes des profils de densité et de température dans la région des surfaces fermées, avec des profils de densité aplatis et des profils de température raides en présence de neutres, alors que l'inverse se produit lorsque l'alimentation du plasma se fait depuis le centre (Fig. 2). Dans la SOL, les profils de température sont peu affectés, tandis que les profils de densité présentent un aplatissement significatif au-delà d'une couche de transition, rappelant les épaulements de profil de densité observés expérimentalement. Les propriétés des fluctuations changent également de manière profonde et opposée : le taux de fluctuation relative de densité diminue d'un facteur 2, tandis que celui de la température des électrons triple dans le plan équatorial externe. De nouvelles asymétries poloïdales, complémentaires de la structure ballonante habituelle liée à la turbulence d'interchange, apparaissent en raison de la source de recyclage localisée à proximité du limiteur.

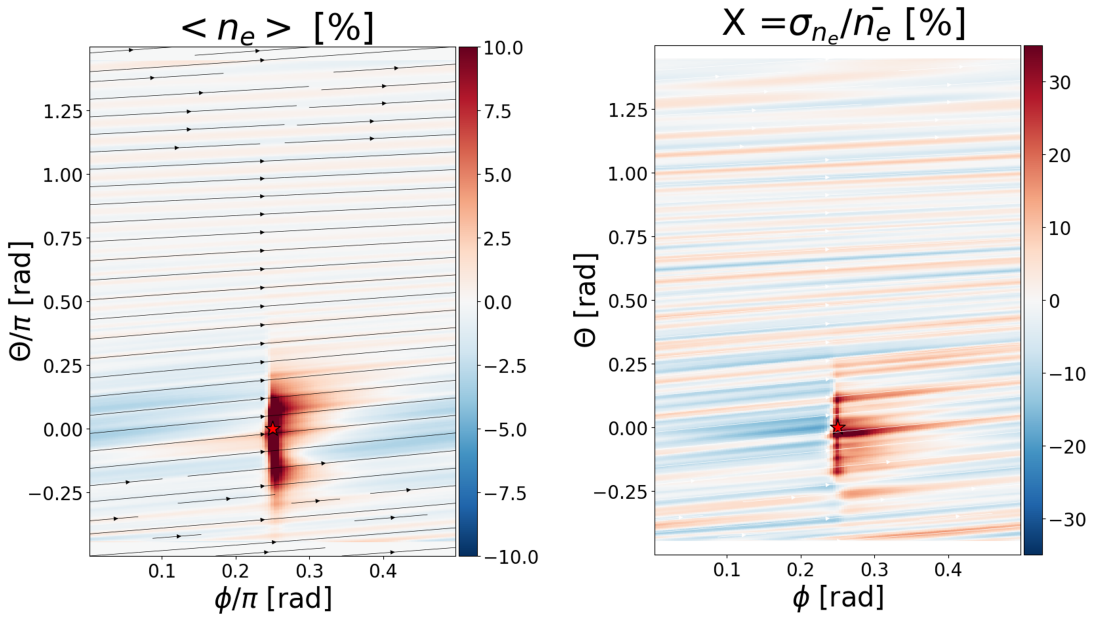

Figure 1. – Fluctuation toroïdale relative des quantités moyennées dans le temps $\frac{\langle X\rangle_t - \langle X\rangle_{t,\varphi}}{\langle X\rangle_{t,\varphi}}$ pour la densité électronique $X = n_e$ (a) et pour le taux de fluctuation relatif de la densité électronique $X = \frac{\mathrm{rms}\,(n_e)_t}{\langle n_e\rangle_t}$ (a), en fonction de $\frac{\Theta}{\pi}$ le long de l'axe vertical ($\frac{\Theta}{\pi} = 0$ est le plan médian extérieur, Θ augmentant dans la direction diamagnétique des électrons) et $\frac{\varphi}{\pi}$ sur l'axe horizontal. L'emplacement de l'injection de gaz est indiqué par une étoile rouge. La surface de flux tracée est située dans la SOL proche, après la séparatrice $R - R_{sep} = 1$cm dans le plan médian externe. Les profils 1D pour chaque quantité se réfèrent à des emplacements poloïdaux spécifiques, en particulier la surface de la jambe interne du divertor à $\Theta = 1.25\pi$rad, le plan médian interne à $\Theta = \pi$rad, le plan médian externe à $\Theta = 0$rad et la surface de la jambe externe à $\Theta = -0,25\pi$rad. Les lignes de champ magnétique sont tracées en noir dans la figure de gauche. Notez que l'échelle de couleur pour le tracé de la densité est saturée afin que l'on puisse voir autre chose que la perturbation locale au voisinage de l'injection, qui est de l'ordre de 40 %.

Avec ou sans neutres, nos simulations sont caractérisées par différentes longueurs de décroissance pour le flux de chaleur dans la SOL proche et lointaine. Ni la longueur de décroissance dans la SOL proche ni la position du point d'inflexion entre la SOL proche et lointaine ne changent de manière significative avec le recyclage des neutres, mais la SOL lointaine s'élargit d'un facteur 2,4 en raison de l'aplatissement des profils de densité. La reconstruction des coefficients de transport en champ moyen à partir des données de turbulence montre que la diffusion perpendiculaire des particules et la conductivité thermique conservent la même distribution spatiale (principalement

une structure ballonnée avec une augmentation marquée dans la SOL), que les neutres soient inclus ou non, mais l'amplitude des coefficients augmente de 100% et 60% respectivement (Fig. 3). Grâce à des simulations dédiées avec des coefficients de transport de neutres artificiellement augmentés et homogène, nous démontrons que tous ces effets s'expliquent par le changement de localisation de la source de particules, forçant le plasma et la turbulence à s'auto-organiser pour découpler les flux de chaleur des flux de particules, et non par un autre effet lié directement à la présence des neutres eux-mêmes.

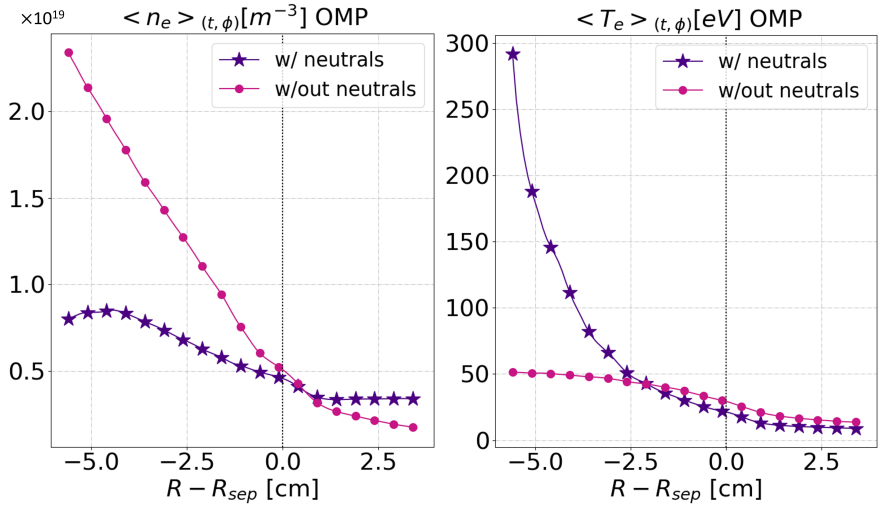

Figure 2. – Comparaison des profils radiaux dans le plan médian externe de la densité électronique (à gauche) et de la température électronique (à droite), moyennés en fonction du temps t et de la position toroïdale φ, dans les deux cas de plasma limité avec neutres ($\star$) et sans neutres ($\bullet$).

Pour étudier l'impact des régimes de densité (Chapitre 4) et répondre aux questions 2 et 3, nous adoptons une géométrie de divertor réaliste favorisant les processus dissipatifs liés aux interactions plasma-neutres. Une configuration de TCV a été choisie en lien avec des expériences en cours menées par EUROfusion, permettant de considérer ces études comme un exercice de modélisation prédictive en vue de futures comparaisons avec les résultats expérimentaux.

Une étude préliminaire, menée avec le code en mode champ moyen 2D, démontre la possibilité d'accéder à un régime de divertor détaché avec le modèle de neutres fluides intégré, dans la plage de densité observée expérimentalement. Cela nous permet également d'évaluer la fidélité de ce modèle en le comparant aux résultats obtenus avec un modèle de neutres cinétiques plus avancé (incluant par exemple les molécules) tel qu'implémenté dans EIRENE. On observe que la phénoménologie capturée par le modèle de neutres fluides est significativement différente de celle obtenue avec des neutres cinétiques, en particulier concernant le pic du flux de particules au point d'impact externe (intersection de la séparatrice et des tuiles de la jambe externe du divertor). La température des électrons au point cible est également

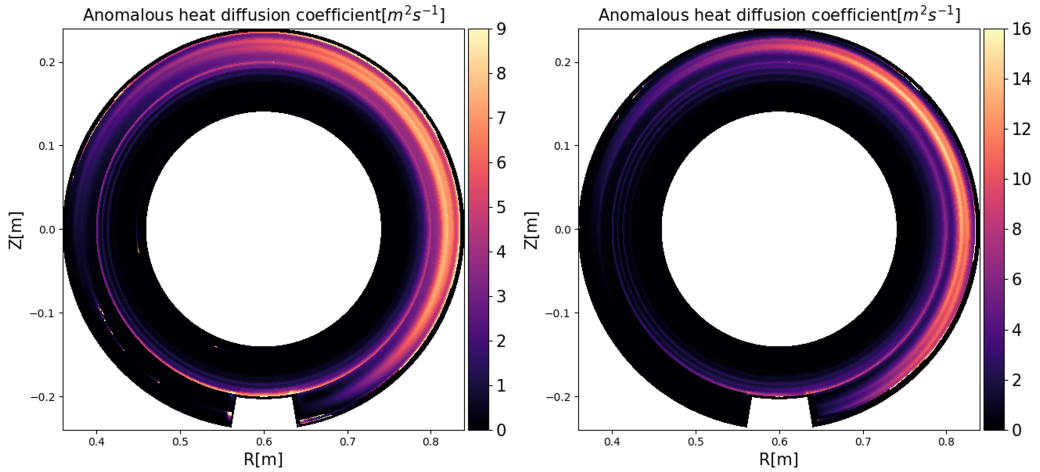

Figure 3. – Coefficients anormaux de transport thermique transversal des électrons $\chi_{\perp,e}$ dans les deux cas de plasma limité considérés, sans neutres (à gauche) et avec neutres (à droite).

systématiquement plus élevée d'un facteur 2 avec les neutres fluides qu'avec EIRENE. On peut donc en conclure que le modèle de neutres fluides n'est pas pertinent pour les études d'extraction de chaleur lorsque la prédiction de l'état du divertor est cruciale. Néanmoins, les tendances principales sont retrouvées, notamment l'augmentation de la densité dans le divertor et la baisse de la température avec l'augmentation de la densité au niveau du plan médian. Plus important encore, en ce qui concerne la turbulence, les deux modèles conduisent à des augmentations similaires de la collisionnalité et à une localisation qualitativement réaliste de la source de particules. Ainsi, pour étudier l'impact des régimes de densité sur le transport turbulent en bord de plasma, notre modèle de neutres fluides offre une approximation suffisante des effets du recyclage des neutres sur les régimes de densité.

Deux simulations de turbulence 3D sont ensuite analysées, l'une à faible densité avec un divertor externe attaché, l'autre à haute densité où la jambe du divertor externe est détachée. Un résultat clé de ces simulations est que la combinaison de la configuration en point-X et de la présence localisée de neutres dans le divertor entraîne des asymétries poloïdales importantes. Les propriétés de l'équilibre plasma et de la turbulence dépendent fortement, dans les deux cas, de la localisation poloïdale considérée (plan médian externe, jambes du divertor, tuiles du divertor). Cela a des implications importantes pour l'interprétation des données expérimentales, se concentrer uniquement sur une position est donc insuffisant. Nos résultats suggèrent donc la nécessité d'une analyse multi-locations poloïdales pour déterminer si les comportements distincts observés à différentes positions peuvent être reproduits.

Globalement, la transition entre les régimes attachés et détachés révèle des changements substantiels dans les propriétés globales et locales du plasma et de la turbulence (comme illustré dans la Fig. 4). Le cas détaché présente des niveaux de fluctuations

relatives de température beaucoup plus faibles presque partout dans le domaine, tandis que le niveau de fluctuations relatives de densité diminue également dans la majeure partie du domaine, à l'exception notable de la SOL lointaine, en particulier dans le divertor externe. L'intermittence des fluctuations de densité tend à augmenter dans le divertor mais à diminuer dans le plan médian externe, tandis qu'elle diminue à tous les points sauf à proximité immédiate de la séparatrice dans la SOL amont pour la température des électrons. Bien que la densité soit partout plus élevée dans le cas de haute densité (sauf à la cible externe qui est détachée), la température d'équilibre est plus basse dans la région des lignes de champ fermées et dans la SOL proche, mais est en réalité plus élevée dans la SOL lointaine. Cela est dû à un aplatissement significatif des profils de température au-delà d'un point d'inflexion dans le plan médian externe dans le cas détaché. Cet aplatissement est également visible sur la densité, rappelant ici encore les épaulements des profils de densité observés expérimentalement. Dans la jambe du divertor externe, les profils de température d'équilibre s'inversent même en raison des pertes d'énergie locales associées à la physique du divertor.

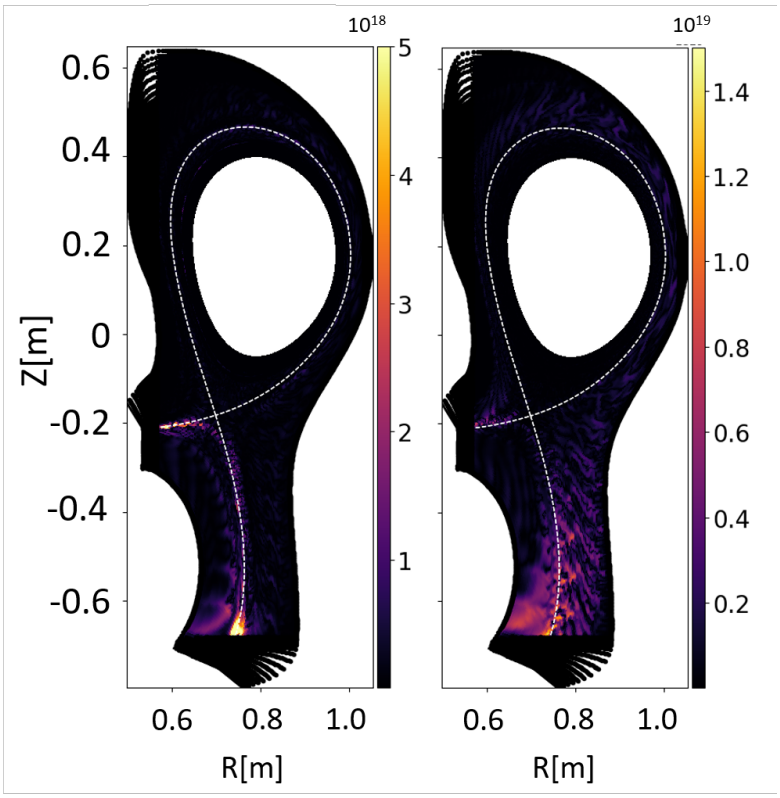

Figure 4. – Cartes poloïdales des fluctuations de densité $n_e - \bar{n}_e$ dans les simulations de plasma en géométrie divertor TCV pour $n_{e,sep} = 0,5 \times 10^{19}\mathrm{m}^{-3}$ (cas attaché, à gauche) et $n_{e,sep} = 1,2 \times 10^{19}\mathrm{m}^{-3}$ (cas détaché, à droite).

En conséquence, on constate que le détachement entraîne une augmentation des longueurs de décroissance des flux de chaleur dans la SOL proche d'environ 1,6, et d'environ 2,7 dans la SOL lointaine (Fig. 5). Ainsi, nos simulations semblent repro-

duire la tendance principale observée dans les expériences, à savoir un élargissement de la SOL, avec un impact plus marqué sur la SOL lointaine que sur la SOL proche au-delà d'un point d'inflexion dans les profils. Cependant, le lien avec les "épaulements de densité" telles qu'elles sont rapportées dans la littérature n'est pas encore clairement établi et nécessiterait une analyse plus approfondie. Premièrement, nos simulations montrent un aplatissement à la fois des profils de densité et de température, et non uniquement de la densité. Deuxièmement, aucune corrélation claire n'est observée avec la collisionalité normalisée identifiée par Carralero, S. Artene, et al. 2018 comme un paramètre clé.

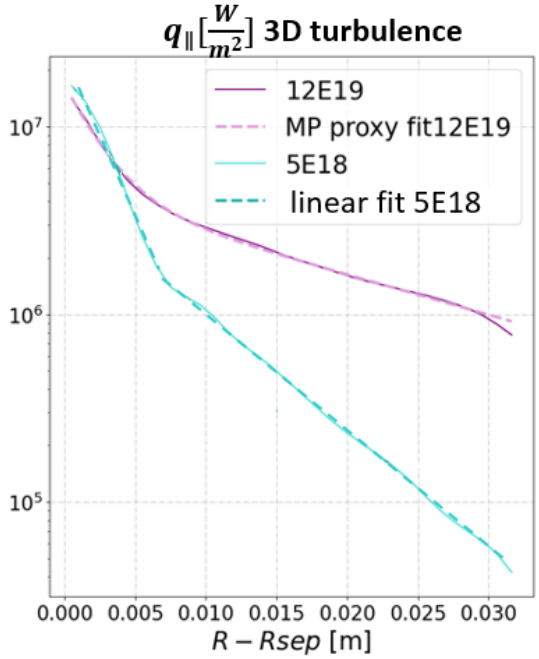

Figure 5. – Comparaison entre le flux d'énergie parallèle reconstruit (voir Eq. 3.8) au plan médian moyenné en temps t et en position toroïdale φ pour le cas attaché (turquoise) et pour le cas détaché (magenta). Les lignes pleines correspondent aux données de la simulation turbulente, tandis que les lignes en pointillé sont le résultat d'ajustements à double exponentielle.

En abordant la troisième question clé, nous avons finalement reconstruit les coefficients de transport en champ moyen à partir de nos simulations de turbulence. Quel que soit le régime de densité considéré, on observe que les coefficients de diffusion perpendiculaires sont non uniformes poloidalement, avec une structure ballonée marquée, combinée à une modulation liée à l'expansion locale du flux. Ce résultat est en accord avec les études antérieures réalisées avec le code TOKAM3X et confirmées dans la littérature. Le détachement entraîne une augmentation importante du coefficient de diffusion des particules, atteignant jusqu'à un facteur 5 par rapport au cas attaché. Cependant, il provoque également un changement dans la conductivité thermique perpendiculaire, qui devient négative dans la région des jambes du divertor extérieur,

en raison de l'inversion du gradient de température, alors que le flux de chaleur turbulent reste dirigé vers l'extérieur. Ce résultat est cohérent avec ce qui a été observé à plus petite échelle dans le cas limité à proximité de l'injection de gaz : en présence de perturbations locales significatives du plasma liées aux neutres, les coefficients de transport sont fortement affectés et peuvent même devenir négatifs (Fig. 6). Un tel résultat soulève des questions fondamentales sur la validité de la description standard diffusive du transport transverse anormal dans les codes de champ moyen (i.e. les codes de transport), car le transport anormal de chaleur perpendiculaire peut être localement découplé du gradient. Un coefficient de diffusion négatif est à la fois impossible à implémenter dans un code (pour des raisons de stabilité) et physiquement incorrect, car il contredit le deuxième principe de la thermodynamique.

Nous proposons dans ce manuscrit plusieurs pistes pour résoudre cette incohérence, l'une heuristique et l'autre basée sur des analogies avec la théorie du transport dans le plasma central. Ces deux approches conduisent à des coefficients de transport avec un comportement plus physique, c'est-à-dire sans discontinuités spatiales ni valeurs négatives. Des études et simulations supplémentaires seraient nécessaires pour trancher entre elles et fournir des recommandations finales à la communauté des codes de champ moyen.

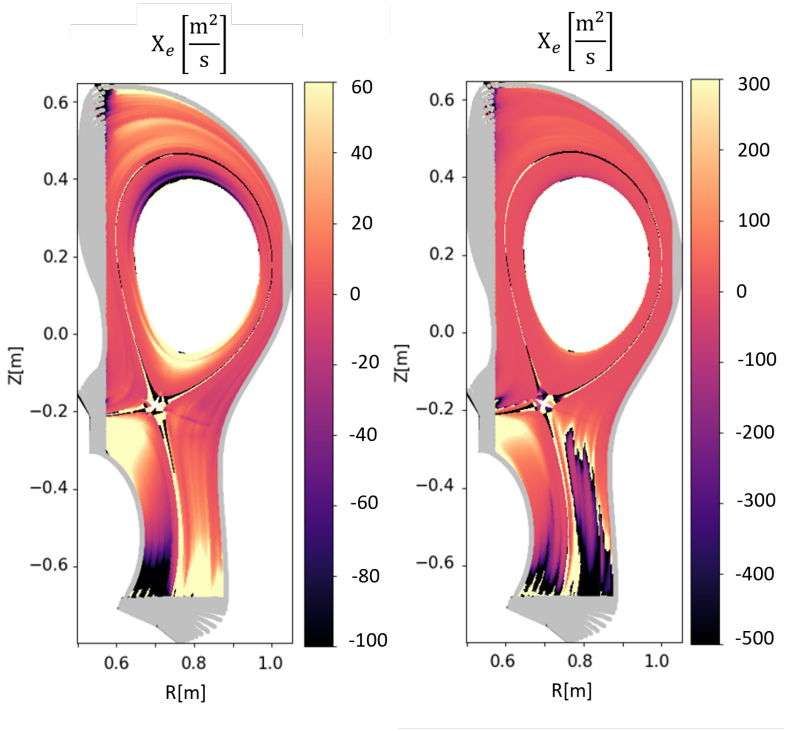

Figure 6. – Coefficients anormaux de transport thermique transversal des électrons $\chi_{\perp,e}$ dans les deux cas de TCV en géométrie divertor considérés, attaché (à gauche) et détaché (à droite).

Enfin, il convient de mentionner que le travail accompli dans cette thèse nous offre un premier retour concernant la dernière question clé sur la méthodologie à

suivre pour converger des simulations de turbulence avec des neutres auto-cohérents. L'ajout du recyclage auto-cohérent dans le modèle modifie fondamentalement le bilan de particules et d'énergie du système. Cela entraîne l'apparition d'échelles de temps supplémentaires pour atteindre un état stationnaire significatif, où les pertes radiatives et les pertes d'énergie du plasma aux cibles équilibrent l'apport d'énergie, et où l'injection de gaz est équilibrée par le pompage. Cette échelle de temps supplémentaire, déjà connue dans les simulations en champ moyen, peut dépasser plusieurs centaines de millisecondes dans les grandes machines, et constitue un obstacle majeur pour les simulations globales de turbulence, qui ne peuvent actuellement couvrir une plage de temps suffisante pour converger avec les ressources de calcul disponibles. Nous avons montré dans cette thèse que certaines grandeurs clés du plasma peuvent encore évoluer sur ces longues échelles de temps, d'où l'importance de ne pas surinterpréter les résultats de simulations qui n'ont pas atteint une pleine convergence. Une option explorée dans cette thèse pour raccourcir le temps nécessaire à l'obtention d'un état stationnaire consiste à utiliser des simulations en champ moyen 2D convergées comme condition initiale pour les simulations de turbulence 3D. Cela nous a permis de réduire par un facteur 2 le déséquilibre entre les flux entrants et sortants par rapport à une simulation démarrée à partir d'une condition initiale arbitraire. Cependant, cela n'a toujours pas suffi pour atteindre la convergence dans un temps raisonnable. Le point critique de cette méthode réside dans le choix des coefficients de transport en champ moyen pour la simulation initiale. Une approche itérative, dans laquelle les résultats d'une simulation précédente de turbulence servent à définir les coefficients de diffusion en champ moyen, pourrait permettre de réduire encore davantage le temps de convergence et mérite d'être explorée.

Dans l'ensemble, les analyses présentées dans cette thèse nous permettent de répondre aux quatre questions clés posées au début du manuscrit. Elles soulèvent également plusieurs questions qui devront être traitées dans un avenir proche. Il faut toutefois garder à l'esprit que les résultats présentés ici reposent uniquement sur un nombre limité de simulations globales de turbulence. Au cours des dernières années, plusieurs codes de la communauté scientifique travaillant sur la turbulence en bord ont acquis la capacité de réaliser des simulations avec des neutres auto-cohérents. Au vu des implications majeures que cela représente pour la physique mise en jeu et des conséquences potentielles pour la modélisation en champ moyen des problèmes d'évacuation de chaleur, il est nécessaire de constituer une base de données exhaustive de simulations globales de turbulence impliquant la physique des neutres. Cette base devrait couvrir une plus large gamme de géométries, de régimes de densité et impliquer différents codes afin d'exclure d'éventuels biais dus à la discrétisation numérique ou aux approximations des modèles. Enfin, l'analyse de ces simulations en termes de coefficients de transport en champ moyen devrait devenir systématique afin d'élaborer un consensus sur les recommandations à formuler pour la communauté de la modélisation en champ moyen. Une comparaison directe avec les résultats expérimentaux est également un pas obligatoire pour renforcer la confiance dans la pertinence des phénomènes mis en lumière par les simulations. Le choix d'une configuration et de conditions expérimentales pour les simulations TCV présentées

dans cette thèse va dans ce sens et devra être complété une fois que les données expérimentales seront pleinement disponibles. Des exercices de validation similaires devront également être réalisés sur d'autres machines pour distinguer les résultats spécifiques à une machine des tendances générales.

Acknowledgments

This PhD has been a personal journey for me. Three years ago, I was not the person I am today: along with various professional insights (and just as many blind spots), I have gained just as many on a personal level. Some of these initially broke me: I often found myself in a whirlwind of emotions that I didn't think I could handle, and even today, I sometimes feel overwhelmed. However, I realize more and more each day that I now have the tools to face all the new challenges and decisions ahead of me. Today, it's safe to say that I can handle the *turbulence*!

The first I would like to thank Prof. Mostacci for encouraging me to embark on this journey and for always believing in me.

None of this would have been possible if I had found myself in a different environment. The IRFM and PIIM have been like a second family to me: the people I met and the connections I made during these three years have been fundamental for personally and professionally developing. Following this wave, I want to start by thanking Nathalie and Valerie for always being a crucial reference point in the lab: thank you for your hard work, which I consider fundamental and infinitely patient. I'm glad for all of yours smiles, the little and comforting chats in the corridor, and most of all, for always taking care of me, not just at work!

I would also like to thank the rest of the IRFM administration and management, both from the IRFM, Frederic, Maria, Sylvie, Virginie, José and also the PIIM, especially Eric, for having made this phD practically possible.

But, most of all, this work wouldn't have been possible without you, Patrick and Yannick, to whom I extend my most sincere gratitude and admiration. Yannick, for being able to stretch the 24 hours of a day into 24,000 and for always being present and available despite your endless commitments: your diplomacy, dedication, and positivity are truly rare, and I will be forever grateful for showing them to me. Patrick, I would have to write another manuscript for thanking you. For guiding me, steering me, and saving me from drowning many times over these three years with a patience and calmness that few would have had: if I ever find myself supervising a PhD student, I hope to mean to them what you have meant to me. You both have my deepest personal and professional respect; thank you for having transmitted to me your way of working. My wish for my career is to resemble you as much as possible.

A special thanks to those I consider two key pillars not only of the lab but of plasma physics as a whole: thanks to Philippe Ghendrih for being the first to welcome me to the CEA, introducing and guiding me through my first steps in this community. I treasure the notes from your lessons, which, besides forming the theoretical foundations

of my research, were also valuable life lessons. Thank you for all the teachings and advice; I will cherish them. Thanks also to Xavier Garbet, for the motivating discussions we had and for helping interpret the results on transport coefficients: thank you for introducing me to a truly fascinating field of research and for the extreme elegance and kindness with which you explain such complex concepts.

Then, I would like to also express my deepest gratitude to the members of my PhD jury for their time, expertise, and valuable feedback on my research.

I thank the entire Soledge team for the work we did together, starting with Guido for the support and for tolerating my existential crises: thanks for all the advices and your leadership, chief. *Asse Porretta - Pistoia* state of mind. Thanks also to Hugo for all the help in debugging our lovely neutral fluids, and for the longest turbulent simulation ever. Thanks to Gloria, who has supported me both professionally and personally and continues to do so, always seeking to protect, motivate, and encourage me. Thanks to everyone who has passed through Soledge, even briefly, and who has contributed in some way to this work. And here I can't forget to thank my first office mates: Hao and Nicolas. Thank you, Hao, for your wisdom and for trying to transmit a bit of calm to me, a whirlwind of chaos. But above all, thank you, Nicolas: your help from the first day has been fundamental. I am proud of what you've become, of your successes, and I hope to share many more with you. Thanks for the coffees, the chats, the countless adventures in Aix, Paris, Finland: you are a dear friend, and always will be.

Thanks also to my three golden boys, with whom I started and, miraculously, finished this journey: thanks to Raff, for sharing all the challenges of coding with me and for our Chinese adventures. I'm still amazed you survived, but otherwise how would I have managed without you? Thanks to my ray of sunshine, Olivier, for always being by my side and understanding me from the first moment, even when there wasn't much to say. And thank you, Yann, for your constant positivity, and for always taking the right choices at the right time.

Thanks to all the colleagues from IRFM, the GTSN, Gysela, and Jorek groups: Yanick, Guilhelme, Virginie, Peter, Abdellahdi, Marina, Eric, Guido, for the coffee break chats, advice, suggestions, and all the help received over these years. A special thanks also to Tullio, Jorge, and Alex, not just colleagues but also friends I could count on. I also want to thank all the other PhD students and interns from the IRFM and PIIM, who honored me by being not just colleagues but friends above all: Mattia, Federica, James, Srikanth, Naren, Picci, Giuseppe, Davide, Lorenzo, Luca C. I also thank my beautiful and strong Lara, Quentin, Nathan, Kirill, Sascha, Theo with whom we shared the joys and pains of the Culham Summer School. With you Theo, Samy, Guilherme, and Nicolas, I also had the honor and duty of ASTHEC: know that the honor is all mine for having met you!

Thanks to those who passed through here over the years, especially Elisabetta: perhaps the first friend I made here, who, despite the stress of thesis submission, was giving an hand to a scared and lost young girl. I also thank the whole Italian community of Cadarache: we know the "I" in IRFM stands for Italians! When you

arrive in another country, your roots help you plant new ones. Thanks to Flavio and Mireille for their hospitality (you'll have me as a tenant for a while yet!), to Beatrice, Fabrice, Vincent. And then to my friends, Stefano, who came as my "replacement" at the end of my internship, initiated into Aix life thanks to a lot of *tigelle*; you've become a key presence for me here, and today I consider you one of my dearest friends. To my little Vale, the best roommate one could wish for. To Giacomo Il Pirata, for being the first to reveal to me the secrets of Aix and CEA from afar, and together with Laura, always being a great friend. To Samu and Serafina, for our tea - gossips nights, for sharing the same dark humor, and for always being there for me: vi voglio bene patati! To Silvia, always close during these tough years, to Lorenzo and his apartment (which we can finally say is truly yours!), to those two dear souls Veronica and Luca, as long as I know, my favorite new-parents, to Paolo for being so Paolo, to Giulia, a bundle of energy and positivity, to Daniela, to Sveva, to Giordana, to Manuel, to Filippo and Blanca, to Alessandro, to Emanuele, to Maria Chiara, to Matteo, to Edoardo. Each of you has left a mark on this journey, and I'm grateful for any of you.

Thanks also to the AUC volley, and to all my teammates: to BF, my favorite place in the world. Sport is made to save your life.

Tears from now, brace yourselves: to my French family.

To Riccardo, for all the little things you do for me without realizing how big they are. I'm proud of you, your journey, your humility: I wish you all the success you deserve. I'll always be here, especially to drag you to the gym at 6 a.m.

To Ludovica, thank goodness you came into my life: you, a little scared and awkward, are a force of nature, and you don't even know it. Thank you for never abandoning me during dark times and always being there like a parachute.

To Valeria, my soulmate (or *SOL*-mate): we always say it, our friendship is the greatest gift CEA has given us. You are a constant source of positive inspiration, you complete me, and you never make me feel wrong. Thank you for being so stubborn, so determined, so full of life: thank you for having step into my life, and please, never leave (you have to squat with me until we're 80). I love you with all my heart. Thank you for bringing my niece Fraise and Romain, my gym bro, my coach, into my life. Thank you for inspiring the change I couldn't bring about on my own, and thank you for being a true and sincere friend.

To Giorgio, for always being my eldest brother: the one who pushes me, whose hand can be *iron or feather*, but who has always been there without judgment, letting me make mistakes (even if he advised me not to) and then being there to pick up the pieces. It doesn't matter if it's helping me with Python, helping me do grown-up things that I can't manage, or having dinner together even if we're eating different things. You are always there, and you bring so much light into my days. And for that, I will never be able to thank you enough.

And then there's you, Alberto. You are my bro, the most similar person to me I have ever met. You're my person. Like Joey and Chandler, Meredith and Cristina, you

and I. Whether you like it or not, you are my best friend. We've been there for each other's deepest moments: fortunately, they've never aligned! But, you've won yourself a walking disaster that you'll have to keep for the rest of your life: you'll have to endure forever my troubles, my crappy car, the trips to Gaggio Montano, my meal plans, my workout sessions, my catastrophic relationships, my parents' messages asking you to keep an eye on me. I'll be happy to do the same, repaying you with our endless dinners, infinite amount of Stanleys, being your personal shopper, always down for beach outings, surprising Liberato's concerts, and visiting Paola and Luigi. I promise to be there for the important and not-so-important things in your life, just as you do every day for me. You are a constant source of inspiration and motivation.

A mandatory italian switch is needed now: alla mia famiglia e ai miei amici di sempre.

Grazie alla mia *peas-in-a-pod*, Berni. Non bastano 200 pagine di tesi per raccontare tutte le nostre storie: l'unica cosa certa è che anche a migliaia di chilometri di stanza, Pirgi tornerà sempre da te (come una minaccia). Sono orgogliosa di quello che sei diventata, delle tue consapevolezze e della tua rinasciata. Ti voglio bene.

Grazie a te Cami, per essere una presenza costante nella mia vita e che seppur non potendoci vivere constantemente, sappiamo di poter sempre contare l'una sull'altra. Bologna è una regola, la nostra, per sempre.

Grazie a te Giacomo, per essermi rimasto vicino nonostante tutto: sei un amico vero e leale. Come mi hai detto tu, non possiamo fermare il tempo e fare in modo di restare sempre vicini, ma anche se il tempo scorre e le nostre vite si allontanano, tu sarai sempre il mio Dadone e sarò sempre lì per te.

Grazie a tutti gli amici che hanno contribuito positivamente a questo esperienza, standomi vicino e incoraggiandomi sempre: a te Lisa, che siamo cresciute insieme e avvicinate sempre di più, a te Anita, per la tua forza e intraprendenza, a Sara e Sofia, per la vostra carica di energia positiva, alla piccola Margot, così tanto saggia, a Gianba e Ele, per continuare a esserci sempre, ai miei palestrati del cuore Omar, Giovanni, Daniel, Donata, e alle uniche "cose" belle che mi ha lasciato il liceo: Zanna, Gugli, Della, Benny e Marta.

E poi, il grazie più grande va alla mia famiglia, che mi ha cresciuto libera, indipendente e non mi ha mai fatto mancare niente. A te mamma, che sei la mia migliore amica, che mi ami incondizionatamente e mi sostegni in ogni scelta, vorrei dirti che questa tua bimba non riuscirà mai a risparmiare un euro e soffrirà sempre di costanti sbalzi d'umore, ma ti amerà sempre come nessuno mai. A te papà, con il sogno grande di avere una figlia femmina (ringrazio il cielo per non avermi chiamato Abramo!), che mi hai cresciuto ripetendomi che sarei potuta diventare tutto quello che avrei desiderato, che mi hai sempre spronato a raggiungere i miei obiettivi e mi hai insegnato sia cosa significa il duro lavoro che il piacere di sapersi ricompensare, a te va tutta la mia stima e l'amore più grande che ci sia. Da oggi chiamami Dottor Topin. A te Andrea, che sei come un secondo papà: ci sei sempre a proteggermi, ad aiutarmi e la tua stima mi riempie il cuore di gioia. Sappi che per me è tutto reciproco, e anche se ogni tanto mi comporto da sorella "più grande", sarò per sempre la tua sorellina. Grazie per tutto

quello che fai per mamma e papà. Vi amo immensamente.

Un grazie a te Federica, per la gioia che mi hai donato nel crescere insieme e condividere tutte le esperienze più portanti. Come ti ho già detto tante volte, sono fiera della donna che sei e di poter essere al tuo fianco, pronta ad affrontare insieme a te (e Cespo!) tante nuove avventure. Non saresti quella che sei senza gli zii, Pat e Pit: sono cresciuta avendo l'onore di essere parte della vostra famiglia, e ve sono grata. Vi voglio un bene gigantesco. Grazie anche agli zii Betta e Claudio, a Mattia e a Elisa e Giovanni per il costante supporto e affetto, da che ne ho ricordo.

I really would like to conclude by "thanking" Marconi, for all the lessons you taught me about resilience and patience: you give me 2000 euros of therapy. Have a nice shut-down and rest in peace, dude!

À Enrico.
Tes mots sont silencieux, mais chaque regard m'apprend la beauté de l'amour pur.

Contents

Affidavit 2

Liste de publications et participation aux conférences 3

Résumé et mots clés 5

Abstract and keywords 7

Résumé étendu et mots clés 9

Acknowledgments 20

Contents 26

List of Figures 29

List of Tables 39

1. Introduction 40
- 1.1. Fusion as energy source in the World energy landscape 40
- 1.2. Magnetic confinement: the tokamak as magnetic fusion device 41
  - 1.2.1. The Lawson criterion 41
  - 1.2.2. Basic principle of magnetic confinement 42
  - 1.2.3. The tokamak configuration 43
- 1.3. The Scrape-Off Layer 44
  - 1.3.1. Closed vs Open magnetic flux surfaces 44
  - 1.3.2. Limited vs Diverted configurations 45
  - 1.3.3. Sheath boundary conditions in a nutshell 46
  - 1.3.4. The SOL width 49
- 1.4. The challenge of the heat exhaust 51
- 1.5. Neutrals recycling and density regimes 52
  - 1.5.1. Plasma-wall interactions 52
  - 1.5.2. Recycling as particle, momentum and energy sources for the plasma 52
  - 1.5.3. Plasma-neutrals interactions 53
  - 1.5.4. Density regimes in tokamaks 55
  - 1.5.5. Detached plasma as operational regime for large machines . . . 57
- 1.6. Transverse transport in the edge of tokamaks 58
  - 1.6.1. Classical vs Neo- Classical vs Turbulent transport 58
  - 1.6.2. On the importance of turbulence 59

1.7. Interaction between turbulence and density regimes 60
1.7.1. Experimental evidences of the interactions between density regimes and perpendicular transport in the edge plasma 60
1.7.2. Modeling self consistently transverse transport and density regimes 63
1.8. Objectives of the thesis and outlines 65

2. Modeling turbulence neutrals interactions with Soledge3X 67
2.1. Drifts fluid models for the edge plasma 67
2.1.1. From particle to fluid description 67
2.1.2. Collisional closures for the edge plasma 71
2.1.3. Drift-fluid approximation 72
2.2. The Soledge3X multi fluid edge code 73
2.2.1. SOLEDGE3X equations 74
2.2.2. SOLEDGE3X simulation domain and geometry 78
2.2.3. Boundary conditions 79
2.2.4. SOLEDGE3X as a mean field or turbulence code 80
2.3. Neutrals description in SOLEDGE3X 82
2.3.1. Extension of SOLEDGE3X coupling to EIRENE for 3D cases . . . 82
2.3.2. Improved fluid neutrals model in SOLEDGE3X 85
2.4. Balances in SOLEDGE3X 89
2.4.1. Particle and Energy balances of the system 89
2.4.2. Conservation of particle and energy 90
2.4.3. Convergence 91
2.5. Summary 92

3. Low density regimes: a study in limited configuration 94
3.1. Simulations set-up 94
3.1.1. Geometry and parameters 94
3.1.2. Neutrals model and particle flux drive 96
3.1.3. Discussion on convergence of the particle balance 97
3.2. Investigation on the impact of a localized gas puff on the toroidal symmetry 102
3.2.1. Evaluation of the toroidal asymmetries due to the gas puff . . . 102
3.2.2. Consequences concerning the possibility to aggregate statistics in the toroidal direction 110
3.3. Impact of neutrals recycling on plasma equilibrium and turbulence . . 112
3.3.1. Fluid neutrals with self consistent diffusion set up 112
3.3.2. Particle and energy sources 113
3.3.3. Impact on plasma time averaged properties 115
3.3.4. Impact on turbulence properties 118
3.3.5. Impact on SOL widths 121
3.3.6. Impact on mean field transport coefficients 125
3.4. Confirmation of the role of the particle source location 130
3.4.1. Simulation set-up: fluid neutrals with constant diffusion 130
3.4.2. Particle and energy sources 133

3.4.3. Equilibrium and turbulence properties 134
3.5. Summary 137

4. Impact of density regimes on edge plasma turbulence in diverted configuration 139
4.1. Simulations set-up 141
4.2. Convergence strategy 143
4.2.1. The use of mean - field solution as initial condition 143
4.2.2. Convergence status of the turbulent case 144
4.3. Recovering density regimes 147
4.3.1. Evaluation of fluid neutrals model against kinetic neutrals . . . 147
4.3.2. An attached and a detached case 151
4.4. Plasma equilibrium conditions 153
4.5. Impact of density regimes on turbulence properties 155
4.5.1. A qualitative change in turbulence properties 156
4.5.2. Characterization of fluctuations 157
4.5.3. Intermittency 162
4.6. Impact on equilibrium profiles 164
4.6.1. SOL decay lengths 165
4.6.2. Discussion: link with density shoulders 170
4.7. Impact of density regime on turbulence driven transport 174
4.7.1. Anomalous transverse transport coefficients 174
4.7.2. Discussion on alternate mean-field transport models 177

Conclusion 185

ANNEXES 202

A. Eirene mesh generator 203

List of Figures

1. Fluctuation toroïdale relative des quantités moyennées dans le temps $\frac{\langle X\rangle_t - \langle X\rangle_{t,\varphi}}{\langle X\rangle_{t,\varphi}}$ pour la densité électronique $X = n_e$ (a) et pour le taux de fluctuation relatif de la densité électronique $X = \frac{\mathrm{rms}\,(n_e)_t}{\langle n_e\rangle_t}$ (a), en fonction de $\frac{\Theta}{\pi}$ le long de l'axe vertical ($\frac{\Theta}{\pi} = 0$ est le plan médian extérieur, Θ augmentant dans la direction diamagnétique des électrons) et $\frac{\varphi}{\pi}$ sur l'axe horizontal. L'emplacement de l'injection de gaz est indiqué par une étoile rouge. La surface de flux tracée est située dans la SOL proche, après la séparatrice $R - R_{sep} = 1\mathrm{cm}$ dans le plan médian externe. Les profils 1D pour chaque quantité se réfèrent à des emplacements poloïdaux spécifiques, en particulier la surface de la jambe interne du divertor à $\Theta = 1.25\pi\mathrm{rad}$, le plan médian interne à $\Theta = \pi\mathrm{rad}$, le plan médian externe à $\Theta = 0\mathrm{rad}$ et la surface de la jambe externe à $\Theta = -0,25\pi\mathrm{rad}$. Les lignes de champ magnétique sont tracées en noir dans la figure de gauche. Notez que l'échelle de couleur pour le tracé de la densité est saturée afin que l'on puisse voir autre chose que la perturbation locale au voisinage de l'injection, qui est de l'ordre de 40 %. 12
2. Comparaison des profils radiaux dans le plan médian externe de la densité électronique (à gauche) et de la température électronique (à droite), moyennés en fonction du temps t et de la position toroïdale φ, dans les deux cas de plasma limité avec neutres ($\star$) et sans neutres ($\bullet$). 13
3. Coefficients anormaux de transport thermique transversal des électrons $\chi_{\perp,e}$ dans les deux cas de plasma limité considérés, sans neutres (à gauche) et avec neutres (à droite). 14
4. Cartes poloïdales des fluctuations de densité $n_e - \bar{n}_e$ dans les simulations de plasma en géométrie divertor TCV pour $n_{e,sep} = 0,5 \times 10^{19}\mathrm{m}^{-3}$ (cas attaché, à gauche) et $n_{e,sep} = 1,2 \times 10^{19}\mathrm{m}^{-3}$ (cas détaché, à droite). . . . 15
5. Comparaison entre le flux d'énergie parallèle reconstruit (voir Eq. 3.8) au plan médian moyenné en temps t et en position toroïdale φ pour le cas attaché (turquoise) et pour le cas détaché (magenta). Les lignes pleines correspondent aux données de la simulation turbulente, tandis que les lignes en pointillé sont le résultat d'ajustements à double exponentielle. 16
6. Coefficients anormaux de transport thermique transversal des électrons $\chi_{\perp,e}$ dans les deux cas de TCV en géométrie divertor considérés, attaché (à gauche) et détaché (à droite). 17

1.1. Deuterium - Tritium fusion reaction with reaction products. 41

1.2. Schematics of the tokamak configuration, image courtesy of EUROfusion 44
1.3. Toroidal magnetic flux surfaces in a tokamak plasma, reproduced from Justin et al. 2015. The figure also represents the 2 main components of the magnetic field (toroidal $\vec{B}_\varphi$ and poloidal $\vec{B}_\theta$) as well as some of the main coordinates systems used in toroidal geometry. 45
1.4. Scrape Off Layer definition via the schematic representations of two different poloidal sections of a tokamak in limited and diverted geometries, reproduced by Yong-Su 2017. 46
1.5. Schematic view of vacuum vessel protection assembly in Tore Supra, showing water cooling panels, guard limiter and toroidal pump limiter structure, as it is presented in Lipa et al. 1997. 47
1.6. 3D schematic illustration of the design of plasma facing components in the divertor of ITER, as reported in Hassanein et al. 2021 47
1.7. Representation of the sheath (with the approximate scale lengths) formation due to charge separation at the edge of plasma. Reproduced from Stangeby et al. 2000. 48
1.8. Schematic representation of the SOL width, together with a simplistic reporting of the perpendicular and parallel fluxes. 50
1.9. Dependency of the reaction rates for ionization, recombination and CX as a function of Te, reported from Zhou et al. 2022 54
1.10. Definition of the flux tube used to describe the two point model. Reproduced from Stangeby et al. 2000. 56
1.11. Snapshots of the evolution of the electron temperature and density profile around the separatrix showing the change in plasma collisionality for a specific AUG plasma discharge, reproduced from Eich et al. 2020 . 61
1.12. Example of density profiles normalized to the separatrix value during a horizontal target L-mode D-fuelling ramp in JET showing characteristic flattening in the Far SOL, Fig. reproduced from Wynn et al. 2018. 61
1.13. Density e-folding length scaling with divertor collisionality in AUG and JET. Black, blue, and red circles represent different levels of P_{IN}. Purple circles correspond to seeded discharges [empty(solid) mean before (after) N2 puffing]. Light blue stars are data points from JET. Straight lines mark the trend for the two regimes (in terms of power). 63

2.1. Examples of computational grids for two different magnetic equilibrium with domain decomposition in SOLEDGE3X, the limited (left) and diverted (right) configuration used later in Chapters 3 and 4 respectively. The numbers indicate the indices of sub-domains of the domain decomposition used to handle arbitrary magnetic geometries. The thick black lines show the position of the wall. 78
2.2. Different application of SOLEDGE3X in 2D mean-field mode (left) in Rivals et al. 2022 or in turbulent mode in Bufferand 2023. Note the absence of fluctuation in the mean-field simulation's result. 81

2.3. EIRENE 3D mesh automatically generated via SOLEDGE3X, and here applied to a circular limiter case. 83
2.4. Ionization source S_n in 3D circular geometry provided by EIRENE. . . . 83
2.5. Trajectories of EIRENE test particles in 3D circular geometry. 84
2.6. Schematic representation of the whole global system constituted by plasma and neutrals, with fluxes contributions. 89
2.7. relative error in the particle conservation (left) and energy (right) in a TCV-X21 simulation, described later in Chapter 4 91

3.1. Representation of the circular domain illustrating the discretization mesh. The colors refer to the domain decomposition used in the code (2 sub-domains here). The black line provides the contouring of the wall with the limiter at the bottom of the machine. 95
3.2. Snapshots of plasma density, temperature and potential for the reference no neutrals case 97
3.3. Time traces of the different components of the plasma particle balance obtained from volume-integrating the ion particle balance equation (Eq. 2.52). Here one can see the evolution of the particle influx from the core region, particle outflux at the limiter and wall, particle source due to neutrals and time derivative of the plasma particle content. The black line is the sum of all these components and represents the particle conservation error, which is negligible. To be noted that the case with neutrals was restarted from the case without neutrals. 98
3.4. Time traces $[ms]$ of particle fluxes integrated in volume $[part/s]$ for the case with neutrals: here one can see the evolution of the particle outflux, particle source and time derivative. The particle conservation check is plotted in black. The red square indicates the time window during which data are analyzed in the rest of this Chapter. 99
3.5. Different time scales existing in turbulence - neutrals codes, courtesy of H. Bufferand. 100
3.6. Poloidal maps of the TNU, as it is expressed in Eq. 3.4, of the time averaged electron density $< n_e >_t$ in Fig. 3.6a and for the time averaged electron temperature $< T_e >_t$ in Fig. 3.6b for the no-neutrals (first column) and the neutrals (second column) case. 103
3.7. Poloidal map of the TNU, as it is expressed in Eq. 3.4, of the relative fluctuation rate, for the electron density (Fig. 3.7a) $X = \mathrm{rms}(n_e)_t / < n_e >_t$, and for the electron temperature $< T_e >_t$ (Fig. 3.7b) $X = \mathrm{rms}(T_e)_t / < T_e >_t$ for the no-neutrals (first column) and the neutrals (second column) case. 105

3.8. Relative toroidal fluctuation of time-averaged quantities $\frac{\langle X\rangle_t - \langle X\rangle_{t,\varphi}}{\langle X\rangle_{t,\varphi}}$ for the electron density $X = n_e$ (a) and temperature $X = T_e$ (b) as a function of $\frac{\Theta}{\pi}$ along the vertical axis ($\frac{\Theta}{\pi} = 0$ is the outboard mid-plane, increasing in the electron diamagnetic direction) and $\frac{\varphi}{\pi}$ on the horizontal axis. The location of the gas puff is indicated with a red star. The plotted flux-surface is located in the near SOL, after the separatrix $R - R_{sep} = 1$cm in the outboard mid-plane. The 1D profiles for each quantities refers to some specific poloidal locations, in particular the Inner Limiter Plate at $\Theta = 1.25\pi$rad, the Inner mid-plane at $\Theta = \pi$rad, the Outer mid-plane at $\Theta = 0$rad and the Outer Limiter Plate at $\Theta = -0.25\pi$rad. Magnetic field lines are plotted in black in the left plots. Note that the color scale for the density plot is saturated so that one can see not only the local perturbation in the vicinity of the puff, which is of the order of 40%. . . 107

3.9. Relative toroidal fluctuation $\frac{X - \langle X\rangle_\varphi}{\langle X\rangle_\varphi}$ for the electron density relative fluctuation rate $X = \frac{\mathrm{rms}\,(n_e)_t}{\langle n_e\rangle_t}$ (a) and electron temperature relative fluctuation rate $X = \frac{\mathrm{rms}\,(T_e)_t}{\langle T_e\rangle_t}$ (b), as a function of the poloidal angle θ along the vertical axis ($\theta = 0$ is the outboard mid-plane, increasing in the electron diamagnetic direction) and the toroidal coordinate φ on the horizontal axis. The location of the gas puff is indicated with a red star. The plotted flux-surface is located in the near SOL, after the separatrix $R - R_{sep} = 1$cm. The 1Ds profiles for each quantities refers to some specific poloidal location, in particular the Inner Limiter Plate at $\Theta = 1.25\pi$rad, the Inner mid-plane at $\Theta = \pi$rad, the Outer mid-plane at $\Theta = 0$rad and the Outer Limiter Plate at $\Theta = -0.25\pi$rad. Magnetic field lines are plotted in black in the left plots. 109

3.10. Poloidal distribution of ΔX_φ as expressed in 3.5 for the time-averaged electron density $< n_e >_t$ (left of 3.10a) and temperature $< T_e >_t$ (right of 3.10a), and the relative fluctuation level for the electron density (left of 3.10b) and temperature (right of 3.10b). 111

3.11. Snapshots of ions density n_i[m^{-3}] (a), electron temperature T_e[eV] (b) and potential Φ[V] (c) for the case with improved fluid neutrals. 113

3.12. Snapshot of total neutrals particle source $S_n[\frac{\mathrm{part}}{\mathrm{sm}^{-3}}]$ (top) and total energy source $S_E[\frac{\mathrm{W}}{\mathrm{m}^{-3}}]$ (bottom) at two different toroidal position (puff location $\varphi = 45°$ (left column) and away from the puff $\varphi = 0°$ (right column) for the case with neutrals considering a pressure diffusion model. 114

3.13. Snapshots on a poloidal cross-section of the ionization source term for TOKAM3X-EIRENE simulation in the plane of the gas puff, as presented in Fan et al. 2019, here expressed in [au] and logarithmic scale. 115

3.14. Poloidal profiles of the electron density (left) and electron temperature (right), averaged in time t and toroidal position φ, for the cases with neutrals ($\star$) and without neutrals ($\bullet$), in the near SOL after the separatrix $R - R_{sep}$ =1cm 116
3.15. Comparison of radial profiles of the electron density 3.15a and electron temperature 3.15b, averaged in time t and toroidal position φ, in the two considered cases with neutrals ($\star$) and without neutrals ($\bullet$). Plots are made at two different poloidal location: outer midplane (first column) and poloidal angle of the low-field side limiter target (second column). 117
3.16. Comparison of radial profiles of the relative fluctuation level (3.16a) and skewness (3.16b) of density fluctuations for the case with self-consistent neutrals ($\star$) and without neutrals ($\bullet$), at two different poloidal locations: outer midplane (first column) and outer limiter (second column). . . . 119
3.17. Comparison of radial profiles of the relative fluctuation level (3.17a) and skewness (3.17b) of electron temperature fluctuations for the case with self-consistent neutrals ($\star$) and without neutrals ($\bullet$), at two different poloidal locations: outer midplane (first column) and outer limiter (second column). 120
3.18. Comparison between the energy flux, as given in Eq. 3.7 at the outer target averaged in time t and toroidal position φ and remapped at the midplane, for the turbulent simulations without recycling (turquoise)) and with recycling (magenta). Note the log scale for the y axis. 122
3.19. Comparison between the proxy parallel energy flux (see Eq. 3.8) at the midplane averaged in time t and toroidal position φ for the turbulent simulations without recycling (turquoise) and with recycling (magenta). Full lines are the actual data from the simulation while dashed lines are the result of the double-exponential fits (Eq. 3.9). Note the log scale for the y axis. 124
3.20. Radial profiles of the flux-surface integrated total particle flux [s^{-1}] (–), and its decomposition in an anomalous flux due to fluctuations (–) of ExB (as in Eq. 3.10) and a mean field flux (–) for the case without neutrals 3.20a and with neutrals 3.20b. Courtesy of McGibbon 2024. 127
3.21. Radial profiles of the flux-surface integrated total electron energy flux [W](–), and its decomposition in an anomalous flux due to ExB fluctuations (with the split on its several contributors (–), (–), (–), (–)) as in Eq. 3.11, and a mean field flux (–). Courtesy of McGibbon 2024. 128
3.22. Anomalous transverse transport coefficients as expressed in Eq. 3.12 shown in 3.22a and as it is in Eq. 3.13) shown in Fig. 3.22b for the case without neutrals. Courtesy of McGibbon 2024. 131
3.23. Anomalous transverse transport coefficients as expressed in Eq. 3.12 shown in 3.23a and as it is in Eq. 3.13) shown in Fig. 3.23b for the case with neutrals. Courtesy of McGibbon 2024. 132
3.24. Snapshots of ions density n_i[m^{-3}] (a), electron temperature T_e[eV] (b) and potential Φ[V] (c) for the case with constant fluid neutrals. 133

3.25. Snapshot of total neutrals particle source $S_n[\frac{\text{part}}{\text{sm}^{-3}}]$ (top) and electron energy source $S_{E,e}[\frac{\text{W}}{\text{m}^{-3}}]$ (bottom) at two different toroidal position (puff location $\varphi = 45°$ (left column) and away from the puff $\varphi = 0°$ (right column)) for the case with neutrals considering a pressure diffusion model. 134
3.26. Poloidal profiles of the electron density (left) and electron temperature (right), averaged in time t and toroidal position φ, for the cases without neutrals (×), with self consistent diffusion (⋆) and constant diffusion (•), in the near SOL after the separatrix $R - R_{sep}$ =1cm 135
3.27. Comparison of the radial profiles of the density, averaged in time t and toroidal position ϕ (left) and density fluctuations (right) in Fig. 3.27a, together with temperature averaged in time t and toroidal position ϕ (left) and temperature fluctuations (right) in Fig. 3.27b for the cases without neutrals (×), with self consistent diffusion (⋆) and constant diffusion (•), at the outer midplane. 136

4.1. Left: magnetic configuration of the TCV-X23 reference scenario. Right: measurements for line integrated average density passing through the magnetic axis (NEL6) in time (bottom) and target ion flux with respect to NEL6 (top). Courtesy of D. Sales de Oliveira et SPC team. 140
4.2. Poloidal cut of the SOLEDGE3X meshes used for modeling 2D mean field transport simulations (left) and 3D turbulence simulations (right). 142
4.3. Mean field simulations particle balances (left) for the plasma system expressed as the time traces of the outflux −, neutrals source −, time derivative − and influx − (equals to zero) and the absolute value of the convergence ratio C_R as expressed in 2.59 given here in percentage for the two density cases $n_{e,sep} = 0.5 \times 10^{19}\text{m}^{-3}$ (top) and $n_{e,sep} = 1.2 \times 10^{19}\text{m}^{-3}$ (bottom). 145
4.4. Poloidal maps of the time averaged electron density $n_e[\text{m}^{-3}]$ and temperature $T_e[\text{eV}]$ for $n_{e,sep} = 0.5\times10^{19}\text{m}^{-3}$ (left) and $n_{e,sep} = 1.2\times10^{19}\text{m}^{-3}$ (right) in converged SOLEDGE3X 2D mean-field simulations which served as starting points for 3D turbulence cases. 146
4.5. Particle balance for the plasma system (left) expressed as the time traces of the outflux − and neutrals source − and convergence ratio C_R (right) as it is defined in Eq. 2.59 expressed in percentage for the two density cases $n_{e,sep} = 0.5 \times 10^{19}\text{m}^{-3}$ (top) and $n_{e,sep} = 1.2 \times 10^{19}\text{m}^{-3}$ (bottom). Compared with Fig. 4.3, only the 2 main contributors to the plasma particle balance are plotted. 147
4.6. Plot of the ion peak particle flux at the targets as a function of n_{sep} in TCV-X23 2D mean-field simulations with the Fluid Neutrals model (FN) and with a kinetic neutrals model in EIRENE (EIR). 148

4.7. Evolution of the peak electron temperature T_e [eV] at the outer target as a function of the separatrix density in TCV-X23 2D mean-field simulations with the Fluid Neutrals model (FN) and with a kinetic neutrals model in EIRENE (EIR). 149
4.8. Plot of the plasma collisionality at the outer target normalized with respect to the one at the lowest density in the scan (see Eq. 4.1) as a function of the separatrix upstream density n_{sep}, for the Fluid Neutrals model (FN) and the kinetic neutrals model in EIRENE (EIR). 150
4.9. Poloidal maps of the ionization source $S_n[\frac{\mathbf{part}}{\mathrm{s}}]$ for the Fluid Neutrals model (FN) and the kinetic neutrals model in EIRENE for two upstream separatrix densities: $n_{sep} = 0.5 \times 10^{19}\mathrm{m}^{-3}$ (left) and $n_{sep} = 1.2 \times 10^{19}\mathrm{m}^{-3}$ (right). 151
4.10. Snapshots of the poloidal maps of the electron density $n_e[\mathrm{m}^{-3}]$ and temperature T_e[eV] for $n_{e,sep} = 0.5 \times 10^{19}[\mathrm{m}^{-3}]$ (left) and $n_{e,sep} = 1.2 \times 10^{19}[\mathrm{m}^{-3}]$ (right) in 3D turbulence cases. 152
4.11. Poloidal profiles of the mean electron temperature T_e [eV], averaged in time t and toroidal position φ, for the two density cases $n_{e,sep} = 0.5 \times 10^{19}\mathrm{m}^{-3}$ (-) and $n_{e,sep} = 1.2 \times 10^{19}\mathrm{m}^{-3}$ (-) at the separatrix. 152
4.12. Poloidal maps of the time and toroidal average neutrals source $S_n[\frac{\mathrm{part}}{\mathrm{s}}]$for $n_{e,sep} = 0.5 \times 10^{19}\mathrm{m}^{-3}$ (left) and $n_{e,sep} = 1.2 \times 10^{19}\mathrm{m}^{-3}$ (right). Here the colorbar is set to show only their positive values. 153
4.13. Poloidal maps of the mean electron density $n_e[\mathrm{m}^{-3}]$, averaged in time and toroidal direction, for $n_{e,sep} = 0.5 \times 10^{19}\mathrm{m}^{-3}$ (left) and $n_{e,sep} = 1.2 \times 10^{19}\mathrm{m}^{-3}$ (central). The right plot shows the relative difference between the high density and low density case, relative to the low density case. . 154
4.14. Poloidal maps of the mean electron temperature T_e [eV], averaged in time and toroidal direction, for $n_{e,sep} = 0.5 \times 10^{19}\mathrm{m}^{-3}$ (left) and $n_{e,sep} = 1.2 \times 10^{19}\mathrm{m}^{-3}$ (central). The third poloidal maps represent the relative difference among the high density and low density case, relative to the low density case. 155
4.15. Poloidal maps of the mean ion temperature T_i [eV], averaged in time and toroidal direction for $n_{e,sep} = 0.5 \times 10^{19}\mathrm{m}^{-3}$ (left) and $n_{e,sep} = 1.2 \times 10^{19}\mathrm{m}^{-3}$ (central). The third poloidal maps represent the relative difference between the high density and low density case, relative to the low density case. 156
4.16. Poloidal maps of the density fluctuations $n_e - \bar{n}_e$ for $n_{e,sep} = 0.5 \times 10^{19}\mathrm{m}^{-3}$ (left) and $n_{e,sep} = 1.2 \times 10^{19}\mathrm{m}^{-3}$ (right). 157
4.17. Poloidal distribution of the relative fluctuations level for the electron density n_e averaged in time t and toroidal position φ, for the two density cases $n_{sep} = 0.5 \times 10^{19}\mathrm{m}^{-3}$ (left) and $n_{sep} = 1.2 \times 10^{19}\mathrm{m}^{-3}$ (center), together with the map (right) of their difference (high - low). 158

4.18. Radial profiles of the absolute (plot (a), top row, in [m^{-3}]) and relative (plot (b), bottom row) fluctuation of the density for the two density cases $n_{e,sep} = 0.5\times10^{19}m^{-3}$ (•) and $n_{e,sep} = 1.2\times10^{19}m^{-3}$ (⋆) at 4 poloidal locations: the outer mid-plane, outer target, mid-outer-divertor (at $Z \approx -0.4$) and inner target (from left to right). The horizontal axis corresponds to the radial distance to the separatrix after remapping along flux-surfaces to the outboard mid-plane. 159
4.19. Poloidal distribution of the relative fluctuations level for the electron temperature T_e averaged in time t and toroidal position φ, for the two density cases $n_{sep} = 0.5\times10^{19}m^{-3}$ (left) and $n_{sep} = 1.2\times10^{19}m^{-3}$ (center), together with the map (right) of their relative difference (high - low). 160
4.20. Radial profiles of the absolute (plot (a), top row, in [eV]) and relative (plot (b), bottom row) fluctuation for the electron temperature for the two density cases $n_{e,sep} = 0.5\times10^{19}m^{-3}$ (•) and $n_{e,sep} = 1.2\times10^{19}m^{-3}$ (⋆) at 4 poloidal locations: the outer mid-plane, outer target, mid-outer-divertor (at $Z \approx -0.4$) and inner target (from left to right). The horizontal axis corresponds to the radial distance to the separatrix after remapping along flux-surfaces to the outboard mid-plane. 161
4.21. Radial profiles of the relative fluctuation for the ion temperature $\frac{\sigma_{T_i}}{\bar{T}_i}$ for the two density cases $n_{e,sep} = 0.5\times10^{19}m^{-3}$ (•) and $n_{e,sep} = 1.2\times10^{19}m^{-3}$ (⋆) at the outer mid-plane (left) and outer target (right). 162
4.22. Radial profiles of the skewness of density fluctuations (left) and electron temperature fluctuations (right) for the two density cases $n_{e,sep} = 0.5\times10^{19}m^{-3}$ (•) and $n_{e,sep} = 1.2\times10^{19}m^{-3}$ (⋆) at the outer mid-plane. . . . 163
4.23. Radial profiles of the mean electron density n_e[m^{-3}] averaged in time t and toroidal position φ, for the two density cases $n_{e,sep} = 0.5\times10^{19}m^{-3}$ (•) and $n_{e,sep} = 1.2\times10^{19}m^{-3}$ (⋆) at the outer mid-plane, mid-divertor region, outer and inner targets. The horizontal axis corresponds to the radial distance to the separatrix after remapping along flux-surfaces to the outboard mid-plane. 165
4.24. Radial profiles of the mean electron temperature T_e [eV], averaged in time t and toroidal position φ, for the two density cases $n_{e,sep} = 0.5\times10^{19}m^{-3}$ (•) and $n_{e,sep} = 1.2\times10^{19}m^{-3}$ (⋆) at the outer mid-plane, mid-divertor region, outer and inner targets. The horizontal axis corresponds to the radial distance to the separatrix after remapping along flux-surfaces to the outboard mid-plane. 166
4.25. Radial profiles of the mean ion temperature T_i[eV] averaged in time t and toroidal position φ, for the two density cases $n_{e,sep} = 0.5\times10^{19}m^{-3}$ (•) and $n_{e,sep} = 1.2\times10^{19}m^{-3}$ (⋆) at the outer mid-plane, mid-divertor region, outer and inner targets. The horizontal axis corresponds to the radial distance to the separatrix after remapping along flux-surfaces to the outboard mid-plane. 167

4.26. Radial profiles of the proxy parallel heat flux (Eq. 3.8) in the outboard mid-plane. Left: from the 2D mean-field simulations used as initial conditions; right: from the time- and toroidal-averaged data from the 3D global turbulence simulations. Full lines are the actual data computed via Eq. 3.8 at the midplane while dashed lines are the result of a single exponential fit respectively for the mean-field cases and turbulent cases as defined in Eq. 3.9. Cyan lines are for the low density case $n_{sep} = 0.5 \times 10^{19}\mathrm{m}^{-3}$ and purple lines for the high density case $n_{sep} = 1.2 \times 10^{19}\mathrm{m}^{-3}$. 168
4.27. Comparison between the proxy parallel energy flux (see Eq. 3.8) at the midplane averaged in time t and toroidal position φ for the low density case $n_{sep} = 0.5 \times 10^{19}\mathrm{m}^{-3}$ (turquoise) and for the high density case $n_{sep} = 1.2 \times 10^{19}\mathrm{m}^{-3}$ (magenta). Full lines are the actual data from the turbulent simulation while dashed lines are the result of the double-exponential fits (Eq. 3.9). Note the log scale for the y axis. 170
4.28. Density decay length in the SOL at the outer midplane for the low $0.5 \times 10^{19}\mathrm{m}^{-3}$ and high $n_{sep} = 1.2 \times 10^{19}\mathrm{m}^{-3}$ density case. 171
4.29. Temperature decay length in the SOL at the outer midplane for the low $0.5 \times 10^{19}\mathrm{m}^{-3}$ and high $n_{sep} = 1.2 \times 10^{19}\mathrm{m}^{-3}$ density case. 172
4.30. Radial profiles of the effective collisionality $\Lambda_{div}[\mathrm{m}^{-1}]$ for $n_{sep} = 0.5 \times 10^{19}\mathrm{m}^{-3}$ and $n_{sep} = 1.2 \times 10^{19}\mathrm{m}^{-3}$. 173
4.31. Poloidal maps of reconstructed ExB anomalous transverse transport coefficients for particles, electron energy and ion energy (from left to right) for the attached case $n_{sep} = 0.5 \times 10^{19}\mathrm{m}^{-3}$. 174
4.32. Poloidal maps of reconstructed ExB anomalous transverse transport coefficients for particles, electron energy and ion energy (from left to right) for the detached case $n_{sep} = 1.2 \times 10^{19}\mathrm{m}^{-3}$. 175
4.33. Poloidal maps of reconstructed ExB anomalous transverse transport coefficients for particles, electron energy and ion energy (from left to right) for the attached case $n_{sep} = 0.5 \times 10^{19}\mathrm{m}^{-3}$. This figure shows the same data as Fig. 4.31 but with different colorbars shared with Fig. 4.34 to ease the comparison with the detached case. 176
4.34. Poloidal maps of reconstructed ExB anomalous transverse transport coefficients for particles, electron energy and ion energy (from left to right) for the detached case $n_{sep} = 1.2 \times 10^{19}\mathrm{m}^{-3}$. This figure shows the same data as Fig. 4.32 but with different colorbars shared with Fig. 4.33 to ease the comparison with the attached case. 177
4.35. Poloidal maps of transport coefficients for the heuristic mean-field transport model (Eq. 4.6 to 4.8), as reconstructed from turbulence data for the attached case $n_{sep} = 0.5 \times 10^{19}\mathrm{m}^{-3}$. 179
4.36. Poloidal maps of transport coefficients for the heuristic mean-field transport model (Eq. 4.6 to 4.8), as reconstructed from turbulence data for the detached case $n_{sep} = 1.2 \times 10^{19}\mathrm{m}^{-3}$. 180
4.37. Poloidal maps of the transport coefficients D_{nn} (left) and $D_{nT,e}$ (right) as defined in Eq. 4.20 for the attached case, $n_{sep} = 0.5 \times 10^{19}\mathrm{m}^{-3}$. 183

4.38. Poloidal maps of the transport coefficients D_{nn} (left) and $D_{nT,e}$ (right) as defined in Eq. 4.20 for the detached case, $n_{sep} = 1.2 \times 10^{19}\mathrm{m}^{-3}$. . . . 183

List of Tables

3.1. Input parameters for the machines dimensions (major and minor radius, heating power and transport coefficients) in SI units, together with the aspect ratio common to all the circular simulations. 95
3.2. Values of fitting parameters for the double exponential fit (Eq. 3.9) of the proxy parallel heat flux in the mid-plane for the cases without and with neutrals recycling. 124

4.1. Single exponential fit parameters λ_q and q_{peak} for the 2D mean-field simulations at low and high separatrix density n_{sep}. 169
4.2. Values of λ_q and q_{peak} extracted from turbulent simulations via a double exponential fit 169
4.3. Values of λ_n and λ_T for the low and high density case obtained via an exponential regression, in the near and in the far SOL at the OMP. . . . 171

A.1. EIRENE mesh files list and contents description. 208

1. Introduction

1.1. Fusion as energy source in the World energy landscape

Throughout the last centuries, beginning from the industrial revolution up to the present day, humanity has grappled with energy demands and more recently the urgent need to combat climate change. The persistent quest for sustainable, clean energy sources to address the climate crisis has become increasingly urgent, seeking alternatives to fossil fuels.

Nuclear fusion is not a novelty. It was envisioned as a potential source of energy almost as soon as it was discovered; in 1920, Arthur Eddington, was among the pioneers exploring the idea of generating power from fusion reactors (Eddington 1979). Currently, fusion research centers and emerging fusion industries, including numerous startups worldwide, are addressing various physics and engineering obstacles and exploring potential solutions. The complexity spans multiple domains, and to establish fusion as a viable energy source, several critical challenges must be overcome. Despite the considerable engineering and physical challenges associated with fusion power generation, it remains an indispensable part of the long term pathway toward de-carbonization. Although the journey towards large-scale energy generation from nuclear fusion may take longer than anticipated (most experts agree not earlier than 2050), the potential benefits are substantial, promising a brighter future.

Nowadays, in the broader nuclear fusion landscape involving as well private-sector initiatives, the most significant undertaking in the field of research is ITER. ITER ambitiously aims to prove the feasibility of nuclear fusion through a worldwide collaborative effort, demonstrating its potential as a practical and sustainable energy source. The name ITER was not chosen without purpose: it stems from Latin, and its meaning is "the way." Moreover, its motto "Bringing a Sun to Earth" signifies more than just a poetic notion.

Nuclear fusion is indeed the dominant mechanism governing the existence of stars. The combination of light hydrogen nuclei to form helium atoms is the primary process fueling the Sun, occurring only under conditions of extreme pressure and temperature, around 10^7K. Such temperatures are necessary for nuclei to overcome Coulomb repulsion and fuse, and result in matter being in a state known as plasma. Plasma is comprised of positive and negative charged particles. Locally the overall sum of charges is roughly zero, ensuring quasi-neutrality. Among all the possible combination of light nuclei, the fusion reaction between deuterium and tritium (illustrated in Fig. 1.1) is regarded as the most promising one, primarily because it has the highest

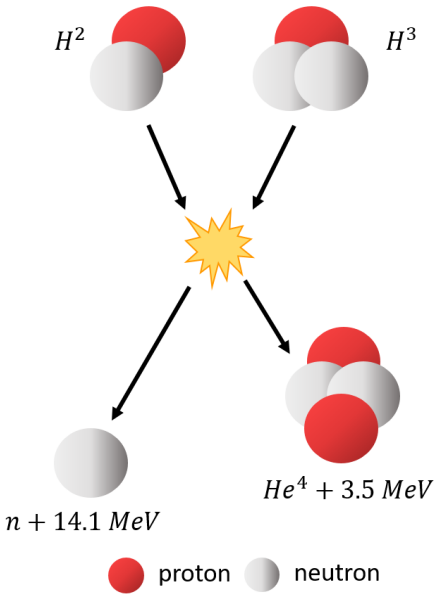

Figure 1.1. – Deuterium - Tritium fusion reaction with reaction products.

reaction cross section and the lowest temperature threshold. This reaction yields Helium-4 nucleus, a neutron capable of sustaining tritium breeding from lithium, and a substantial amount of kinetic energy carried by the two reaction products, distributed in 14.1MeV for the neutron and 3.5MeV for the Helium-4 nucleus.

1.2. Magnetic confinement: the tokamak as magnetic fusion device

1.2.1. The Lawson criterion

Fusion on Earth is only feasible by "confining" the plasma in order to reach fusion compatible conditions without spending more energy than what fusion reactions will produce. To demonstrate that, let us derive a 0D energy balance for a basic system in which fusion is assumed to occur. For effective energy production, the total energy gain from fusion P_{fusion} must at least offset the energy initially injected in the system by external means P_{heat}:

$$P_{fusion} \geq Q P_{heat}, \tag{1.1}$$

where Q is the energy multiplication factor. 2 key thresholds in Q can be considered: $Q = 1$, i.e. when the system produces as much energy by fusion reactions as was used to generate them, is referred to as the break-even; $Q = \infty$, i.e. when the system is self-sustained and does not need external energy input to maintain fusion reaction,

is referred to as ignition. P_{fusion} can be split into 2 components: $P_\alpha \approx 0.2 P_{fusion}$, the energy from fusion reactions carried by α particles (the 3.5MeV of Fig. 1.1) and assumed to remain in the system as α particles are charged particles and will enter the composition of the plasma; $P_{neutron}$, the energy carried by neutrons and assumed to escape the plasma with no further interaction with it. The 0D energy balance of the plasma imposes:

$$P_{heat} + P_\alpha = P_{losses}, \tag{1.2}$$

which combined with the previous equation gives the following condition:

$$P_{fusion} \geq \frac{Q}{1+0.2Q} P_{losses}. \tag{1.3}$$

We now express power densities P_{fusion} and P_{losses} as a function of plasma conditions: $P_{fusion} = n_D n_T < \sigma v > E_{fusion}$ and $P_{losses} \simeq \frac{3nk_BT}{2\tau_E}$. n_D and n_T refers respectively to the densities of deuterium and tritium, and they can be assumed to be equal to $n_D = n_T = n/2$, with n the total fuel ions density within the system, $< \sigma v >$ to the reaction cross section dependent on the temperature T and $E_{fusion} = 17.6MeV$. τ_E is the energy confinement time (characteristic time of the energy loss rate of the plasma), while k_B the Boltzmann constant. Using some approximate fit for the fusion reaction cross-section as a function of T, one finally can express the previous inequality as:

$$nT\tau_E \geq f(Q), \tag{1.4}$$

where $f(Q)$ is an increasing function of Q (expression not detailed here). Eq. 1.4 is known as the Lawson criterion, of which a proper derivation can be found in Hsieh et al. 2022, and the term $nT\tau_E$ is named triple product. In essence, the Lawson criterion sets a threshold for the triple product, beyond which a net energy gain from the fusion reaction is achieved. Maximizing the energy amplification factor necessitates maximizing the triple product.

In practice, the achievement of the Lawson criterion on Earth has been pursued along 2 opposite approaches: *inertial* confinement using lasers or *magnetic* confinement via strong magnetic fields. In the former, subjecting deuterium-tritium targets to intensely energetic lasers or microwave pulses leads to the generation of an extremely high density plasma at the expenses of τ_E. In the latter approach, one tries on the contrary to maximize τ_E while keeping density and temperature as high as possible. In this thesis, we focus on the physics in magnetic confinement fusion devices and will not address inertial confinement fusion.

1.2.2. Basic principle of magnetic confinement

Confining plasmas using a magnetic field $\vec{B}$ is possible because plasmas consist of charged particles. When a charged particle, like an ion or electron, moves through a magnetic field $\vec{B}$, it experiences the Lorentz force, expressed in Eq.1.5.

$$\vec{F} = q(\vec{v} \times \vec{B}). \tag{1.5}$$

Here, q is the charge of the particle, and $\vec{v}$ is its velocity. When a charged particle enters a magnetic field, it girates around the field lines rather than moving in a straight line. This helical motion confines the particle along the field's direction, limiting its movement perpendicular to the field. The radius of this helix, known as the gyroradius (or Larmor radius), is determined by the particle's charge, mass, velocity, and the strength of the magnetic field.

$$\rho_L = \frac{v_\perp}{\omega_c} \tag{1.6}$$

In Eq. 1.6, $v_\perp$ is the component of the particle's velocity perpendicular to the magnetic field and $\omega_c = \frac{qB}{m}$ the gyro-frequency. Under typical fusion conditions (Deuterium plasma, $T = 10$ keV, $B = 6$ T) the order of magnitude of the Larmor radius is millimeters, making it one of the smallest scales to consider in a fusion device.

As a result of the Lorentz force, particles are confined in the plane transverse to the magnetic field and free to move only along the direction of the magnetic field $\vec{B}$. To address this, one needs either to constrain the movement of particle along the direction of $\vec{B}$ (this can be done by imposing a longitudinal gradient in the amplitude of the magnetic field) or to close magnetic field's lines on themselves. The later strategy is the one used in toroidal magnetic fusion devices as the Tokamak, in which magnetic field lines live on nested toroidal surfaces. We will see later that, although confinement in magnetic fusion devices is generally effective, it is not perfect.

1.2.3. The tokamak configuration

Among the magnetic confinement designs, the most investigated solution is called *tokamak*, developed as a toroidal (or doughnut-shaped) container. The first design of the tokamak has origins in Russia, and the acronym means "toroidal chamber with magnetic coils". Its main characteristic with respect to other toroidal magnetic confinement devices is the fact that the plasma itself is used as a conductor to carry current that will contribute to the generation of the confinement field.

The tokamak configuration reported in Fig. 1.2 relies on coils positioned around the machine. The toroidal field coils generate a several tesla toroidal magnetic field. The toroidal field is the main contributor to the confinement of the plasma. However, this field is not sufficient to achieve large enough confinement times to obtain large Q factors, as the curvature of the toroidal field is responsible for the existence of a transverse drift of particles. In the tokamak configuration, the effects of these drifts are compensated by a rotational transform resulting from an additional poloidal component of the magnetic field being produced by a current circulating in the plasma along the toroidal direction. This current is induced in the plasma by transformer effect, by varying the current flowing through a coil located along the symmetry axis of the torus, called the central solenoid. In addition to this, outer poloidal field coils

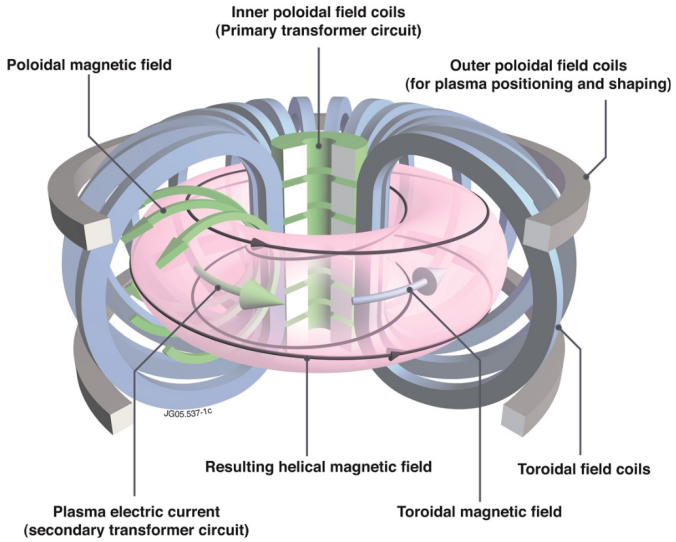

Figure 1.2. – Schematics of the tokamak configuration, image courtesy of EUROfusion

are needed for plasma positionning and shaping, as well as producing a vertical component of the magnetic field needed to compensate the hoop force on the plasma current loop.

The primary functions of the confining field are to increase insulation against radial heat transport and manage the interface of the plasma and the "first wall," the inner part of the vessel in direct view of the plasma, in order to avoid particle and energy losses as well as structural damage.

To initiate fusion reactions in a tokamak, creating a vacuum within the chamber is necessary. Then, gaseous fuel is injected and a toroidal electric field is generated in the chamber by varying the current in the central solenoid, which then leads to the break down, consisting in the ionization of the gas followed by the generation of a current. The energized plasma particles collide and heat up, while auxiliary heating systems increase the temperature to the threshold needed to overcome the Coulombian repulsion and facilitate collisions between nuclei.

1.3. The Scrape-Off Layer

1.3.1. Closed vs Open magnetic flux surfaces

The helical magnetic field $\vec{B}$ can be decomposed into a toroidal component B_ϕ and a poloidal component B_θ as reported in Fig. 1.3. The field lines wind around nested toroidal surfaces named magnetic flux surfaces, also illustrated in Fig. 1.3. Indeed, each flux surface can be uniquely labelled according the magnetic flux, defined as the flux of the magnetic field through the horizontal plane between the magnetic axis and the considered flux surface (Stangeby et al. 2000).

Since the confinement in a tokamak is not perfect, because of collisions and tur-

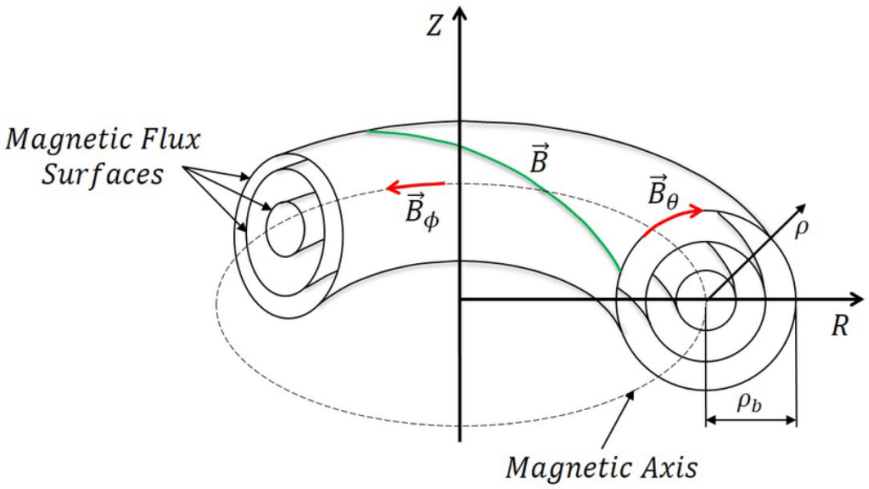

Figure 1.3. – Toroidal magnetic flux surfaces in a tokamak plasma, reproduced from Justin et al. 2015. The figure also represents the 2 main components of the magnetic field (toroidal $\vec{B}_\varphi$ and poloidal $\vec{B}_\theta$) as well as some of the main coordinates systems used in toroidal geometry.

bulences, the plasma will be slowly transport accross flux surfaces until hitting some object on its way. At this point, distinguish open and closed flux surfaces should be distinguished: closed flux surfaces in the so-called confined plasma do not intersect any object, while beyond a given radius they do. The Last Closed Flux Surface (LCFS) marks the transition between the two regions and in the specific case of the divertor configuration (introduced in the next section) the separatrix. The area located radially outside the LCFS is commonly referred to as the Scrape-Off Layer (SOL), as it is a region where plasma density and temperature sharply decrease radially.

1.3.2. Limited vs Diverted configurations

In practice, two main configurations are possible concerning the edge plasma in the design of a tokamak, and they are going to be used both in this manuscript: the limited and the diverted ones.

The difference between the two configurations essentially stems from the magnetic configuration and the shape of the LCFS as illustrated in Fig. 1.4. In the limited configuration, the LCFS is defined by a dedicated object, the limiter, protruding in front of the rest of the vacuum vessel. In the divertor configuration, an additional poloidal magnetic field is generated in the divertor region via a dedicated coil. The current in the coil is in the same direction as the plasma current, thus generating a poloidal field rotating in the same direction as the poloidal field of the plasma. The sum of the 2 fields leads to the existence of a null-point for the poloidal field where the corresponding flux surface exhibits an *X-point* similarly to the separatrix in the phase space of a harmonic pendulum (see Fig. 1.4). By analogy, the LCFS is then called

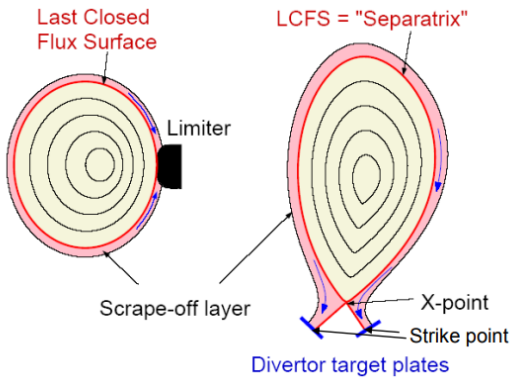

Figure 1.4. – Scrape Off Layer definition via the schematic representations of two different poloidal sections of a tokamak in limited and diverted geometries, reproduced by Yong-Su 2017.

separatrix. All the region of the plasma below the vertical position of the X-point is often referred to as the divertor region, and the specific region under the X-point and under the separatrix is known as the private flux region.

Both the limiter and the divertor serve to manage the heat and particle exhaust, detailed in Section 1.4. Although high performance tokamaks currently rely on diverted configurations, the plasma always goes through a limited configuration at startup so that the latter is still relevant, and will be studied in simulations described in Chapter 3.

As depicted in Fig. 1.6 which provides a schematic for the ITER divertor, the divertor, located at the bottom of the machine, is designed to create a buffer region between the confined plasma and the target plates where the heat and particles can be safely handled, and has thus superior exhaust capabilities than a limiter (both for particles and heat).

1.3.3. Sheath boundary conditions in a nutshell

The presence of solid objects in the SOL leads to the existence of specific boundary conditions for the plasma, defining particle and energy deposition on the surfaces of the plasma facing components.

As the plasma approaches the walls, a thin region of net charge, known as the *sheath*, forms very close to the solid surface, characterized by the onset of a discrepancy between the species densities, with $n_e < n_i$, as illustrated in Fig. 1.7. This occurs because electrons, being lighter than ions, are more mobile and they can reach the surface more quickly, causing a depletion of negative charges in the plasma and a negative polarization of the wall with respect to the plasma. In the sheath region, the potential Φ becomes increasingly negative compared to the upstream plasma (further away from the wall). This creates a potential drop across the sheath that repels electrons and accelerates ions. Equilibrium is established when ions and electrons

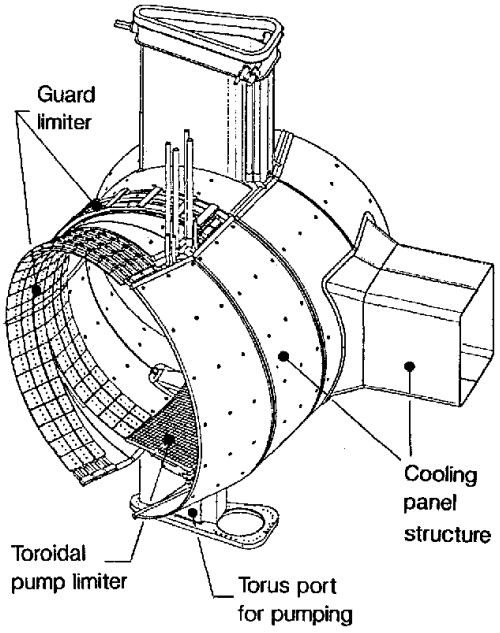

Fig. 1 Schematic view of vacuum vessel protection assembly, showing wafer cooling panels, guard limiters and toroidal pump limiter structure.

Figure 1.5. – Schematic view of vacuum vessel protection assembly in Tore Supra, showing water cooling panels, guard limiter and toroidal pump limiter structure, as it is presented in Lipa et al. 1997.

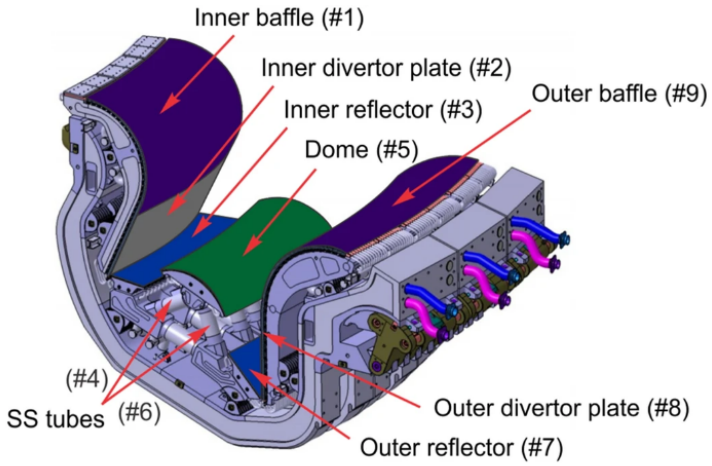

Figure 1.6. – 3D schematic illustration of the design of plasma facing components in the divertor of ITER, as reported in Hassanein et al. 2021

attain the same velocity, resulting in no net current at the surface.

The sheath typically has a thickness of a few Debye lengths ($\lambda_D = \sqrt{\frac{\epsilon_0 k_B T_e}{n_e e^2}}$), ranging from $3\lambda_D$ to $10\lambda_D$ according to Stangeby et al. 2000, although it can be thicker depending on the specific conditions of the plasma and the material surface. This thickness

ensures that the plasma can effectively shield the electric fields near the surface.

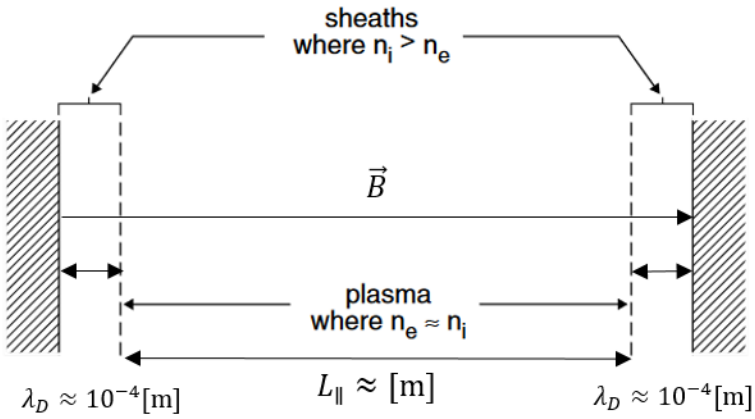

Figure 1.7. – Representation of the sheath (with the approximate scale lengths) formation due to charge separation at the edge of plasma. Reproduced from Stangeby et al. 2000.

An analytical derivation of the boundary conditions such phenomenology imposes to the plasma can be made within the simplistic assumption of a simple single ion species plasma, a collisionless and isothermal sheath, an incidence of the magnetic field normal to the wall ($\vec{b}\cdot\vec{n} = \pm 1$) and maxwellian (or truncated maxwellian) distributions at any point in space. In such a framework, it is possible to derive conditions for the existence of an asymptotic match between a collision-less sheath and a collisional plasma. One finds that the outgoing ion parallel velocity (parallel with respect to the magnetic field, outgoing with respect to the plasma) at the sheath entrance (*se*) must be at least equal to a critical value related to the group velocity of acoustic waves in the plasma. This relation is known as Bohm criterion and it does ensure that the ion flux eventually balances the electron flux.

$$u_{\parallel,i}\vec{b}\cdot\hat{n} > c_s\vec{b}\cdot\hat{n} = \sqrt{\frac{k_B(T_e+T_i)}{m_i}}\vec{b}\cdot\hat{n} \tag{1.7}$$

where $\vec{b} = \frac{\vec{B}}{B}$ is the unit vector along the magnetic field's direction and $\hat{n}$ is the unit vector normal to the wall orientated towards the solid.

The Bohm criterion also provides the potential drop in the sheath, the current at the sheath entrance when e.g. the potential fluctuates and the energy fluxes at the sheath entrance. The sheath potential drop is such that it repels the bulk of electrons while allowing ions to accelerate towards the wall. To reach ambipolar conditions (equal ion and electron flux), and taking the wall potential as the reference zero potential, the electrostatic potential has to reach the following value at the sheath entrance:

$$\Phi^{se} \approx -\frac{k_B T_e}{e} 0.5 \ln\left(2\pi \frac{m_e}{m_i}\left(1+\frac{T_i}{T_e}\right)\right) \equiv -\frac{k_B T_e}{e}\Lambda \tag{1.8}$$

where the Coulombian logarithm is assumed to be negative due to its quantity $\frac{m_e}{m_i} << 1$. This potential is often referred to as the floating potential as it is the plasma potential at which no current is exchanged between the wall and the plasma. In reality, current is locally allowed to flow and the boundary condition can be generalized into a relation between the potential at the sheath entrance and the current reaching the wall along the direction of the magnetic field:

$$\vec{j}_{\parallel} = n_i u_{\parallel,i} e\left(1 - e^{\Lambda - \frac{e\Phi^{se}}{k_B T_e}}\right) \tag{1.9}$$

The heat flux to the surface from the plasma has contributions from both ions and electrons. In a simple sheath model, it can be demonstrated Stangeby et al. 2000 that the total heat flux carried by electrons q_e is proportional to the convected heat flux:

$$q_e = \gamma_e n_e u_{\parallel,e} T_e \tag{1.10}$$

with γ_e the electron sheath transmission coefficient, typically in a range between 4 and 7, depending on the plasma conditions considered (see possible refinements in Fig. 4.8 of ibid.). The ion heat flux q_i obeys the same type of boundary condition:

$$q_i = \gamma_i n_i u_{\parallel,i} T_i \tag{1.11}$$

where γ_i is the ion sheath transmission coefficient, typically equal to 2.5 according to ibid. One can recognize a fundamental property of the sheath in the fact that $\gamma_e > \gamma_i$, i.e. that it acts as a filter to repel slow electron so that only fast electrons can go through the sheath and they carry in average more energy than the average energy of the electron population. The ions on the contrary all fall in the sheath potential well.

All of these relations are obtained in a simplified frame, based on many assumptions. Refinements can be taken into account, in particular considering a non-normal incidence to the magnetic fields (Chodura 2005); however, even the simplest expression of Bohm criterion explained here captures most of the basic features of the sheath.

1.3.4. The SOL width

The Bohm condition implies that the wall acts as a significant sink for both particles and energy, absorbing plasma so efficiently that, beyond the virtual boundary of the sheath entrance, everything happens as if the plasma essentially expands into empty space. This leads to a rapid decay in plasma parameters when moving radially out of the confined plasma into the Scrape-Off Layer. In the simplest models, the decay of plasma parameters such as density, temperature, and heat flux is exponential and can be described using different decay lengths or SOL widths denoted by λ_n for the density, λ_{T_e} for the electron temperature, and so on. This can be shown simply using a 1D model of the SOL plasma. The fluid particle balance in flux tubes connected to

the wall gives:

$$D_\perp \frac{\partial^2 n}{\partial r^2} = \frac{n c_s}{L_\parallel}, \tag{1.12}$$

where we have assumed that the cross-field radial particle flux follows Fick law, $-D_\perp \partial n/\partial r$. The right-hand side models the parallel losses due to the Bohm boundary conditions on both ends of the fields lines of length $L_\parallel$. The previous equation has an obvious exponentially decaying solution:

$$n = n_0 e^{-r/\lambda_n}, \tag{1.13}$$

with $\lambda_n = \sqrt{\frac{L_\parallel D_\perp}{c_s}}$. This expression shows that the SOL width stems from a competition between the perpendicular transport level (measured by $D_\perp$) and parallel transport / losses (measured by $L_\parallel / c_s$).

The actual experimental behavior does not always follow this simple exponential decay model. However, the use of an e-folding length is still useful for defining the width of the SOL—the radial distance over which the plasma parameters decrease. This quantity is often measured in the outer part of the mid-plane of the machine, as illustrated in Fig. 1.8.

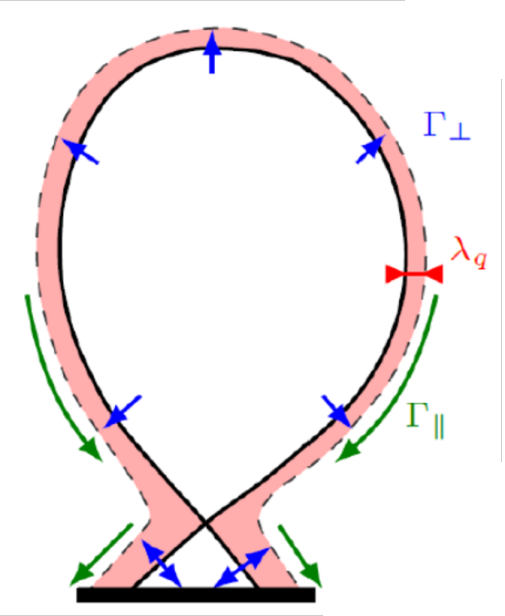

Figure 1.8. – Schematic representation of the SOL width, together with a simplistic reporting of the perpendicular and parallel fluxes.

Let us put some typical numbers in Eq. 1.13. In a typical medium sized tokamak, one has: $L_\parallel = 50$m, $c_s = 10^5$, $D = 1[\frac{m^2}{s}]$, $n_0 = 1 \times 10^{19}[m^{-3}]$, $\lambda_n \in [1-5]$ cm. This way, the SOL width is significantly smaller than the typical machine size. This can be explained qualitatively by the fact that, due to the magnetic confinement, the parallel transport is much faster than the perpendicular one. In this fashion, particles entering

the SOL are lost before having the time to move outwards radially, making the SOL width narrow compared to the machine size.

The SOL width is a crucial parameter for the design of plasma devices. To predict this width, it is important to highlight the existence of several experimental scaling laws that describe, in particular, the radial decay of the parallel heat flux and its associated decay length, λ_q. One of the most used in the plasma edge community for H-mode plasmas is the Eich scaling law (Eich et al. 2020).

$$\lambda_q \simeq 1.6 \times \frac{a}{R} \frac{\sqrt{m_i T_{sep}}}{eB_{pol}} \tag{1.14}$$

In Eq. 1.14, a and R are the minor and major radii, m_i the ion mass, $T_{sep} = T_e = T_i$ the electron and ion temperatures at the separatrix, and B_{pol} the poloidally averaged poloidal magnetic field. This experimental result indicates that the SOL power flux channel width λ_q scales inversely with the amplitude of the poloidal magnetic field $\vec{B_p}$. This means that λ_q is expected to decrease as one moves to larger machines with larger plasma currents (hence poloidal field).

1.4. The challenge of the heat exhaust

In order to contextualize the issue of power exhaust in tokamaks, let us investigate the power balance for an ITER burning plasma.

ITER burning plasmas are expected to be heated with 50MW of external heating and achieve $Q = 10$, meaning that $500 \times 0.2 = 100$MW of fusion power will additionally heat up the plasma through alpha particles. About 30% of this power is expected to be radiated, leaving $P_{exhaust} \approx 100$MW of thermal power transported by the plasma to the walls. The resulting power flux per unit of surface, mainly localized at the limiter or divertor targets, can be estimated as:

$$q_{wall} = \frac{P_{exhaust}}{S_{wet}}, \tag{1.15}$$

where $S_{wet} = 2 \times 2\pi R_0 \lambda_q f_{geo}$ is the plasma wetted surface, R_0 being the major radius, λ_q the heat flux decay length and f_{geo} a geometrical spreading factor related to the magnetic flux expansion and the geometry of the targets. The factor of 2 stems from the presence of 2 targets, one on the low-field side and one of the high-field side. Typical values for ITER are $R_0 = 6$ m, $f_{geo} \approx 10$, and $\lambda_q \approx 1$mm from the Eich's scaling law, giving:

$$q_{wall} \approx 130 \frac{\text{MW}}{\text{m}^2} \gg q_{lim} \tag{1.16}$$

i.e., a non mitigated heat flux much greater than the engineering limit in steady state for plasma facing components, which is of the order of 10 - 20 $\frac{\text{MW}}{\text{m}^2}$ RA Pitts et al. 2011.

To prevent material damage, a robust power exhaust strategy is crucial. Energy fluxes

must be distributed over a wider area. Geometric solutions such as flux expansion or tile tilting are implemented (as already apparent in the f_{geo} factor above), but these alone are insufficient.

The envisaged strategy to manage high heat fluxes relies on the natural presence of neutrals in the edge plasma, facilitating transfer of power to non-confined particles (photons and neutrals) via atomic and molecular reactions before reaching the wall. Additionally, turbulence in the peripheral region, where plasma is closer to the wall, will help broadening the width of the Scrape-Off-Layer (SOL) (Eich et al. 2020), further aiding in heat spreading. This point will be further addressed in Section 1.7.

1.5. Neutrals recycling and density regimes

1.5.1. Plasma-wall interactions

Contact of plasma with a solid material leads to a series of processes known as plasma - wall interactions, or PWIs. These processes include material erosion via sputtering or trapping of the initial projectile ion in the solid. However, the most remarkable of these phenomena is the surface recombination, which takes place when plasma ions striking the wall promptly neutralize, forming atoms or even molecules. In this situation, the fast impinging ions can either be backscattered or stick to the surface of the material. In the first scenario, after being accelerated in the sheath the ion recombines with an electron from the surface and is thus backscattered as a fast neutral atom. In the second scenario, the initial nucleus is likely to bind with another and be re-emitted from the surface as a molecule of thermal kinetic energy (at the wall temperature).

1.5.2. Recycling as particle, momentum and energy sources for the plasma

For most materials used in plasma-wall interactions, the vast majority ($> 99\%$) of impacting particles re-enters the plasma until they get ionized again. This is known as "recycling", and is parametrized by the particle recycling coefficient R_n. The later is defined as the ratio of the flux of particles re-entering the plasma volume as neutrals to the ion flux impacting the wall. An energy recycling coefficient R_E can be introduced in a similar way, representing the average ratio between the energy of the emitted neutral particle and the incident energy of the incoming ion. In fact, depending on the wall material, a significant fraction of the energy fluxes flowing out of the plasma can thus be reflected into the plasma.

The recycling process is a dominant process in the plasma particle balance. To demonstrate this, let us consider a simple 0D reservoir model that will provide an estimate of the weight of the recycling source to the external fuelling mechanism. Calling Γ_{PUFF} the fueling source for neutrals, Γ_{LOSS} the losses of neutrals and Γ_{REC} the recycling source, the balance can be written as:

$$0 = \Gamma_{PUFF} - \Gamma_{LOSS} + \Gamma_{REC} \tag{1.17}$$

where, $\Gamma_{LOSS} = n_i c_s S_{wet}$, $\Gamma_{REC} = R_n \Gamma_{LOSS}$ and Γ_{PUFF} is a control parameter. This can be simply solved to get the equilibrium ion density of the plasma:

$$n_i = \frac{\Gamma_{PUFF}}{c_s S_{wet}(1 - R_n)} \tag{1.18}$$

and eventually the ratio of the recycling particle source over the gas puff rate:

$$\frac{\Gamma_{REC}}{\Gamma_{PUFF}} = \frac{R_n}{1 - R_n} \tag{1.19}$$

This way, the ratio of the recycling source to external fuelling is of the order of $\frac{R_n}{1-R_n}$. For values of recycling coefficient close to 1 (e.g.. $R_n \approx 0.99$), the plasma particle source and eventually the density would increase by a factor of 100 compared to what would be observed in the absence of recycling. This way, external actuators represent only a small portion of the total plasma particle source.

Most edge plasma models assume that the wall material becomes saturated with trapped particles in such a short time frame that the local recycling coefficient can be regarded as being 1. In this scenario, only the surfaces of the pumps exhibit a non-unit local recycling coefficient, resulting in a global average recycling coefficient smaller than 1. Consequently, the tokamak vacuum chamber behaves as a quasi-closed system concerning particle balance, with the injected and pumped fluxes a small fraction of the recycled flux. When the particle balance is reached, the pumped flux and the injected flux are equal and define the "throughput".

1.5.3. Plasma-neutrals interactions

Recycling involves an entire zoology of plasma neutrals reactions inside the plasma volume, as highlighted in Rivals et al. 2022. In the following work, only three main reactions will be discussed: ionization, recombination and charge exchange.

Ionization is the process by which neutral atoms or molecules (X) in the plasma are transformed into ions (X^+) through the removal of an electron:

$$X + e^- \longrightarrow X^+ + 2e^- \tag{1.20}$$

This process occurs above an energy threshold corresponding to the ionization potential of the atom X. For Hydrogen isotopes, ionization starts to be important at relatively low temperatures, typically at a few eVs, and behaves with the electron temperature as reported in Fig. 1.9. The latter figure also shows a density dependence related to the contributions of ionization from excited states of the atom, whose population depends on the density and temperature conditions through collisionnal and radiative processes. As a result, the energy cost of ionization is larger than the ionization potential, as radiation is emitted in the process due to successive partial excitation /

de-excitation processes.

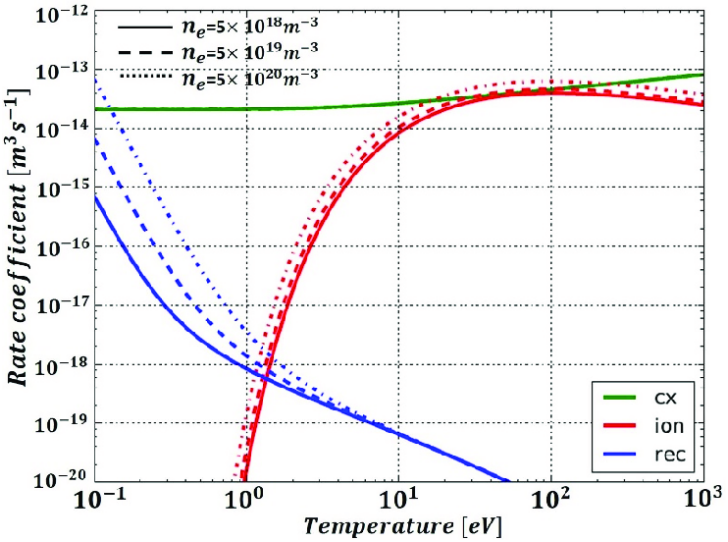

Figure 1.9. – Dependency of the reaction rates for ionization, recombination and CX as a function of Te, reported from Zhou et al. 2022

On the other hand, the charge exchange process involves a neutral (X) colliding with an ion (Y^+):

$$X + Y^+ \longrightarrow X^+ + Y \tag{1.21}$$

The 2 ion species can be the same ($X = Y$) as will be the case for the simple plasmas considered in this manuscript and the reaction rate is much larger for resonant processes. As a result of the collision the neutral and the ion exchange an electron. In terms of particle balance, this reaction does not change the plasma or neutral gas composition when $X = Y$. However, everything happens as if the ion and the neutral have swapped their energy and momentum in the process. Depending on the local conditions and the energy of the neutral, this process can result either in an energy sink or in a energy source for the plasma. As shown in Fig. 1.9, the charge-exchange reaction occurs at a substantial and relatively constant reaction rate across the relevant temperature range. This observation is one of the bases for the Improved Fluid Neutrals model described in the next chapter.

As it will be discussed in Section 2.3.2, the model used to described the neutrals physics (Horsten et al. 2017) will also include the volumetric recombination where plasma ions become neutrals by capturing a free fast electron. There are two processes through which this can occur, radiative recombination (the inverse of photoionization which is typically negligible in tokamak plasma conditions)

$$X^+ + e^- \longrightarrow X + \nu \tag{1.22}$$

and three body recombination, the inverse of ionization:

$$X^+ + e^- + e^- \longrightarrow X + e^- \tag{1.23}$$

The importance of the later strongly increases with density, since it involves three colliding particles. Volumetric recombination becomes an important mechanism at temperatures typically below 1 eV (Fig. 1.9).

1.5.4. Density regimes in tokamaks

All the aforementioned processes contribute to dissipating a significant amount of energy and momentum from the plasma, resulting in a strong impact on the plasma conditions. This energy is primarily converted into radiation, which is emitted isotropically and absorbed by the wall, or transferred to neutrals particles. All of these phenomena allow an increase of the surface area on which power exiting the plasma is distributed on the wall compared to the plasma wetted area. These processes are further enhanced with a divertor configuration, for which the magnetic and wall geometry promote neutral compression, resulting in stronger plasma-neutral interactions.

The sources/sinks related to plasma-neutral interaction all scale with the local density, more precisely either the product of the plasma density times the neutral density or the square of the ion density. If one were able to achieve sufficiently high density in the divertor while maintaining plasma stability, the plasma would reach a state where it transfers all its momentum and energy to photons and neutrals before reaching the wall. Under such conditions, plasma fluxes to the wall become negligible, and the entirety of heat fluxes are carried by neutrals and photons to a much larger surface area of the solid material. The plasma temperature also decreases in the vicinity of the target plates and can drop to the recombination temperature (typically below 1 eV). In this scenario, the plasma no longer reaches the solid wall, and its boundary conditions are solely determined by the layer of neutral particles in front of the targets. This state is referred to as a detached plasma, and the phenomenon is known as plasma detachment. The changes of plasma states, from the lowest density case where momentum and energy dissipation are minimal to the highest density case where the plasma recombines before reaching the wall, are termed "density regimes" or "divertor regimes".

These regimes can be described via a simple model called the Two - Points model, as it is done in Stangeby et al. 2000.

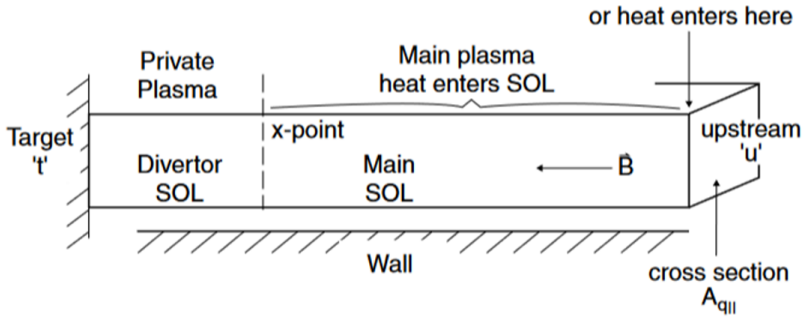

Figure 1.10. – Definition of the flux tube used to describe the two point model. Reproduced from Stangeby et al. 2000.

By straightening out the SOL as it is drawn in Fig. 1.10, a flux tube domain is obtained along which one can relate the density and temperature at the target and upstream. Usually, the "upstream" location refers to the stagnation point where the plasma parallel flow velocity reverses [1].

The basic Two - Points model does not take neutrals into account and assumes energy conservation, where the fluxes, being conserved, do not experience any reduction at the wall, but only a decrease in the energy per particle. The model in its simplistic form does not solve any particle balance, but only a momentum, an energy and a pressure balance where the unknowns are the target density n_t and temperature T_t, and the upstream temperature T_u.

At low upstream densities, the model neglects temperature difference between the upstream and the target, $T_u = T_t = T$. In addition, since no phenomena involve loss of momentum along field lines, the total pressure $p = 2nT + m_i n v_\parallel^2$ is conserved and considering a Bohm criterion at the target

$$p_u = p_t \tag{1.24}$$

$$2n_u T = n_t T + \frac{1}{2} m_i n_t c_s^2 \tag{1.25}$$

$$n_u = 2n_t \tag{1.26}$$

From Eq. 1.26 one obtains the target particle flux

$$\Gamma_t = 2n_u c_{s,t} \tag{1.27}$$

In conditions of very low density, the flux of particle scales linearly with the upstream

1. The existence of such a point in the SOL in the consequence of the continuity of the parallel velocity field combined with the fact that the plasma necessarily has a negative parallel velocity on one side of the field line and a positive one on the other side

temperature is primarily dictated by the physics of the sheath, characterizing a regime known as the "sheath-limited regime."

As density increases and temperature decreases, the plasma enters into the "conduction limited regime" where strong parallel temperature gradients develop to carry the heat flux. The target temperature can then be neglected compared to the upstream temperature, so that one can rewrite the basic two-point model as:

$$n_u T_u = 2 n_t T_t \tag{1.28}$$

$$T_u^{\frac{7}{2}} = T_t^{\frac{7}{2}} + \frac{7}{2}\frac{q_\parallel L}{\kappa_{0,e}} \tag{1.29}$$

$$q_\parallel = \gamma T e n_t c_{s,t} \tag{1.30}$$

From which one can recover the target particle flux density as

$$\Gamma_t = \frac{n_u^2}{q_\parallel^{\frac{3}{7}}} \left(\frac{7}{2}\frac{L}{\kappa_{0,e}}^{\frac{4}{7}} \right) \frac{\gamma e^2}{2 m_i} \propto n_u^2 \tag{1.31}$$

The particle flux is found to follow a "stronger" quadratic trend on the upstream temperature, with respect to the low density regimes.

The basic Two-Points model only refer to a reduction of temperature per particle at the wall, due to particle and energy conservation within the system, which is relevant only for the plasma itself without including the physics of neutrals (recycling). In order to describe higher density regimes it is mandatory to introduce refinements to this model. As it is reported in Stangeby et al. 2000, volumetric power losses due to radiation and charge exchange loss can be included by introducing a power loss factor f_{power}. The plasma flow toward the target will experience momentum loss due to the frictional collisions with neutrals, viscous forces and volume recombination. To account for them, a momentum loss factor is introduced as f_{mom}. In general, parallel heat convection plays some role even if parallel conduction dominates, and it is therefore useful to introduce a conduction factor f_{cond}.

This improved models helps understand the detachment onsets after the so-called rollover of the target particle flux, when it starts to decrease with the upstream density.

1.5.5. Detached plasma as operational regime for large machines

The existence of these regimes offers a clear mitigation strategy for the heat (as well as particle) exhaust issues in large-scale devices, where plasma-neutral interaction processes become dominant contributors to the edge plasma particle, momentum, and power balance (R.A. Pitts et al. 2019; Rivals et al. 2022; Krasheninnikov et al. 2017). To adhere to engineering constraints regarding the maximum heat flux density to solid surfaces, reactors with solid divertors like ITER and DEMO will operate in high-density

or detached regimes. It is important to point out that in these regimes, the presence of impurities will also play a crucial role by enabling detachment at lower densities due to the increase in radiation losses Militello 2022. Expected values of density and temperature for ITER targets are of the order of $n_e \approx 10^{19} - 10^{21} m^{-3}$ and $T_e \approx 1 - 10eV$, as reported in Aymar et al. 2002; R.A. Pitts et al. 2019.

This point is crucial as it highlights that SOL physics related studies must consider high recycling or detached conditions to be applicable for reactors. This is the case in particular for the understanding of the transverse transport.

1.6. Transverse transport in the edge of tokamaks

Detached regimes are the key for future fusion reactors; however, their achievement is intrinsically dependent on the SOL width λ_q which determines the plasma wetted area in Equation 1.15. This way, λ_q is a critical parameter in the context of density regimes (Lipschultz et al. 2016). In Section 1.3.4 it was shown how the SOL width hinges on a delicate balance between several key factors:

— Parallel transport,
— Perpendicular transport,
— Boundary conditions imposed on the plasma at the target plates.

The following sections will provide an illustration about the transverse transport mechanisms responsible in the determination of the transport coefficients at the edge of tokamaks.

1.6.1. Classical vs Neo- Classical vs Turbulent transport

Identifying the key factors responsible for transverse transport at the edge of tokamaks has been, and continues to be, a major topic of debate within the plasma physics community. Even today, there is considerable controversy over what primarily governs transport in the SOL (see Goldstone 1961, Eich et al. 2020, scott 2002, Giacomin and Ricci 2020, Fedorczak, J.P. Gunn, Nace, et al. 2017 and Fedorczak, J.P. Gunn, Pascal, et al. 2012).

Various theories are used to describe transverse transport, ranging from Classical and Neo-classical formulations (Hinton et al. 1976) to turbulent transport (Scott 2007).

Classical transport theory is based on the collisional diffusion of particles and heat across magnetic field lines. This theory assumes that collisions between particles, such as ions and electrons, are the primary mechanism for transport. It provides formulas for the perpendicular diffusion coefficient $D_\perp$ and thermal conductivity κ both of which depend on collisionality and are typically much smaller than in the parallel direction in a strongly magnetized plasma. These values cannot explain the levels of cross field transport observed in tokamaks (Fundamenski et al. 2003).

The Neoclassical transport theory refines the classical approach by accounting for the effects of the tokamak's toroidal geometry, which introduces additional transport mechanisms beyond simple collisional diffusion. This theory considers the drift

motions of particles in the presence of curved and non-uniform magnetic fields, leading to effects such as trapped particles, banana orbits, and poloidal asymmetries (Helander 2012). Neoclassical theory predicts transport coefficients that are generally higher than those of classical theory but still often falls short of explaining the high levels of transport observed in the edge plasma (Fundamenski et al. 2003). Moreover, the neoclassical theory is theoretically not valid in the SOL since it applies to closed field lines. However this does not prevent trying to apply it anyway for describing the near SOL physics. For example, in (Goldstone 1961), the author demonstrates the possibility to reproduce Eich's scaling law observed in H-mode with a theory based only on drifts and curvature without taking into account turbulence.

Turbulent transport theory addresses the shortcomings of classical and neoclassical theories by considering the effects of turbulence, which is driven by small-scale instabilities and fluctuations. To illustrate how fluctuations can be responsible for transverse transport, let us consider a convective particle flux:

$$\vec{\Gamma}_n = n\vec{u}, \tag{1.32}$$

where n is the plasma density and $\vec{u}$ is the local fluid velocity (see next chapter). If one decomposes both quantities into a time-average (notated here with an overbar) and a fluctuating part, e.g. $n = \bar{n} + \tilde{n}$ with by definition $\tilde{n} = 0$, then the time-averaged flux is equal to:

$$\bar{\vec{\Gamma}}_n = \bar{n}\bar{\vec{u}} + \overline{\tilde{n}.\tilde{\vec{u}}} \tag{1.33}$$

The second term in the right-hand side is a turbulent flux, i.e. an average flux resulting from the correlations between the density fluctuations and the velocity fluctuations. This way, provided an instability mechanism exists that generates fluctuations in the plasma, one can expect these fluctuations to contribute to transverse fluxes. The amplitude of the turbulent flux then depends on the amplitude of fluctuations and on the phase difference between the fluctuations of fields involved.

In the edge of a tokamak, turbulence appears as localized filaments or intermittent structures, commonly known as blobs (Kirk et al. 2006). Turbulence has been shown to significantly enhance transverse transport in L-mode (Fedorczak, J.P. Gunn, Pascal, et al. 2012) plasmas, though conclusions in H-mode are still under investigation. Turbulent transport coefficients are typically an order of magnitude higher than those predicted by classical or neoclassical theories and align more closely with experimental observations in the edge plasma.

1.6.2. On the importance of turbulence

At the plasma edge, various types of instabilities can drive turbulence, each categorized by its underlying physical mechanisms, which may coexist and interact within the SOL.

The most commonly referenced instabilities in edge plasmas are Drift Waves and Interchange Instabilities (Scott 2005 and Ghendrih, Dif-Pradalier, et al. 2022). In

the first case, turbulence is driven by density and temperature gradients, generating fluctuations that propagate perpendicular to both these gradients and the magnetic field. In the second case, turbulence primarily arises from the unfavorable curvature of the magnetic field combined with pressure gradients.

Regardless of the instability driving the turbulence, the resulting phenomena are similar: the radial outward motion of turbulent structures promotes the transport of particles and heat across the magnetic field. While turbulence may vary in significance across different regimes, it remains a crucial factor in transport. This is a fundamental point in the debate questioning its role and the further determination of λ_q.

The initial perspective suggests that turbulence is likely influenced by the specific confinement regime being considered (e.g., L-mode versus H-mode). For instance, in H-mode, turbulence might not be a dominant player despite the presence of substantial gradients that would typically drive turbulence (Grenfell, Spolaore, et al. 2020). This paradox highlights the importance of investigating the mechanisms that lead to its suppression. Turbulence may not have the same weight in all the regimes, but it is anyway a key ingredient to the transport: this leads to the conclusion that if turbulence is present, it must be accurately modeled, if it is absent, it is equally important to model in a self-consistent manner why and under what conditions it does not occur.

1.7. Interaction between turbulence and density regimes

1.7.1. Experimental evidences of the interactions between density regimes and perpendicular transport in the edge plasma

There is evidence proving that the divertor regime has an impact on turbulence and thus cross field transport, both in the near and in the far SOL. In fact, neutrals ionization largely determine the localization of the particle source, and affect plasma conditions and as a result collisionality, an important parameter for turbulence.

Studies of the near SOL, such as the one carried out in Eich et al. 2020, have demonstrated that the Scrape-Off-Layer λ_q is wider in higher density regimes than in sheath-limited plasmas.

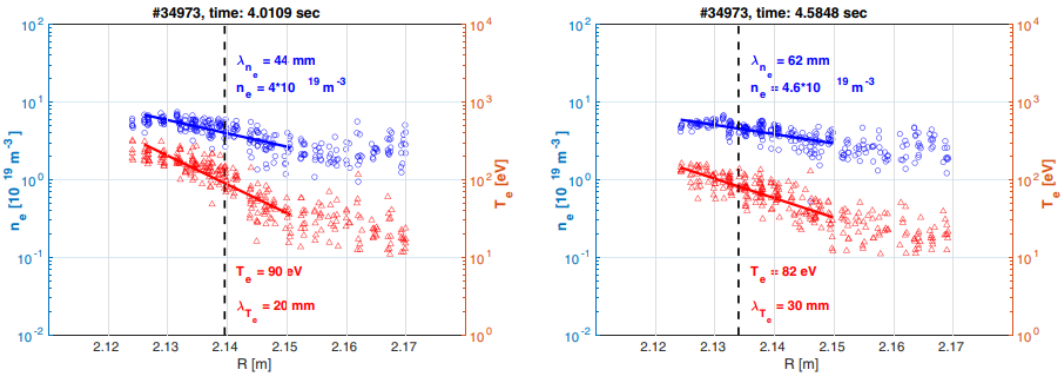

Figure 1.11. – Snapshots of the evolution of the electron temperature and density profile around the separatrix showing the change in plasma collisionality for a specific AUG plasma discharge, reproduced from Eich et al. 2020

.

Here in Fig. 1.11 a significant change of the density and temperature fall-off lengths is visible when comparing 2 instants of the same ASDEX-Upgrade discharge differing only by their collisionality. The decay lengths are found 1.5 times larger for both the temperature and the density in denser and cooler (so more collisional) conditions. In the same study, the analysis of an experimental database demonstrated that the decay lengths are growing functions of a parameter α_t directly proportional to the plasma collisionality as would be expected by basic turbulence theory. This leads the author to conclude that this widening is related to an increase in anomalous transport when moving from low-recycling to high-recycling regimes.

In the far SOL, the formation of density shoulders (Wynn et al. 2018) is another example of the strong correlation between SOL turbulent transport and density regimes.

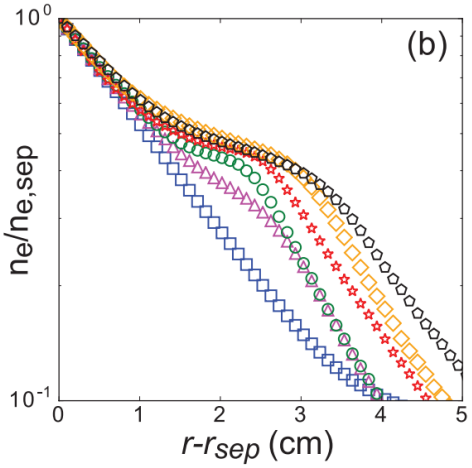

Figure 1.12. – Example of density profiles normalized to the separatrix value during a horizontal target L-mode D-fuelling ramp in JET showing characteristic flattening in the Far SOL, Fig. reproduced from Wynn et al. 2018.

Density shoulders are a universal phenomenon, captured in all the machines: here in Fig. 1.12, an example is reported for JET, where the authors demonstrate via a density scan that the SOL density profiles exhibit an inflection point and become flatter in the far SOL as the line average density $\bar{n}_e$ increases. Such widening of the far SOL might have harmful effects in future machines as it could lead to increased fluxes on the first wall, out of the divertor region, inducing erosion.

Further studies have highlighted a possible correlation between plasma conditions in the divertor and the existence of the shoulders (Carralero, Manz, et al. 2015). Here, it is reported that shoulders appear as response of turbulence transport to high recycling conditions with a strong role is played by divertor collisionality. As explained in ibid., on the onset of detachment the collisionality in the SOL is increased. The SOL width λ_N increases together with the size of turbulence filaments as well as their propagation velocity, which enhances the corresponding perpendicular particle transport. The study identifies a dimensionless parameter determining the existence or not of the phenomenon in the form of an effective collisionality, measured in a two region model of the SOL (midplane and divertor). As discussed in ibid., the relation between filament regime transition and the shoulder formation has also been shown in JET (Carralero, Müller, et al. 2015), where independent measurements of collisionality in the divertor and midplane regions suggested that only the collisionality in the divertor region could account for the disconnection process:

$$\Lambda_{div} = \frac{L_\parallel / c_s}{1/\nu_{ei}} \frac{\Omega_i}{\Omega_e} \propto n_{div} T_{div}^{-3/2}, \tag{1.34}$$

where, the density and the temperature are considered in the divertor. In Carralero, Manz, et al. 2015, the threshold for the transition to shoulders in experiments is found to be for $\Lambda_{div} \sim 1$ at the midplane, as illustrated in Fig. 1.13. When $\Lambda_{div} < 1$, the SOL density width λ_n is almost constant for 2 orders of magnitude of variation of Λ_{div}. For $\Lambda_{div} > 1$, a brutal and rapid increase of λ_n is observed. Similar trends are seen on the size of turbulence filaments. These results suggest a connection between divertor conditions, the filaments propagation in the edge and the resulting transverse transport.

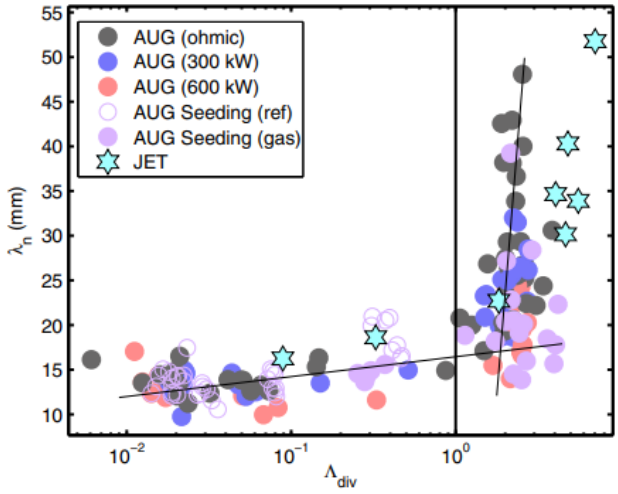

Figure 1.13. – Density e-folding length scaling with divertor collisionality in AUG and JET. Black, blue, and red circles represent different levels of P_{IN}. Purple circles correspond to seeded discharges [empty(solid) mean before (after) N2 puffing]. Light blue stars are data points from JET. Straight lines mark the trend for the two regimes (in terms of power).

Overall, for both near and far SOL the level of turbulence seems to depend on density regimes, impacting overall the heat exhaust issue. It is mandatory to take both the two physics into account, and their interaction in the edge is highly nonlinear and requires to be modeled self consistently.

1.7.2. Modeling self consistently transverse transport and density regimes

So far, there has been few modelling studies addressing turbulent transport and density regimes simultaneously (Tamain, Baudoin, et al. 2018, Giacomin, Ricci, et al. 2022, Zholobenko et al. 2021Mancini, Ricci, Vianello, Giacomin, et al. 2021 and Mancini, Ricci, Vianello, Van Parys, et al. 2023). However, the need for such combined studies emerges clearly from the experimental evidences described previously.

Historically, the two physics have been tackled independently by using distinct numerical tools: mean-field and turbulent codes. These 2 classes of codes rely on very different approaches concerning the description of transverse transport:

— Mean field codes are 2D transport codes focused on the "mean" or average behavior of fields. In order to lighten the computation cost related to transverse transport, these codes do not model fluctuations nor the resulting turbulent transport self-consistently. Instead, a gradient-diffusion approach is used, in which one assumed that the anomalous fluxes can be locally described using a Fick's type diffusion, with the flux being proportional to the local gradient of a

plasma quantity, e.g. for the particle turbulent flux:

$$\overline{\tilde{n}\tilde{\vec{u}}} \equiv -D_{\perp}\vec{\nabla}n, \tag{1.35}$$

where $D_{\perp}$ is the so-called anomalous diffusion coefficient. Similarly, an anomalous heat conduction coefficient is introduced to describe the transverse energy transport as a function of the local temperature gradient. These strong assumptions allow one to solve equations only for the non-fluctuating part of plasma fields and reduce the system to 2D by exploiting the toroidal axisymmetry of the system. In such approach perpendicular diffusion coefficients are typically set to large values, typically around 1 m^2/s to match experimental profiles.

— Turbulence codes rely on the direct modeling of turbulent fluctuations and consequentially the transverse turbulent transport derives self-consistently from the fluctuations. This requires resolving the small spatial and temporal scales associated with turbulence, which is extremely costly in terms of computing power. Moreover, modelling turbulence in a realistic geometry requires working in a 3D geometry as toroidal fluctuations are necessary for turbulence to develop in the models. In turbulence codes, no ad-hoc anomalous diffusion coefficient are necessary although perpendicular diffusion are often still present in the model to account for collisions-driven or sub-discretization-grid transport. In that case, the perpendicular diffusion coefficients are set to small of the order of 0.01 m^2/s.

Presently, the predominant approach for interpreting density regimes and detachment dynamics relies on the utilization of 2D mean field codes. The reason for this is that the simplification made on the description of turbulent transport allowed focusing on the self-consistent integration of relevant PWI and recycling physics. However, this approach overlooks some fundamental aspects of edge turbulent transport. Specifically, the cross-field turbulent transport is typically described through transport coefficients specified as ad-hoc input parameters, which are then adjusted to align with experimental profiles at specific locations within the machine. This method has demonstrated limitations, as mean-field codes have not been able to accurately replicate phenomena such as density shoulders without resorting to artificial modifications of the transport coefficients (Zito et al. 2021).

Turbulence is investigated via turbulent codes, developed almost as a separated theory branch, becoming a distinct area of research on its own, active and ongoing. The main focus relies on identifying the dominant mechanisms triggering the turbulence in the edge plasma and understanding how they influence plasma background and machine conditions. Numerous codes have been developed over decades for this purpose, evolving from 2D (see Sarazin et al. 1998 and Garcia et al. 2004) to 3D simulations, incorporating increasingly complex geometries (refer to B.D. Dudson, M.V. Umansky, et al. 2009 and Tamain, Ghendrih, Tsitrone, et al. 2010). Turbulent modes did not include neutrals physics and only recently an effort has been made to incorporate neutrals dynamics in codes as GBS (Halpern et al. 2016), GRILLIX (Stegmeir et al. 2018), BOUT++ (B. D. Dudson et al. 2015) and SOLEDGE3X (Bufferand,

Bucalossi, et al. 2021).

In this PhD work, we will bridge the two approaches, by considering turbulence models that include neutrals. The results presented in the following chapters advance beyond the current state of self-consistently modeling by providing simulations that examine interactions between turbulence and neutrals in detached regimes.

1.8. Objectives of the thesis and outlines

This thesis work delves into the modeling of plasma - neutral interactions in the plasma periphery, and their impact on turbulent transport. The objective of this PhD project is to leverage the advanced capabilities provided by the SOLEDGE3X edge multi-fluid code to investigate the interplay between turbulent transport and neutrals as a function of the density regimes of tokamak edge plasmas. SOLEDGE3X offers all the features needed to address self-consistently the intricate dynamics at play; however, in the course of this thesis, part of the effort was dedicated to further developing models in SOLEDGE3X in order to improve the description. It is worth to mention that this research will heavily rely on numerical simulations executed on state-of-the-art High-Performance Computing systems, in particular on MARCONI machine (for its architecture, see Iannone et al. 2018).

In the course of this manuscript, we want to answer the following key questions related to the interaction between neutrals recycling and edge plasma turbulence:

1. does one need specific methodology to run turbulence simulations with self-consistent neutrals?
2. how does the localization of the particle source due to fuelling and recycling impact turbulent transport in the edge plasma?
3. can simulations reproduce a change in turbulent transport between low and high density regime?
   a) can one reproduce and explain the appearance of SOL shoulders?
   b) how does the SOL width respond to density regimes?
4. what recommendations can be made to mean-field codes to model this phenomenology?

In order to address and try to answer the questions reported above, the structure of the manuscript is outlined as follows: the geometry and the models used in the simulations are reported in Chapter 2, together with the contributions in developing the model performed by this author. Then, a preliminary study investigating the impact of neutrals recycling on turbulent transport in the edge plasma of tokamaks: as a first step, one considers here an idealized circular limited geometry 3.2, aiming at paving the way towards more complex simulations. One analyzes the effect of changing the particle flux drive of a simulation from an artificially prescribed particle flux from the core to a self-consistent fuelling by gas-puff and particle recycling. A relatively low density regime is addressed in order to highlight the lowest order effects. More deeply, the impact of the gas puff perturbation on the toroidal symmetry is

discussed and the self-organization of turbulence with respect to the interaction with neutrals all together with the characteristic fluctuations are provided.

Subsequently, Chapter 4 focuses on simulations conducted in experimentally relevant diverted high recycling regimes for a dedicated TCV (*Tokamak à Configuration Variable*) magnetic equilibrium. A significant observation regarding the need to accelerate simulations and achieve particle convergence, is discussed in order to rely on the results presented. The outcomes of these simulations are analyzed to elucidate the underlying physics and compare them with experimental observations, particularly to demonstrate the role of density regimes, from low recycling up to detachment, in the impact on turbulent transport. The conclusive discussion of Chapter 4 concerns the way to include the observed effect on transport in 2D mean-field codes.

2. Modeling turbulence neutrals interactions with Soledge3X

The main motivation of this Chapter addresses the essential need for modeling and developping predictive capabilities in understanding and designing complex systems. Plasma, as a prime example of a complex system, requires high-fidelity simulations. This effort is crucial for the development of future fusion devices, such as ITER and DEMO, and necessitates numerical codes capable of self-consistently capturing the intricate physics involved.

In this Chapter, the numerical methods and the tools employed for simulating the cases discussed in Chapter 3 and 4 are presented. To advance towards a self-consistent modeling approach for edge plasma, the SOLEDGE3X edge multi-fluid code is employed to model turbulent transport and neutral particle dynamics in three-dimensional geometry. The modifications made in the code during the course of this thesis are presented to highlight what enabled the subsequent work.

2.1. Drifts fluid models for the edge plasma

Plasma dynamics can be captured through various approaches, ranging from the particles descriptions, to the more simplified fluid models, the latter being the focus of this work.

2.1.1. From particle to fluid description

In accordance with the particle description approach, the dynamics of each individual particle within the plasma is considered. For a given system comprising particles of mass m and electric charge q, each characterized by coordinates $\vec{x}_p$ and velocities $\vec{v}_p$, the fundamental law of dynamics can be applied for each individual particle:

$$m\frac{d\vec{v}_p}{dt} = \vec{F} = q\vec{E} + q\vec{v}_p \times \vec{B} \tag{2.1}$$

$$\frac{d\vec{x}_p}{dt} = \vec{v}_p. \tag{2.2}$$

Although this model seems straightforward [1], the number of particles in even mod-

1. Note that gravitational forces are negligible.

erately sized fusion devices becomes prohibitively large for individual tracking. Calculating the dynamics of every particle would surpass the memory capacity of all existing high-performance computers, making this approach feasible only for local simulations. This limitation implies the use of statistical models that consider the dynamics of large numbers of particles collectively, such as kinetic and fluid models.

However, the kinetic approach remains computationally intensive. In essence, this method relies on the distribution functions f (for electrons and ions), which represents the probability density of finding a particle at a specific position with a given velocity at a particular time. Kinetic theory shows that the distribution function satisfies a transport equation

$$\partial_t f + \vec{u} \cdot \vec{\nabla}_x f + \frac{\vec{F}}{m} \cdot \vec{\nabla}_v f = C. \tag{2.3}$$

Here C is a collision operator representing the effect of self collisions as well as collisions with other species (e.g. ions created by ionization of neutrals) on the distribution function. Solving Equation 2.3 requires discretizing the 6D phase space $(\vec{x}, \vec{v})$, which demands an impractically large number of grid cells.

Alternatively, a specialized approach known as the gyrokinetic model is used for magnetized plasma. This method introduces additional assumptions about forces and frequencies beyond those in the kinetic approach and reduces the phase space from 6D to 5D. The gyrokinetic model, initially suited for core plasma studies, is now extended for describing the edge plasma and is implemented in codes such as GYSELA (Dif-Pradalier, Ghendrih, et al. 2022), GENE-X (Görler et al. 2011) and XGC (C. S. Chang et al. 2004) though in practice it remains highly computationally demanding.

In this work, the tool used is based on a fluid approach, which is a lower fidelity description than the ones discussed above. In the following, the basic set of fluid equations is outlined, while noting that their implementation in SOLEDGE3X is made by applying additional assumptions.

Commencing with the kinetic equation 2.3, one can derive the complete set of fluid equations through subsequent steps. Initially, Eq. 2.3 is multiplied by $(\vec{u}\otimes)^k$, where k denotes the desired order of fluid moment and $\otimes$ a tensorial product. Subsequently, integration over all possible velocities in the velocity space is performed.

For $k = 0$:

$$\int \partial_t f \, d\vec{v} + \int \vec{v} \cdot \vec{\nabla}_x f \, d\vec{v} + \int \frac{\vec{F}}{m} \cdot \vec{\nabla}_v f \, d\vec{v} = \int C \, d\vec{v}. \tag{2.4}$$

By re-working each term present in Eq. 2.4, one obtains

1. $\int \partial_t f \, d\vec{v} = \partial_t \int f \, d\vec{v} = \partial_t n$
2. $\int \vec{v} \cdot \vec{\nabla}_x f \, d\vec{v} = \int \vec{\nabla}_x \left(\vec{v} \cdot f\right) d\vec{v} = \vec{\nabla}_x \cdot \int f \vec{v} \, d\vec{v}$
3. $\int \frac{\vec{F}}{m} \cdot \vec{\nabla}_v f \, d\vec{v} = \int \vec{\nabla}_v \cdot \left(\frac{\vec{F}}{m} f\right) d\vec{v}.$

n is the fluid density of the particles, $\vec{u}$ the fluid velocity, expressesed as $\vec{u} = \frac{1}{n} \int f \vec{v} \, d\vec{v}$. Equation 2 can be re-written as $\vec{\nabla}_x \cdot n\vec{u}$. The fluid velocity is the averaged velocity associated with the entire particle population at a given position in

space. The final term derived from the first moment of the kinetic equation ($k = 0$), equation (3) is re-expressed using Gauss' divergence theorem: $\oint(\frac{\vec{F}}{m}f)d\vec{S}_v$. Assuming a sufficiently fast decay of the distribution function (which is necessary for fluid moments to be defined) the result of Gauss integration is zero.

Under these assumptions, Eq. 2.4 adopts the form of the continuity equation or particle balance.

$$\partial_t n + \vec{\nabla}_x \cdot (n\vec{u}) = S_n \tag{2.5}$$

The equation comprises the time derivative of the density and the divergence of the particle flux, equated to a source term. The source term here in Eq. 2.5 results from the "reactive part" of the collision term $\int C d\vec{v}$ in 2.4 (e.g ions created by ionization or electrons lost in recombination).

Increasing the order of the moment to $k = 1$ yields the momentum equation.

$$\int \vec{v}\partial_t f d\vec{v} + \int \vec{v}\left(\vec{v}\cdot\vec{\nabla}_x f\right) d\vec{v} + \int \vec{v}\left(\frac{\vec{F}}{m}\cdot\vec{\nabla}_v f\right) d\vec{v} = \int \vec{v} C d\vec{v} \tag{2.6}$$

By re-working the first terms in the Eq. 2.6, one simply obtains $\int \partial_t\left(\vec{v}f\right) d\vec{v} = \partial_t \int \vec{v} f d\vec{v} = \partial_t (n\vec{u})$ from the definition of fluid density and velocity.

The second term can be re-arranged via the introduction of a perturbation on the fluid velocity, $\vec{w}$ into $\vec{v} = \vec{u} + \vec{w}$, leading to $\int \vec{v}\otimes\vec{v} f d\vec{v} = \int \vec{u}\otimes\vec{u} f d\vec{w} + \int \vec{u}\otimes\vec{w} f d\vec{w} + \int \vec{w}\otimes\vec{u} f d\vec{w} + \int \vec{w}\otimes\vec{w} f d\vec{w}$.

When considering the tensor properties, one may observe that $\int \vec{u}\otimes\vec{w} f d\vec{w}$ and $\int \vec{w}\otimes\vec{u} f d\vec{w}$, are equal to zero by definition of $\vec{w}$.

At this point we can define the pressure tensor, $\overline{\overline{P}} = m\int \vec{w}\otimes\vec{w} f d\vec{w}$, thereby determining the form of:

$$\int \vec{v}\otimes\vec{v} f d\vec{v} = n\vec{u}\otimes\vec{u} + \frac{\overline{\overline{P}}}{m} \longrightarrow \vec{\nabla}_x \cdot \int \vec{v}\otimes\vec{v} f d\vec{v} = \vec{\nabla}_x \cdot \left(n\vec{u}\otimes\vec{u} + \frac{\overline{\overline{P}}}{m}\right)$$

Finally, the last term $\int \vec{v}\left(\frac{\vec{F}}{m}\cdot\vec{\nabla}_v f\right) d\vec{v}$ is developed by using an integration by parts and get the most recognizable form of the momentum balance equation. By integrating the collisional operator $\int \vec{v} C d\vec{v}$, one gets the collision force $\vec{R}$ and the momentum source $\vec{S}_u$.

$$\partial_t (mn\vec{u}) + \vec{\nabla}_x \cdot \left(mn\vec{u}\otimes\vec{u} + \overline{\overline{P}}\right) = nq\left(\vec{E} + \vec{u}\times\vec{B}\right) + \vec{R} + \vec{S}_u \tag{2.7}$$

The two first terms on the left-hand side represent the time variation in local momentum and its advection. Similar to velocity, momentum is a vector quantity.

On the right-hand side of equation 2.7, the momentum source $\vec{S}_u$ accounts for possible external forces or atomic and molecular reactions between species, and the collision force $\vec{R}$ describes the exchange of momentum resulting from Coulomb collisions.

In high collisionality conditions as will be considered here for the edge plasma, the distribution function is a quasi-maxwellian and so the thermodynamic pressure (or scalar pressure) $p = \frac{1}{3}\left(\mathrm{tr}\left(\overline{\overline{P}}\right)\right) = nT$ [2]. The total pressure tensor can be written as $\overline{\overline{P}} = p\mathbf{I} + \overline{\overline{P_b}}$, with $\mathbf{I}$ the identity matrix and $\overline{\overline{P_b}}$ a residual pressure tensor, to be accounted if the nature of plasma is anisotropy when the distribution function is not an isotropic maxwellian. Again, in high collisionality conditions, the corrective term will be small compared to p.

The resolution of the pressure tensor necessitates an additional time evolution equation. This equation is the energy balance equation, corresponding to an increase in moment order up to $k = 2$. In mathematical terms, this implies that the energy balance equation is a matrix equation, while the momentum balance is a vector equation, and the particle balance is a scalar equation.

By defining the total energy

$$\overline{\overline{E}} = \frac{1}{2}mn\vec{u}\otimes\vec{u} + \frac{1}{2}\overline{\overline{P}}, \tag{2.8}$$

and taking its trace

$$E = \frac{1}{2}mn\vec{u}^2 + \frac{3}{2}p = \frac{1}{2}mn\vec{u}^2 + \frac{3}{2}nT. \tag{2.9}$$

The evolution of Eq. 2.9 is given by:

$$\frac{\partial E}{\partial t} + \vec{\nabla}_x \cdot \left(\left(E+p\right)\vec{u} + \overline{\overline{P_b}}\cdot\vec{u} + \vec{q}\right) = \vec{u}\cdot\left(en\vec{E} + \vec{R}\right) + Q + S_E. \tag{2.10}$$

The term for the conductive heat flux $\vec{q}$ corresponds to the trace of the third-order momentum, forming a three-dimensional tensor.

In addition, the right-hand side of Eq. 2.10 includes an energy source term S_E, an internal energy exchange term Q and the work done by forces acting on the plasma, i.e. the work of the electrostatic force $qn\vec{u}\cdot\vec{E}$ and the work done by frictional forces between species $\vec{u}\cdot\vec{R}$.

Once again, the energy balance introduces another unknown term with the conductive heat flux $\vec{q}$, which requires an additional equation for solution. This will occur each time an additional fluid equation is derived by moving up in the order m, effectively resulting in an infinite chain of fluid equations. This is obviously not usable in practice and one has to truncate the chain at some order m and express the order $m+1$ moment as a function of the lower order moments to close the system. This procedure is called closure.

2. Please note that in the following Chapters, all the temperatures are expressed in units of energy $T_e \equiv k_B T_e$.

2.1.2. Collisional closures for the edge plasma

As emerges from the previous discussion, without a proper closure, the fluid system of equations remains under-determined for any finite number of moments, as it involves a number of unknowns larger than the number of equations. Closures make the system solvable by introducing constitutive relations between fluid moments that uniquely determine the quantities that are not described by a time-evolution equation. They rely on specific assumptions and so are depend on the exact system one tries to model.

Depending on the nature of the fluid model and the level of detail required, different closure models may be applied. In edge plasma physics, the Braginskii closure (Braginskii 1965), being the simplest and most commonly employed, has been implemented in the vast majority of edge plasma codes from SOLPS (Wiesen et al. 2015), EDGE2D (Simonini et al. 1994) up to SONIC (Kawashima et al. 2006, Shimizu et al. 2009). It offers expressions for the unknown terms as a function of the pressure (p), density (n), and velocity (u), along with coefficients derived from collision theory.

The Braginskii closure was derived only for a simple plasma composed of a single ion species with electrons and does not deal with the possibility of collisions between two species of similar mass (i.e. D and T), only between species with very different mass. However, many others closures may be adopted: beside Bragisnkii's, SOLEDGE3X offers the opportunity to close the system of equations with the more advanced Zhdanov closure (Zhdanov 2002). Like Braginskii's, the Zhdanov's closure assumes collisions as the dominant force in the plasma, but they differ in the extent of assumptions considered. In this work though, since a simple hydrogenic plasma will be the object of the study, the two closures boil down to the same terms (Makarov et al. 2021), so we focus here only on the Braginskii closure.

The Braginskii closure relies on a key assumption of high plasma collisionality ν^*. This requires that the shortest timescales in the system, such as fluctuation frequencies, remain longer than the collision time. Consequently, the mean free path of plasma particles between collisions λ must be shorter than the connection length L, $\lambda << L$.

$$\nu^* = \omega \tau_{e*} >> 1 \tag{2.11}$$

where $\tau_{e*} = 3(2\pi)^{\frac{3}{2}} \frac{\epsilon_0^2 \sqrt{m_e T_e}^{3/2}}{e^4 n_e ln\Lambda}$ is the electron collision time in reference plasma conditions with $ln\Lambda$ the Coulombian logarithm (see Stangeby et al. 2000), and ω refers to the characteristic frequency of interest in the plasma (e.g. turbulence correlation time or growth rate). When ν^* is much greater than 1, the collision frequency is much higher compared to the characteristic frequency of other processes: in practical terms, this means that collisions are frequent and dominate the plasma behavior.

The Braginskii closure (Braginskii 1965) provides an expression for the pressure stress tensor $\overline{\overline{\Pi}}$, in the collisional limit, the heat flux $\vec{q}$, the collisional force $\vec{R}$ and the internal energy exchange term Q.

In the Braginskii closure, the pressure stress tensor represents the anisotropic and

dissipative effects of the plasma due to magnetic fields and collisions. Together with the isotropic pressure $p\overline{\overline{I}}$, where p is the scalar pressure and $\overline{\overline{I}}$ the identity matrix, it gives the total plasma pressure $\overline{\overline{P}}$ in Eq. 2.12.

$$\overline{\overline{P}} = p\overline{\overline{I}} + \overline{\overline{\Pi}}, \tag{2.12}$$

$$\overline{\overline{\Pi}} = -3\eta_0\overline{\overline{W}} - \eta_1\left(\vec{b}\vec{b} - \frac{1}{3}\overline{\overline{I}}\right)\left(\vec{\nabla}\cdot\vec{u}\right) - \eta_2\left[\vec{b}\left(\vec{b}\cdot\overline{\overline{W}}\right) + \left(\vec{b}\cdot\overline{\overline{W}}\right)\vec{b}\right] - \eta_3\left(\vec{b}\vec{b} - \frac{1}{3}\overline{\overline{I}}\right)\left(\vec{b}\cdot\overline{\overline{W}}\cdot\vec{b}\right). \tag{2.13}$$

In Eq. 2.13 the term $\overline{\overline{W}} = \frac{1}{2}\left(\vec{\nabla}\cdot\vec{u} + \left(\vec{\nabla}\cdot\vec{u}\right)^T\right) - \frac{1}{3}\left(\vec{\nabla}\cdot\vec{u}\right)\overline{\overline{I}}$ is the traceless rate of strain tensor, where $\vec{\nabla}\cdot\vec{u}$ is the divergence of the velocity, $\vec{b} = \frac{\vec{B}}{B}$ is a unit vector aligned with the magnetic field. η_0, η_1 and η_2 are viscosity coefficients strictly dependent on the plasma conditions.

The expression for the heat flux is given as:

$$\vec{q} = -\kappa_\parallel \nabla_\parallel T\vec{b} - \kappa_\perp \vec{\nabla}_\perp T \tag{2.14}$$

where $\kappa_\parallel$ and $\kappa_\perp$ are respectively the parallel and perpendicular heat conductivities. For electrons, they are equal to $\kappa_{\parallel e} = 3.16\frac{n_e T_e}{m_e \nu_{ei}}$ and $\kappa_{\perp e} = 4.66\frac{n_e T_e \nu_{ei}}{m_e \omega_{ce}}$. For ions, they are equal to $\kappa_{\parallel i} = 3.9\frac{n_i T_i}{m_i \nu_{ii}}$ and $\kappa_{\perp i} = 2\frac{n_i T_i \nu_{ii}}{m_i \omega_{ci}}$, where $\nu_{ii} = \frac{4\sqrt{\pi}e^4 n_i ln\Lambda}{3\sqrt{m_i}{T_i}^{3/2}}$ is the ion-ion collision frequency.

The parallel component of the collisional force $R_{\parallel i}$ undergone by ions is given by:

$$R_{\parallel i} = m_e n_e \nu_{ei} 0.51\left(u_{\parallel e} - u_{\parallel,i}\right) + 0.71 n_e \nabla_\parallel T_e. \tag{2.15}$$

The latter has two terms, a friction force proportional to the difference of fluid velocities between electrons and ions, and a thermal force related to the electron temperature gradient. The force undergone by the electrons is by definition the opposite. The Braginskii closure also provides expressions for the perpendicular part of the collision force, but it will not be used in the rest of this manuscript so we will not detail them.

The internal energy exchange term Q is provided as:

$$Q = 3\frac{m_e}{m_i} n_e \nu_{ei}\left(T_e - T_i\right), \tag{2.16}$$

for the ions, the opposite by definition for the electrons.

2.1.3. Drift-fluid approximation

The moment balance equation Equation 2.7 can be decomposed into parallel and perpendicular components by projecting it using a scalar product $(\vec{b}\cdot)$ and a cross product $(\vec{b}\times)$. In the fluid model, three velocity components need to be resolved; how-

ever, two of these are primarily influenced by the Lorentz force, which is a dominant factor in a magnetized plasma. Under the assumption of strong magnetization, it is possible to derive an explicit analytical approximate expression for the perpendicular velocities. This approach is called drift-ordering, and one refers to the fluid models employing it as drift-fluid models.

The fundamental assumption underlying the drift fluid approximation is that the Lorentz force is the dominant term in the perpendicular momentum balance equation. To exploit this assumption, one introduces a small parameter $\epsilon_c = \frac{\omega}{\omega_c}$ where ω is the characteristic frequency of the time evolution of fluid quantities and ω_c is the gyro-frequency of particles. One also assumes that the same small parameter characterizes the ratio between the characteristic gradient scale L of fluid quantities and ρ_L the Larmor radius of particles: $\epsilon_c = \frac{\rho_L}{L}$. Under the assumption that $\epsilon_c \ll 1$ one can then expand the perpendicular velocity as a series of powers of ϵ_c:

$$\vec{u}_\perp \sim \vec{u}_\perp^{(0)} + \epsilon_c u_\perp^{(1)} + o(\epsilon_c). \tag{2.17}$$

Injecting this expansion into the perpendicular momentum balance equation, one can then identify terms at increasing order in ϵ_c starting at order 0. This leads to the following expression for the perpendicular fluid velocity of the guiding center of particles at zeroth order, known as drift velocity:

$$\vec{u}_\perp^{(0)} = \frac{\vec{B} \times \vec{\nabla}\phi}{B^2} + \frac{\vec{B} \times \vec{\nabla}p}{qnB^2}, \tag{2.18}$$

sum of the "E cross B" drift velocity $\vec{u}_E = \frac{\vec{E}\times\vec{B}}{B^2}$, which contains the expression of the electrostatic potential $\vec{E} = -\vec{\nabla}\phi$, and the diamagnetic drift velocity $\vec{u}_* = \frac{\vec{B} \times \vec{\nabla}p}{qnB^2}$.

One can then express the first order correction to the drift velocity by inserting the zeroth order drifts expressions in higher order inertial terms of the perpendicular momentum balance as detailed in Bufferand, Balbin, et al. 2022. The resulting drift velocity is called the polarization drift:

$$\vec{u}_\perp^{(1)} \equiv \vec{u}_{\perp,pola} = \frac{\vec{b}}{n\omega_c} \times [\frac{\partial}{\partial t}\left(n\vec{u}_\perp^{(0)}\right) + \vec{\nabla}\cdot\left(n\left(u_\parallel \vec{b} + \vec{u}_\perp^{(0)}\right) \otimes \vec{u}_\perp^{(0)}\right). \tag{2.19}$$

The fluid-drift approach simplifies the momentum balance equation to only the parallel direction, removing the perpendicular velocity as an unknown variable in the system. The expression of the drift velocities is actually the approximated solution of the perpendicular component of the momentum balance equation, at a given order of the small parameters.

2.2. The Soledge3X multi fluid edge code

The results presented in this manuscript were obtained by using the SOLEDGE3X code (Bufferand, Bucalossi, et al. 2021), resulting from the merging of the SOLEDGE2D

2D mean-field code(Bufferand, Ciraolo, et al. 2015) and TOKAM3X (Tamain, Bonhomme, et al. 2013a) 3D turbulence code.

2.2.1. SOLEDGE3X equations

In Section 2.1.1 the general fluid equations were introduced, but the fluid model adopted in SOLEDGE3X differs from this generic version due to additional approximations made for numerical purposes.

An electrostatic turbulence model is considered here, although SOLEDGE3X has recently been extended to model electromagnetic turbulence (Düll et al. 2024). The plasma model solved by SOLEDGE3X is based on a drift-multifluid approach, and so the perpendicular momentum balance is solved using drift velocities according to standard drift-ordering (more details in Bufferand, Bucalossi, et al. 2021).

Since the work presented in this manuscript deals with a pure deuterium plasma, the set of equations implemented in SOLEDGE3X is given for a single hydrogen specie.

$$\frac{\partial}{\partial t} n_i = -\vec{\nabla} \cdot (n_i \vec{u}_i) + S_n. \tag{2.20}$$

Eq. 2.20 is the mass balance equation describing the evolution in time of the ions density n_i. Here, the ions fluid velocity $\vec{u}_i$ can be decomposed in a parallel component determined by Eq. 2.22 $u_{\parallel,i}\vec{b}$, and a perpendicular drift $\vec{u}_{\perp,i}$, provided by zeroth order drift velocities, like they are defined in section 2.1.3. S_n is the volume source of ions, from ionisation and recombination of neutrals (see 2.3.2).

After the decomposition, Eq. 2.20 can be explicitated as:

$$\frac{\partial}{\partial t} n_i = -\vec{\nabla} \cdot \left(n_i \left(u_{\parallel,i} \vec{b} + \vec{u}^{(0)}_{\perp,i} \right) \right) + \vec{\nabla} \cdot \left(D_\perp \vec{\nabla}_\perp n_i \right) + S_n. \tag{2.21}$$

In Eq. 2.21 an anomalous diffusive part has been added artificially for numerical purpose, $\vec{\nabla}(D \cdot \nabla_\perp n_i)$ with D named diffusion coefficient. We will see later that its interpretation and amplitude differ depending on the different transport modes (reported in Section 2.2.4) in which SOLEDGE3X can be run.

The particle balance for electrons is directly obtained from the quasi-neutrality equation. $n_e = Z_i n_i = n_i$, Where, $Z_i = 1$ is the ions charge number. Following the velocity decomposition, in order to define the parallel component of the velocity a parallel momentum balance equation for ions is solved in SOLEDGE3X:

$$\frac{\partial}{\partial t} \left(m_i n_i u_{\parallel,i} \right) = -\vec{\nabla} \cdot \left(m_i n_i u_{\parallel,i} \left(u_{\parallel,i} \vec{b} + \vec{u}^{(0)}_{\perp,i} \right) \right) - \nabla_\parallel p_i + e n_i E_\parallel + R_\parallel + S_\Gamma - \vec{b} \cdot \vec{\nabla} \cdot \bar{\bar{\Pi}}_\parallel. \tag{2.22}$$

In Eq. 2.22, the terms $E_\parallel = -\nabla_\parallel \Phi$ is the parallel electric field, S_Γ is the external momentum source including sources due to ionization, recombination and charge exchange processes (see Section 2.3.2). The closure terms $\bar{\bar{\Pi}}_\parallel$ and $R_\parallel$ are obtained by applying the Braginskii closure. The parallel projection of the divergence of the stress

tensor $\bar{\bar{\Pi}}_{\parallel}$ in Eq. 2.22 gives:

$$\vec{b}\cdot\vec{\nabla}\cdot\bar{\bar{\Pi}}_{\parallel} = \frac{2}{3}\nabla_{\parallel}\pi_{\parallel} + \pi_{\parallel}\vec{\nabla}\cdot\vec{b}, \tag{2.23}$$

where $\pi_{\parallel} = -3\nu_0(\nabla_{\parallel}u_{\parallel} - \vec{\kappa}\cdot\vec{u} - \frac{1}{3}\vec{\nabla}\cdot\vec{u})$ expresses the departure from an isotropic maxwellian, and it is used to compute the stress tensor, where $\nu_0 = \frac{4\sqrt{\pi}n_e e^4 ln\Lambda}{\sqrt{n_i}\epsilon_0 T_e^{3/2}}$ is the collisional frequency in which $ln\Lambda$ is the Coulombian logarithm and ϵ_0 the permittivity of free space, while $\vec{\kappa} = \left(\vec{b}\cdot\vec{\nabla}\right)\vec{b}$ is the magnetic curvature . The collision force experienced by the ions due to electrons $R_{\parallel}$ is given by Eq. 2.15.

Rearranging these quantities (refer to Bufferand, Balbin, et al. 2022 for a more detailed explanation), leads to the following form for Eq. 2.22

$$\begin{aligned}\frac{\partial}{\partial t}\left(m_i n_i u_{\parallel,i}\right) = &-\vec{\nabla}\cdot\left(m_i n_i u_{\parallel,i}\left(u_{\parallel,i}\vec{b} + \vec{u}^{(0)}_{\perp,i}\right)\right) - \nabla_{\parallel}p_i \\ &+ en_i E_{\parallel} + R_{\parallel} + S_{\Gamma} - \left(p - \frac{1}{3}\pi_{\parallel}\right)\cdot\vec{\nabla}\cdot\vec{b} \\ &+\vec{\nabla}\cdot\left(D_{\perp}u_{\parallel,i}\vec{\nabla}_{\perp}n_i + \nu_{\perp}n_i\vec{\nabla}_{\perp}u_{\parallel,i}\right) \\ &+\vec{\nabla}\cdot\left(\nu_{\parallel}\nabla_{\parallel}u_{\parallel,i}\vec{b}\right)\end{aligned} \tag{2.24}$$

In Eq. 2.24, the parallel viscosity is given as $\nu_{\parallel} = \nu_0 T_i^5/2$; additionally, like it happened in Eq. 2.21, the contribution of an additional perpendicular viscosity $\nu_{\perp}n_i\vec{\nabla}_{\perp}u_{\parallel,i}$ is added to account either for anomalous transport or subgrid transport depending on the way the code is run (as discussed in Section 2.2.4).

The parallel momentum balance of electrons simplifies to a generalized Ohm's law (Eq. 2.25) by neglecting all terms on the left-hand side of the momentum equation referring to the electronic mass m_e, and by applying the decomposition of $R_{\parallel}$ as given by Braginskii closure above.

$$j_{\parallel} = \sigma_{\parallel}\left(-\nabla_{\parallel}\phi + \frac{\nabla_{\parallel}p_e}{en_e} + \frac{0.71\nabla_{\parallel}T_e}{e}\right), \tag{2.25}$$

where $j_{\parallel} = n_e e(u_{\parallel,i} - u_{\parallel,e})$ is the parallel current. The parallel conductivity is given by $\sigma_{\parallel} = 1.96\frac{n_e e^2\tau_e}{m_e}$, with the electron collisional time defined as $\tau_{coll,e} = \frac{T_e^{3/2}}{n_e ln\Lambda}$.

Finally, SOLEDGE3X solves the energy balance equation for ions 2.26 and electrons 2.27. By naming $\epsilon_i = \frac{3}{2}n_i T_i + \frac{1}{2}m_i n_i u_{\parallel,i}^2$ the ion energy density, the energy balance for ions can be written as:

$$\begin{aligned}\frac{\partial}{\partial t}\epsilon_i = -\vec{\nabla}\cdot\left(\epsilon_i\left(u_{\parallel,i}\vec{b}+\vec{u}^{(0)}_{\perp,i}\right)+pu_{\parallel,i}\vec{b}\right)+\\ \vec{\nabla}\cdot\left(D_\perp\frac{\epsilon}{n_i}\vec{\nabla}_\perp n_i + m_i n_i \nu_\perp u_{\parallel,i}\vec{\nabla}_\perp u_{\parallel,i} + \chi_{\perp i} n_i \vec{\nabla}_\perp T\right)\\ -\vec{\nabla}\cdot\left(\frac{2}{3}\cdot u_{\parallel,i}\pi_\parallel\cdot\vec{b}\right)+S_{E,i}+u_{\parallel,i}R_\parallel+en_i u_{\parallel,i}E_{\parallel i}\\ +\vec{\nabla}\cdot\left(u_{\parallel,i}\nu_\parallel\nabla_\parallel u_{\parallel,i}\vec{b}\right)+\vec{\nabla}\cdot\left(\kappa_{\parallel i}\nabla_\parallel T_i\vec{b}\right)+Q,\end{aligned} \tag{2.26}$$

$$\begin{aligned}\frac{\partial}{\partial t}\epsilon_e = -\vec{\nabla}\cdot\left(\epsilon_e\left(u_{\parallel e}\vec{b}+\vec{u}^{(0)}_{\perp,e}\right)\right)+p_e u_{\parallel e}\vec{b}\\ +\vec{\nabla}\cdot\left(D_\perp\frac{\epsilon_e}{n_e}\vec{\nabla}_\perp n_e+\chi_{\perp e}n_e\vec{\nabla}_\perp T_e\right)\\ -u_{\parallel e}R_\parallel - en_e u_{\parallel e}E_{\parallel i}+S_{E,e}+\vec{\nabla}\cdot\left(\kappa_{\parallel e}\nabla_\parallel T_e\vec{b}\right)-Q.\end{aligned} \tag{2.27}$$

In Eq. 2.26, $S_{E,i}$ stems for the ions energy source term, the collisional energy equipartition term Q derives from Braginskii's closure and it is expressed in SOLEDGE3X as in Eq. 2.28

$$Q = 3\frac{m_e}{m_i}\frac{n_e}{\tau_e}(T_e - T_i). \tag{2.28}$$

The parallel thermal conductivity for ions is given as $\kappa_{\parallel,i} = 3.9\frac{n_i T_i}{m_i \nu_{ii}}$ (scaling as $T_i^{5/2}$), smaller compared to the one for electrons appearing in Eq. 2.27 as $\kappa_{\parallel,e} = 3.16\frac{n_e T_e}{m_e \nu_{ei}}$ (scaling as $T_e^{5/2}$).

In the electron energy balance equation, the current SOLEDGE3X version assumes adiabaticity of the electron flux with respect to the ion flux, replacing all electron advection velocities by their ion counterpart. This approximation effectively leads to neglecting the contribution of current in the energy balance equation of electrons.

In both energy balance equations, additional perpendicular diffusion terms (the terms in $\chi_{\perp e}$ and $\chi_{\perp i}$) are added to account either for anomalous transport or subgrid transport depending on the way the code is run (as discussed in Section 2.2.4).

The current balance is solved in addition to the above set of equations to obtain the electrostatic potential. In the drift-ordering frame, taking into account the quasi-neutrality assumption, the current equation (or vorticity equation) hence becomes an equation for the electrostatic potential:

$$\vec{\nabla}\cdot\left(j_\parallel\vec{b}+\vec{j}_{\nabla B}+\vec{j}_{pola}+\vec{j}_{diff}\right)=0. \tag{2.29}$$

$\vec{j}_{\nabla B}$ is the current carried by the ∇B drift, $\vec{j}_{pola}$ is the polarisation current for which the electron polarisation velocity is neglected and $\vec{j}_{diff}$ is an anomalous diffusive current term added for the same purpose as perpendicular diffusion terms in other equations. After various analytical manipulations and assumptions described in

details in Bufferand, Baudoin, et al. 2017, Eq. 2.29 takes the form of a vorticity equation:

$$\partial_t \Omega + \vec{\nabla} \cdot \vec{F}_\Omega = \vec{\nabla} \cdot \left[j_\parallel \vec{b} + \vec{j}_* \right] + \vec{\nabla} \cdot \left(\zeta \vec{\nabla}_\perp \Omega \right) \tag{2.30}$$

where $j_\parallel$ is given by equation 2.25, $\Omega = \vec{\nabla} \cdot [\left(\frac{m_i n_i}{B^2} \vec{\nabla}_\perp \phi + \frac{1}{e} \vec{\nabla}_\perp p \right)]$ is the vorticity and $\vec{F}_\Omega$ the flux of vorticity as defined in ibid. The term $\vec{j}_* = n_i e \vec{u}_{*i} - n_e e \vec{u}_{*e}$ is the diamagnetic current (see detailed expression in ibid.). Like for the other equations, an additional perpendicular diffusion term is artificially added to the model whose role will be discussed in Section 2.2.4.

2.2.2. SOLEDGE3X simulation domain and geometry

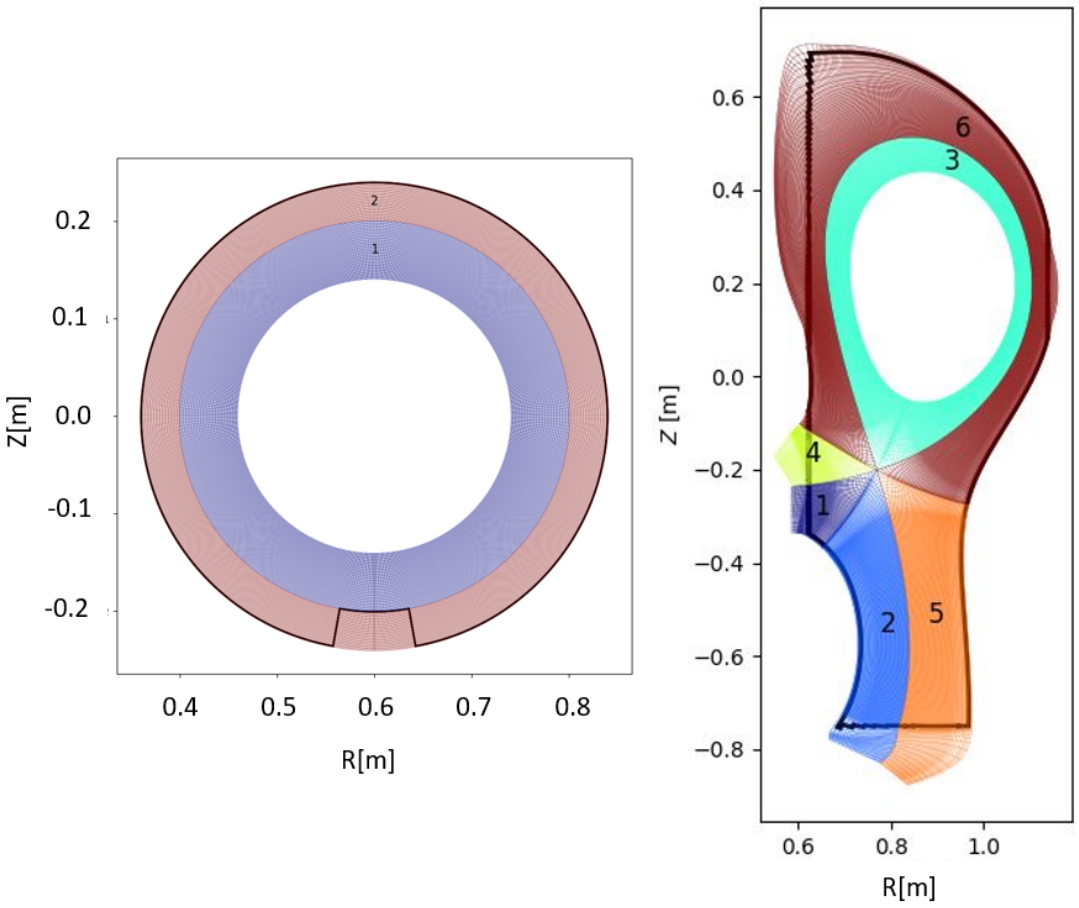

Figure 2.1. – Examples of computational grids for two different magnetic equilibrium with domain decomposition in SOLEDGE3X, the limited (left) and diverted (right) configuration used later in Chapters 3 and 4 respectively. The numbers indicate the indices of sub-domains of the domain decomposition used to handle arbitrary magnetic geometries. The thick black lines show the position of the wall.

SOLEDGE3X is a versatile tool for the edge modeling, offering the possibilities to the users to be run as a 2D mean field code (from the legacy of SOLEDGE2D, see Bufferand, Ciraolo, et al. 2015) or as a 3D turbulent code (like the ancestor TOKAM3X, see Tamain, Bonhomme, et al. 2013a). SOLEDGE3X operates with arbitrary axisymmetric toroidal magnetic geometries. The domain extends from an inner ring (the innermost closed surface, corresponding to the outer part of the closed field lines) out to an outermost closed flux surface usually located outside the wall. The wall is included in the mesh through the use of immersed boundary conditions. At places where the mesh does not extend beyond the wall (this is sometimes the case in order to save on the modelled

plasma volume when the wall is located far from the plasma, as visible at some poloidal positions of the TCV mesh in Figure 2.1), it is assumed that a wall lies all along the last flux surface described by the mesh. As illustrated in Fig. 2.1, the code can handle an idealized circular-limited geometry, similar to a Tore Supra magnetic equilibrium (Dif-Pradalier, J. Gunn, et al. 2011), which will be discussed in Chapter 3, as well as a realistic wall and plasma geometry with X-point(s), which will be explored in Chapter 4. This versatility is achieved through the use of a domain decomposition inherited from the SOLEDGE2D code (Bufferand, Ciraolo, et al. 2015), enabling the code to describe any axi-symmetric magnetic geometry and allowing it to explore a wide range of configurations.

Following this approach, it is essential to impose boundary conditions both at the core-edge interface and at the edge-wall boundary.

2.2.3. Boundary conditions

This section offers an overview on the boundary conditions applied in SOLEDGE3X. 3 types of boundary conditions are found in the simulation domain: at interface with the core plasma (innermost flux surface), at the wall in the presence of non-zero magnetic field incidence (typically at the target plates) and at the wall where the magnetic field is tangential to the solid surface (typically at the outermost flux surface).

For the core boundary, homogeneous Neumann boundary conditions are imposed on any field X:

$$\vec{\nabla} X \cdot \hat{n} = 0 \tag{2.31}$$

where $\hat{n}$ is here a unit vector normal to the boundary. This boundary condition is complemented with a zero flux boundary conditions for all transported quantities (particles, momentum, energy). A narrow buffer region with artificially increased perpendicular diffusion coefficients is added to reduce turbulence activity at the boundary itself. Power input (as well as particle input when neutrals are not self-consistently included) is modelled via a poloidally and toroidally uniform source term added in this buffer region.

Bohm-Chodura boundary conditions are applied at boundaries where the wall is not tangential to the magnetic field. In practice, these take the form of the following constraints on fluxes leaving the plasma:

$$u_{\parallel,i}\vec{b}\cdot\hat{n} \geq c_s\vec{b}\cdot\hat{n} - \vec{u}^{(0)}_{\perp,i}\cdot\hat{n} \tag{2.32}$$

$$\vec{j}\cdot\hat{n} = \vec{\Gamma}_{n,i}\cdot\hat{n}e\left(1 - e^{\Lambda - \frac{e\phi}{T_e}}\right) \tag{2.33}$$

$$\vec{\Gamma}_{E,e/i}\cdot\hat{n} = \gamma_{e/i}\vec{\Gamma}_{n,e/i}\cdot\hat{n}T_{e/i} \tag{2.34}$$

where $\hat{n}$ is the unit vector normal to the wall and orientated towards the wall, $\vec{\Gamma}_{E,e/i}$ is the total energy flux for electrons/ions, $\vec{\Gamma}_{n,e/i}$ is the total particle flux for electrons/ions and $\vec{j}$ is the total current. $\frac{\Lambda T_e}{e}$ is the floating sheath potential drop, as presented in

Eq. 1.8, and $c_s = \sqrt{\frac{T_e+T_i}{m_i}}$ is the acoustic velocity. The sheath heat transmission factors are taken equal to $\gamma_i = 2.5$ for ions and $\gamma_e = 4.5$ for electrons in all the simulations performed for this work.

Wall boundaries where the magnetic field is tangential to the solid have to be treated separately. As discussed in Chapter 1, Bohm-Chodura boundary conditions are in theory not applicable at too low angles of incidence. In fact, no consensus exists in the literature concerning sheath boundary conditions at grazing incidence. The choice that was made in SOLEDGE3X is to apply boundary conditions that are sufficient to determine uniquely the solution of the system while trying to perturb it as little as possible and avoiding unphysical behaviours. For this purpose, homogeneous Neumann boundary conditions are applied on all fields $\vec{\nabla} X \cdot \hat{n} = 0$. Here however, contrary to the core boundary, one does not block outgoing fluxes (in contrast with incoming fluxes, to make sure that no particle or energy flux enters the plasma from the wall, which would not be physical).

2.2.4. SOLEDGE3X as a mean field or turbulence code

From the balance equations outlined in Section 2.2.1, the expressions for the total particle flux 2.35 and energy flux 2.37, 2.36 computed in SOLEDGE3X are derived. Two important free parameters appear in their expressions: the perpendicular particle diffusivity $D_\perp$, the perpendicular viscosity $\nu_\perp$ and the perpendicular heat diffusivity $\chi_{\perp e/i}$ (which is species related).

$$\vec{\Gamma}_{n,\perp} = -D_\perp \vec{\nabla}_\perp n + n\left(\vec{u}_\parallel + \vec{u}_{E\times B} + \vec{u}_{\nabla B,ions}\right) \tag{2.35}$$

$$\vec{\Gamma}_{E,e\perp} = -\chi_{\perp e}\vec{\nabla}_\perp T_e + \epsilon_e\left(u_{\parallel,i}\vec{b} + \vec{u}^{(0)}_{\perp,i}\right) \tag{2.36}$$

$$\vec{\Gamma}_{E,i\perp} = -\chi_{\perp i}\vec{\nabla}_\perp T_i - m_i n_i \nu_\perp u_{\parallel,i}\vec{\nabla}_\perp u_{\parallel,i} + \epsilon_i\left(u_{\parallel,i}\vec{b} + \vec{u}^{(0)}_{\perp,i}\right) \tag{2.37}$$

Note in the electron flux the use of the ion velocity due to the adiabatic flow assumption already mentioned above.

The code can be run either as a 2D mean field transport or a 3D turbulent code, see Fig. 2.2.

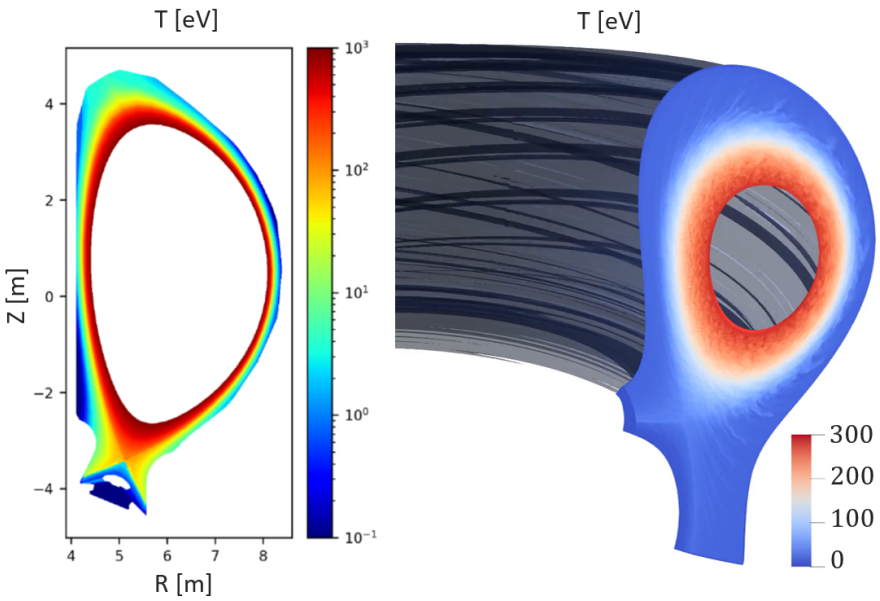

Figure 2.2. – Different application of SOLEDGE3X in 2D mean-field mode (left) in Rivals et al. 2022 or in turbulent mode in Bufferand 2023. Note the absence of fluctuation in the mean-field simulation's result.

In 2D simulations, the code inherently dampens turbulence: in fact, in the parallel direction turbulent fluctuations have wave numbers $k_{\parallel} \simeq 0$, and since in 2D by construction $k_{\varphi} = 0$, $k_{\theta} \simeq 0$ and fluctuations in the poloidal direction are suppressed. As a result forcing the simulation to 2D kills turbulence. Cross-field transport has then to be modeled, and mean-field codes introduce anomalous diffusive transport, that is set diffusion coefficients to large values, typically around 1 m^2/s.

When the code is used as a 3D turbulence code, turbulent fluctuations are self-consistently modelled and the cross-field turbulent transport they drive as well. In that case, the perpendicular diffusion coefficients are still present in SOLEDGE3X equations but do not have the same physical interpretation. They are use to model any transport mechanism at sub-grid scales, typically transport due to collisions or to turbulence occurring at a scales below the grid resolution. In that case, the diffusion coefficients are set to much smaller values, of the order of 0.01 m^2/s. The diffusion terms are then essentially used to ensure the numerical robustness of the code and the related diffusive fluxes are in general negligible compared with the fluxes arising from turbulence.

In summary and in practice, the following is done to run SOLEDGE3X in each mode:
— 2D mean-field: force the geometry to 2D (single point in the toroidal direction

and drop toroidal derivatives) and run with large anomalous perpendicular transport coefficients
— 3D turbulence: run with full 3D discretization (several poloidal planes and toroidal derivatives self-consistently computed) and run with typicall hundred times smaller perpendicular transport coefficients

In this work, SOLEDGE3X is primarily used in the turbulent mode to self-consistently describe cross-field turbulent transport, although some 2D mean-field simulations are also analyzed in Chapter 4.

2.3. Neutrals description in SOLEDGE3X

As formerly discussed in Sec. 1.7, neutrals play a fundamental role in determining reactors operating regimes and their dynamic has to be included in edge plasma codes, especially for studies like the present aiming at tackling the link between turbulence and density regimes.

SOLEDGE3X offers two options to model neutrals: either the coupling with the external Monte Carlo code EIRENE (Reiter et al. 2005), for a full physics kinetic description of the neutrals dynamics, or a lower fidelity fluid description, directly embedded in the plasma solver.

2.3.1. Extension of SOLEDGE3X coupling to EIRENE for 3D cases

At the beginning of this PhD, the coupling to EIRENE worked only in 2D; the SOLEDGE3X-EIRENE package has been extensively used as a 2D mean-field solver to study density regimes and detachement in the edge plasma of various tokamaks from TCV (Yang, Ciraolo, Février, et al. 2023) to ITER (Rivals et al. 2022) through WEST (Yang, Ciraolo, Bucalossi, et al. 2022). More details can be found in (Rivals et al. 2022).

Part of the technical work on coupling SOLEDGE3X in 3D with EIRENE was completed during this PhD, where in an initial endeavor to use the kinetic neutrals model of EIRENE in 3D turbulent simulations, a dedicated tool has been incorporated into the code. This tool facilitates the automatic generation of the EIRENE mesh for simple wall geometries, i.e. when the plasma-wall boundary is everywhere aligned with edges of mesh cells (in the generic case of a wall not aligned with the mesh cells, the code requires relatively heavy pre-treatment tools at the mesh generation stage). The process involves generating the EIRENE triangular mesh directly by splitting the SOLEDGE3X quadrangular mesh into triangles. An example of the application of the tool is reported in Fig. 2.3.

Further details and the methodology for 3D coupling with EIRENE are discussed in the dedicated Appendix A.

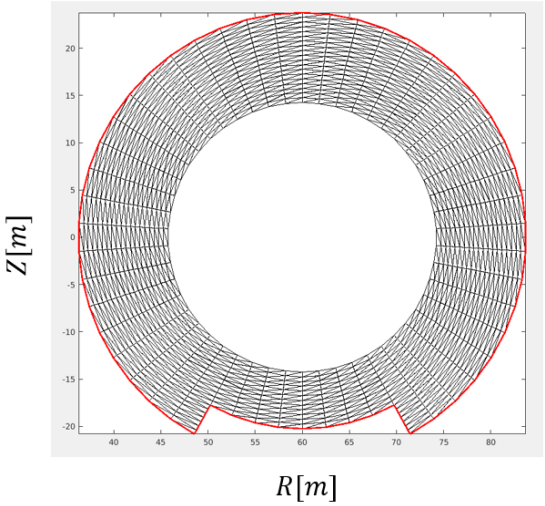

Figure 2.3. – EIRENE 3D mesh automatically generated via SOLEDGE3X, and here applied to a circular limiter case.

A test run for the coupling was conducted in 3D with EIRENE at reduced resolution (i.e., without turbulence) on the grid plotted on Fig. 2.3. Figure 2.4 displays the resulting ionization source, where recycling occurs at the limiter corners. Figure 2.5 shows the sample trajectories of neutrals particles, confirming that neutrals behave as expected.

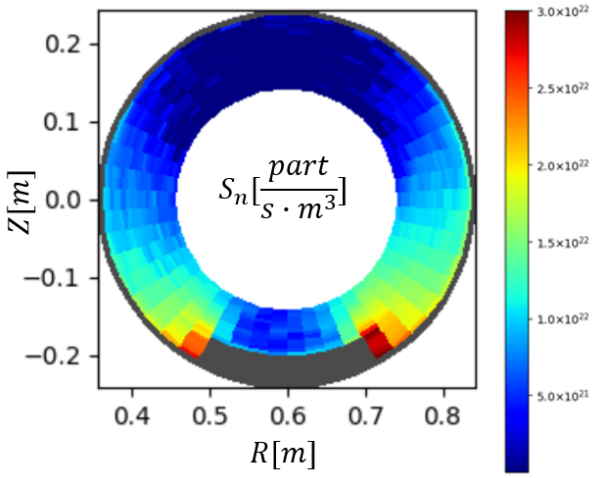

Figure 2.4. – Ionization source S_n in 3D circular geometry provided by EIRENE.

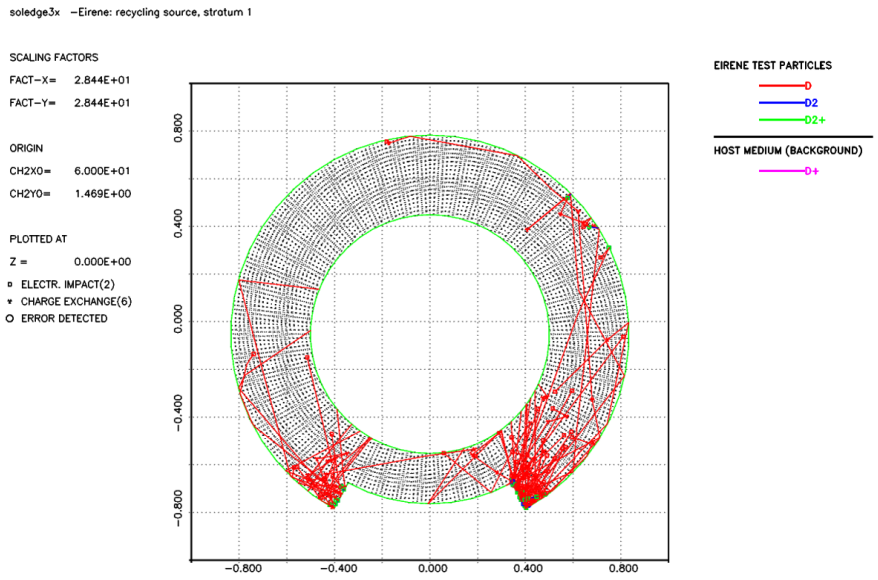

Figure 2.5. – Trajectories of EIRENE test particles in 3D circular geometry.

The results presented in Fig. 2.4 and Fig. 2.5 demonstrate the capability of using EIRENE as a neutrals solver in 3D. This capability is however currently limited to low-resolution simulations. Initially, we believed that the straightforward coupling approach used for TOKAM3X in 3D (Tamain, Bufferand, Ciraolo, et al. 2014, Fan et al. 2019) could be extended to SOLEDGE3X. However, the advancements made in SOLEDGE3X, relative to TOKAM3X, pose a significant challenge. Thanks to major numerical improvements, SOLEDGE3X allows for much higher grid resolutions, which we believe are important for accurately assessing turbulence phenomena, and e.g. SOL width. In addition, the STYX interface between SOLEDGE3X and EIRENE now requires more memory due to additional diagnostics for mean-field transport. These evolutions have essentially made 3D turbulent simulations incompatible with current supercomputers.

Several strategies could help overcoming this technical limitation. Updating EIRENE to a new version that supports hybrid MPI-OpenMP parallelization would partially alleviate the limitation by removing the need to duplicate the grid in memory at node level. However, this version had not been officially released in the first half of this PhD and has not yet been integrated with the code. A more ambitious strategy would involve implementing a domain decomposition scheme in EIRENE, a major effort also underway but not yet mature. A third strategy would be to use a coarser grid for neutrals. Indeed, currently the grid used in EIRENE is based on the plasma grid and is strongly over-resolved in a substantial part of the computational domain. Going this way would necessitate additional tools to make the EIRENE mesh independent from the plasma solver mesh and developing interpolation tools between the two grids. Eventually, all these strategies have been evaluated and considered impractical given the time constraints of this thesis. Although efforts are underway to address this bottleneck, they are beyond the scope of this study.

At that point, it became evident that making a choice was necessary: either use the advanced kinetic neutrals model proposed by EIRENE at the cost of reducing the mesh resolution and the accuracy of the turbulence description, or keep a highly resolved discretization of the plasma turbulence at the cost of reducing the fidelity of the neutrals description. Given the state of the art of turbulence modelling, we opted for the second option. Indeed, the point of our study is to evaluate the impact of neutrals physics and density regimes on edge turbulence. For this purpose, which is a fully new branch of study in edge turbulence modelling, we considered that one does not need an accurate and quantitative description of plasma-neutral interactions. Capturing qualitative aspects, such as the location and intensity of the particle source as well as an approximate level of energy dissipation by radiation, is sufficient. The strategy was then to maintain a more accurate description of turbulence while progressively incorporating neutrals physics with a less precise model, as long as it captured the main trends related to neutrals recycling and density regimes.

Eventually, the decision was made to integrate a fluid neutrals model for atoms into SOLEDGE3X, which is adequate to meet the high-resolution demand needed for turbulence modeling. Nevertheless, developing the foundational tools for the 3D SOLEDGE3X-EIRENE coupling has been a valuable investment for future work on turbulence-neutrals simulations.

2.3.2. Improved fluid neutrals model in SOLEDGE3X

The fluid neutrals model implemented in this thesis follows the model for charge exchange-dominated regimes proposed in Horsten et al. 2017. Due to time constraints due to the PhD duration, the model developed in SOLEDGE3X lacks several features compared to the one proposed in Van Uytven et al. 2022, primarily related to missing boundary conditions and the momentum/energy balance equations. The decision to simplify the model was made to accommodate the time required to run full turbulence simulations and obtain results. However, all the efforts presented in the following were concentrated on replicating the realistic localization of the recycling source as it is in EIRENE.

We will show in Chapter 3 and 4 that the fluid neutrals model we implemented is able to capture key relevant aspects of plasma neutrals interactions for the issue addressed in this manuscript.

This model specifically accounts for three main neutral-plasma interactions: ionization, recombination, and charge exchange, considering only neutral atoms (not molecules). It is valid in regimes where charge-exchange reactions dominate other plasma-neutral interactions and the inertial terms in the neutrals' momentum balance. This requires the local fluid velocity of atoms to be small compared to their acoustic velocity, a condition generally met in the divertor volume, a few collision lengths from the target. The collision length associated with charge exchange reactions (scaling with $\frac{u_n}{K_{cx} n_i}$ where u_n is the neutrals fluid velocity, K_{cx} is the volume reaction rates of charge exchange reactions and n_i the ion density) should also be small compared to other gradient lengths, a condition typically met at high densities

and low temperatures near the strike points, as discussed in Coroado et al. 2022a.

The fluid neutrals description in SOLEDGE3X currently relies on a hierarchy of 3 different models. They all share the same set of base equations:

$$\partial_t n_n + \vec{\nabla} \cdot \vec{\Gamma}_n = S_{n_n} \tag{2.38}$$

$$S_{n_n} = n_i n_e K_r - n_n n_e K_i + S_{ext} \tag{2.39}$$

Equation 2.38 is the particle balance for the neutral atoms' fluid. The particle source is driven by recombination and ionization and include and additional term S_{ext} which is used to handle gas puff, neutrals recycling and pumping (see below).

Additionnaly, all the models are built around the assumption of atoms temperature being equal to that of corresponding ions ($T_n = T_i$), mainly due to the strong charge-exchange collisions that tend to equalize the temperature of neutrals with that of ions (hypothesis of charge exchange dominated regime). Under this hypothesis, due to the strong character of the charge-exchange collisions, the neutrals population is thermalized with the ion population.

The 3 different neutrals models in SOLEDGE3X differ concerning the expression of the neutrals particle flux $\vec{\Gamma}_n$. At the very beginning of this thesis, it was based on a basic diffusion driven by neutrals density for each neutral species but 2 other options have progressively been implemented in the code, incorporating additional physics into the neutrals flux (as listed in 2.40, 2.41 or 2.43). The 3 models have successively been used in this thesis and are the following:

1. A fluid neutrals solver based on a simple diffusion equation with constant diffusion coefficients D_n and a neutrals flux given by a simple Fick's Law

$$\vec{\Gamma}_n = -D_n \vec{\nabla} n \tag{2.40}$$

2. A pressure diffusion model, where the flux is provided as

$$\vec{\Gamma}_n = -D_p^n \vec{\nabla} p_n \tag{2.41}$$

and the diffusion coefficients is expressed as

$$D_p^n = \frac{1}{m_i \left(n_i K_{cx,m} + n_e K_i \right)} \tag{2.42}$$

Here, $p_n = n_n T_n = n_n T_i$ represents the neutral pressure, and D_n^p denotes the pressure-diffusion coefficient, derived from K_i and $K_{cx,m}$, which respectively stand for the ionization rate coefficient and the linearized momentum charge-exchange rate coefficient (see Van Uytven et al. 2022). In Chapter 3, the neutrals model used is this one.

3. A pressure - diffusion plus convection model, which uses the same pressure diffusion coefficients 2.42 but also includes the contribution of an advective part

in the definition of the neutrals flux

$$\vec{\Gamma}_n = n_{n,eq}\vec{u}_i - D_p^n \vec{\nabla} p_n, \tag{2.43}$$

where $n_{n,eq} = \frac{n_i n_e K_r + n_n n_i K_{cx,m}}{n_i K_{cx,m} n_e K_i}$, while $\vec{u}_i$ is the ion fluid velocity (see Horsten et al. 2017 for more details). The study in Chapter 4 has been carried out relying on this latter version.

As discussed later in Section 2.4 and in the dedicated simulation Chapters 3 and 4, the inclusion of a self-consistent description of injected and recycled neutrals significantly alters the global balances of the system, with both plasma and neutrals now acting as reciprocal sources. On the plasma side, the impact of neutrals is incorporated through source terms in the plasma equations 2.20 to 2.26.

$$S_n = n_n n_e K_i - n_i n_e K_r \tag{2.44}$$

$$S_{E,i} = -m_i v_i^2 n_n n_e K_{cx,m} + R_E \frac{\epsilon_i}{n_i} n_n n_e K_i - \epsilon_i n_e K_r \tag{2.45}$$

$$S_{E,e} = -n_n n_e K_i T_{loss} - n_i n_e K_r T_{loss,r} \tag{2.46}$$

$$S_\Gamma = -\left(n_n n_e K_{cx,m} + n_e n_i K_r + n_e n_n K_i\right) \cdot \vec{u_{\parallel,i}}. \tag{2.47}$$

Eq. 2.44 takes into account the contribution of neutrals to the plasma particle source. Their impact on energy sources is very different for ions (Eq.2.45) and electrons (Eq.2.46). Concerning electrons, each ionization (respectively recombination) event is associated with an average energy loss T_{loss} (respectively $T_{loss,r}$) from Stangeby et al. 2000, as $T_{loss} = 25 + 170 \cdot e^{-T_e[eV]/2}$ and $T_{loss,r} = min(250, 8e^{T_e[eV]/9})/T_0$ (coarse fit to match AMJUEL database, see Reiter et al. 2000). This stand for the potential energy necessary to ionize a neutral as well as for radiation losses in the process. Concerning ions, each recombination event leads to the loss of the energy of the recombining ion. Energy recycling is addressed by assuming that ionizing neutrals deposits a fraction R_E of the local energy into the plasma. An additional term stems from the charge exchange reaction, assuming that each reaction leads to the loss of the initial ion's flow kinetic energy but that the new ion does not bring any flow kinetic energy to the ion population. Similarly, all the reactions contribute to the ion parallel momentum source.

The use of the energy recycling coefficient R_E deserves some discussion. This represents a simplistic approach to account for the fact that neutrals partially recycle plasma energy upon returning from the wall. A more comprehensive, self-consistent description would involve solving the energy balance equation for neutrals, a task planned for future work. However, this assumption does not impact the conclusions drawn in this study, which primarily rely on the spatial distribution of the particle source and on energy radiative losses due to ionization cooling the plasma. In the simulations presented here, R_E is set to a fixed value of 25%.

In the neutrals particle source S_{n_n} (Eq.2.39) the additional term S_{ext} is used to model particle injection by gas puff (or any other mean), particle recycling as well as

pumping. To model gas puff, S_{ext} is simply set to a non zero value in a cell adjacent to the wall where the gas puff valve is lcocated. For recycling, S_{ext} is set to a non zero value in each discretization cell in contact with the wall, with an amplitude chosen so that the flux of particle coming in the simulation box via this source is proportional to the out-flux of ions at the plasma wall interaction surface on the edge of this cell. The proportionality factor is the particle recycling coefficient R_n.

In mean-field simulations, pumping is typically achieved by setting recycling coefficients below 1 at the designated pump(s) location(s). However, setting $R_n < 1$ would only impact the incident flux of ions with the recycling model we have just described. In reality, one wants this $R_n < 1$ condition to affect both plasma and neutral particles reaching the pump, all the more as the pumping primarily impacts neutrals due to the pump's placement. In SOLEDGE3X, this is practically implemented by adding a neutral particle sink S_{sink} in S_{ext} in all cells in contact with the wall, using the following expression:

$$S_{sink} = -\Gamma_{1W}\,(1 - R_n)\,\frac{dS}{dV}, \tag{2.48}$$

where $\Gamma_{1W} = \frac{1}{4} n_n \sqrt{\frac{8T_n}{\pi m_N}}$, is the one-way (half-maxwellian) particle flux, dS is the surface of the cell in contact with the wall and dV its volume.

Finally a neutrals flux limiter is implemented to regulate the neutrals behaviour and match better the behaviour in kinetic simulations. The presence of low density areas might lead to the divergence of neutral diffusion coefficient, since its expression varies as 1/n. This is nonphysical as it leads to transport of neutrals much faster than their thermal velocity; in order to prevent this kind of situation, in the model a flux limiter for neutrals is introduced. The maxium allowed flux is defined as

$$\Gamma_{n,max} = \frac{n_n}{4}\sqrt{\frac{8T_n}{\pi m_N}}, \tag{2.49}$$

depending on the neutrals density n_n, temperature T_n and mass m_N. The neutrals particle is then forced to not exceed this value by forcing its asymptotic behaviour:

$$\vec{\Gamma}_n^{lim} = \frac{\vec{\Gamma}_n}{1 + \frac{|\vec{\Gamma}_n|}{\Gamma_{n,max}}}. \tag{2.50}$$

Several refinements are proposed in Horsten et al. 2017 and subsequent papers from the same team and will be object of future work. The current model should obviously not be used for studies depending strongly on divertor dissipation mechanisms but provides a first order description of the distribution of neutral particles and their impact on the plasma.

2.4. Balances in SOLEDGE3X

2.4.1. Particle and Energy balances of the system

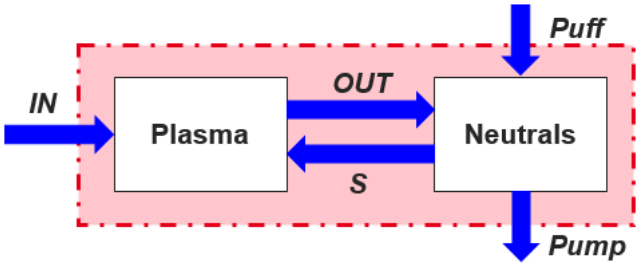

Figure 2.6. – Schematic representation of the whole global system constituted by plasma and neutrals, with fluxes contributions.

Using the schematic shown in Figure 2.6 as a reference, one can identify three different systems: the plasma, the neutrals and the plasma and neutrals taken together. In the following, the particle and energy balances for each of these systems are discussed.

First, the particle balance equation for the plasma is simply:

$$\frac{\partial}{\partial t}N = \Gamma_{IN} - \Gamma_{OUT}. \tag{2.51}$$

$N = \int\int\int ndV$ is the total particle content, so $\frac{\partial}{\partial t}N$ represents the rate of change of the particle content within the plasma volume over time. $\Gamma_{IN} = \int\int_{(\theta,\phi),IN} \vec{\Gamma}_n \cdot d\vec{s}$ is the influx computed at the inner boundary of the domain with Γ_{part} the particle flux and $d\vec{s}$ the normal vector to the core boundary, orientated towards the simulation domain. $\Gamma_{OUT} = -\int_{(\theta,\phi),out} \vec{\Gamma}_n \cdot d\vec{s}$ correspond to outflux computed at the outer boundary of the domain. In the absence of neutrals, no source term appears in the balance equation, as the plasma is self-sustained by the influx from the hot core region. On the other hand, once considering the closed subsystem that includes the neutrals, neutrals provide a volumetric source to the plasma. The particle balance for the plasma takes the form:

$$\frac{\partial}{\partial t}N = \Gamma_{IN} - \Gamma_{OUT} + S, \tag{2.52}$$

where the total volumetric source is defined as $S = \int\int\int S_n dV$.

Now, the particle balance for neutrals as an independent system can be written as:

$$\frac{\partial}{\partial t}N_n = \Gamma_{PUFF} + R_n\Gamma_{OUT} - \Gamma_{PUMP} - S, \tag{2.53}$$

where $N_n = \int\int\int n_n dV$ is the volume integrated neutral density. On the left-hand side, Γ_{PUFF} is the the neutral gas puff rate and $\Gamma_{PUMP} = \int\int\int |S_{sink}| dV$ is the pumped flux from the wall (see Eq. 2.48).

The total particle content is given as sum of both plasma and neutrals densities: here, as discussed in Section 2.3.2 and outlined in equations 2.44, 2.45, 2.46, and 2.47, the neutrals exchange particles with the plasma through the term S. Consequently, the balance for the overall system composed by neutrals and plasma can be rewritten as follows:

$$\frac{\partial}{\partial t}(N+N_n) = \Gamma_{PUFF} + \Gamma_{IN} - \Gamma_{PUMP} - (1-R_n)\Gamma_{OUT}. \tag{2.54}$$

In SOLEDGE3X, a similar approach can be applied to the energy balance, though there is a crucial distinction: only the plasma energy balance is relevant, as there is no corresponding energy balance equation for neutrals (which, in this model, effectively acquire energy from an undefined source). Here, considering directly the effect of the neutrals, the energy balance for ions is given as:

$$\frac{\partial}{\partial t}E = \Gamma_{E,IN} - \Gamma_{E,OUT} + S_E, \tag{2.55}$$

where the total ion energy content is given as $E = \int\int\int \epsilon_i dV$. $\Gamma_{E,IN} = \int_{(\theta,\phi),IN} \vec{\Gamma_E} \cdot d\vec{s}$ is the energy influx computed at the inner boundary of the domain with Γ_E the ions energy flux and $d\vec{s}$ the normal vector to the core boundary, orientated towards the simulation domain. $\Gamma_{E,OUT} = -\int_{(\theta,\phi),out} \vec{\Gamma_E} \cdot d\vec{s}$ corresponds to outflux computed at the outer boundary of the domain. The volumetric energy source is defined as $S_E = \int\int\int S_E dV = \int\int\int \left(S_{E,int} + S_{E,i}\right) dV$, where the internal energy $S_{E,int}$ counts as the energy exchange between electrons and ions while $S_{E,i}$ refers to Eq. 2.45.

Similarly for electrons we have

$$\frac{\partial}{\partial t}Ee = \Gamma_{Ee,IN} - \Gamma_{Ee,OUT} - S_{Ee}, \tag{2.56}$$

with the total electrons energy content given as $E_e = \int\int\int \epsilon_e dV$. $\Gamma_{E_e,IN} = \int_{(\theta,\phi),IN} \vec{\Gamma_{E_e}} \cdot d\vec{s}$ is the electrons energy influx computed at the inner boundary of the domain with Γ_{Ee} the electrons energy flux. $\Gamma_{E_e,OUT} = -\int_{(\theta,\phi),out} \vec{\Gamma_{E_e}}, \cdot d\vec{s}$ corresponds to the outflux computed at the outer boundary of the domain, directed towards the core. The volumetric energy source is defined as $S_{Ee} = \int\int\int S_{Ee} dV = \int\int\int \left(S_{E_e,int} + S_{E,e}\right) dV$, where the internal energy $S_{E_e,int}$ counts as the energy exchange between ions and electrons while $S_{E,e}$ refers to Eq. 2.46.

2.4.2. Conservation of particle and energy

SOLEDGE3X, as a numerical tool for solving mass, momentum, and energy equations, must ensure the conservation laws for these physical quantities. This entails that the production of these quantities within a closed volume must precisely match the flux of that quantity across the boundary of the volume.

Verifying conservation serves as a sanity check for the code and is a valuable tool for identifying the dominant terms in the balances. The numerical approach followed by SOLEDGE3X relies on finite volumes which should conserve to machine precision

these quantities. To check that, let us compute the relative error ε_r, defined for particle and energy respectively as

$$\varepsilon_r = \frac{\frac{dN}{dt} - \Gamma_{IN} + \Gamma_{OUT} - S}{H(\Gamma_{IN}) + H(S)} \tag{2.57}$$

$$\varepsilon_r = \frac{\frac{dE}{dt} - \Gamma_{E,IN} + \Gamma_{E,OUT} - S_E}{H(\Gamma_{E,IN}) + H(S_E)} \tag{2.58}$$

where, for a generic quantity X the function $H(X)$ refers to $H(X) = max(X, 0)$.

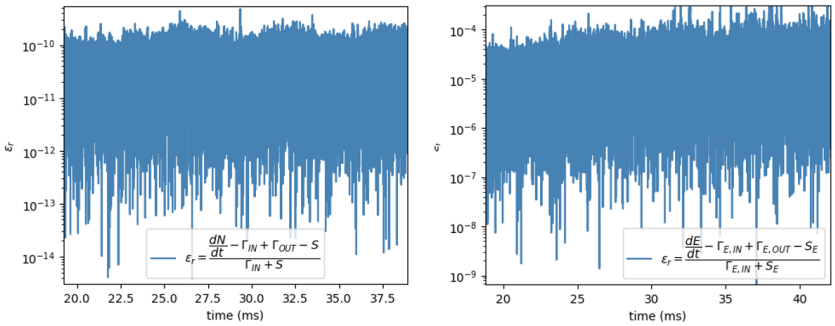

Figure 2.7. – relative error in the particle conservation (left) and energy (right) in a TCV-X21 simulation, described later in Chapter 4

.

Fig. 2.7 shows the relative error in the particle and energy balance for ion and electrons in a typical SOLEDGE3X 3D turbulent simulation including neutrals. One can see that the finite volume scheme achieves excellent conservation properties for both quantities with an average error of the order of 10^{-10} for particles and 10^{-5} for the energy, not exceeding 10^{-9} and 10^{-3} respectively during fluctuations.

2.4.3. Convergence

Convergence refers to the attainment of a stationary state ("steady state"), where a specific physical quantity no longer evolves over time. This implies that from Eq. 2.53 $< \frac{\partial}{\partial t} N >_t \longrightarrow 0$ and from Eq. 2.55, $< \frac{\partial}{\partial t} E >_t \longrightarrow 0$, where the average is performed on a time window large enough to eliminate turbulence driven fluctuations, namely over several correlation times. Once this state is achieved, the solutions are expected to remain unchanged if simulations are pushed further and results are assumed to accurately represent the statistically steady state conditions the plasma would reach in experiments.

However, the key difference in reaching convergence in terms of particle and energy balance, whatever driving mechanism is accounted for, is that most energy is not recycled, making the system primarily driven by the core and the outflux to the wall.

This generally results in faster convergence compared to the particle balance, however it can be challenging to reach for turbulent neutrals cases (see Chapter 4).

In the mean field simulations community, determining convergence involves applying standard criteria, with one of the most used being the convergence ratio C_R introduced in Wiesen et al. 2015. For the whole system plasma and neutrals, the particle convergence achievement requires that

$$C_R = \left| \frac{< \frac{\partial}{\partial t} (N + N_n) >_t}{\Gamma_{IN} + \Gamma_{PUFF}} \right| \lesssim 1 - 2\% \tag{2.59}$$

This criteria can already be challenging to reach in 2D mean field simulations, as emerge in Sureshkumar et al. 2025 for ITER simulations which require 1 s to converge (higher than the confinement time for ITER!).

When extending to turbulence, by definition the system never achieve a stationary solution [3], but instead fluctuates around a constant mean. The convergence then needs to be defined in a statistical manner, involving the use sliding time averages which introduces some uncertainty concerning the choice of the width of the time-averaging window. More problematic is the fact that turbulence simulations cannot run on extremely long time scales due to their high numerical cost so that convergence in turbulent simulation can be difficult to reach within reasonable computing time. This will raise questions about the significance of observation in simulations that are not fully converged according to criterion 2.59. This will be discussed in Chapter 4.

2.5. Summary

Chapter 2 delves into the methodology used to model turbulence and neutral interactions with SOLEDGE3X. We first introduced the different classes of models used to describe the plasma edge. The chapter provides an overview of the primary models used in edge plasma simulations, ranging from particular description, touching briefly the kinetic and gyrokinetic models, up to fluid approaches. For the fluid approach, the chapter addresses the necessity of system closure and discusses common closures in plasma physics, including Braginskii and Zhdanov. It also introduced the drift-ordering, which is an approximation at the heart of drift-fluid models such as the one used in SOLEDGE3X.

The chapter then presents the SOLEDGE3X code itself, detailing its main set of equations and boundary conditions. The discussion includes a focus on how turbulence is modeled in SOLEDGE3X, along with a dedicated section on neutrals. This section highlights the efforts made in this work to enable self-consistent simulations that incorporate both turbulence and neutrals, beginning with the 3D coupling to the kinetic Monte Carlo code EIRENE and extending to a hierarchy of fluid neutral models

3. Note that because of Monte Carlo noise, mean field simulations using EIRENE for neutrals also reach a statistically steady state and cannot in general be converged to machine precision. This is also a reason why such convergence criteria has been originally introduced.

now available in SOLEDGE3X. Finally, the chapter describes the system's particle and energy balances in terms of conservation and convergence.

3. Low density regimes: a study in limited configuration

In this Chapter, we present a first study analyzing the impact of neutrals recycling on edge turbulence and transport physics. The intermediate fidelity fluid neutrals model introduced in the previous chapter is used for that purpose. As a first step before tackling relevant high recycling regimes in diverted geometry (done in Chapter 4), we here consider an idealized circular limited geometry in low recycling regime. This study will hence allow us to highlight the first order effects related to the change in the particle flux drive of simulations from an artificial influx from the core (as done previously in simulations not including neutrals) to a self-consistent model involving gas puffing and neutrals recycling. We will in particular investigate the impact of the localization of the particle source both radially and poloidally in the vicinity of the limiter and of the gas-puff valve.

3.1. Simulations set-up

In this chapter, 3 different turbulence simulations will be considered:

1. a reference simulation without neutrals
2. a simulation with self-consistent neutrals recycling using the intermediate fidelity fluid neutrals model (Eq. 2.41) to investigate the impact of a localized recycling source (and gas puff) drive
3. a simulation with self-consistent neutrals recycling using the lowest-fidelity fixed diffusion fluid neutrals model (Eq. 2.40) with artificially enhanced diffusion coefficient to demonstrate that the localization of the particle source is the determinant player

We here after describe the set-up of these simulations, starting with common parameters before highlighting the differences.

3.1.1. Geometry and parameters

A plasma composed of a single ion species, namely deuterium is considered. We use a circular limited magnetic configuration with a toroidally symmetric limiter located at the bottom part of the poloidal plane, i.e. in the direction of the ions ∇B drift with the chosen magnetic field's direction (see Fig. 3.1 giving a view of the geometry in the poloidal direction).

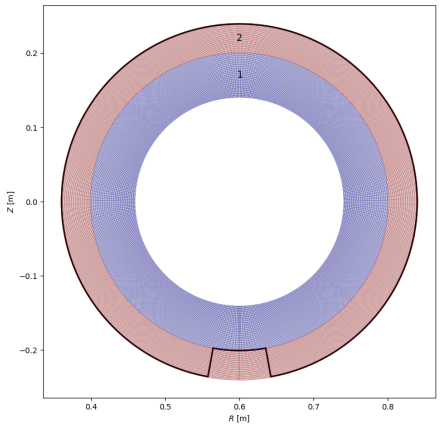

Figure 3.1. – Representation of the circular domain illustrating the discretization mesh. The colors refer to the domain decomposition used in the code (2 subdomains here). The black line provides the contouring of the wall with the limiter at the bottom of the machine.

A small machine size has been chosen in order to ensure that turbulence can be well resolved : the minor radius at the separatrix is $a = 20$cm, with a major radius of $R_0 = 60$cm, roughly equivalent to a tokamak of the size of COMPASS (see Panek et al. 2006). The simulated domain has a radial of 10cm extension around the separatrix. The computational grid is constituted by $\sim 10^7$ points, with 100 points in the radial direction, 1024 points in the poloidal direction and 128 points in the toroidal one. The resolution at the mid-plane is in the range of 1 mm, close to a Larmor radius ρ_L in the expected conditions at the separatrix in such machine ($\rho_L \approx 8$mm for Deuterium at 30 eV and 1 T).

The simulated domain is a quarter of torus, with periodic boundary conditions in the toroidal direction. This is done to reduce the computing cost. By doing this, one models effectively only toroidal mode numbers multiples of 4 but it was shown in TOKAM3X that it did not impact significantly the turbulence and transport properties. In spite of this, all the parameters given after (e.g., the heating power) are for a full-torus equivalent simulation. The profile of the safety factor is chosen parabolic as a function of the minor radius, with a minimum value of 3 at the core boundary and a maximum value of 6 at the wall. A total input power of 62.5kW equally distributed between electrons and ions is prescribed.

Key parameters common to the simulations presented in this chapter are summarized in Table 3.1.

R_0**[m]**	a**[m]**	P **[kW]**	$D_\perp[\frac{\mathbf{m}^2}{s}]$	$\chi_{\perp,e}[\frac{\mathbf{m}^2}{s}]$	$\chi_{\perp,i}[\frac{\mathbf{m}^2}{s}]$	$\nu_{\perp,i}[\frac{\mathbf{m}^2}{s}]$
0.6	0.2	62.5	10^{-2}	10^{-2}	10^{-2}	10^{-2}

Table 3.1. – Input parameters for the machines dimensions (major and minor radius, heating power and transport coefficients) in SI units, together with the aspect ratio common to all the circular simulations.

The cross-field transport coefficients $D_\perp$, $\nu_\perp$ and $\chi_{\perp,e,i}$ assume a small value ($10^{-2} m^2 s^{-1}$) meant to describe subgrid transport.

3.1.2. Neutrals model and particle flux drive

Two different fueling mechanisms are driving (and differentiating) the three cases considered in this chapter: a simulation driven by a symmetric particle source coming from the core, another one driven by a toroidally localized gas puff in the outer midplane with recycling, and finally one including both gas puff and recycling but with a large and spatially homogeneous diffusion coefficient.

The case without neutrals, that will serve as a reference, refers to a 3D turbulent simulation in which neutrals are not modelled so neither neutral puffing nor recycling is considered. Beside the heating power injected from the core boundary, the simulation is driven by a particle source originating from the core, which is uniform in both the poloidal and toroidal directions, with an influx rate full torus equivalent set at $2.5 \times 10^{21} \frac{\text{part}}{s}$. Fig. 3.2 shows poloidal snapshots of the density, electron temperature and potential in this reference simulation: these cases exhibit a usual phenomenology for 3D limited turbulent simulations as already reported in Tamain, Ghendrih, Bufferand, et al. 2015 and in Nace et al. 2016. Turbulence is characterized by intermittent field-aligned filaments, with a clear ballooning structure.

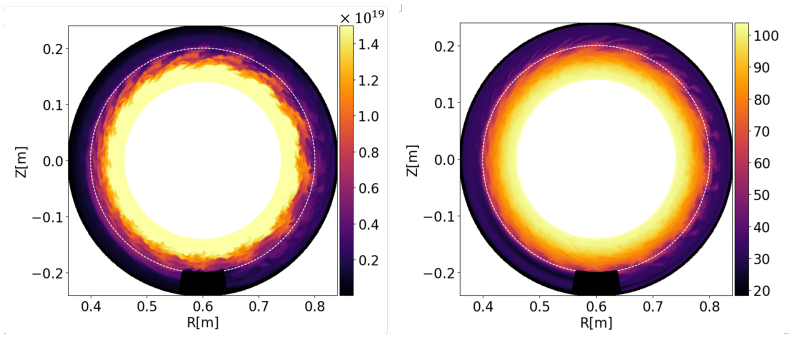

(a) $n_e[m^{-3}]$ (b) $T_e[eV]$

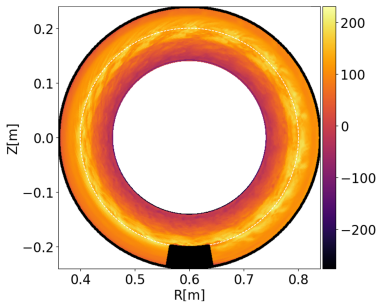

(c) $\Phi[V]$

Figure 3.2. – Snapshots of plasma density, temperature and potential for the reference no neutrals case

To include neutrals recycling in the 2 other simulations, the reference scenario without neutrals was modified by deactivating the core particle source, tuning on the fluid neutrals model (including recycling) and replacing the core particle in-flux by a gas puff introduced at the outer midplane wall, located at a toroidal angle of ($\varphi = 45°$). In section 3.2 and 3.3 the intermediate fidelity fluid neutrals model with self-consistent pressure-diffusion (Eq. 2.41) is used, while section 3.4 will make use of the coarser model with fixed diffusion (Eq. 2.40) in order to demonstrate that the particle source location is the key player.

The intermediate fluid neutrals case will present a dedicated tuning of the gas puff to accelerate the convergence for particle balance, as explained in Section 3.1.3. The recycling coefficient for the neutrals was set at $R_n = 0.98$, while the energy recycling coefficient was chosen as the 25% of the ions' energy.

3.1.3. Discussion on convergence of the particle balance

In this section, the time status of the simulation is described. Overall, the circular simulations, starting from the case without neutrals to the inclusion of neutrals using the improved fluid neutrals model, have covered a total plasma time of 5 ms.

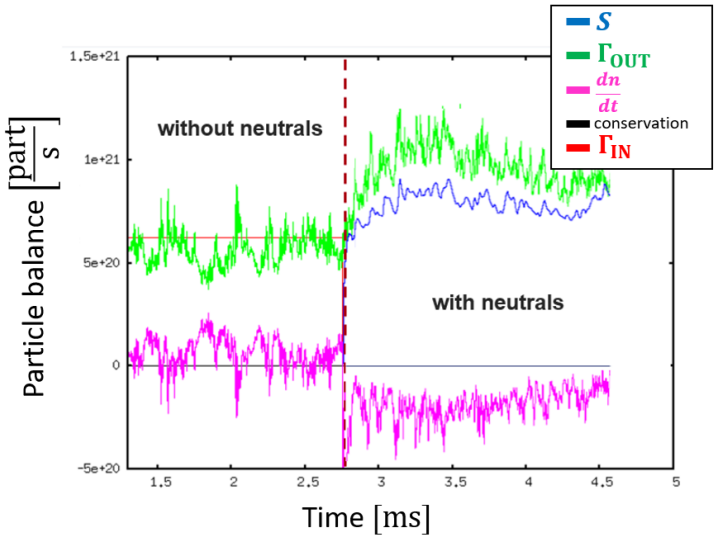

Figure 3.3. – Time traces of the different components of the plasma particle balance obtained from volume-integrating the ion particle balance equation (Eq. 2.52). Here one can see the evolution of the particle influx from the core region, particle outflux at the limiter and wall, particle source due to neutrals and time derivative of the plasma particle content. The black line is the sum of all these components and represents the particle conservation error, which is negligible. To be noted that the case with neutrals was restarted from the case without neutrals.

The time traces shown in Fig. 3.3 illustrate the time evolution of the different contributions to the particle balance equation in 2.4. The left side of the plot presents fluxes from the case without neutrals. At $t \approx 2.75$ms, the simulations was restarted from its final state with the neutrals model turned on according to the setup discussed in the previous section.

Incorporating neutrals into the turbulent code significantly alters the driving mechanism of the simulation, shifting the dominant terms in the particle balance. When turbulence is driven by flux from the core, the dominant terms are the particle influx from the core Γ_{IN} (in red) and the outermost flux surface particle outflux Γ_{OUT} (in green). This simulation has reached convergence from the particle balance point of view as the out-flux and the in-flux balance each other when averaged over a time scale significantly larger than the turbulence correlation time, resulting in the time derivative term oscillating around zero.

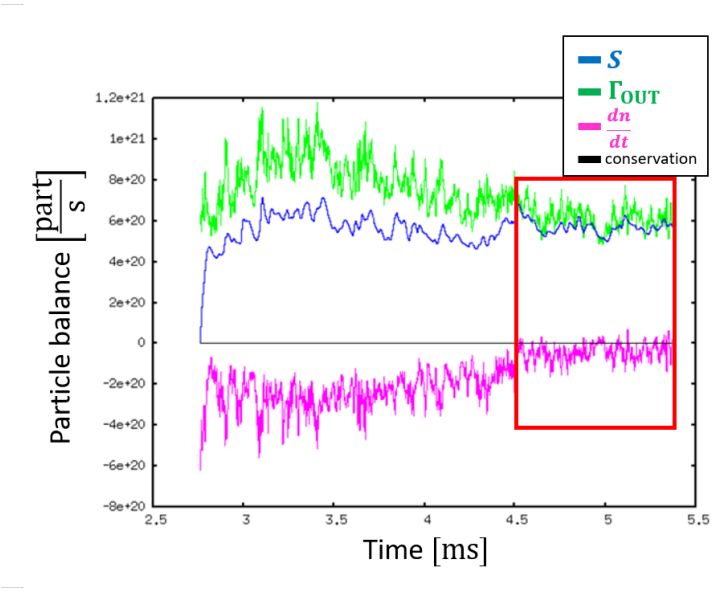

Figure 3.4. – Time traces $[ms]$ of particle fluxes integrated in volume $[part/s]$ for the case with neutrals: here one can see the evolution of the particle outflux, particle source and time derivative. The particle conservation check is plotted in black. The red square indicates the time window during which data are analyzed in the rest of this Chapter.

When neutrals are included (in the right side of plot 3.3), the source term S (in blue) and the particle outflux Γ_{OUT} (in green) rapidly become dominant while the in-flux term immediately disappears by construction. Zooming on the right-side of plot 3.3, after restarting from the case without neutrals, one sees that the source term rapidly builds up in less than 100μs, as shown in Fig. 3.4. This behaviour is due to the fact that the pressure diffusion coefficient related to charge-exchange collisions is actually very large, leading to a fast equilibration of the neutrals density with respect to the plasma conditions and target fluxes. However, the simulation with self-consistent neutrals has not yet converged at this point ($t \approx 2.7$ms), with a residual discrepancy of the order of 30% between the plasma out-flux and the total ion due to neutrals, evidenced by the non-zero time derivative. This flux imbalance remains for the following 1.5 ms although its relative amplitude tends to slowly decrease. The slope suggests that reaching a converged state might require more time than what can be achieved reasonably in terms of computational resources.

It is worth at this point to go deeper in the discussion started in Section 2.4.3. There we said that including neutrals recycling poses significant challenges for achieving convergence even for 2D mean field simulations. Our plots here illustrate that for flux-driven 3D turbulence simulations this point is all the more so critical, particularly when considering the computing resources necessary to achieve a simulation.

Fig. 3.4 already reveals a wide range of timescales, at least four, driven by turbulence physics on one hand and particle balance on the other. These scales are schematized in Fig. 3.5.

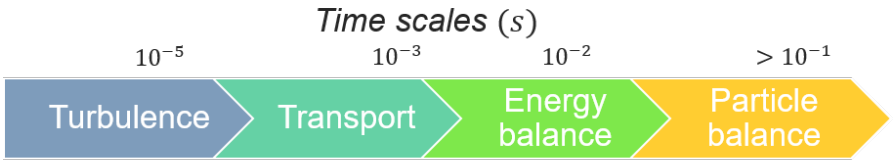

Figure 3.5. – Different time scales existing in turbulence - neutrals codes, courtesy of H. Bufferand.

The first scale is the turbulence time scale, defined as the time needed for turbulence to develop for given equilibrium conditions (density, temperature, gradients...). This is the time scale necessary to reach a pseudo-steady-state in gradient-driven simulations where turbulence is modelled for a fixed plasma background. It is intrinsically dependent on the growth rate of the modelled instabilities, e.g. for the interchange instability $\gamma_I = c_s\sqrt{\frac{\vec{\nabla}p\cdot\vec{\nabla}B}{pB}}$, $\tau_{turb} = \tau_I \approx \frac{\sqrt{aR}}{c_s}$. Generally, this scale is the fastest one observed in the simulations, of the order of some μs. It is of the same order as the correlation time of small-scale fluctuations.

The time scale of equilibration of neutrals with respect to the plasma background conditions (not shown in Fig. 3.4 which focuses on the plasma and not the neutrals) is of the same order of magnitude. In the simulation analysed here, this time scale is of the order of 50μs. It depends on the amplitude of the diffusion or pressure-diffusion coefficient of neutrals and on the ionization mean-free path of neutrals (effectively determining the characteristic length of the domain in which neutrals exist) but in most conditions will remain short compared with the second time scale of interest for the plasma.

The second characteristic timescale is recognized as the transport time, i.e. the duration required for the large scale equilibrium of the plasma (profiles, poloidal asymmetries) to develop and reach a steady-state for given sources. It is directly related to the confinement time of the plasma and can be interpreted as the time needed for a given plasma quantity (particle or energy) to travel from the source to the sink (wall). It is of the order of a few ms in the considered simulation.

The 2 slowest time scales recognized in the system are related to the convergence of the particle and energy balances and correspond to the time scale needed to equilibrate the in-flux and out-flux of a given conserved quantity for the whole system consisting of the plasma and neutrals. These are significantly slower than the transport time due to recycling processes which reinject particles and energy in the system. When the effective recycling coefficient for a quantity is large (close to 1), it requires a large number of recycling cycles (ie., deposition of the quantity in the plasma ->

transport to the wall -> recycling as neutrals) to get to an equilibrium. One can demonstrate this based on the 0D particle balance of the plasma similar to the one already considered in section 1.5.1:

$$\frac{\partial}{\partial t}(nV) = \Gamma_{PUFF} - \Gamma_{LOSS} + \Gamma_{REC} \tag{3.1}$$

where n is the electron density, $\Gamma_{LOSS} = nc_sS_{wet}$, $\Gamma_{REC} = R_n\Gamma_{LOSS}$, Γ_{PUFF} is the fuelling puff rate, c_s the sound speed at the targets, S_{wet} is the plasma wetted surface of the wall and V is the volume of the plasma. One gets:

$$\frac{\partial}{\partial t}(nV) = \Gamma_{PUFF} - (1-R_n)\, nc_sS_{wet} \tag{3.2}$$

The generic solution to this equation is:

$$n = n_\infty + (n_0 - n_\infty)\, e^{-\frac{1-R_n}{\tau_0}t} \tag{3.3}$$

where $n_\infty = \frac{\Gamma_{PUFF}}{(1-R_n)c_sS_{wet}}$ is the steady-state density the system will converge to and n_0 is the initial density. $\tau_0 = \frac{V}{c_sS_{wet}}$ is the characteristic time of the system in the absence of recycling and can be interpreted in this 0D model as the transport time discussed above. One immediately sees that the evolution time of the system with recycling scales as $\frac{1}{1-R_n}$. With $R_n = 0.98$ as in our simulations, one hence expects an increase by a factor of 50 of the time needed to get the system to a statistical steady-state for a given gas puff amplitude.

Currently, most results reported in the literature come from simulations that are shorter than the particle balance convergence time, meaning they have not formally reached a steady state. An open question remains about how to address the slowest time scale when using a 3D turbulent code. In the following and in ending part of the following Chapter 4, we partially started to address this issue showing different strategies for accelerating the convergence.

The first strategy presented in this Chapter, is mostly "cheating": to save a considerable amount of time while ensuring relevant results, the gas puff value was adjusted in Fig. 3.4 starting from $t = 4.4$ms to achieve a pseudo-steady-state. By doing so, we have tuned the total source term to make it match the amplitude of the outflux of particles and the simulation rapidly reached a statistically converged steady state. In the next 2 sections the simulation with neutrals is statistically analyzed in a time frame beyond $t = 4.5$ms, marked by the red window of Fig. 3.4.

This approach, where the puff is adapted to the transient plasma solution in order to achieve more rapid convergence of the particle balance, is acceptable in the frame of the study led in this Chapter as we are interested in a generic investigation on the impact of neutrals recycling. Should one target comparison with experiments instead, one would need to fix the gas puff to the experimental value and wait for the convergence to be reached. This raises fundamental questions on the way to drive these simulations and the significance of the results on shorter time scales before

convergence.

3.2. Investigation on the impact of a localized gas puff on the toroidal symmetry

Before analyzing all the simulations in terms of plasma equilibrium [1] and turbulence, there is a key point to discuss. Unlike simulations without neutrals, those that include neutrals lack axi-symmetry. The presence of the gas puff at the midplane induces a breaking of the toroidal symmetry in the simulated domain, a symmetry that was maintained in the case without neutrals where the plasma fueling mechanism was driven by a toroidally uniform source from the core. The toroidal symmetry of turbulence simulations is often exploited to increase available data for statistics by exploiting the ergodic hypothesis and aggregating statistics not only in the time direction but also in the toroidal direction. This may not be a valid assumption anymore in simulations with a localized gas puff. Quantifying the loss of axi-symmetry is hence mandatory to establish the way to carry on the analysis of turbulence. This may also provide some insights on the physics of gas puff imaging, demonstrating the possible implications for the interpretation of this diagnostic.

3.2.1. Evaluation of the toroidal asymmetries due to the gas puff

The loss of symmetry in the toroidal direction may impact differently all the plasma and turbulent fields. In this section one is looking both at the amplitude and localization of the toroidal asymmetries generated by the puff perturbation on the time averaged plasma properties and turbulence properties.

3.2.1.1. Evaluation of toroidal non uniformity

In order to investigate the impact of the loss of toroidal symmetry due to gas puff, one is going to compare the non neutrals case with the neutrals case with pressure diffusion transport. The evaluation is made via the computation of the toroidal non-uniformity (TNU) of the plasma solution, defined for any field X as:

$$TNU_X = \frac{max(X)_\varphi - min(X)_\varphi}{X_\varphi} \tag{3.4}$$

The toroidal non-uniformity measures how non-homogeneous the time-averaged field X is along the toroidal direction and provides a measure of how extended the perturbation due to the localization of the gas puff is on the experimentally measured quantities like density or temperature.

1. In the rest of this manuscript, we will often refer to the time-averaged plasma properties as equilibrium conditions. This is in opposition to turbulence fluctuations properties.

In Fig. 3.6, we start first to compare side by side the TNU for the time averaged plasma quantities $< n_e >_t$ and $< T_e >_t$ between the 2 simulations. One has to account for a difference on the statistical error of $\approx \sqrt{2}$ due to the sampling size for the time windows in which statistics are performed on the two simulations.

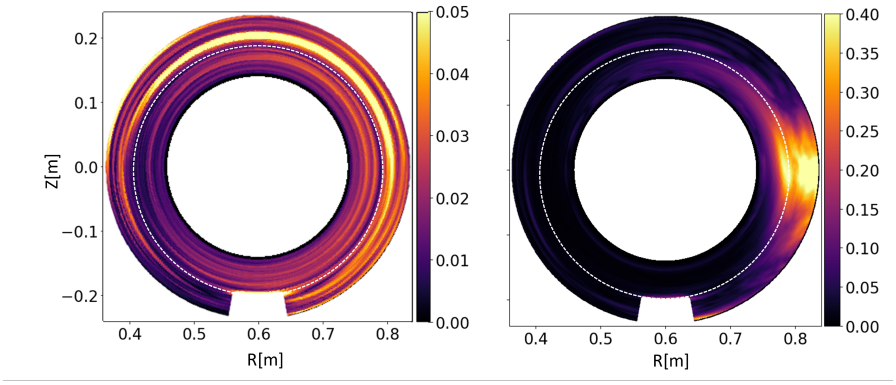

(a) $X \equiv < n_e >_t$

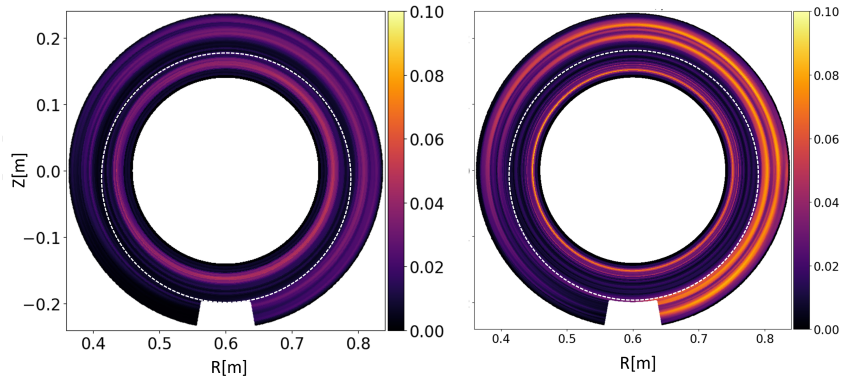

(b) $X \equiv < T_e >_t$

Figure 3.6. – Poloidal maps of the TNU, as it is expressed in Eq. 3.4, of the time averaged electron density $< n_e >_t$ in Fig. 3.6a and for the time averaged electron temperature $< T_e >_t$ in Fig. 3.6b for the no-neutrals (first column) and the neutrals (second column) case.

Two things have to be emphasized. We first demonstrate that the case without neutrals (plots on the first column) is axi-symmetric within some statistical error bar: the maximum amplitude of the density's and temperature's TNU is around 5%, with a clear ballooning pattern that can be related to the fact that fluctuations are more important on the LFS and so more likely to generate toroidal non-uniformities there. The presence of the higher TNU ring on T_e close to the center of the simulation domain is more difficult to explain but likely due to a perturbative effect linked to boundary conditions. This gives an order of magnitude of the statistical errors due to the finite set of data as the TNU would boil down to 0 with an infinite time series. The second thing

is that, if the same analysis is applied to the case with neutrals, one can observe the existence of a perturbation of the symmetry for the plasma properties, with different amplitudes depending which one is considered. Compared with the reference case without neutrals, the perturbations on the density are statistically important, reaching a maximum of 40 to 50 % (Fig. 3.6a). The TNU turns out significantly less for the temperature, here in Fig. 3.6b where the colorbar is reduced with respect to the figure for the density, exhibiting values ranging up to a maximum of 10 %, just larger than the evaluated statistical error.

A clear difference can be observed between the pattern of the perturbation on the density and on the temperature. While the perturbation on the density is mainly localized in the outboard mid-plane in the vicinity of the gas-puff, the small perturbation on the temperature extends much further away along flux surfaces in the SOL. The explanation lies on the difference in the parallel transport mechanisms associated with these quantities. While density parallel transport is purely convective, heat parallel transport also includes a parallel conduction term stemming from the collisional closure. Except in cold plasma conditions observed at or when getting close to detachment (not the case here), this term usually dominates parallel heat transport, leading to a rapid flattening of temperature profiles in the parallel direction and a reduction of local inhomogeneities.

The comparison between the TNU for the relative fluctuations level of the electron density and temperature, for the case with and without neutrals, are reported in Fig. 3.7.

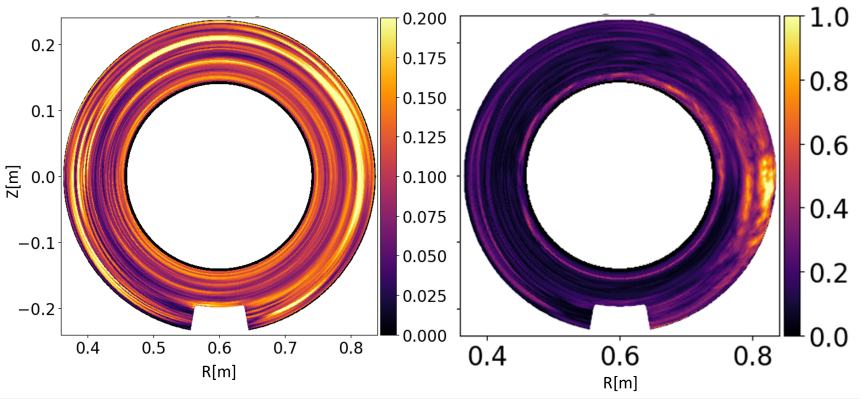

(a) $X = \mathrm{rms}\,(n_e)_t \,/ < n_e >_t$

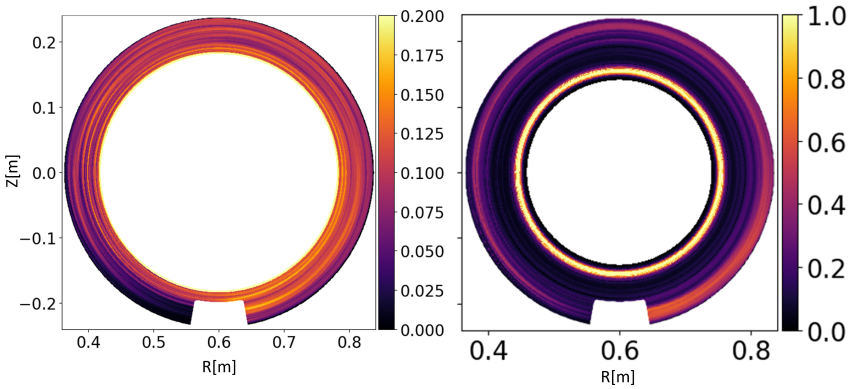

(b) $X = \mathrm{rms}\,(T_e)_t \,/ < T_e >_t$

Figure 3.7. – Poloidal map of the TNU, as it is expressed in Eq. 3.4, of the relative fluctuation rate, for the electron density (Fig. 3.7a) $X = \mathrm{rms}\,(n_e)_t \,/ < n_e >_t$, and for the electron temperature $< T_e >_t$ (Fig. 3.7b) $X = \mathrm{rms}\,(T_e)_t \,/ < T_e >_t$ for the no-neutrals (first column) and the neutrals (second column) case.

As could be expected, the level of TNU due to the limited statistic is larger for the fluctuation level than for time-averaged quantities (the statistical error is expected to increase with the order of the considered statistical moments). For density and temperature fluctuations, the reference simulations exhibits about 20% of TNU. When the neutrals puff is included however, this value raises considerably to 100% for the density and 50% for the electron temperature. The perturbation in front of the puff is again very localized for the density relative fluctuations. The distribution for the temperature appear smoother, once again likely due to the fast parallel conduction of energy.

It does emerge that the density but also the turbulence properties are significantly impacted by the gas puff, although the amplitude of the perturbation strongly depends on the type of transport associated with the considered field. Let us now looking into details, picking up some relevant flux surfaces.

3.2.1.2. Flux surface structure of toroidal asymmetry

In order to understand the spatial distribution of the perturbations, we now plot the quantities mentioned above for selected flux surfaces.

To make the non-toroidally symmetric perturbation induced by the puff much more visible, Fig. 3.8 shows for a given field X, $\frac{\tilde{X}-<X>_\phi}{<X>_\phi}$ where the values are direct expressed in percentage.

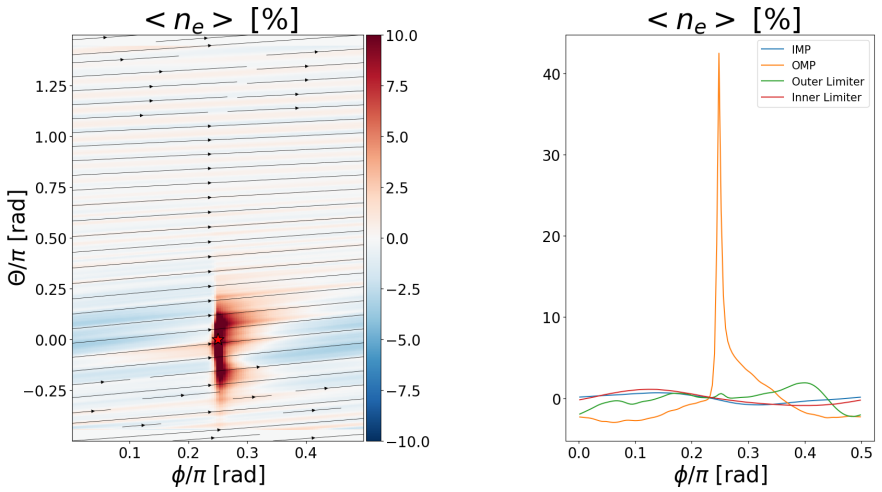

(a) $X \equiv n_e$

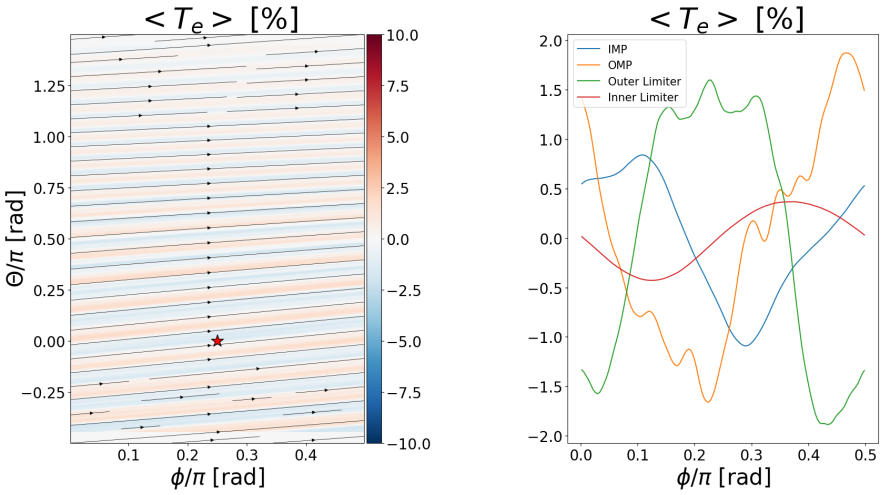

(b) $X \equiv T_e$

Figure 3.8. – Relative toroidal fluctuation of time-averaged quantities $\frac{\langle X\rangle_t - \langle X\rangle_{t,\varphi}}{\langle X\rangle_{t,\varphi}}$ for the electron density $X = n_e$ (a) and temperature $X = T_e$ (b) as a function of $\frac{\Theta}{\pi}$ along the vertical axis ($\frac{\Theta}{\pi} = 0$ is the outboard mid-plane, increasing in the electron diamagnetic direction) and $\frac{\varphi}{\pi}$ on the horizontal axis. The location of the gas puff is indicated with a red star. The plotted flux-surface is located in the near SOL, after the separatrix $R - R_{sep} = 1$cm in the outboard mid-plane. The 1D profiles for each quantities refers to some specific poloidal locations, in particular the Inner Limiter Plate at $\Theta = 1.25\pi$rad, the Inner mid-plane at $\Theta = \pi$rad, the Outer mid-plane at $\Theta = 0$rad and the Outer Limiter Plate at $\Theta = -0.25\pi$rad. Magnetic field lines are plotted in black in the left plots. Note that the color scale for the density plot is saturated so that one can see not only the local perturbation in the vicinity of the puff, which is of the order of 40%.

As anticipated from the TNU poloidal distribution, the amplitude and the spatial

localization of the perturbation for density and temperature is extremely different, as shown in Fig. 3.8.

Starting with the density, the gas puff (whose position is marked with a red star on the left plots of Fig. 3.8) drives a strong local perturbation at the puff location and extends in the immediate vicinity of it, at the outboard midplane and at the toroidal position of $\varphi = \pi/4$ rad, with a maximum amplitude of 40 %. This local perturbation has a relatively large poloidal extension of $\approx \pi/4$rad. It exhibits an asymmetric wake in the toroidal direction due to the direction of the parallel flow (orientated towards larger toroidal angles at this poloidal location).

As expected from the TNU, the perturbation of the gas puff on the average temperature does not exceed significantly the statistical error of the asymmetric simulation: there is no evident sign of the impact of the puff itself.

We now turn to the fluctuation rate. Looking at the same specific flux surface in the near Scrape-Off-Layer (corresponding to $R - R_{sep} = 1$cm in the outboard mid-plane), the gas puff is found to drive a non-axisymmetric perturbation of the amplitude of the relative fluctuations by up to 30% (relative change of relative fluctuation rate), illustrated here for the density and the electron temperature in Fig. 3.9. Similarly to the time averaged values, the response of the temperature fluctuation rate is different from the one of the density. The density fluctuation rate exhibit higher local perturbation than the temperature. However, the later propagates along flux tubes all the way up to the target plates when the perturbation on density fluctuation remains mainly localized in the vicinity of the puff.

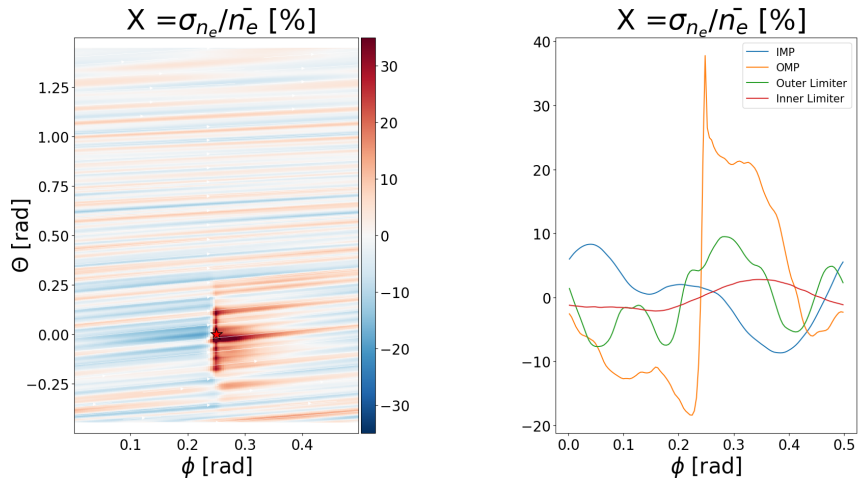

(a) $\frac{\tilde{n}_e}{\bar{n}_e}$

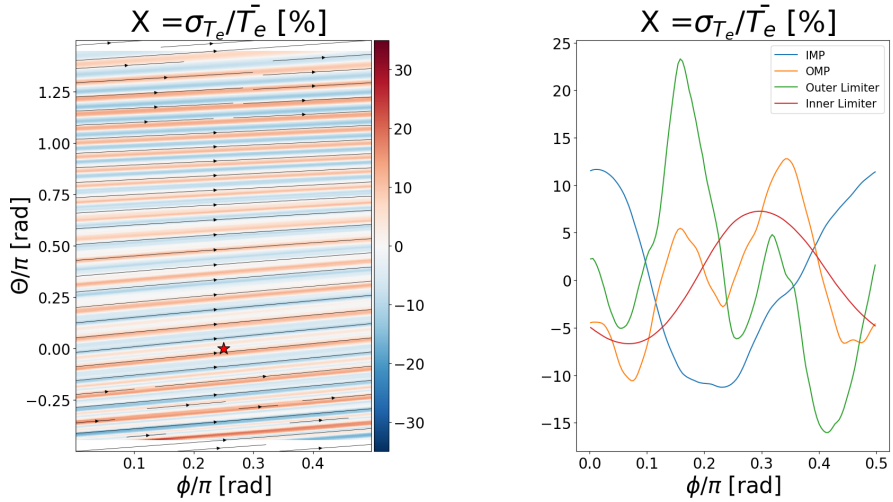

(b) $\frac{\tilde{T}_e}{\bar{T}_e}$

Figure 3.9. – Relative toroidal fluctuation $\frac{X-\langle X\rangle_\varphi}{\langle X\rangle_\varphi}$ for the electron density relative fluctuation rate $X = \frac{\mathrm{rms}\,(n_e)_t}{\langle n_e\rangle_t}$ (a) and electron temperature relative fluctuation rate $X = \frac{\mathrm{rms}\,(T_e)_t}{\langle T_e\rangle_t}$ (b), as a function of the poloidal angle θ along the vertical axis ($\theta = 0$ is the outboard mid-plane, increasing in the electron diamagnetic direction) and the toroidal coordinate φ on the horizontal axis. The location of the gas puff is indicated with a red star. The plotted flux-surface is located in the near SOL, after the separatrix $R - R_{sep} = 1$cm. The 1Ds profiles for each quantities refers to some specific poloidal location, in particular the Inner Limiter Plate at $\Theta = 1.25\pi$rad, the Inner mid-plane at $\Theta = \pi$rad, the Outer mid-plane at $\Theta = 0$rad and the Outer Limiter Plate at $\Theta = -0.25\pi$rad. Magnetic field lines are plotted in black in the left plots.

The different localization and amplitude between the perturbation on the density and on the temperature fluctuations can be once again explained by the different available parallel transport mechanism for each quantity. While it results purely from convection for the particles, a large conductive contribution prevails for the energy at the considered temperature ($T_e \approx 12eV$), leading to a spreading of the perturbation along the parallel direction much further away from the puff.

In conclusion, it has been proven that the gas-puff impacts mean-field quantities and turbulence properties quite significantly. The perturbation is both localized in the immediate vicinity of the gas puff and along the connected flux-tubes. We note that this might raise questions concerning imagining diagnostic which do rely on gas-puff for measurements. In fact, such local perturbation of both the plasma time-averaged and fluctuating quantities due to the gas puff had already been reported in Coroado et al. 2022b or, in a more extreme manner, for supersonic molecular beam injection in Tamain, Bonhomme, et al. 2013b; Tamain, Bufferand, Carbajal, et al. 2016. The main point of this section was not to provide a detailed analysis of this issue which is left to dedicated studies. We nevertheless need to discuss the possible impact this may have on the statistical analysis of these simulations.

3.2.2. Consequences concerning the possibility to aggregate statistics in the toroidal direction

Usually, one takes advantage of the toroidal symmetry to aggregate turbulence statistics both in time and in the toroidal direction using an ergodic assumption. This aggregation may not be legitimate anymore in the case with neutrals, with a localized gas puff.

However, the loss of symmetry does not necessarily hinder the aggregation of the whole toroidal direction to perform statistics on fluctuations properties, as the local perturbation might have only a limited weight in the statistics. To assess this, we calculate the absolute difference between the toroidal average on the whole torus of the plasma solution and the toroidal average computed on the toroidal planes near the puff in a range comprised within $\varphi \in [60° - 30°]$, defined for any field X as

$$\Delta X_\varphi = \left| \frac{\langle X \rangle_\varphi - \langle X \rangle_{\varphi \in [30°;60°]}}{\langle X \rangle_\varphi} \right| \tag{3.5}$$

Following this approach, it is possible to plot the distribution of Eq. 3.5 in the poloidal plane for several fields of interest, ranging from the plasma quantities to the turbulence properties. The highest difference among all the fields is found to be relatively small.

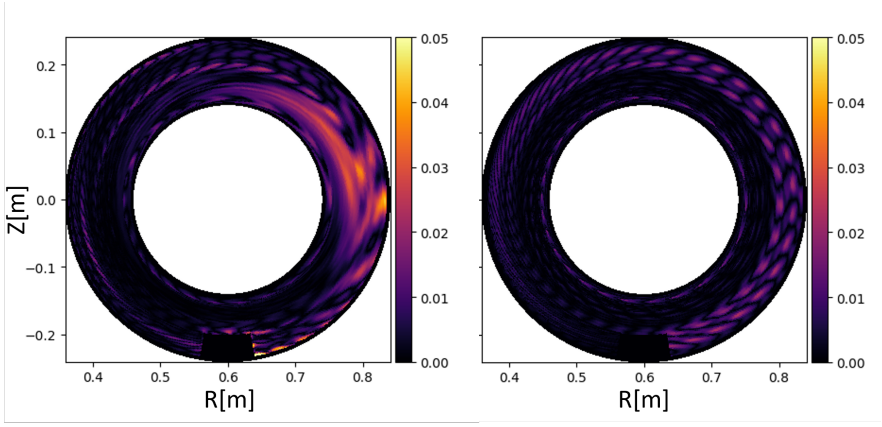

(a) $X =< n_e >_t$ and $X =< T_e >_t$

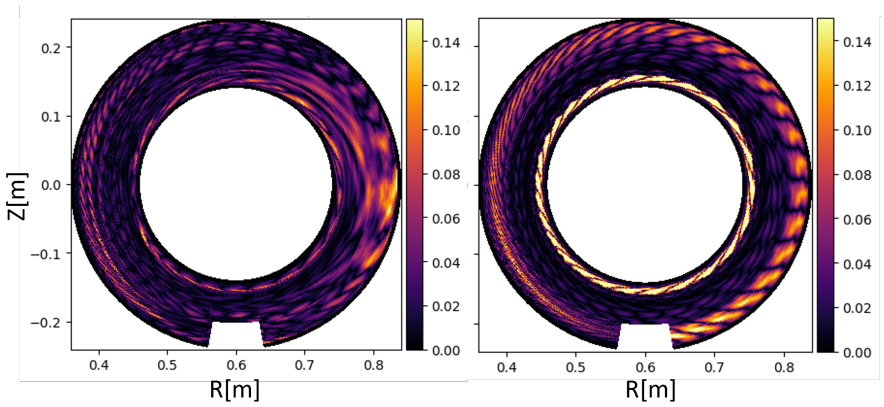

(b) $X = \tilde{n}_e / < n_e >_t$, $X = \tilde{T}_e / < T_e >_t$

Figure 3.10. – Poloidal distribution of ΔX_φ as expressed in 3.5 for the time-averaged electron density $< n_e >_t$ (left of 3.10a) and temperature $< T_e >_t$ (right of 3.10a), and the relative fluctuation level for the electron density (left of 3.10b) and temperature (right of 3.10b).

In particular, in Fig. 3.10 the ΔX_φ is computed for the time-averaged electron density and temperature, and the fluctuations rate: concerning the plasma quantities the maximum value is less than 4% for the density and less than 2% for the temperature. Turbulence properties are more impacted, with local differences in the relative fluctuation level reaching up to 14%, exhibiting higher differences and doubling in the edge the value obtained for the plasma properties. However, the amplitude is not large and despite the colorbar is saturated for a comparison with the plasma properties, the highest value is not greater than 5% - 15%

Note that Fig. 3.10 shows a complex pattern, with clear poloidal modes emerging. These can relatively easily be explained by the definition of the quantity that is plotted (a partial integral over a periodic direction) which will select specific modes out of the solution. For this reason, we do not dwell on the pattern itself. What matters is the maximum amplitude given by the colorbar.

This way, although significant local perturbations are induced by the gas puff, statistical averages along the toroidal direction are not dramatically perturbed. The breaking of symmetry does not prevent performing statistical analyses including aggregation of data along the toroidal direction. However, it adds on top of the statistics a kind of error-bar, defining beyond which amplitude of change, the variations in terms of statistic are significant or not. Only variations of the statistical properties beyond the systematic error due to the toroidal asymmetry (e.g., 4% for the averaged density) will be reported and discussed. Statistical properties presented afterwards are hence performed by aggregating both the time and toroidal direction.

3.3. Impact of neutrals recycling on plasma equilibrium and turbulence

In this section we discuss the overall impact of the neutrals on the plasma equilibrium and on turbulence is now addressed. By doing so, we partially replicate the study performed with TOKAM3X (Tamain, Baudoin, et al. 2018). As explained above, the work here differs from the latter by the use of a higher fidelity turbulence description (better description of the Reynolds stress in the model, higher grid resolution...) at the cost of adopting a lower fidelity fluid neutrals approach. This will allow us to highlight the observations that are robust and do not depend sensitively on the neutrals model.

3.3.1. Fluid neutrals with self consistent diffusion set up

In subsection 3.1, the geometries and the drive for the simulations with neutrals have already been described. Neutrals physics is taken into account based on the second level in the hierarchy of fluid neutrals models implemented in SOLEDGE3X, in which the neutrals diffusion is self-consistently calculated based on the charge-exchange dominated advanced neutrals model (see section 2.3.2). At the time the following simulations were conducted, this was the best model available in the code for turbulence studies as the one comprising advection was only incorporated into the code at a later stage and used in Chapter 4. As a result, the neutrals flux corresponds directly to Eq. 2.41. The fueling is provided through a gas puff positioned on the wall at the outer midplane at a specific toroidal location ($\varphi = 45°$). In this case, the gas puff rate was fixed at $2.15 \times 10^{21} \frac{\text{part}}{s}$, together with a recycling coefficient for the neutrals of $R_n = 0.98$: again, these values were chosen in order to get approximately the same plasma density at the separatrix as in the reference case and are full torus equivalent numbers for the puff rate.

We also want to point out a few additional specifics of the simulation with neutrals presented in this section. First, the neutrals pressure diffusion coefficient D_n^p was scaled down by a factor of 50 to have a neutrals distribution more concentrated around the limiter in spite of the small size of the machine considered here. The point of this is to get an ionization source from recycling similar to what would be observed in a bigger machine in terms of relative spatial distribution. This point is discussed

in section 3.4 in which on the contrary an artificially large diffusion coefficient is adopted in order to highlight the impact of the localization of the source. Moreover, the outer wall and the limiter front plate have effectively a 0 recycling coefficient: in the idealized geometry considered here, non-negligible plasma particle fluxes flow out of the domain at places where the wall is tangential to flux surfaces (outer wall and front of the limiter). In the numerical model used for this study, these tangential wall surfaces were not considered as recycling. This effectively leads to a global effective recycling coefficient lower than the one imposed on the rest of the wall (at the target plates) where most of the plasma out-flux is found.

An illustration of how the simulation looks like is reported in Fig. 3.11, showing the ions density, the electronic temperature and the potential at a given time.

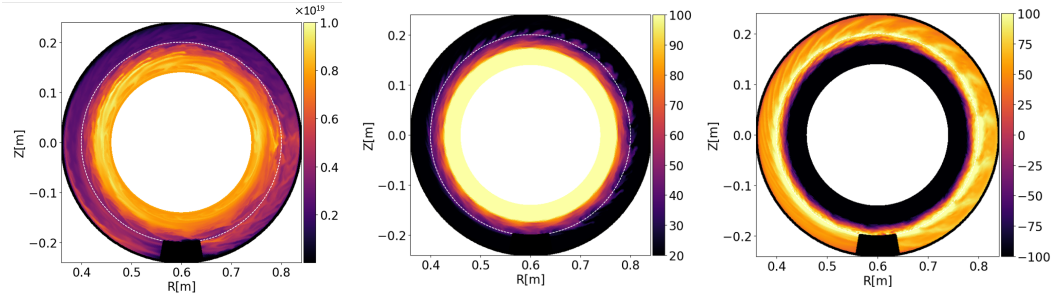

(a) n_i (b) T_e (c) Φ

Figure 3.11. – Snapshots of ions density n_i[m^{-3}] (a), electron temperature T_e[eV] (b) and potential Φ[V] (c) for the case with improved fluid neutrals.

Compared to Fig. 3.2, which presents the main plasma quantities for the reference case without neutrals, the inclusion of neutrals significantly alters the overall plasma equilibrium. An initial comparison of the density reveals the impact of the change in the driving mechanism. The presence of neutrals leads to a decrease in core density, while it increases at the edge and around the limiter, where the source is now located. An opposite trend is visible on the temperature, with a steep increase in the closed flux surfaces region and a drop in the SOL. The potential profile is also altered, most likely in response to the changes on the ion pressure profile in the core and the electron temperature in the SOL. Fluctuations seem to exhibits a similar pattern as in the no neutrals reference case, although their relative amplitude is smaller for the density and larger for the temperature, as will be confirmed by a more detailed analysis.

3.3.2. Particle and energy sources

Let us first characterize the particle and energy sources imposed to the plasma by neutrals. Instantaneous values of the particle and ion energy source are plotted in Fig. 3.12. For comparison, the particle source poloidal distribution from previous studies with TOKAM3X and kinetic neutrals is given in Fig. 3.13

The first thing one can observe is that the poloidal distribution of the particle source with the fluid neutrals model is qualitatively similar to the one obtained with EIRENE in TOKAM3X. The recycling source is localized in the vicinity of the limiter, typically within 10 cm of the target plates. The toroidally localized puff also results in a local particle source with an amplitude stronger than the recycling source in the same plane, but it is localized only in the immediate toroidal vicinity of the gas valve. The particle source is positive at every point in space, demonstrating that recombination is negligible in the conditions considered here.

The sign of the energy source on the opposite strongly depends on the position. Coarsely speaking it is negative in the Scrape-Off-Layer, both around the limiter and the gas puff, but turns out positive inside the last closed flux surface. The negative source in the SOL is due to the energy losses associated with ionization reactions. The positive source in the core are due to the chosen energy recycling mechanism which scale like the local temperature of the plasma. Overall however, the contribution of plasma-neutral-interactions is negative as expected.

One can also notice in the figures that turbulence activity is clearly visible in the sources. This is easily understood as being due to the fact that sources are proportional to the local plasma density and that the ionization cross-section also depends on T_e, so that dense and hot plasma filaments locally enhance sources.

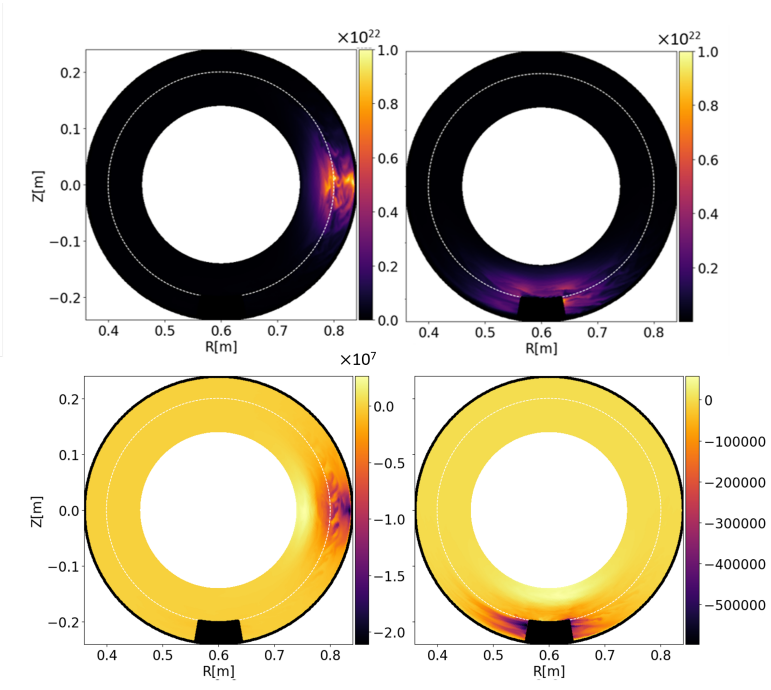

Figure 3.12. – Snapshot of total neutrals particle source $S_n[\frac{\text{part}}{\text{sm}^{-3}}]$ (top) and total energy source $S_E[\frac{\text{W}}{\text{m}^{-3}}]$ (bottom) at two different toroidal position (puff location $\varphi = 45°$ (left column) and away from the puff $\varphi = 0°$ (right column) for the case with neutrals considering a pressure diffusion model.

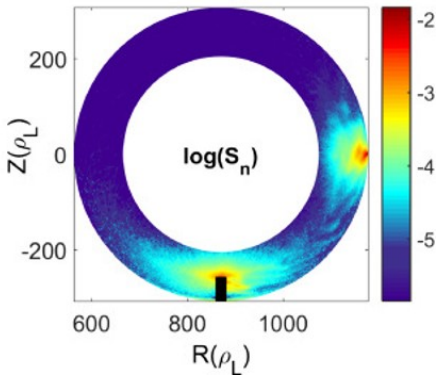

Figure 3.13. – Snapshots on a poloidal cross-section of the ionization source term for TOKAM3X-EIRENE simulation in the plane of the gas puff, as presented in Fan et al. 2019, here expressed in [au] and logarithmic scale.

3.3.3. Impact on plasma time averaged properties

We now turn to a comparison of plasma equilibrium (time-averaged) properties between the simulation without neutrals and the one with self-consistent neutrals recycling.

Fig. 3.14 shows the poloidal distribution of the time and toroidally averaged density (left) and electron temperature (right) in a flux surface in the near Scrape-Off Layer ($R - R_{sep} \approx$1cm) for the two considered cases, without and with neutrals. The limiter targets are localized on the left and right ends of the plots. As could be expected, one can see that the presence of neutrals leads to a significant cooling of the plasma: the electron temperature drops in a range between 30 to 50% depending on the exact poloidal location with respect to the reference case. The temperature at the low-field side target for example goes down from 18eV to 10eV. The density seems less impacted with a slight increase all across the poloidal direction, with a minimum difference in the outboard mid-plane. This is actually related to the fact that the gas puff amplitude was tuned to roughly keep the density around the separatrix constant from the reference case to the neutral case, despite the change in the fueling mechanism. As the neutral recycling is strongly localized in the poloidal direction, one could expect also an increase of poloidal asymmetries with the appearance of stronger poloidal gradients. The amplitude of these gradients provides an evaluation of the density regime the Scrape-Off Layer is in. Such enhanced gradients are visible on the density profile as the increase of the density is more sensitive close to the targets, especially on the low-field side, than in the middle of the SOL. Nevertheless, the additional asymmetry driven by the neutrals has an amplitude of the same order of magnitude as the asymmetries already naturally present in the SOL in the absence of neutrals due to drifts and curvature. This suggests that the simulation with neutrals considered here is in relatively low recycling conditions. This statement is confirmed by the temperature profile which does not exhibit significantly stronger gradients in the presence of neutrals than without.

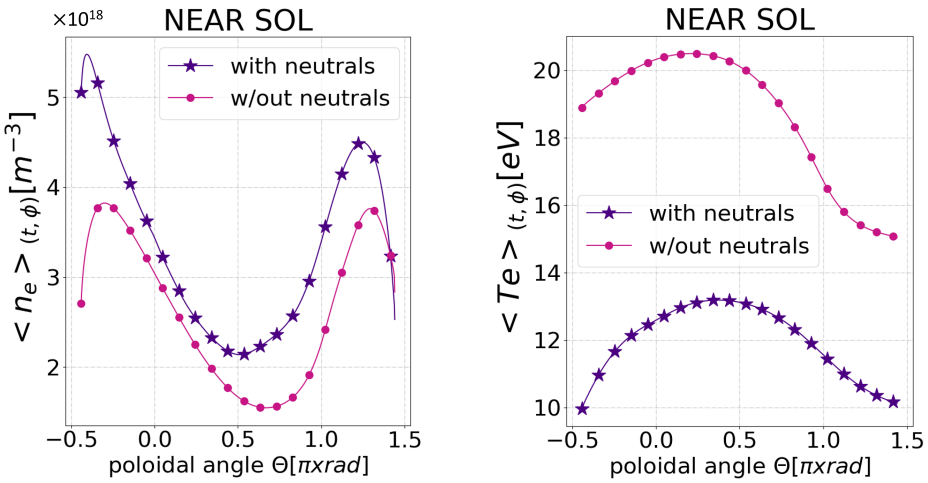

Figure 3.14. – Poloidal profiles of the electron density (left) and electron temperature (right), averaged in time t and toroidal position φ, for the cases with neutrals (⋆) and without neutrals (•), in the near SOL after the separatrix $R - R_{sep}$ =1cm

In spite of the fact that the simulation with neutrals is in a low recycling regime, switching from a drive of the particle flux from the core to a self-consistent drive from gas puff and recycling has a major impact on radial profiles. This is illustrated in Fig. 3.15 which compares in the 2 cases the time- and toroidally-averaged density and electron temperature profiles at the outboard mid-plane and at the poloidal position of the low-field side target. The most striking change is observed as a reversal of the density and temperature gradients in the closed flux surfaces. While in the case without neutrals the density profile exhibits steep gradients and the electron temperature is on the contrary relatively flat, the situation reverses with neutrals. This way, in spite of a similar outboard mid-plane separatrix density, the case with neutrals shows a drop by a factor of 2 of the density at the center of the simulation domain. On the other hand, the electron temperature at the inner boundary of the domain increase by a factor of 3. This trend is poloidally symmetric and observed also at the poloidal positions corresponding to target plates. It is similar to the one reported in Tamain, Baudoin, et al. 2018 and can be explained by the re-localization of the particle source in the outer half of the simulation domain. While in the simulation without neutrals both the power and particle fluxes come from the core and flow through the closed flux-surfaces region, only a power flux builds up in the simulation with neutrals, with a minor particle flux driven by the small portion of neutrals recycling deep into the plasma. Such result would actually have been obtained even in a mean-field simulation where plasma transverse fluxes are driven by diffusion. In turbulence simulations, as considered here, it however requires a reorganization of turbulence properties as one will discuss after.

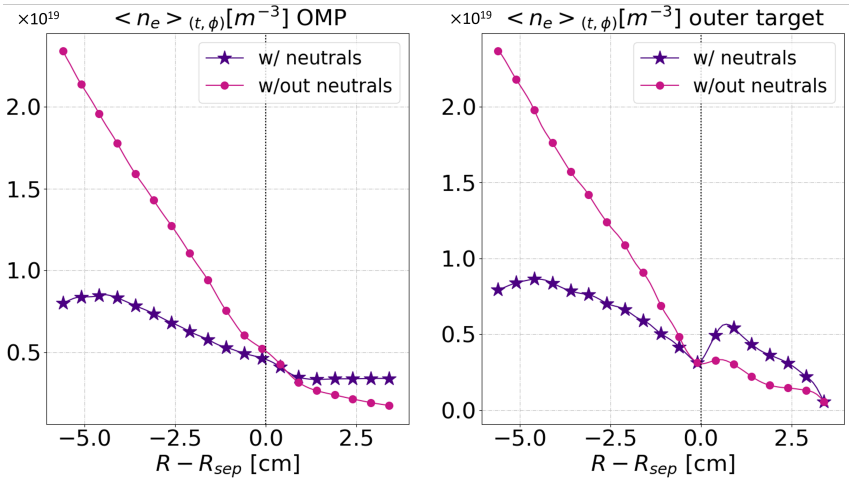

(a) n_e

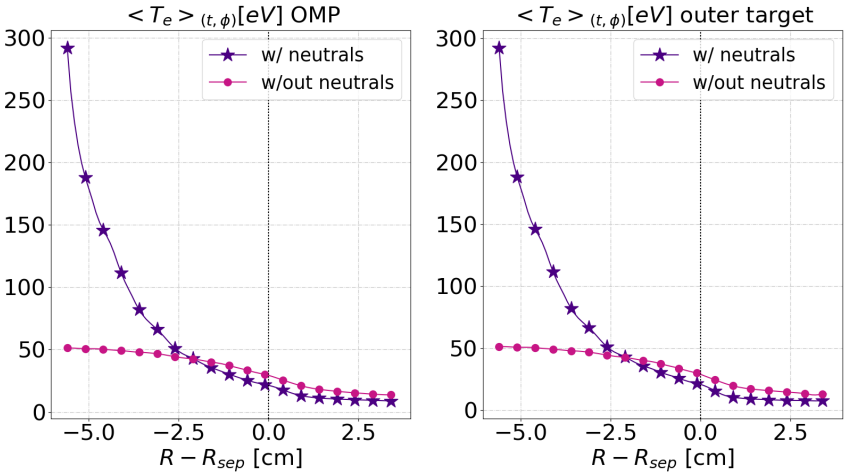

(b) T_e

Figure 3.15. – Comparison of radial profiles of the electron density 3.15a and electron temperature 3.15b, averaged in time t and toroidal position φ, in the two considered cases with neutrals (⋆) and without neutrals (•). Plots are made at two different poloidal location: outer midplane (first column) and poloidal angle of the low-field side limiter target (second column).

Moving further out, beyond approximately $R-R_{sep}$ > -2cm, the particle flux driven by recycling starts building up, leading to a flattening of electron temperature gradients back to values similar to the case without neutrals. The density profile however remains significantly flatter because of two effects: first, the temperature of the edge plasma is lower with neutrals, leading to a decrease of parallel losses at the targets; second, the SOL is partially refuelled by a direct particle source from the gas puff and recycling neutrals. At this point, one cannot also exclude a change in the efficiency of turbulent transport, as will be discussed after. The flattening of the density profiles is more marked in the outer part of the SOL with a clear inflexion of the slope at $R - R_{sep} \approx 1$cm. This phenomenology is reminiscent of the observation of density

shoulder in experiments, although further analysis and simulations at higher density regimes would be necessary to confirm the link between the two. A proper analysis on this will be further addressed in section 3.3.5. The effect of the localized recycling particle source is also particularly obvious on the density profile at the outer target, with a locally reversed gradient in the vicinity of the separatrix.

3.3.4. Impact on turbulence properties

The previous results demonstrate a non local impact of neutrals fuelling/recycling with a global reorganization of profiles. Since profiles both result from and drive turbulent transport, this suggests an associated change in turbulence.

In order to discuss the re-organization of the turbulence due to the presence of neutrals, we now focus on fluctuations defined for any field X as its time-varying part: $\tilde{X} \equiv X - < X >_t \equiv X - \bar{X}$. We are going to investigate 2 key properties of fluctuations:

1. the relative fluctuation rate for the density $\frac{\sigma_{n_e}}{\bar{n}_e}$, where σ_{n_e} is the standard deviation of the density fluctuations, which characterizes their amplitude
2. their skewness, which is the 3rd order moment of the probability distribution function of fluctuations. For a a quantity X, it is defined as

$$\text{skew}(X) \equiv \frac{< (X - < X >_t)^3 >_{t,\varphi}}{< (X - < X >_t)^2 >_{t,\varphi}^{3/2}} \tag{3.6}$$

   and characterizes the intermittency of the fluctuations by measuring the left right asymmetry of the distribution function. It is equal to zero for a gaussian distribution.

As above, the results are shown as radial profiles at 2 different poloidal positions, the outer midplane and close to the outer limiter target and plotted as a function of $R - R_{sep}$ remapped in the mid-plane. Fig. 3.16 shows the radial profiles of the relative fluctuation level and skewness of density fluctuations while Fig. 3.17 provides the same plots for the electron temperature.

Looking first at the density fluctuations (fig. 3.16), a significant quantitative change is observed between the 2 cases, especially at the outboard midplane: the relative fluctuation level for the case with neutrals decreases by a factor of about 2 both in the closed field lines region and in the near SOL ($R - R_{sep} < 2$cm) and by up to a factor of 3 in the outer SOL ($R - R_{sep} > 2$cm). Similar impact is found at the bottom of the machine in the closed flux surfaces for $R - R_{sep} < -2$cm, with a fluctuation level overall half as large as in the mid-plane due to the natural ballooned character of turbulence. Further out however, as the relative fluctuation level increases with the radius, the change in the density fluctuation level is much less marked than in the outboard mid-plane, highlighting a possible local role of the recycling source to push up the density fluctuations.

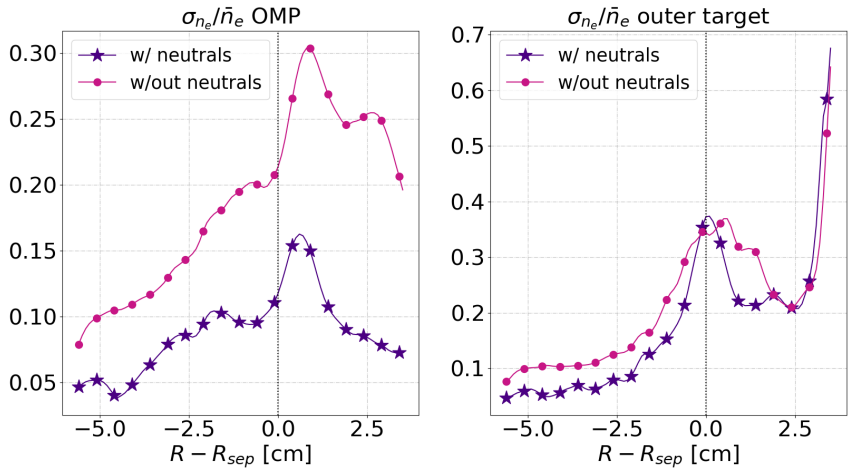

(a) $\frac{\sigma_{n_e}}{\bar{n}_e}$

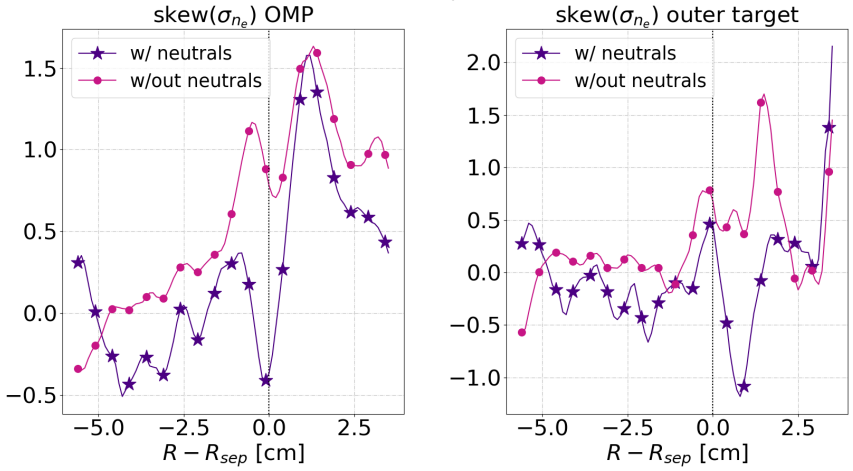

(b) skew(n_e)

Figure 3.16. – Comparison of radial profiles of the relative fluctuation level (3.16a) and skewness (3.16b) of density fluctuations for the case with self-consistent neutrals (⋆) and without neutrals (•), at two different poloidal locations: outer midplane (first column) and outer limiter (second column).

Looking now at the skewness of density fluctuations (two bottom figures of fig. 3.16), one first retrieves a generic feature observed in experiments (see Zweben et al. 2014 and Nold et al. 2010) and previous modelling work (Tamain, Bufferand, Ciraolo, et al. 2014) with an increase of the skewness as a function of the radius in the outboard mid-plane. Here again, the difference between the case with neutrals and the reference case is more marked in the outboard-mid-plane than in the vicinity of the limiter. In the mid-plane, the inclusion of neutrals results in a significant decrease of the skewness by ~ 0.5 inside the separatrix, the skewness becoming significantly negative with neutrals. This trends seems to break in the SOL mid-SOL ($R - R_{sep} \approx 1$cm) where the skewness in the case with neutrals significantly rises to the same positive level as without neutrals. At the poloidal location of the outer target, the difference in

skewness between the 2 cases is less marked, with the exception of the near SOL ($1 < R - R_{sep} < 2$cm) where the case with neutrals exhibits a large drop by -1.5 of the skewness into negative values, highlighting again a poloidally localized effect of the recycling particles.

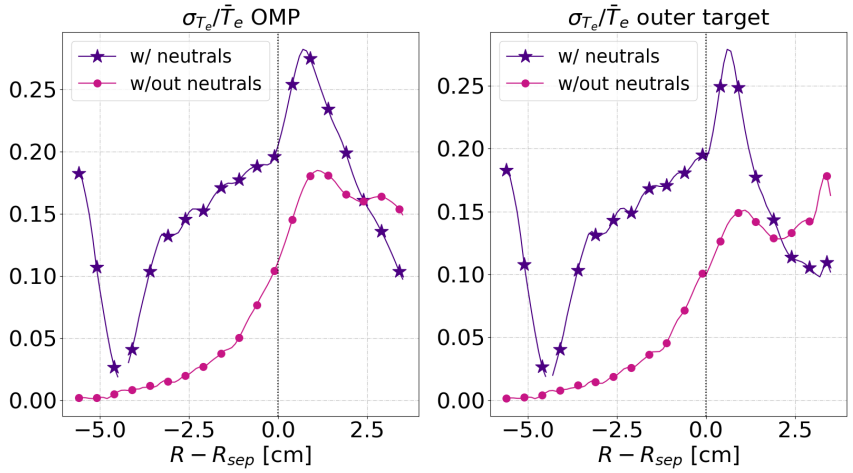

(a) $\frac{\sigma_{T_e}}{\bar{T}_e}$

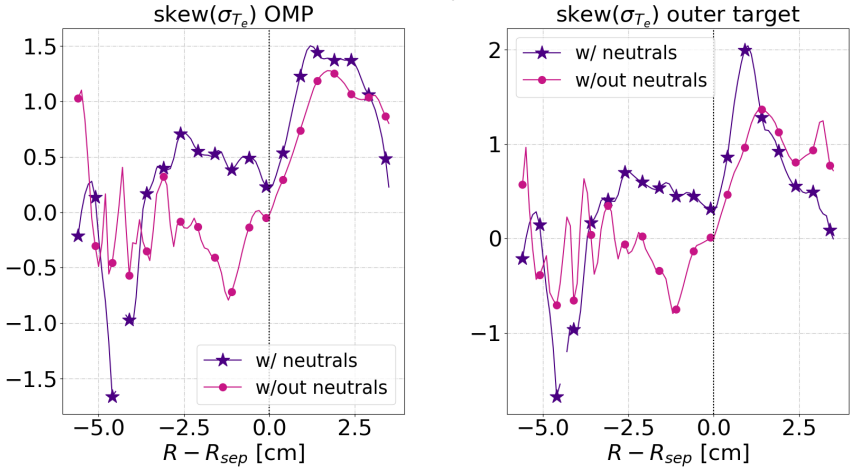

(b) skew(T_e)

Figure 3.17. – Comparison of radial profiles of the relative fluctuation level (3.17a) and skewness (3.17b) of electron temperature fluctuations for the case with self-consistent neutrals (⋆) and without neutrals (•), at two different poloidal locations: outer midplane (first column) and outer limiter (second column).

The response of electron temperature fluctuations (Fig. 3.17) is roughly the opposite of that observed on density fluctuations. The need to transport a radial heat flux with little particle flux in the closed field lines region leads to a dramatic increase by a factor of ~ 3 of the electron temperature fluctuation level in the presence of neutrals. This trend remains true in the near SOL before reversing in the far SOL

where temperature fluctuations drop with neutrals. Concerning the skewness, the impact of neutrals seems less marked than on the density, except in the outer part of the closed flux surfaces ($-2 < R - R_{sep} < 0$cm) where a significant increase of +1 is observed, corresponding to the region where the neutrals recycling starts becoming sensitive. Compared with density fluctuations, the behaviour of electron temperature fluctuations does not exhibit any significant difference between the mid-plane and the vicinity of the outer target, neither for the fluctuation level nor for the skewness. This can once again be explained by the more effective transport of heat due to parallel conduction, leading to a stronger coupling of the whole poloidal direction for temperatures than for density, at least in the low recycling conditions considered here.

Overall, one finds that turbulence properties have self-organized in response to the relocalization of the particle sources around the limiter (and in front of the puff). In the closed flux surface region in particular, temperature fluctuations take over density fluctuations to ensure the transverse turbulent transport of energy. This differences propagate in the outboard mid-plane SOL. In open flux surfaces, the poloidal localization of the recycling source also induces a stronger differentiation of density fluctuation properties as a function of the poloidal position. Due to fast parallel transport, temperature fluctuations exhibit much less marked poloidal asymmetries, whether neutrals are present or not.

3.3.5. Impact on SOL widths

In this section, the change in the heat transport due to the introduction of a realistic recycling source is investigated after the evaluation of $q_{\parallel}$ and λ_q, by fitting the heat flux profiles.

To begin with, we compute the parallel heat flux reaching the target directly from the poloidal energy fluxes in the code, after projection onto the parallel direction:

$$q_{\parallel} = \frac{q_{pol}}{\vec{b} \cdot \hat{n}}. \tag{3.7}$$

Here q_{pol} is the total poloidal heat flux (electrons plus ions), and $\hat{n}$ is the unit vector normal to the target plate pointing away from the plasma. Note that the $q_{\parallel}$ computed in this fashion corresponds actually to the parallel projection of the total poloidal heat flux. The parallel is however the main one and it is this total heat flux to which the Bohm boundary condition is applied. Moreover, this procedure mimics the one actually followed in experiments when reconstructing the parallel heat flux from infra-red camera measurements at the targets.

Fig. 3.18 shows the profile of the heat flux thus calculated at the outer target plate, with the x-axis expressed as a function of the distance to the separatrix after remapping along flux surfaces to the midplane.

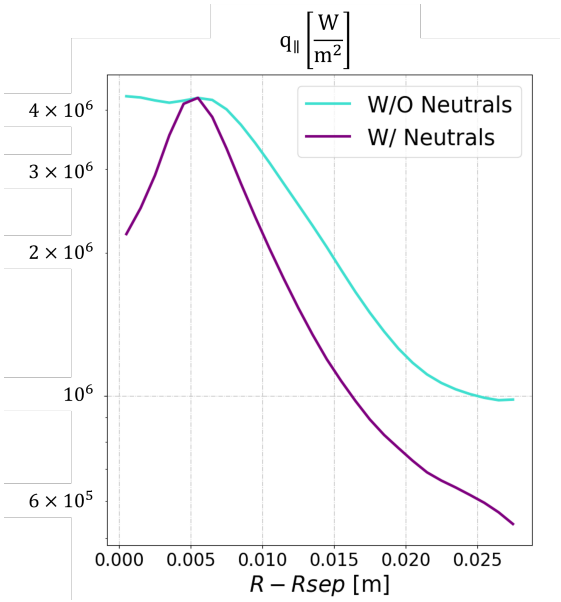

Figure 3.18. – Comparison between the energy flux, as given in Eq. 3.7 at the outer target averaged in time t and toroidal position φ and remapped at the midplane, for the turbulent simulations without recycling (turquoise)) and with recycling (magenta). Note the log scale for the y axis.

The heat flux amplitude is everywhere lower in the case with neutrals, highlighting the role of recycling acting as an energy sink. While the curves exhibit approximately an exponential decay in the mid-SOL (6mm $< R - R_{sep} <$ 15 – 20mm), the near SOL is characterized by non-monotoneous profiles in both cases. This is already true in the case without neutrals, in which the profile is almost flat in the first 6 mm. This behaviour is due to the brutal discontinuity the transition from closed to open flux surfaces induces in these limited cases, with the presence of the limiter corner and of strong localized ExB flows. In the case with neutrals, the profiles even reverse in the near SOL, with $q_\parallel$ increasing up to a maximum at $R - R_{sep} = 5$mm. This local dip in the heat flux is likely generated by the locally enhanced energy losses associated with recycling neutrals close to the targets in the near SOL. This way, applying an exponential fit in these conditions makes little sense and would bring little information, especially concerning the decay length in the near SOL.

In order to evaluate $q_\parallel$ and λ_q, we need to adopt a different approach and evaluate it away from the target plates, upstream from neutral losses and away from local discontinuities at the limiter corner. For this purpose we will use a proxy defined in Eq. 3.8 inspired from sheath boundary conditions on heat fluxes (Eq. 1.10 and 1.11):

$$q_{\parallel,proxy} = n_e \sqrt{\frac{T_e + T_i}{m_i}} (\gamma_e T_e + \gamma_i T_i) \tag{3.8}$$

.

The use of this proxy is justified by the fact that one cannot directly compute in the mid-plane the parallel heat flux from the poloidal flux as we did at the target.

Indeed the poloidal heat flux at the target results from the poloidal integral of the radial transport of energy into SOL flux surfaces. In the same way as a stagnation point can be defined for the parallel flow of particles (i.e., a poloidal position where the parallel fluid velocity is zero), a stagnation can be defined where the parallel flux of energy reaches zero (it is outgoing at both target plates, i.e. negative at one target and positive at the other one, and so has to go through a zero value by continuity somewhere between the two). The poloidal heat flux reaching the targets hence builds up from this stagnation point, roughly located in the mid-plane, to the target. If one used the real parallel heat flux circulating in the plasma to compute λ_q at the mid-plane, assuming the stagnation point is there one would end up with a quasi-zero parallel heat flux. The proxy on the contrary provides an estimate of the heat flux that would be observed if a solid surface was placed in such plasma conditions. We note that the proxy and the real heat flux boil down to the same quantity at the limiter targets because of Bohm boundary conditions on the heat flux. The use of a mid-plane proxy for the estimate of parallel heat flux and their decay length is also common in experiments.

Fig. 3.19 shows the radial profiles of $q_{\parallel,proxy}$ for the 2 cases. Like at the target, the heat flux is systematically lower in the case with neutrals, by about 30% in most of the near and mid-SOL, confirming how the neutrals are responsible for a significant dissipation of the heat fluxes. In the mid-plane however, the heat flux proxy monotonously decreases with the radius which allows analysing the profiles in terms of SOL widths.

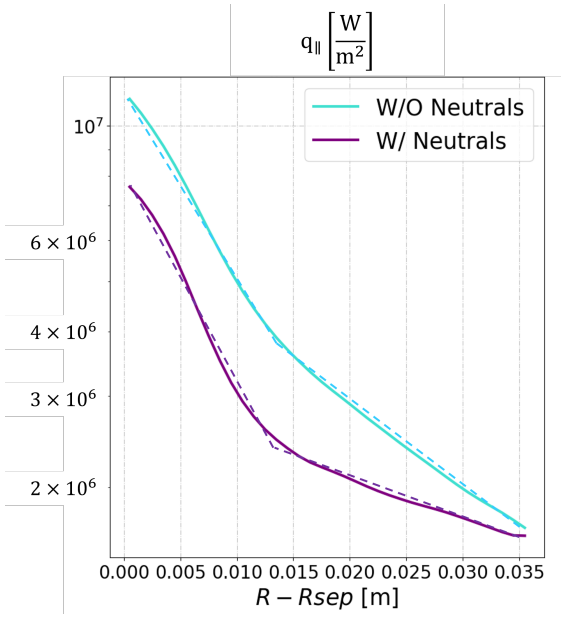

Figure 3.19. – Comparison between the proxy parallel energy flux (see Eq. 3.8) at the midplane averaged in time t and toroidal position φ for the turbulent simulations without recycling (turquoise) and with recycling (magenta). Full lines are the actual data from the simulation while dashed lines are the result of the double-exponential fits (Eq. 3.9). Note the log scale for the y axis.

From the profiles of $q_{\parallel,proxy}$, one applies a double exponential fit:

$$q_{\parallel,proxy} = q_{NEAR} e^{-\frac{R-Rsep}{\lambda_{q,NEAR}}} + q_{FAR} e^{-\frac{R-Rsep}{\lambda_{q,FAR}}} \tag{3.9}$$

where the fitting parameters are the near / far SOL widths $\lambda_{q,NEAR/FAR}$ and the amplitude of near /far SOL components $q_{NEAR/FAR}$. The result of the fits are shown in Fig. 3.19 with dashed lines and the value of the fitting parameters given in Table 3.2.

CASE	$\lambda_{q,NEAR}[mm]$	$q_{NEAR}[\frac{W}{m^2}]$	$\lambda_{q,FAR}[mm]$	$q_{FAR}[\frac{W}{m^2}]$
W/out neutrals	~ 10	0.81×10^7	~ 31	0.38×10^7
W/ Recycling	~ 11	0.63×10^7	~ 73	0.23×10^7

Table 3.2. – Values of fitting parameters for the double exponential fit (Eq. 3.9) of the proxy parallel heat flux in the mid-plane for the cases without and with neutrals recycling.

The amplitude of the fitting fluxes is found as expected from the visual analysis 30 to 40% lower in the case with neutrals than without. The decay lengths values are found to not change too much in the near SOL. However, the profile for $q_{\parallel,proxy}$ with neutrals is found to flatten in the far SOL, where the value of $\lambda_{q,FAR}$ is 2.4 times as large with neutrals recycling as without neutrals.

Overall, in spite of changes in the turbulence properties and equilibrium profiles, as well as a significant energy dissipation due to neutrals, the SOL heat flux width seems to be only weakly impacted by the inclusion of neutrals in the simulations, except for a flattening of the far SOL. The latter is mainly due to a flattening of the density profile, which is reminiscent of the appearance of density shoulders. At this point, and with these single case comparison, it is however difficult to conclude that this effect and the one reported from experiment stem from similar physics. This mild impact is of course valid only in the geometry and low density regime considered here and might not hold for stronger plasma neutrals interaction in divertor geometry at high density regimes as will be seen in Chapter 4.

3.3.6. Impact on mean field transport coefficients

3.3.6.1. Convective versus conductive turbulent heat transport

We are now going to turn to the consequences of the self-consistent inclusion of neutrals on anomalous transport coefficients as interpreted by mean-field models. This is a relatively straightforward task for particle transport for which the anomalous flux carried by fluctuations of the density and of the ExB velocity is given by:

$$\Gamma_n^{\psi,\text{anom}} = \langle \tilde{n}_e \tilde{\vec{u}}_E \rangle_{t,\varphi} \cdot \vec{n}^\psi \tag{3.10}$$

where $\vec{n}^\psi$ is at each point the unit vector orthogonal to flux surfaces and pointing away from the plasma center, and the tildes stand for the fluctuating part of fields (for any field $X = \langle X \rangle_{t,\varphi} + \tilde{X}$).

For energy transport however, the picture is more complex as several terms enter the anomalous ExB flux. The electron energy flux carried by the ExB velocity is the following:

$$\Gamma_{Ee}^{\psi,\text{anom}} = \frac{3}{2}\left(\langle \tilde{n}_e \tilde{\vec{u}}_E \rangle_{t,\varphi} \langle T_e \rangle_{t,\varphi} + \langle \tilde{T}_e \tilde{\vec{u}}_E \rangle_{t,\varphi} \langle n_e \rangle_{t,\varphi} + \langle \tilde{n}_e \tilde{T}_e \rangle_{t,\varphi} \langle \vec{u}_E \rangle_{t,\varphi} + \langle \tilde{n}_e \tilde{T}_e \tilde{\vec{u}}_E \rangle_{t,\varphi}\right) \cdot \vec{n}^\psi \tag{3.11}$$

in which 4 terms are found. The first one can be interpreted as a convective heat flux since it is simply the anomalous particle flux multiplied by the time-averaged temperature. The second one can be identified as a conductive component, while it is more difficult to label simply the last 2. We will see however that their contribution is small. The same type of exercise could be attempted for the ion energy flux, but leads to much more complex expressions due to the presence of the flow's kinetic energy in the ion energy density. This is left for future work.

Due to the spatial redistribution of the particle source when moving from the case without neutrals to the case with neutrals, one can expect a significant change in the various components of the previous turbulent fluxes. In closed flux surfaces in particular, the case without neutrals should exhibit both a particle and energy flux while the case with neutrals should exhibit only an energy flux as the particle source is now located in the outer part of the simulation box in the vicinity of the sinks. Since

the total amount of power to transport is the same in the 2 cases, this necessarily means that the convective component of the heat flux should be replaced by another one (or several other ones) in the case with neutrals.

All these observations are confirmed by looking at Figures 3.20 and 3.21 which shows the radial profiles of the flux-surface integrated ExB fluxes, decomposed by components according to Eq. 3.10 and Eq. 3.11.

Focusing first on the case without neutrals, one sees that the particle flux and the total energy flux both rapidly build up close to the inner boundary of the simulation domain (where the core fluxes are injected as sources). The particle flux is then mostly constant until the separatrix, beyond which it finally drops due to the particle sink at the targets. Recalling that the total injected particle flux in this case is $2.5 \times 10^2 1 s^{-1}$, one can see that the ExB radial flux accounts for more than 90% of it, with turbulence representing the overwhelming contribution. The integrated ExB electron energy flux is also relatively constant until the separatrix although a slow variation can be observed between 27 and 25 kW, out of the 31.25 kW of total heating power injected on electrons. This way ExB advection is also the dominant contributor of heat transport. The radial variation can be explained by 2 reasons: 1-the electron energy on its own is not a conserved quantity as electrons exchange energy with ions and the electrostatic field; 2- other transport mechanisms (mean-field drifts, turbulent contribution of the curvature drift, or remnant perpendicular diffusion) can transport a non negligible portion of the electron energy. The decomposition of the electron ExB energy flux reveals that the convective component is by far the largest contributor in the innermost part of closed flux surfaces. When moving closer to the separatrix however, a non negligible conductive contribution arises and in the SOL eventually, the flux is split roughly equally between the convective and the conductive components. This results are in line with those already published in Tatali et al. 2021, with the TOKAM3X turbulence code at the time.

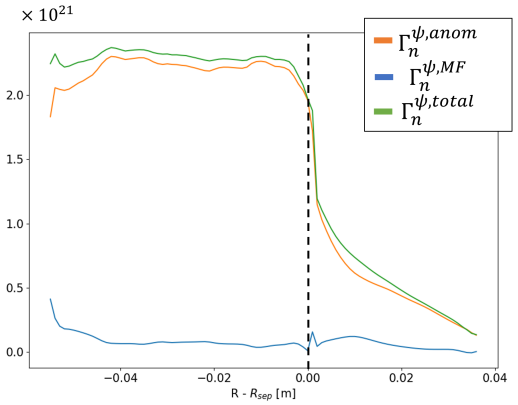

(a) $\int_{\varphi,\theta} \Gamma_{N,\text{no neut}}$

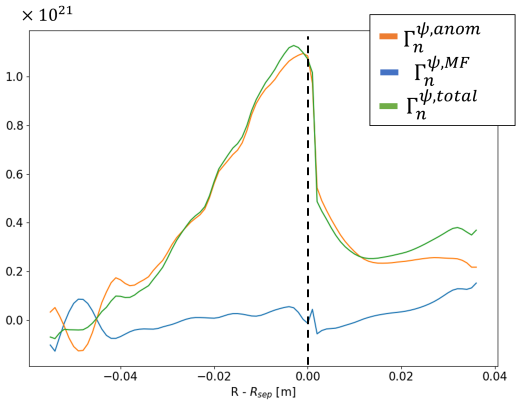

(b) $\int_{\varphi,\theta} \Gamma_{N,\text{with neut}}$

Figure 3.20. – Radial profiles of the flux-surface integrated total particle flux $[s^{-1}]$ (–), and its decomposition in an anomalous flux due to fluctuations (–) of ExB (as in Eq. 3.10) and a mean field flux (–) for the case without neutrals 3.20a and with neutrals 3.20b. Courtesy of McGibbon 2024.

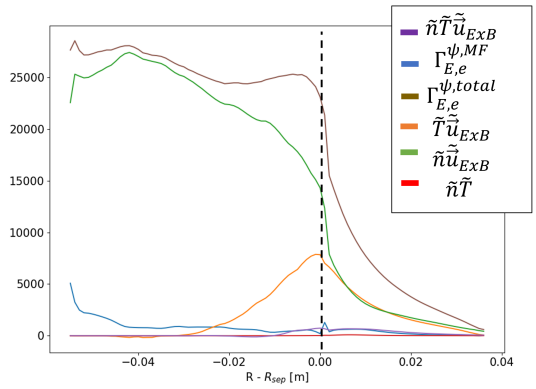

(a) $\int_{\varphi,\theta} \Gamma_{E,e}$no neut

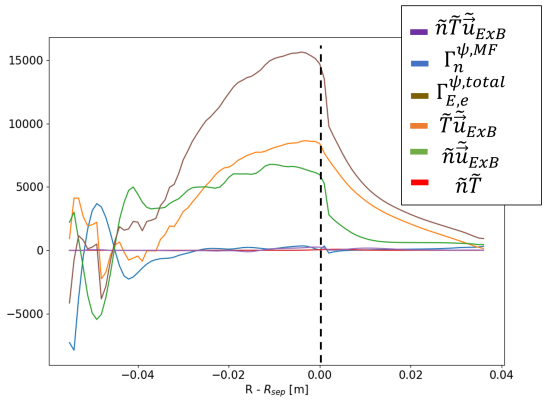

(b) $\int_{\varphi,\theta} \Gamma_{E,e}$with neut

Figure 3.21. – Radial profiles of the flux-surface integrated total electron energy flux [W](–), and its decomposition in an anomalous flux due to ExB fluctuations (with the split on its several contributors (–), (–), (–), (–)) as in Eq. 3.11, and a mean field flux (–). Courtesy of McGibbon 2024.

If we now turn to the case with neutrals, one immediately sees a dramatic impact on the fluxes. The first observation is that the total ExB fluxes are not constant anymore in the radial direction in the closed flux surfaces region and tend to build up as one moves outwards. While this was expected for the particles due to the localization of the source in the outer part of the domain (as explained above), this is less expected for the ExB energy flux since all the power enters the simulation domain from the core. One can also notice that the total ExB energy flux is now significantly smaller than the 31.25 kW of heating power on electrons. This is due to the fact that other transverse energy transport mechanisms than ExB advection are present with a significant amplitude in the innermost part of the simulation domain. One can speculate that the drop of the plasma parallel resistivity due to the decrease of the density / increase of the temperature close to the core is responsible for a stabilization of turbulence in the innermost part of the domain, as reported in Tatali et al. 2021 during a dedicated

collisionality scan. The decomposition of the energy ExB flux shows a qualitative difference with the no-neutrals case as conductive transport becomes a dominant player in most of the domain, especially in the SOL.

3.3.6.2. Anomalous transport coefficients

From the anomalous fluxes we have just discussed, it is possible to investigate the effect of including neutrals on the anomalous diffusive transport coefficients as they are used in 2D mean-field models. Such analysis is necessary to draw conclusions and recommendations for mean-field modelling based on self-consistent turbulence simulations.

The anomalous transverse particle diffusion coefficient can be computed as

$$D_{\perp}^{\text{anom}} \equiv -\frac{\Gamma_n^{\psi,\text{anom}}}{\vec{\nabla}\langle n_e\rangle_{t,\varphi}\cdot\vec{n}^{\psi}} \tag{3.12}$$

As for the energy diffusion coefficient, it describes the non-convective part of the energy flux and can be computed as

$$\chi_{\perp e}^{\text{anom}} \equiv -\frac{\Gamma_{Ee}^{\psi,\text{anom}} - \frac{3}{2}\langle T_e\rangle_{t,\varphi}\Gamma_n^{\psi,\text{anom}}}{n_e\vec{\nabla}\langle T_e\rangle_{t,\varphi}\cdot\vec{n}^{\psi}} \tag{3.13}$$

Figures 3.22 and 3.23show the poloidal maps of the anomalous transport coefficients obtained from the 2 simulations. Let us first focus on the case without neutrals as a reference. The anomalous particle diffusion coefficients exhibits a clear $m = 1$ poloidal mode with strong ballooning associated with the favourable curvature for the development of interchange instabilities on the low-field side of the machine. This is especially true in the SOL. Its amplitude is typically twice as large in the SOL as inside the LCFS. One can also notice clear striations in the $D_{\perp}$ map in the closed flux surfaces region, which correspond to low order rational flux surfaces where turbulent transport is enhanced. The perpendicular heat conduction similarly shows an $m = 1$ ballooning pattern in the SOL, with an amplitude about twice as large as for particle transport. In the closed flux surface region however, $\chi_{\perp,e}$ is rapidly goes down to very small values compared with $D_{\perp}$ when moving inwards away from the LCFS. This is consistent with the minor contribution of the conductive component of the anomalous ExB flux in that region.

Moving to the case with neutrals, the picture shares a lot of similarities with the no neutrals case but also significant differences. Looking first at $D_{\perp}$, the $m = 1$ ballooning structure is still present. We observe a drop in the core compared with the no neutrals case, which is consistent with the smaller contribution of ExB turbulence to fluxes at the center of the simulation domain. In the SOL however, the amplitude of $D_{\perp}$ is about a factor of 2 larger than in the case without neutrals, explaining the flattening of the density profiles there. The black pattern in the middle of the ballooning structure is a region of negative diffusion due to the perturbative presence of the gas puff, demon-

strating that a gradient-diffusion description is probably not adapted when external actuators locally perturb the plasma. Concerning heat anomalous conduction, the case with neutrals exhibits the same poloidal distribution as the reference case. Like for the particle perpendicular diffusion, the amplitude in the SOL is found 70% larger with neutrals than without. Interestingly, the increased weight of the conductive ExB anomalous flux in the closed field lines region does not translate into a larger perpendicular conduction coefficient, showing that it is the increase in the time-averaged temperature gradient that is entirely responsible for the increase of this contribution to the heat flux.

To summarize, the main impact of the inclusion of self-consistent neutrals recycling in terms of transport coefficients is an increase of their amplitude by a factor close to 2. No major change of their poloidal distribution is observed apart from a drop of $D_\perp$ in the center of the simulation domain which is likely due to a stabilization of turbulence at lower collisionality (it self due to the increase of T_e and the drop of n_e). The fact that negative transport coefficients are rebuilt in the vicinity of the gas puff suggest however that the gradient-diffusion description of perpendicular transport might face limits in the presence of strong localized perturbations to the plasma.

3.4. Confirmation of the role of the particle source location

The results obtained in the previous section demonstrate a significant impact of the inclusion of neutrals and self-consistent recycling in the simulations. This includes a reorganization of equilibrium profiles, fluxes and a change in turbulence properties. We have sketched in the discussion about fluxes a possible explanation for this reorganization, suggesting this is mostly due to the relocalization of the particle source in the outer part of the plasma, while it is located in the central part in the reference case without neutrals. However, one cannot at this point rule out a direct effect of the neutrals (e.g. on the growth rate of instabilities) related to the other sources and sinks they impose to the plasma.

In order to investigate this further, we propose in this section a numerical experiment based on a simulation with neutrals, but with a fixed and voluntarily large neutrals diffusion coefficient in order to obtain a particle source much more diffuse in the plasma. We will compare it to the no-neutrals case and the previously discussed case with neutrals, that we will refer to for ease (even though it is a slight abuse of language) as the self-consistent neutrals case.

3.4.1. Simulation set-up: fluid neutrals with constant diffusion

For the purpose of this numerical expeirment, we used the coarsest fluid neutrals model available in SOLEDGE3X, i.e. the one based on a fixed diffusion (Eq. 2.40). This allowed us to have full control on the distribution of the particle source. The diffusion coefficient was set to $D_n = 1000 \frac{\mathrm{m}^2}{s}$.

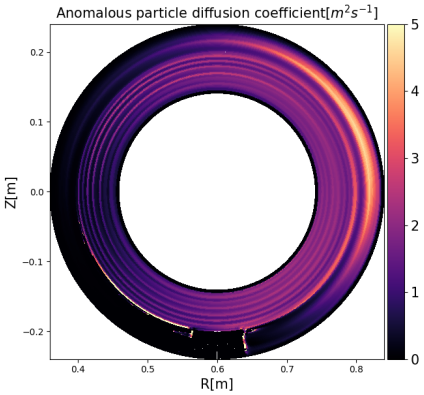

(a) $D_{\perp}^{\text{anom, no neut}}$

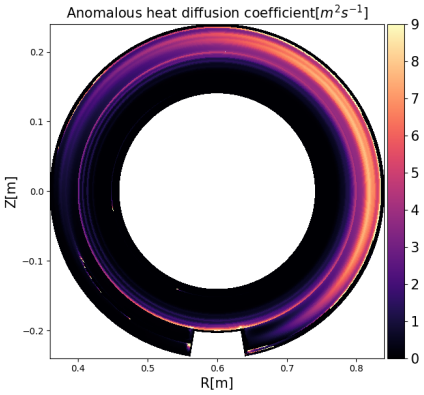

(b) $\chi_{\perp}^{\text{anom, no neut}}$

Figure 3.22. – Anomalous transverse transport coefficients as expressed in Eq. 3.12 shown in 3.22a and as it is in Eq. 3.13) shown in Fig. 3.22b for the case without neutrals. Courtesy of McGibbon 2024.

.

The simulation was driven by a puff located in the outboard mid-plane, with a fueling rate fixed at $2.675 \times 10^{20} \frac{\text{part}}{s}$. With such puff, we will see that one gets a significantly larger plasma density at the separatrix in the mid-plane. This way, one cannot claim that the effect of neutrals fuelling in this simulation in terms of density is low compared to the case with the CX-determined pressure diffusion coefficient. It is interesting to note that the puff rate here is close to 10 times smaller than the one used to drive the self-consistent neutrals case but one anyways will get a larger separatrix density. This can be interpreted as being due to the fact that particles have a longer effective confinement time when they recycle far from the targets plates as will be the case here.

Snapshots of the main plasma fields for the artificially spread neutrals case are plotted in Fig. 3.24. Compared with the two previous simulations (Fig. srefrefcase and 3.11), one immediately sees that the plasma state is closer to that observed in the

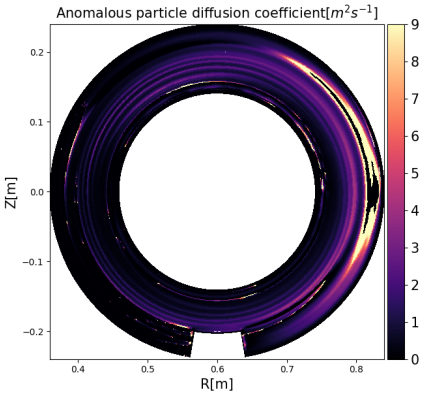

(a) $D_{\perp}^{\text{anom, neut}}$

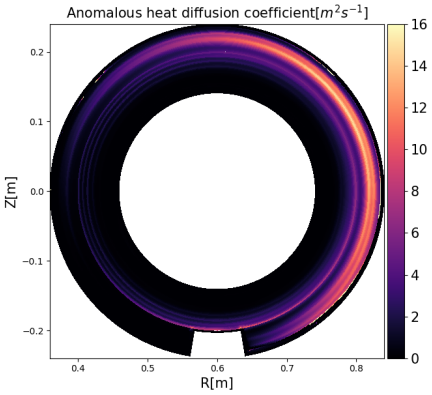

(b) $\chi_{\perp}^{\text{anom, neut}}$

Figure 3.23. – Anomalous transverse transport coefficients as expressed in Eq. 3.12 shown in 3.23a and as it is in Eq. 3.13) shown in Fig. 3.23b for the case with neutrals. Courtesy of McGibbon 2024.

.

case without neutrals than in the self-consistent neutrals case.

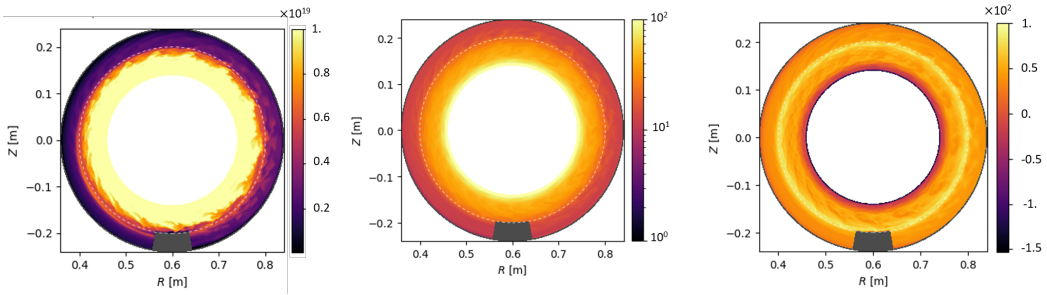

(a) n_i (b) T_e (c) Φ

Figure 3.24. – Snapshots of ions density n_i[m^{-3}] (a), electron temperature T_e[eV] (b) and potential Φ[V] (c) for the case with constant fluid neutrals.

3.4.2. Particle and energy sources

As depicted from the plots in Fig. 3.25, the uniform diffusion imposed by this naive approach results in a widespread distribution of neutral sources throughout the domain, significantly differing from the pattern observed in the self-consistent neutrals simulation. The neutrals diffusion is so large that the neutrals density propagates up to the inner boundary of the simulation domain where the neutrals get blocked by the Neumann (so zero diffusive flux) boundary condition. This results in a neutrals particle source distributed relatively evenly in the closed flux surface region and not localized in the vicinity of the limiter targets.

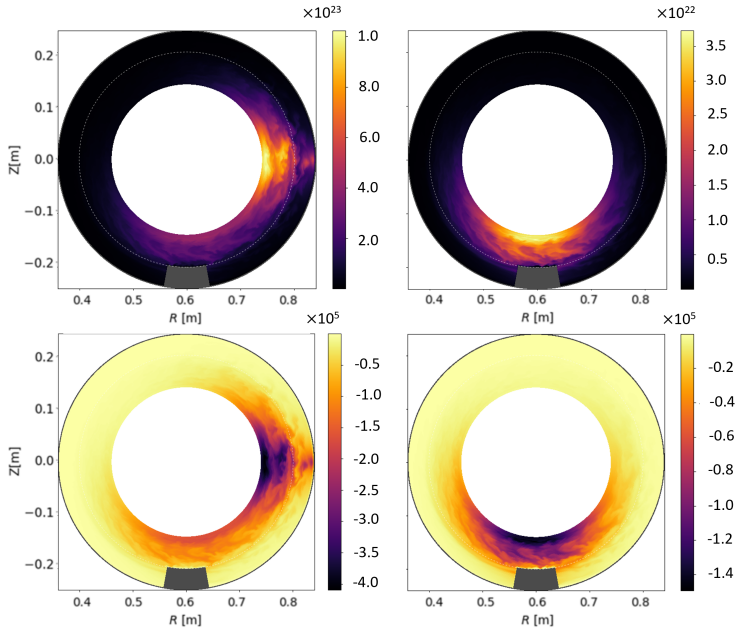

Figure 3.25. – Snapshot of total neutrals particle source $S_n[\frac{\text{part}}{\text{sm}^{-3}}]$ (top) and electron energy source $S_{E,e}[\frac{\text{W}}{\text{m}^{-3}}]$ (bottom) at two different toroidal position (puff location $\varphi = 45°$ (left column) and away from the puff $\varphi = 0°$ (right column)) for the case with neutrals considering a pressure diffusion model.

This way, the case with artificially diffuse neutrals has a particle source which is closer to the case without neutrals than to the case with self-consistent neutrals, while having particle sources entirely driven by neutrals ionization. The plots show also the distribution of the electron energy source to highlight the losses due to ionization, again resulting in a stronger and much more spread contribution with respect the case of improved neutrals.

3.4.3. Equilibrium and turbulence properties

The poloidal distribution of time- and toroidally-averaged density (left) and electron temperature (right) in a flux surface located in the near Scrape-Off Layer ($R - R_{sep} \approx 1$ cm) are plotted in Fig. 3.26, comparing the reference case without neutrals, the self-consistent and the constant diffusion neutral models. The limiter targets are located at the left and right ends of the plots.

The poloidal distribution of the density and of the temperature in the diffuse neutrals case is much more similar to the one in the no neutrals case than to the one in the self-consistent neutrals case. The density is overall larger in the diffuse neutrals case due to the chosen puff amplitude (leading to high mid-plane density a the separatrix), but the local density peak in the vicinity of the outer target that was visible with the self-consistent neutrals is not present. The electron temperature is only slightly lower

than in the no neutrals case (overall larger than in the self-consistent neutrals case) with an extremely similar profile.

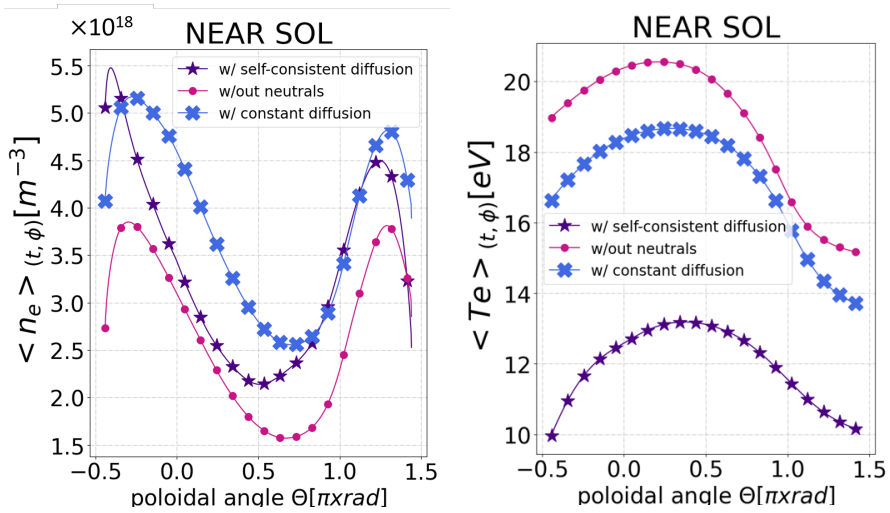

(a) $< n_e >_{t,\varphi}$ (b) $< T_e >_{t,\varphi}$

Figure 3.26. – Poloidal profiles of the electron density (left) and electron temperature (right), averaged in time t and toroidal position φ, for the cases without neutrals (×), with self consistent diffusion (⋆) and constant diffusion (•), in the near SOL after the separatrix $R - R_{sep}$ =1cm

Fig. 3.27 shows the radial profiles in the outboard mid-plane of the averaged density and electron temperature, as well as profiles of their relative fluctuation rate. The 3 simulations are compared. The picture that emerges is that the case with diffuse neutrals is somehow intermediate between the case without neutrals and the case with self-consistent neutrals, although much closer to the former than to the latter. The density at the midplane shows steeper profiles in both the near and far SOL in case of constant diffusion, unlike the self-consistent diffusion case where the profiles tend to flatten significantly. They are nevertheless less steep than in the no neutrals case, as evidenced by the central density which is lower in spite of a higher separatix density. The opposite trends are visible on the averaged temperature profile which is much flatter than that with self-consistent neutrals diffusion but still slightly more peaked than the no neutrals one.

Similar observations can be made for the fluctuation rates. The density fluctuations level with constant highly diffusive neutrals is quantitatively similar to the ones observed without neutrals, while the temperature fluctuations exhibit some intermediate level between the no neutrals case and the self-consistent neutrals case, although again closer to the case without neutrals.

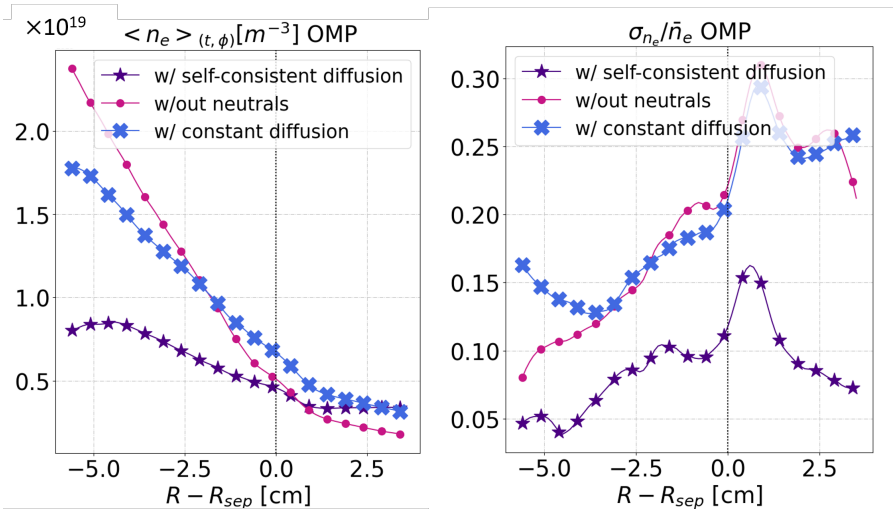

(a) $< n_e >_{t,\varphi}$

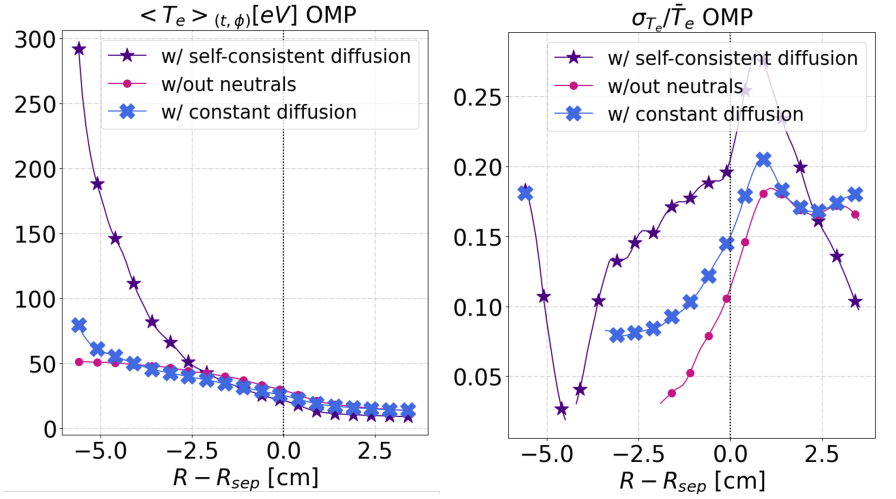

(b) $< T_e >_{t,\varphi}$

Figure 3.27. – Comparison of the radial profiles of the density, averaged in time t and toroidal position ϕ (left) and density fluctuations (right) in Fig. 3.27a, together with temperature averaged in time t and toroidal position ϕ (left) and temperature fluctuations (right) in Fig. 3.27b for the cases without neutrals (×), with self consistent diffusion (⋆) and constant diffusion (•), at the outer midplane.

Similar conclusions can be made for all the other metrics considered previously in this chapter: overall the case with highly diffusive neutrals is much closer to the no neutrals case in terms of turbulence and resulting equilibrium than to the case with self-consistent neutrals. This is the case in spite of the puff rate having been set to such value that the density in the mid-plane was higher with highly diffusive neutrals (hence using a relatively larger neutrals source). We can hence conclude that the main drive for the reported changes in the equilibrium and turbulence properties in the low

density regimes reported here is the localization of the particle source and not the fact that the particle source is due to neutrals ionization instead of some artificial influx from the code.

3.5. Summary

In this chapter, we have discussed how the inclusion of self-consistent neutrals fuelling and recycling in edge plasma turbulence simulations impacts the self-organization of the plasma turbulent transport and equilibrium. Our results demonstrate that, even in low recycling regime, the decorellation between the localization of the particle source and that of the power input is a major change for the system. In particular, the radial decorrelation (with the power input coming from the core while the particle input is located in the edge) leads to a drastic change of anomalous heat transport mechanisms. This leads to a reversal of the slope of the density and temperature profiles in the closed flux surfaces region and a qualitative change of turbulence properties. These changes also propagate in the SOL where they change density and temperature profiles but not too significantly the heat flux decay length, at least in the near SOL. We also showed that the poloidal localization of the particles recycling source is responsible for the generation of additional poloidal asymmetries, both on time averaged plasma properties and turbulence fluctuations.

As a side results, our simulations have highlighted that even a moderate gas puff can perturb the plasma both locally and non-locally along the flux tube connected to the gas valve. The perturbation concerns not only time-averaged quantities but also the characteristics of turbulence fluctuations, raising possible concern about gas puff imaging diagnostics. Dedicated studies would be necessary to provide a detailed assessment of the practical consequences of such phenomenology.

The analysis of these simulations has also highlighted an inherent difficulty with running simulations with neutrals related to the fact that self-consistent recycling adds a long time scale in the system. This can dramatically extend the time simulations need to run before reaching quasi-steady state conditions, defined as conditions in which the various fields statistically don't evolve on time scales larger than a few turbulence correlation times. In the circular limited simulations considered in this chapter, this problem was circumvented by artificially tuning the gas puff to reach quick particle balance, but such approach can not be applied when the goal is to compare oneself to experiments where the puff rate is a constrained parameter. We will discuss in the next chapter some methods aiming at shortening the time scale of convergence of turbulence simulations with neutrals, but the issue remains largely open.

Finally, let us note that these results were obtained in a circular limited magnetic configuration, which is of interest in the start-up phase of future machine. However, the configuration of interest for flat top conditions is the divertor configuration. By construction, this configuration further localizes the particle source away from the confined plasma and with stronger poloidal localization close to the target plates. We

hence expect the effects highlighted here to be even more manifest. More importantly, the divertor configuration allows an easier access to high density regimes and detachment, in which the impact of neutrals on the edge plasma is expected to be even more important.

4. Impact of density regimes on edge plasma turbulence in diverted configuration

After having investigated the effect of realistic particle sources in low density regimes and idealized circular limited plasmas, we now move to cases of interest for reactors, i.e. higher density regimes in divertor geometry. While the TOKAM3D code was tailored for modeling idealized circular limited discharges, its successors TOKAM3X and SOLEDGE3X were developed with flexibility in describing magnetic geometry as a crucial feature. The ability to handle diverted configurations, in particular, was deemed essential, as all currently designed or under-construction machines, as well as the vast majority of currently operating medium-sized tokamaks, are or will be in divertor configuration. The machine chosen for the study in diverted configuration presented in this work is TCV (Tokamak à Configuration Variable) BP Duval et al. 2024 for several reasons, primarily due to its extensive experimental dataset collection (which will eventually allow comparisons between the simulations reported here and experiments), magnetic configuration flexibility and the relatively small size of the machine which makes it suitable for turbulence modelling at reasonable cost.

In a previous validation exercise, named TCV-X21, TCV was already used to define a reference scenario for turbulent code validation (Oliveira et al. 2022). The TCV-X21 scenario featured an outer divertor leg of intermediate length and was designed to address sheath-limited regimes with the objective to limit as much as possible the impact of neutrals, not included in turbulence codes at the time. Data for X21 are accessible in the SPC team's git repository (EPFL/SPC 2021), simulating a lower single null, deuterium L-mode ohmic plasma.

The scenario we are interested in this chapter, that we will refer to as the TCV-X23 for simplicity, aims at extending this exercise to high recycling conditions up to detachment.

Figure 4.1 displays the experimental data from "Mancini et al. 2024, presenting two distinct pulses in the TCV-X23 configuration, both featuring a density ramp from attached to detached divertor conditions. The orange curve corresponds to a pulse with a forward magnetic field (named FF76186) being the focus of this work, while the blue curve represents a pulse (named FF76142) with a reverse magnetic field, which will be addressed in future studies.

For the purpose of reaching detachment conditions, the TCV-X23 scenario not only runs at larger density (see target ion fluxes and electron density in Fig. 4.1) but was also run with a longer outer divertor leg to promote plasma-neutral interaction, as

it is depicted in the left plot of Fig. 4.1. This choice aligns with the objectives of EUROFusion Tokamak Exploitation workpackage and the TSVV3 project (European boundary plasma modeling towards reactor-relevant simulations) as validation exercises. The top right panel of the figure is the integrated ion flux to the outer divertor target as measured by Langmuir probes, which exhibits a clear roll-over indicating that detached conditions have been reached.

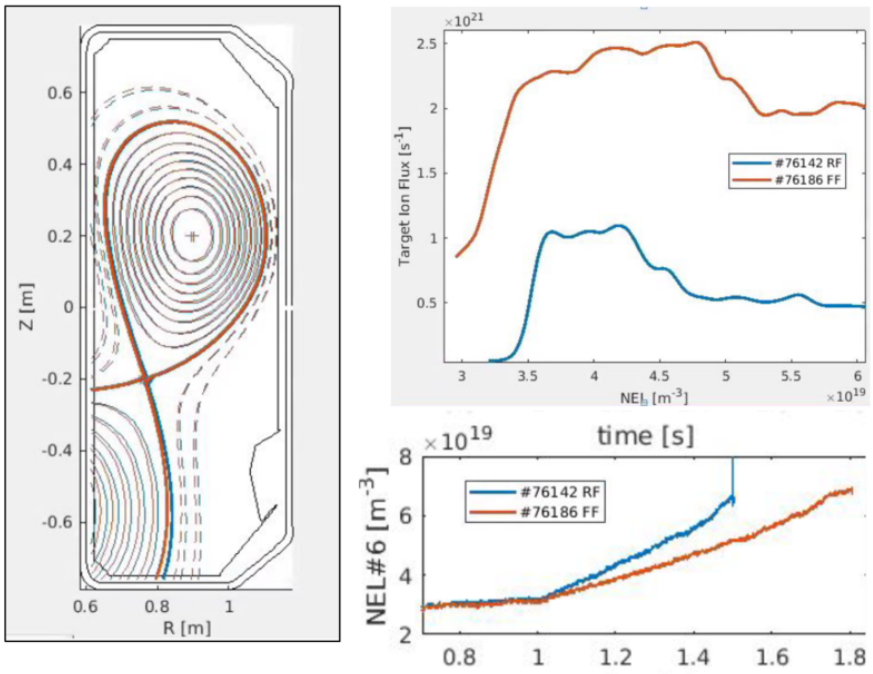

Figure 4.1. – Left: magnetic configuration of the TCV-X23 reference scenario. Right: measurements for line integrated average density passing through the magnetic axis (NEL6) in time (bottom) and target ion flux with respect to NEL6 (top). Courtesy of D. Sales de Oliveira et SPC team.

The work and results presented in this chapter precedes the experiments. Although comparable trends are known from past TCV experiments, the specific experiments for direct comparison have not yet been fully completed due to the limited quality of the data acquired in the first experimental session, making them unsuitable for post-processing and comparison with turbulence codes. The aim of this chapter is to prepare the ground for the validation exercise, by analyzing the outputs from SOLEDGE3X simulations and preparing them for comparison with experimental data once available. Identifying the trends in how turbulence properties and transport behavior evolve across different density regimes will enable us to compare and validate the simulations results with respect to the experimental trends observed in TCV.

With this mindset, the focus is on targeting specific diagnostics to compare simulation results: the statistical properties of turbulence in the divertor (particularly in the middle of the leg) will be compared to RDPA (Reciprocating Divertor Probe Array)

profiles H. De Oliveira et al. 2021. This diagnostic features a radial array of twelve Langmuir Mach-probes that provide two-dimensional (2D) measurements across the TCV divertor plasma up to the X-point (Février et al. 2021). Additionally, measurements of n_e and T_e will be compared with those obtained from the Thomson-Scattering diagnostic. Moreover, SOL width λ_q will be confronted to those recalculated from the simulations. Conducting a comprehensive analysis of these simulations will finally provide a global picture of the trends one might expect for machines operating in high density regime conditions and provide a preliminary understanding of them.

4.1. Simulations set-up

The input values used to tune the simulation parameters are taken from the specific shot in forward (or direct) field (shown in Fig. 4.1) meaning that the ion grad-B drift is orientated towards the lower X-point.

A simple plasma composed of a single ion species, namely deuterium, is considered. From the injected power and the core radiated power measured by bolometry in "Mancini et al. 2024, the power at the separatrix has been estimated to be of the order of 140kW, that we will assume as equally distributed between electrons and ions. The values of the electron density at the separatrix in the outboard mid-plane from the experimental dataset (Mancini 2024) are found to be respectively $n_{e,sep} = 0.5\times10^{19}\mathrm{m}^{-3}$ and $n_{e,sep} = 1.2\times10^{19}\mathrm{m}^{-3}$ for the beginning of the density ramp (attached conditions) and the end of the density ramp (detached conditions). These values will be used to drive 2 separate simulations, a low density one and a high density one, which should allow us to compare an attached and a detached plasma.

Figure 4.2 shows the computational meshes used in SOLEDGE3X for the studies presented in this chapter. Two different meshes are showed: a low resolution one used for 2D mean-field studies (on the left) and a high resolution one used for 3D turbulence simulations (on the right). More details on the rationale for using 2 different meshes will be given in the next section.

One recognizes in both meshes the equilibrium from Fig. 4.1, divided into six topological zones for the needs of the code's numerical discretization based on piece-wise structured meshes. A notable difference with experiments is the fact that the first wall of the machine is taken closer to the plasma in the simulations in order to reduce the computing cost associated with computing a large number of degrees of freedom in a quasi-empty very far SOL. In our simulations, an artificially close wall is located along a flux surface chosen a bit further out than the first flux surface in contact with the vacuum vessel in the outboard mid-plane. This choice was made in order to model the entirety of the most relevant part of the SOL (the one connecting the 2 targets) while still leaving some space for the neutrals to diffuse upstream from the divertor in the small private SOL that exists in the bottom outer corner of the vacuum vessel. For the 3D turbulence simulations, the considered simulation domain in the toroidal direction is a quarter of torus with periodic boundary conditions as already used in the previous chapter.

TCV is here modelled in realistic size, i.e. with a minor radius at the separatrix of 20cm, and a major radius of 90cm. For the high resolution mesh used for turbulence simulations, the resolution at the midplane is about 1.5 mm and less than 1 mm at the outer target.

The particle fueling mechanism is provided by a gas puff located on the wall at the outer midplane, at a given toroidal position ($\varphi = 45°$). The gas puff rate is regulated by a feedback scheme implemented in SOLEDGE3X, which automatically tunes the puff in time to get the wanted value of the density at the outboard mid-plane separatrix. The neutrals model employed in these simulations refers to the highest fidelity one described in Eq. 2.43, which takes into account also the convection contribution provided by the neutrals. The recycling coefficient for the neutrals is chosen compatible with a carbon-like machine as TCV is and fixed at $R_n = 0.95$ following previous comparisons with TCV experiments in mean-field simulations (Yang, Ciraolo, Février, et al. 2023).

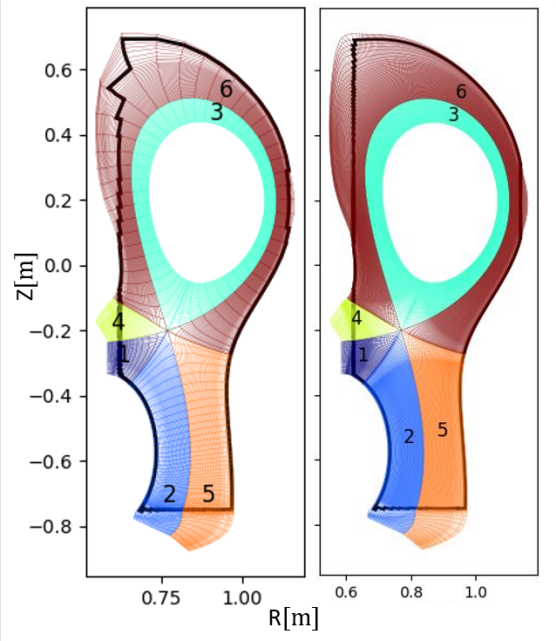

Figure 4.2. – Poloidal cut of the SOLEDGE3X meshes used for modeling 2D mean field transport simulations (left) and 3D turbulence simulations (right).

Finally, the amplitudes of the perpendicular diffusion coefficients appearing in each fluid equation were set to $0.01\mathrm{m}^2\mathrm{s}^{-1}$ (same as in the previous chapter) in order to provide minimum sub-grid transport necessary for the numerical stability of the code.

4.2. Convergence strategy

4.2.1. The use of mean - field solution as initial condition

As already discussed in section 3.1.3, the inclusion of neutrals recycling leads to the appearance in the system of slow time-scales related to the convergence of the energy and particle balances. Given the numerical cost of 3D turbulence simulations, it is not possible to envisage running simulations for the duration of these characteristic times until they reach full convergence. Moreover, since the objective of our simulations is eventually to match experimental conditions at given upstream densities, we cannot rely on the trick used in the previous chapter where the amplitude of the fuelling was adapted to artificially reach particle balance.

In an attempt to accelerate the convergence of the turbulent simulations towards a meaningful steady-state, we have adopted a different strategy to drive the simulation. The basic idea is to use converged 2D mean-field simulations as a starting point for 3D turbulence simulations. 2D mean-field simulations are much faster to push to steady-state as they compute a single poloidal plane. They can also be run with a coarser mesh because they do not need to capture small scale turbulence structures, which in turn enables the use of larger time steps. All together, this allows one to push a TCV mean-field case to convergence in just a few hours of computing time on a single HPC node (48 cores on the Marconi supercomputer).

In practice the following procedure was followed:

1. Run 2D mean-field simulations (including drifts) with appropriately chosen anomalous transverse transport coefficients up until steady-state, i.e. convergence of the energy and particle balances. In this phase, several parameters including the gas puff, were tuned to achieve the targeted plasma conditions. The coarse resolution grid of Fig. 4.2 was used for that purpose.
2. Interpolate the final solution from the 2D coarse grid to the 3D fine grid, assuming axisymmetry.
3. Drop the perpendicular diffusion coefficients to $0.01\mathrm{m}^2\mathrm{s}^{-1}$ and restart the simulations in 3D on a much larger number of computing nodes (64 nodes were used on Marconi for the cases reported here).

A critical point in this procedure is the choice of anomalous transport coefficients in the first step. If non-linearities due to fluctuations in plasma-neutrals interactions are not too important, one can assume that a 2D mean-field simulation adopting anomalous transport coefficients consistent with turbulent transport in the 3D turbulence simulation should lead to a plasma equilibrium which is also the mean of the statistically steady state equilibrium of the 3D turbulence simulation. In that case, the 3D turbulence simulation would start in a readily converged state and could be run solely for the time needed to gather statistical information about fluctuations. This is obviously impossible as this would require knowing in advance the result of the turbulence case. A possible solution is then to use an iterative approach in which one would start with a reasonable guess of transport coefficients, run the 2D

mean-field case to convergence, use the final state as an initial condition to run a 3D global turbulence simulation, run it sufficiently long to extract some information about anomalous transport and then iterate the method by using these newly derived anomalous transport coefficients as input to a 2D mean-field simulation.

In this work, we have performed a single iteration of this scheme due to limited time. However we will touch at the end of this chapter upon the next iteration of such procedure. Our initial guess for anomalous transport coefficients is hence inspired from former TCV simulations run with SOLEDGE3X-EIRENE (Yang, Ciraolo, Février, et al. 2023). Their values were taken as follows: $D_\perp = 1[\frac{m^2}{s}]$, $\chi_{\perp,i} = \chi_{\perp,e} = 2[\frac{m^2}{s}]$ and $\nu_\perp = 1[\frac{m^2}{s}]$.

Fig. 4.3 shows the history in terms of particle balance of our 2 simulations at low and high density during the 2D mean-field phase. It plots as a function of time the contributions to the particle balance of the plasma as described in Eq. 2.52 as well as the time evolution of the convergence ratio C_R. The various steps correspond to changes in input parameters to tune the gas puff and recycling coefficient (to eventually use the one prescribed above) and obtain the targeted density at the separatrix. At each step, the convergence ratio takes a significant duration, of the order of 50 ms, to reach a converged steady-state. This is found to be slighlty larger for the high density case, around 80-100 ms. Including fine parameter tuning, it took more of the order of a second of plasma time to get a relevant starting point for our turbulence simulations, a time scale beyond any duration achievable for a 3D global turbulence simulation.

The initial conditions provided by the converged mean field simulations are reported in Fig.4.4, showing the electron density and temperature obtained for the two different density values at the separatrix in steady state.

4.2.2. Convergence status of the turbulent case

From the interpolation of the 2D plasma solutions on the 3D grid, turbulence was initiated by triggering a small perturbation in the system [1]. The time traces reported in Figure 4.5 depict the transition from the 2D converged cases to 3D with turbulence, for both the low and high density plasma simulations. We have also included the final milliseconds of the 2D cases in the plot. The start of the 3D turbulent simulations occurs at t= 0.5 ms for the low-density case (top left plot in Fig. 4.5) and at t = 1.0 ms for the high-density case (bottom left plot in Fig. 4.5).

As could be expected, in both cases the transition to a 3D turbulence model leads to a significant departure from convergence in terms of particle balance. Both the volume integrated particle source and the plasma outflux drop rapidly on a time-scale of about 500 μs. In the mean-time, fluctuations related to the growth of turbulence rapidly emerge on the curves. One can already notice on these global integrated quantities that the high density case exhibits much larger fluctuations than the low

1. The addition of a white noise perturbation in the simulation is actually not necessary to run a 3D turbulent simulation but it shortens the linear growth phase by pre-exciting fluctuations, rather than waiting for them to grow from numerical noise due to finite numerical precision.

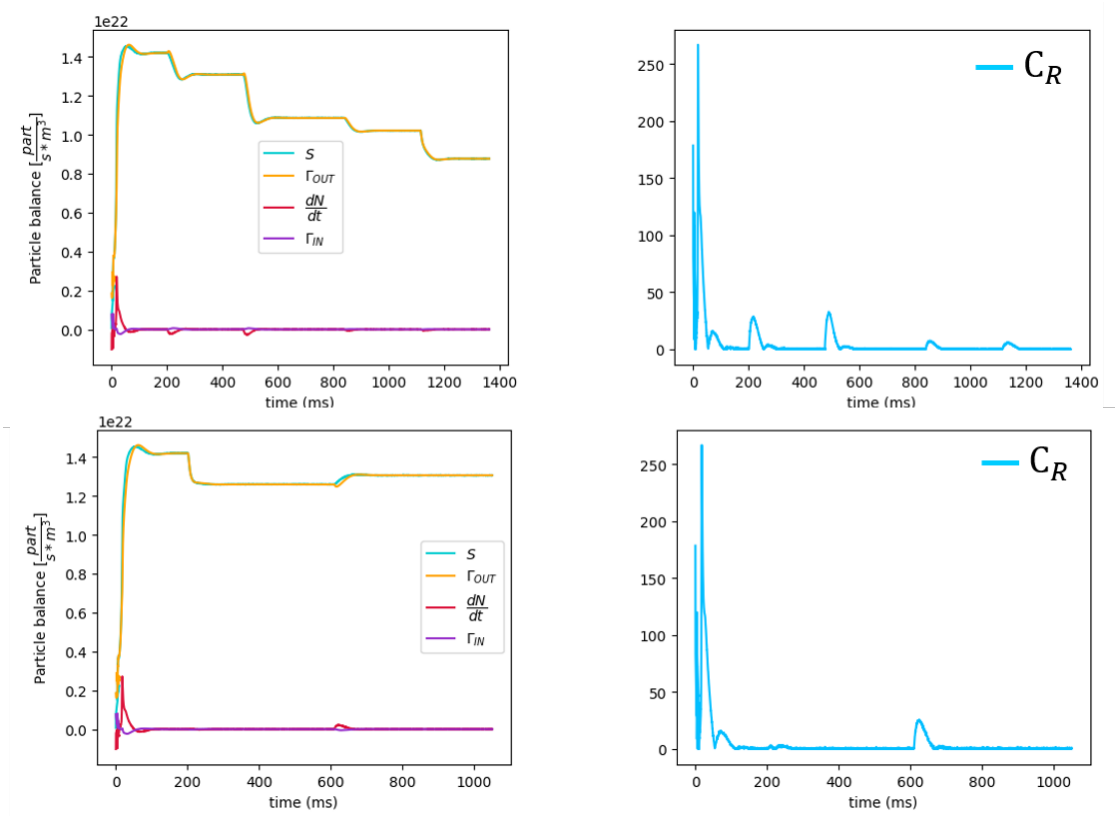

Figure 4.3. – Mean field simulations particle balances (left) for the plasma system expressed as the time traces of the outflux –, neutrals source –, time derivative – and influx – (equals to zero) and the absolute value of the convergence ratio C_R as expressed in 2.59 given here in percentage for the two density cases $n_{e,sep} = 0.5 \times 10^{19}\mathrm{m}^{-3}$ (top) and $n_{e,sep} = 1.2 \times 10^{19}\mathrm{m}^{-3}$ (bottom).

density case, suggesting a different behaviour of turbulence as we will analyse below. Eventually, after the first 0.5 to 1 ms, the two curves seem to stabilize at a lower level. This indicates that one has passed the first 2 time scales (turbulence growth and response of equilibrium profiles) discussed in section 3.1.3.

At that point however, the 2 curves have departed from each other, leading to an imbalance of 30% and 50% in terms of convergence ratio C_R respectively for the low density case and the high density case. This indicates that the 2 simulations have not reached a steady state and would evolve further on a much slower time scale until they reach energy and particle balance. From these graphs as well as from the 2D mean-field simulations, it is clear that waiting for this time scale is beyond the simulation time achievable at reasonable cpu and wall-clock time [2]. It is important to point out that the use of the 2D mean-field simulations as a starting point was not vain. A similar

2. Each of these 3D turbulence simulations amounted to a total cost of roughly 1.5E6 CPUs hours on 64 x 48 cpus on the MARCONI supercomputer.

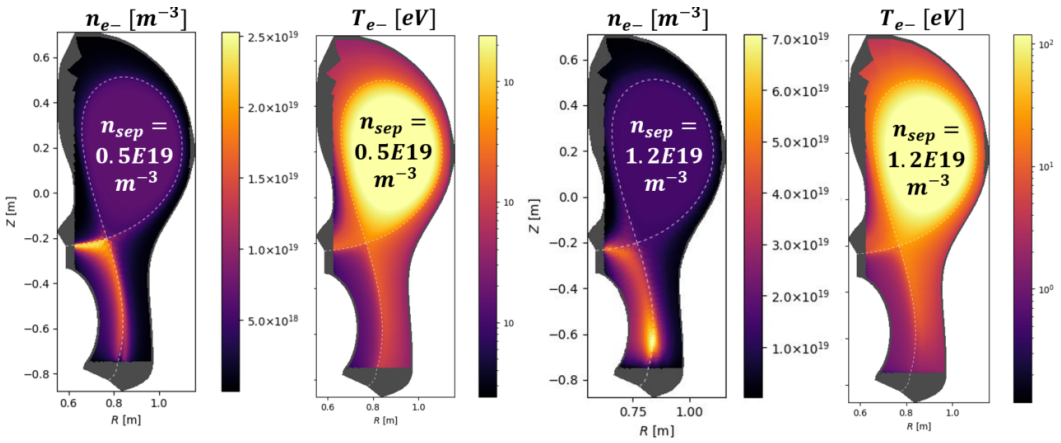

Figure 4.4. – Poloidal maps of the time averaged electron density $n_e[\mathrm{m}^{-3}]$ and temperature $T_e[\mathrm{eV}]$ for $n_{e,sep} = 0.5\times10^{19}\mathrm{m}^{-3}$ (left) and $n_{e,sep} = 1.2\times10^{19}\mathrm{m}^{-3}$ (right) in converged SOLEDGE3X 2D mean-field simulations which served as starting points for 3D turbulence cases.

low density 3D turbulence simulation started from arbitrary initial conditions was found to stabilize around $C_R \sim 70\%$, i.e. about twice as far from a converged particle balance. This way, in spite of not being a game changer, the strategy adopted helps to get closer to an eventual steady-state solution in a shorter amount of time.

Waiting for the simulations to reach a closed particle and energy balance would likely change the final state of the plasma and the divertor conditions. This way, we cannot use these simulations to conclude anything relevant concerning the density regimes one would achieve for the considered heating power and fueling conditions. However, since the simulations have been run beyond the timescale for the self-organization of the plasma turbulent transport and equilibrium profiles, one can use what is effectively a slow transient to analyze the transverse transport properties in given divertor conditions as observed in the simulations. The analysis of the 3D simulations presented hereafter has hence been performed using statistical averages and moments computed in the time windows indicated by purple boxes in in Fig. 4.5.

Let us finish by stating that the discussion on the time scales in 3D turbulence simulations with neutrals recycling is a fundamental one for flux driven global simulations, i.e. it is not specific to SOLEDGE3X. As long as no strategy has been found to drastically reduce the time needed to reach a steady-state in terms of energy and particle balance, investigations will be limited to the transient phase. This means that the observed phenomenology has to be interpreted with care.

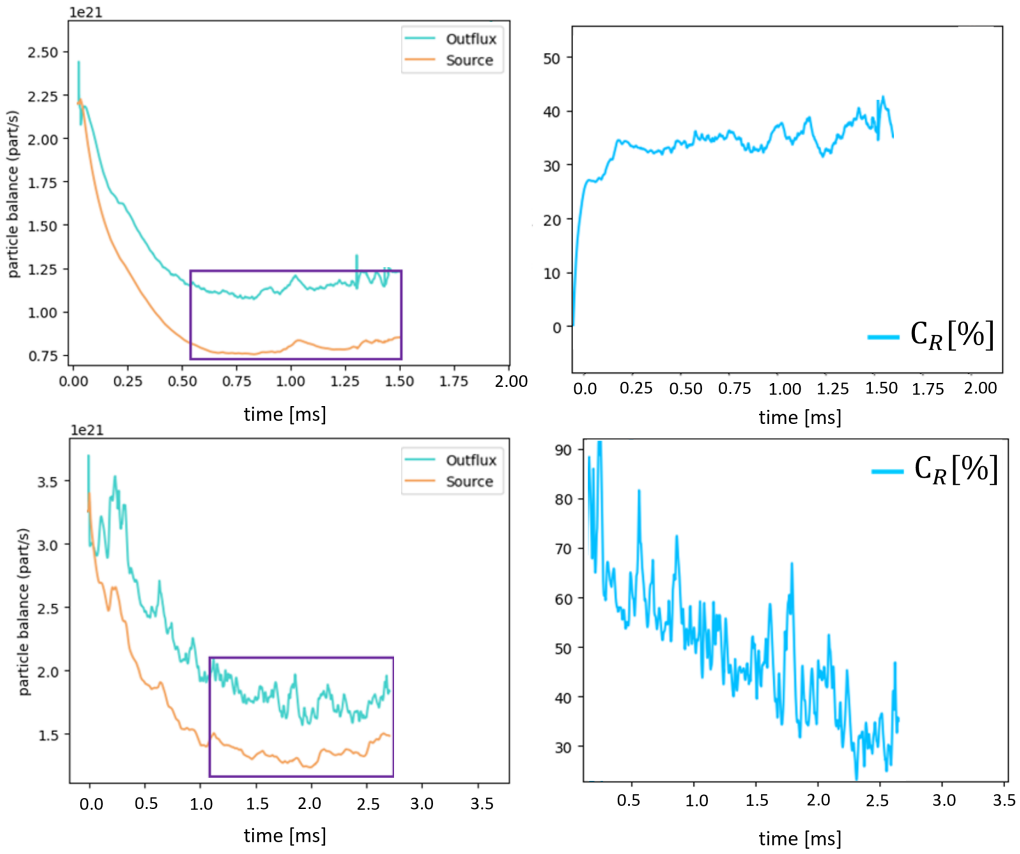

Figure 4.5. – Particle balance for the plasma system (left) expressed as the time traces of the outflux – and neutrals source – and convergence ratio C_R (right) as it is defined in Eq. 2.59 expressed in percentage for the two density cases $n_{e,sep} = 0.5 \times 10^{19}\mathrm{m}^{-3}$ (top) and $n_{e,sep} = 1.2 \times 10^{19}\mathrm{m}^{-3}$ (bottom). Compared with Fig. 4.3, only the 2 main contributors to the plasma particle balance are plotted.

4.3. Recovering density regimes

4.3.1. Evaluation of fluid neutrals model against kinetic neutrals

Before analyzing in depth the outcome of the 3D turbulence simulations in the 2 cases described above, the strategy adopted for running the turbulent cases from 2D mean-field simulations also provides the opportunity to compare the fluid neutrals model implemented in SOLEDGE3X with a full kinetic model implemented in EIRENE. Indeed, the resolutions in 2D mean-field simulations are such that the coupling of SOLEDGE3X to EIRENE can be used in practice for these cases. This allows us to evaluate how closely the plasma conditions generated by our fluid neutrals model align with those produced by a more comprehensive kinetic neutrals model, ensuring that

the use of this simplified fluid model is appropriate despite its crude approximation.

One has to note here that no attempt was made to run EIRENE with a kinetic neutrals model close to the fluid neutrals model assumptions. In particular, EIRENE simulations here have been run with both atoms and molecules, as it is standard with EIRENE, while the fluid neutrals model only includes atoms. This way, we don't expect to see a perfect or even a good match between the 2 models. The goal is mainly to assess whether plasma conditions obtained with the fluid neutrals models, and specifically their evolution between the low density and the high density case, are qualitatively comparable with what would be obtained with a more advanced neutrals model.

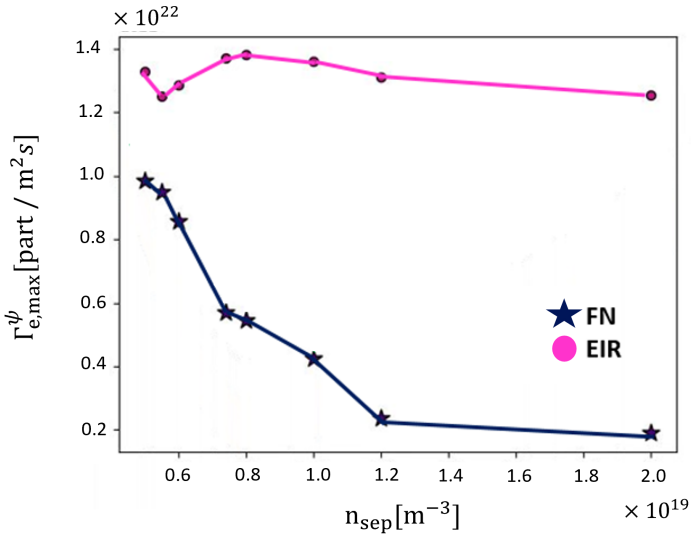

Figure 4.6. – Plot of the ion peak particle flux at the targets as a function of n_{sep} in TCV-X23 2D mean-field simulations with the Fluid Neutrals model (FN) and with a kinetic neutrals model in EIRENE (EIR).

An scan of the outboard mid-plane separatrix density was run with the 2 neutrals models. Figure 4.6 shows the peak ion particle flux at the outer target as a function of the upstream density for the 2 cases. The fluid neutrals model and the kinetic neutrals model exhibit significantly different behaviors. The particle and heat fluxes at the target are found to be much lower for the fluid neutrals: the peak particle flux is systematically higher with EIRENE than it is with fluid neutrals. The difference is of 30% for the low density cases but reaches a factor of 6 at the highest density. This is due to the fact that in the fluid neutrals model the peak particle flux actually drops by a factor of 5 from the low to the high density case, while it conserves the same order of magnitude throughout the scan with kinetic neutrals, presenting a local maximum around $n_{sep} = 0.8 \times 10^{19} \mathrm{m}^{-3}$. This way, the fluid neutrals cases seem to rollover earlier compared to EIRENE cases, and the drop of the flux after the maximum is much stronger.

This result highlights largely the imperfections of the fluid neutrals model, which will

require lot of refinements in future work. The present discrepancies with the kinetic neutrals model makes the current fluid neutrals model unsuitable for a quantitative analysis of dissipative processes in the divertor, e.g. a prediction of the peak heat flux for a given heating power and fueling. We will see however that for other key metrics, the fluid neutrals model captures main relevant trends and does not prevent to study the changes observed in turbulence properties at different density regimes.

Figure 4.7 shows the evolution of the peak electron temperature at the outer target as a function of the upstream separatrix density for the 2 models. Here again a quantitative match is not observed, with a factor of 2 of difference between the 2 models, the kinetic neutrals cases being systematically cooler. However, the qualitative trend is very well reproduced by the fluid neutrals model with the temperature decreasing towards an asymptotic temperature of the order of 1 eV.

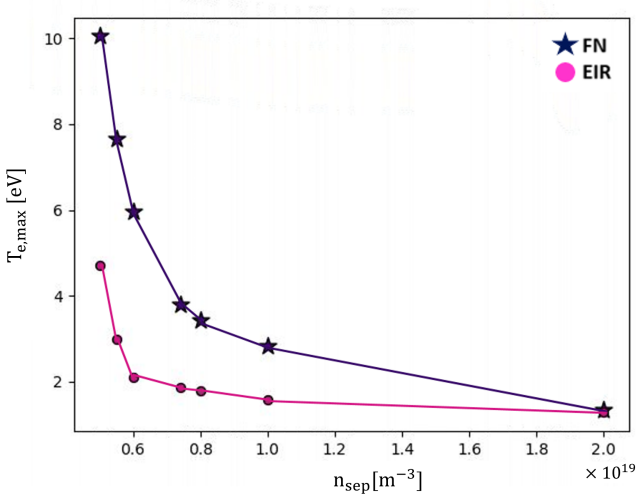

Figure 4.7. – Evolution of the peak electron temperature T_e [eV] at the outer target as a function of the separatrix density in TCV-X23 2D mean-field simulations with the Fluid Neutrals model (FN) and with a kinetic neutrals model in EIRENE (EIR).

From the turbulent transport point of view, this drop of the temperature is expected to have a strong impact on the phenomenology as it will lead to strong changes of the plasma collisionality. Fig. 4.8 compares the evolution as a function of the upstream density of the collisionality of the plasma at the outer target relative to the one found in the lowest density case:

$$\frac{\nu_{col}}{\nu^0_{col}} = \left(\frac{n_e / n^0_e}{T_e / T^0_e} \right)^{3/2}, \tag{4.1}$$

where n^0_e and T^0_e are the electron density and temperature for $n_{sep} = 0.5 \times 10^{19}$. As expected the collisionality increases for both models with the density. More importantly, the relative increase of the collisionality from the low density cases to the high density case is similar for both models. Relying on the discussion of Chapter 2, in this

fashion the impact of density regimes on turbulence via the change of the plasma collisionality will qualitatively be captured with the fluid neutrals model.

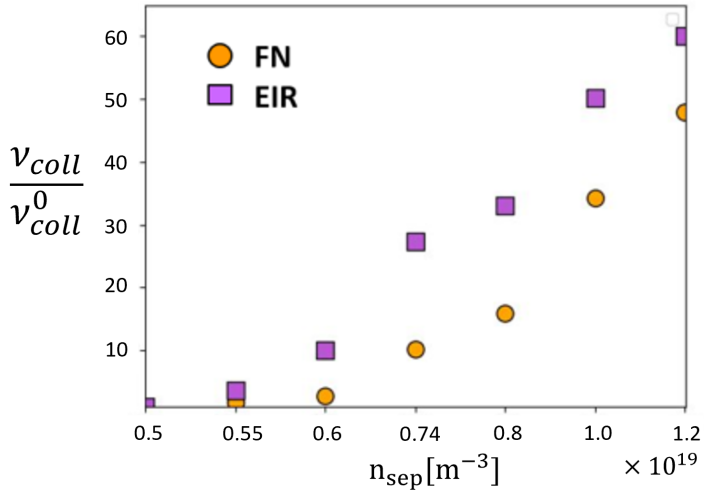

Figure 4.8. – Plot of the plasma collisionality at the outer target normalized with respect to the one at the lowest density in the scan (see Eq. 4.1) as a function of the separatrix upstream density n_{sep}, for the Fluid Neutrals model (FN) and the kinetic neutrals model in EIRENE (EIR).

The localization of the particle ionization source is also a key factor as highlighted in Chapter 3. Figure 4.9 makes a comparison between the particle source distribution with the 2 neutrals models for a low and a high density case. Here again, the fluid neutrals model behaves qualitatively reasonably. The localization of the particle source is roughly captured (mostly along the divertor legs). For both models, the high density case exhibits a detachment of the particle source from the outer target, highlighting that the plasma has reached detached conditions. The ionization front however appears less deep inside the divertor region with fluid neutrals than with EIRENE.

Overall, this comparison between the fluid neutrals model currently implemented in SOLEDGE3X and a state-of-the-art kinetic neutrals model solved with EIRENE highlights important limits of the fluid neutrals model that will need to be refined in the future. These differences make the fluid neutrals model likely unsuitable for quantitative heat exhaust studies in which the prediction of divertor target conditions for given upstream conditions is the targeted result. For what we are after in this study however, i.e. the impact of density regimes on turbulent transport, key metrics indicate a satisfactory behavior of the fluid neutrals model. The plasma response in terms of collisionality as well as the evolution of the localization of the particle source are qualitatively accurate. For this work, which aims to analyze the mutual interaction with turbulence, this qualitative representation is the most crucial aspect and what matters for turbulent studies. It is also in line with the state-of-the-art in other turbulence codes Eder et al. 2022, although a few studies with kinetic neutrals

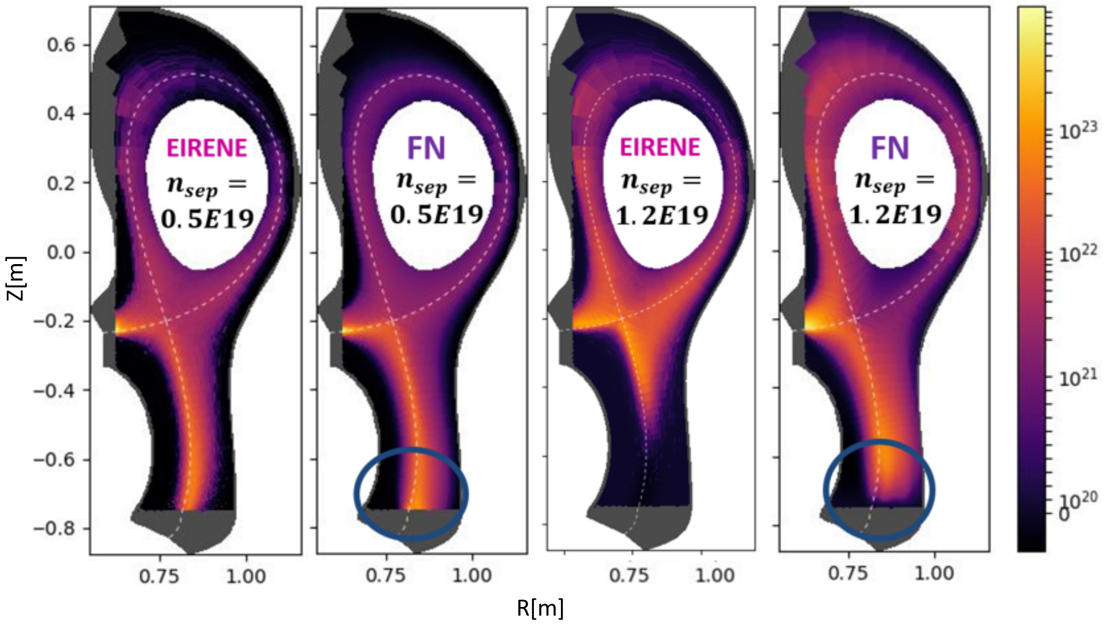

Figure 4.9. – Poloidal maps of the ionization source $S_n[\frac{\text{part}}{\text{s}}]$ for the Fluid Neutrals model (FN) and the kinetic neutrals model in EIRENE for two upstream separatrix densities: $n_{sep} = 0.5 \times 10^{19}\text{m}^{-3}$ (left) and $n_{sep} = 1.2 \times 10^{19}\text{m}^{-3}$ (right).

and turbulence can be found in the literature Mancini, Ricci, Vianello, Giacomin, et al. 2021; Tamain, Baudoin, et al. 2018.

4.3.2. An attached and a detached case

We now turn to the density regimes effectively obtained in the two considered 3D turbulence simulations obtained with the fluid neutrals model. This section offers evidence that the low density case corresponds to attached high recycling conditions while the high density case corresponds to a detached outer target.

To start with, we have plotted in Fig. 4.10 the poloidal map of the electron density and temperature at an arbitrary instant for the 2 considered cases. Both the low density and the high density cases are characterized by a larger density in the divertor than in the upstream SOL and separatrix. The divertor density is more than twice as large in the high density case as in the low density case, except in the very vicinity of the outer target, where a drop of the density starts being visible at high density. Concerning the temperature, both cases exhibit a significant drop between the mid-plane and the targets, but the high density case goes down to much lower values of the order of 1 eV at both targets, vs 20 eV and 5 eV respectively at the inner and outer target in the low density case. Fig. 4.11 provides a more quantitative comparison of the poloidal distribution of the electron temperature in the near SOL. At such low temperature, one expects recombination to become a significant player compared with ionization. This

way, the plasma equilibrium indicates that the low density case is in a high density regime but is still attached, while the high density case has likely reached detachment.

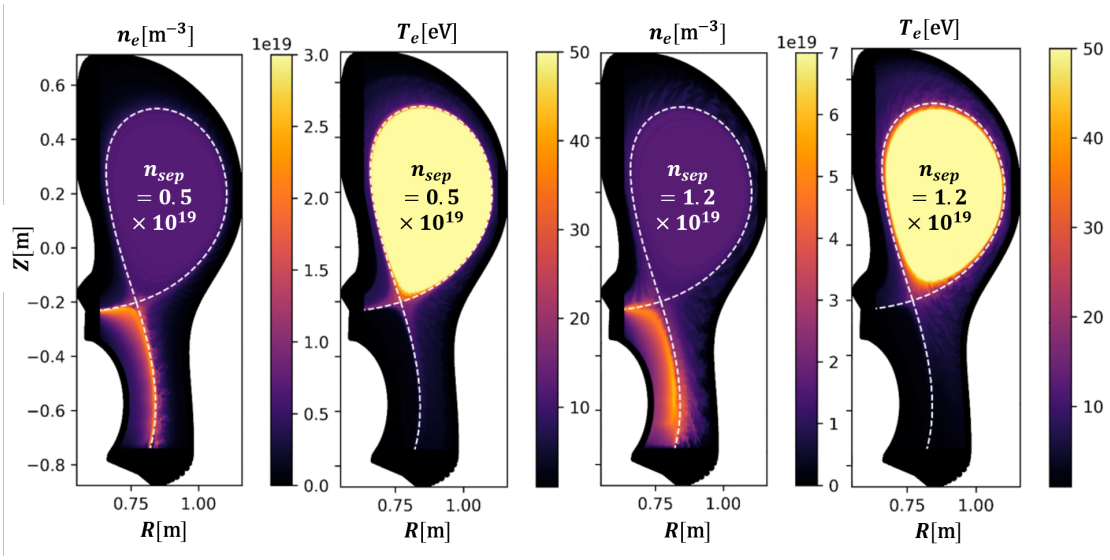

Figure 4.10. – Snapshots of the poloidal maps of the electron density n_e[m^{-3}] and temperature T_e[eV] for $n_{e,sep} = 0.5 \times 10^{19}$[m^{-3}] (left) and $n_{e,sep} = 1.2 \times 10^{19}$[m^{-3}] (right) in 3D turbulence cases.

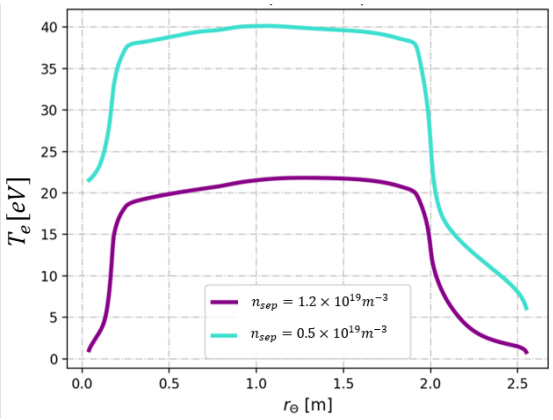

Figure 4.11. – Poloidal profiles of the mean electron temperature T_e [eV], averaged in time t and toroidal position φ, for the two density cases $n_{e,sep} = 0.5 \times 10^{19}$m^{-3} (-) and $n_{e,sep} = 1.2 \times 10^{19}$m^{-3} (-) at the separatrix.

The detachment in the high-density case can be demonstrated further by plotting the total time- and toroidally-averaged particle source due to interactions with neutrals $\langle S_n \rangle_{t,\varphi}$ (Fig. 4.12). In both cases the particle source is largely localized in the divertor. Similarly to what was observed in the 2D mean-field density scans, the average ionization source clearly detaches in the outer divertor. While ionization is visible up to the outer target in the low density case, the ionization front moves about 20 cm

away from the target in the high density case. Such detachment of the ionization front is not observed at the inner target in spite of the low temperatures reached there. Such feature (the outer target detaching before the inner target) is actually a commonly observed feature in TCV (see for example Harrison et al. 2017).

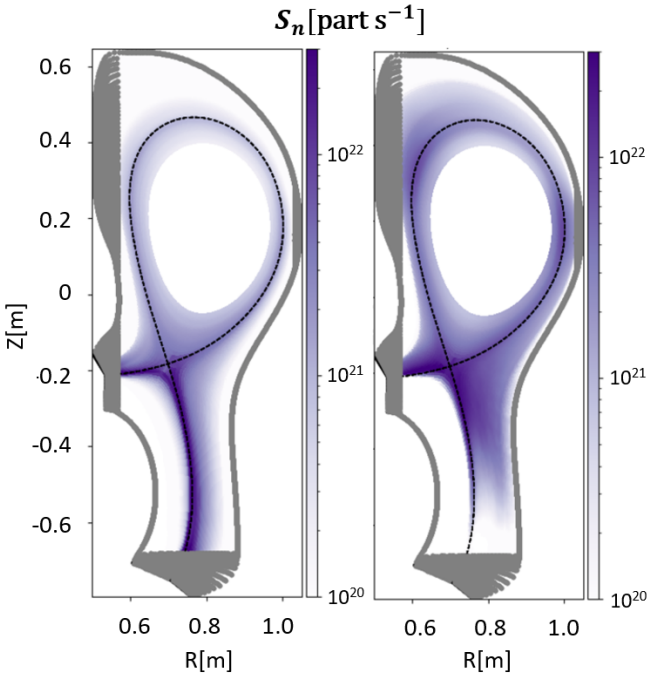

Figure 4.12. – Poloidal maps of the time and toroidal average neutrals source $S_n[\frac{\text{part}}{\text{s}}]$for $n_{e,sep} = 0.5 \times 10^{19}\text{m}^{-3}$ (left) and $n_{e,sep} = 1.2 \times 10^{19}\text{m}^{-3}$ (right). Here the colorbar is set to show only their positive values.

In brief, the two 3D turbulent simulations presented here provide access to sensible conditions from high-recycling attached to detached divertor targets. This behavior is also in line with preliminary experimental analysis indicating the onset of outer divertor detachment in the investigated range of densities. In the remainder of this chapter, we will regularly refer to the low density case as the *attached* case and to the high density case as the *detached* case. Let us analyze in the next sections the impact of this change of density regime on plasma equilibrium and turbulence properties.

4.4. Plasma equilibrium conditions

The discussion will now focus on the plasma equilibrium conditions for the two cases, that is on the analysis of time and toroidal averages of the main plasma quantities.

Fig. 4.13 shows the poloidal maps of the time and toroidally averaged plasma density for both 3D turbulence simulations, along with the relative difference between them,

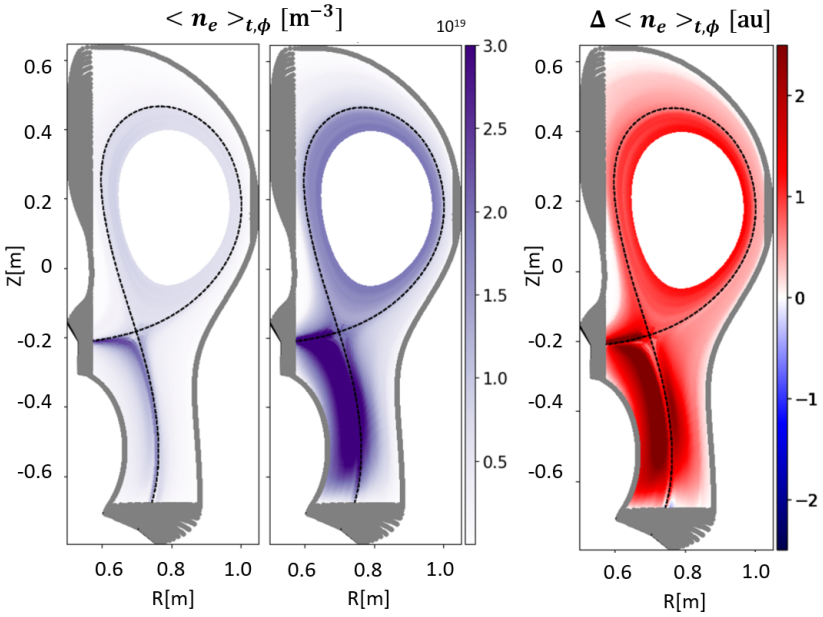

Figure 4.13. – Poloidal maps of the mean electron density n_e[m^{-3}], averaged in time and toroidal direction, for $n_{e,sep} = 0.5 \times 10^{19}$m^{-3} (left) and $n_{e,sep} = 1.2 \times 10^{19}$m^{-3} (central). The right plot shows the relative difference between the high density and low density case, relative to the low density case.

allowing for both quantitative and qualitative comparisons of the main differences observed. As could be expected, the high-density simulation exhibits higher density values at almost every point in the simulation domain. A larger difference is found in the divertor region, both in the main SOL and in the Private Flux Region (PFR). However, in the immediate vicinity of the outer target, the density for the high-density case decreases compared to the low-density case. This is clearly illustrated in the third poloidal map of Fig. 4.13, where a blue region contrasts with the predominantly red high-density areas. This local reduction of the density can be related to the detachment of the ionization front at the outer target.

The overall picture for the mean electron temperature is reported in Fig. 4.14. The individual plots for the time and toroidal averaged temperature for the two density cases (left and central plots of Fig. 4.14) reveal that the temperature is lower in the high-density scenario inside the separatrix and in the near SOL. In contrast, it is slightly higher (5 to 10%) in the outer part of the main SOL, especially at the top of the machine and in the mid-plane. The radial position where the SOL starts being hotter in the high density case than in the low density case does not correspond to the same flux surface at all poloidal positions, occurring further out in the divertor than upstream. The temperature in the PFR is barely affected by the change in density regime. At the outer targets, the temperature in the high-density case reaches approximately 0.1 eV, consistent with values observed under detachment conditions in several machines.

Same conclusions as for T_e can be drawn for the ion temperature T_i from the

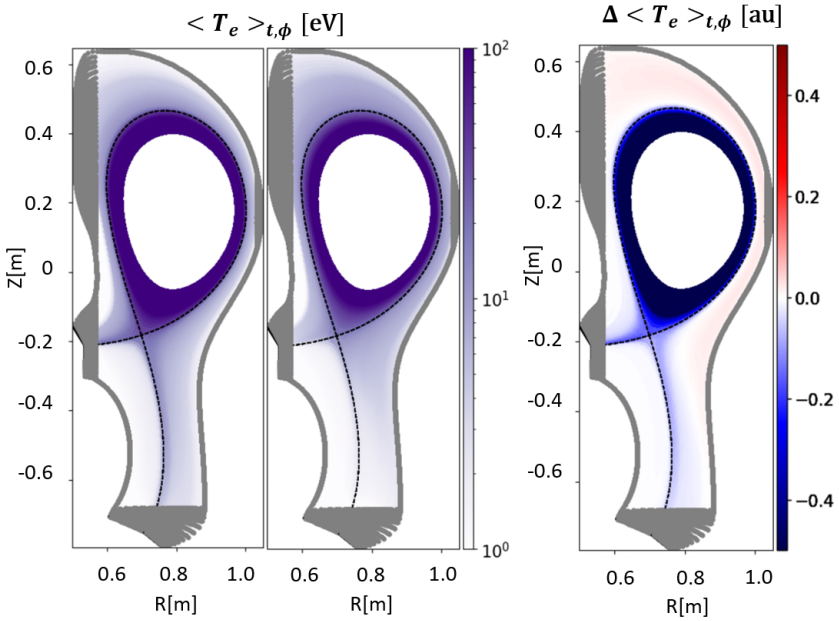

Figure 4.14. – Poloidal maps of the mean electron temperature T_e [eV], averaged in time and toroidal direction, for $n_{e,sep} = 0.5 \times 10^{19}\mathrm{m}^{-3}$ (left) and $n_{e,sep} = 1.2 \times 10^{19}\mathrm{m}^{-3}$ (central). The third poloidal maps represent the relative difference among the high density and low density case, relative to the low density case.

poloidal maps reported in Fig. 4.15. Overall, T_i follows T_e extremely closely, most likely due to strong energy equipartition due to collisions (Eq. 2.28). The only notable difference with respect to the electron temperature is in the far SOL where the warming up in the detached case is less marked than for the electron temperature.

These strong changes observed in the plasma conditions for the two density cases are likely to impact significantly turbulence properties, as we will see in the next section.

We will now explore the changes in turbulence properties in detail.

4.5. Impact of density regimes on turbulence properties

Similarly to chapter 3, we define here fluctuations for any field X as its time-varying part: $\tilde{X} \equiv X - \langle X \rangle_{t,\varphi} \equiv X - \bar{X}$. Hereafter, one will discuss both absolute fluctuations levels, defined through the standard deviation σ over time and in the toroidal direction, and relative fluctuations, the so-called fluctuation level, where the absolute fluctuations for a given field are normalized by the field time- and toroidal-average. However, in many cases turbulent fluctuations in edge plasmas exhibit non-Gaussian behavior. Standard statistical measures like mean and variance are not sufficient to

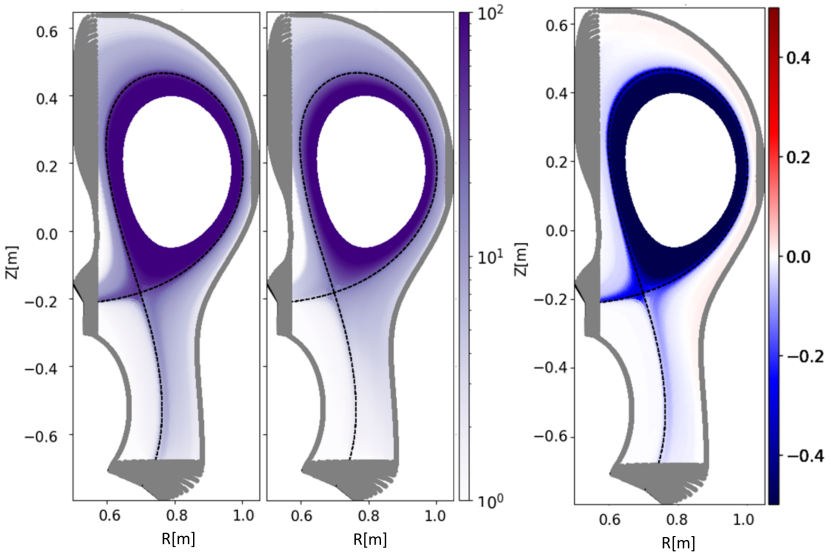

Figure 4.15. – Poloidal maps of the mean ion temperature T_i [eV], averaged in time and toroidal direction for $n_{e,sep} = 0.5 \times 10^{19}\mathrm{m}^{-3}$ (left) and $n_{e,sep} = 1.2 \times 10^{19}\mathrm{m}^{-3}$ (central). The third poloidal maps represent the relative difference between the high density and low density case, relative to the low density case.

measure these non-gaussian properties. Additionally, the third-order statistical moment known as skewness will thus be examined to provide supplementary information on the nature of turbulence:

$$skew(X) = \frac{\overline{\left(X - \bar{X}\right)^3}}{\sigma^3} \tag{4.2}$$

4.5.1. A qualitative change in turbulence properties

Before getting into the details of the statistical properties, it is worth to compare qualitatively the turbulence in the two different plasma conditions. In fact, turbulence structures already exhibit significant visual differences depending on the density background they are associated with.

To illustrate this, Fig. 4.16 provides a snapshot of density fluctuations at an arbitrary time, where changes in the shape, size, and propagation of the blobs are perceptible. At the higher density, we observe more turbulence in the divertor (corresponding to an increased fluctuation level as discussed in detail in Section 4.5.2) and more elongated structures propagating radially outwards. The Scrape Off layer is observed to widen with turbulence in high recycling regimes, not only in the divertor but also in the main SOL.

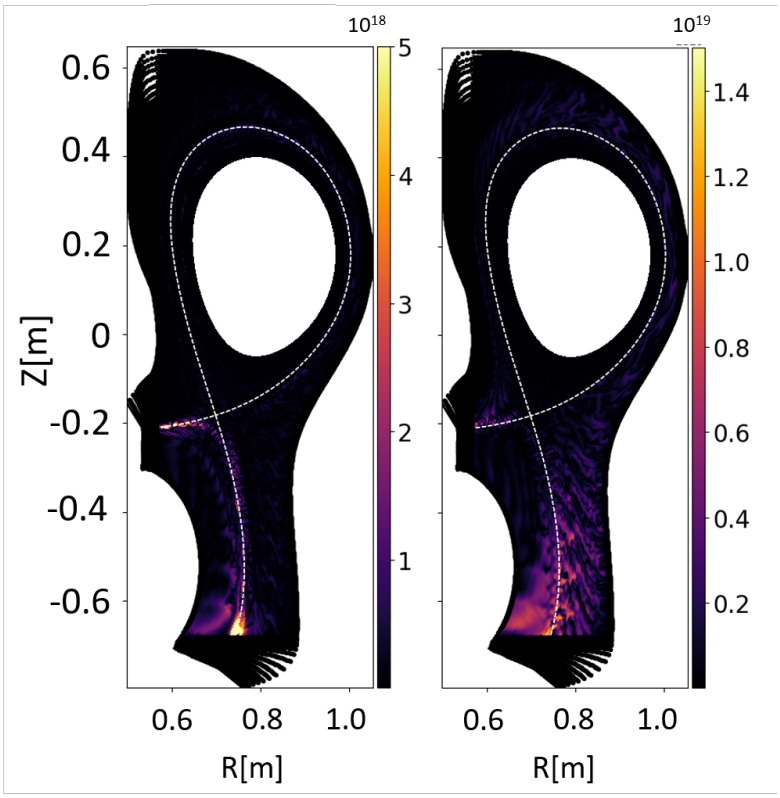

Figure 4.16. – Poloidal maps of the density fluctuations $n_e - \bar{n}_e$ for $n_{e,sep} = 0.5 \times 10^{19}\mathrm{m}^{-3}$ (left) and $n_{e,sep} = 1.2 \times 10^{19}\mathrm{m}^{-3}$ (right).

4.5.2. Characterization of fluctuations

Let us now provide a more quantitative analysis. We start the density relative fluctuation level whose poloidal maps in the 2 cases are reported in Fig. 4.17.

One can observe similarities but also significant quantitative differences between the two cases. In both cases, the fluctuation level tends to increase as one moves out of the plasma, with especially larger fluctuation levels in the SOL than in the closed field lines region. The very far SOL in particular, in the shadow of the inner and outer wall, is characterized by large fluctuation levels of the order of 100%. One can also notice that the vicinity of the targets stands out in terms of fluctuation level. The last 20 cm before the outer target for example are characterized by density relative fluctuation levels about twice as large as further upstream.

When comparing the 2 cases, a general trend emerges of a drop of the density relative fluctuation level in most of the domain when moving from low to high density. Here again, the poloidal pattern is complex with local areas, such as the far SOL or the immediate vicinity of the outer strike point, exhibiting on the contrary an increase. It is important to remember however that the time averaged density is also globally larger in the high density case, so that this decrease in the relative fluctuation level corresponds in fact still to an increase in terms of the absolute amplitude of

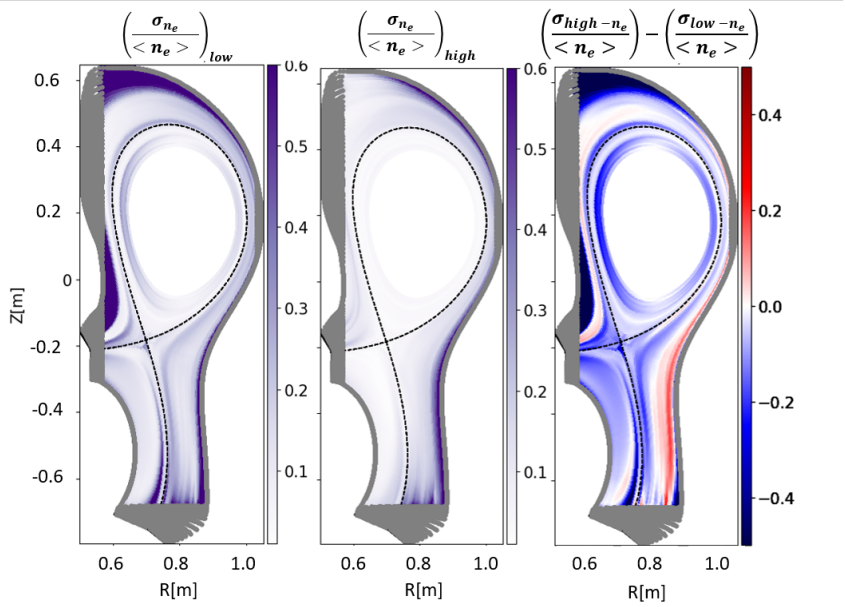

Figure 4.17. – Poloidal distribution of the relative fluctuations level for the electron density n_e averaged in time t and toroidal position φ, for the two density cases $n_{sep} = 0.5 \times 10^{19} \mathrm{m}^{-3}$ (left) and $n_{sep} = 1.2 \times 10^{19} \mathrm{m}^{-3}$ (center), together with the map (right) of their difference (high - low).

fluctuations.

Profiles of the absolute and relative fluctuations for the density provide more insights into the dynamics at play. These are given in Fig. 4.18 at 4 separate poloidal locations: outer mid-plane (OMP), along the outer and inner targets and in the middle of the outer divertor leg (at Z ≈ -0.4). Concerning the outer and the inner targets, due to the strong gradients at play, we decided to shift the poloidal position for the plots respectively 1 mm and 2 mm up the strike points.

Starting with the absolute fluctuations (plot (a)), a general increase is observed in the SOL for the high-density case compared to the low-density case, at the notable exception of the outer target. In the mid-plane and at the inner divertor target, the radial trend reverses: while the fluctuation level decreases when moving outwards beyond $R - R_{sep} \approx 5$mm in the low density case, it is mostly constant in the high density case. As a consequence, the absolute fluctuation level in the far SOL is found to be more than 5 times larger in the far SOL of the detached case than in the attached case. In the middle of the outer divertor leg, a radially decreasing profile is found in both cases, but with much higher fluctuation levels in the detached case (factor of 4 to 5). The outer target is a notable exception with almost no change of the fluctuation level in the SOL, although a clear increase is visible in the private flux region (PFR).

The relative fluctuations (plot (b)), however, exhibit entirely different trends due to the important changes in the poloidal distribution of the mean density. At the exception of the outer target (which we recall is detached), the relative density fluctuations level increases radially in all cases at all poloidal positions. Its amplitude is also very

comparable at all poloidal locations, ranging between 15 and 25%. One can however notice a significant decrease by 5 to 10% of the relative fluctuation level in the near SOL for $R - R_{sep} < 2$cm in the high density case compared to the low density case (corresponding to a quarter, up to half of the reference value). At the inner target and in the mid-outer-divertor leg the far SOL on the contrary exhibits an increase by about 5% of the relative fluctuation rate in the detached case. Such increase is not seen in the mid-plane where the plasma is intercepted by the wall closer to the separatrix. The outer target again stands out with no clear change of the relative fluctuation level between the 2 cases.

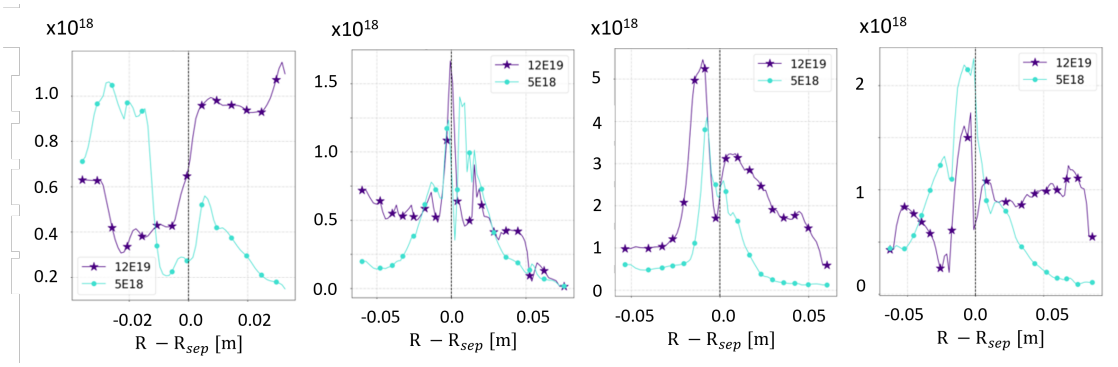

(a) σ_{n_e} [m^{-3}]

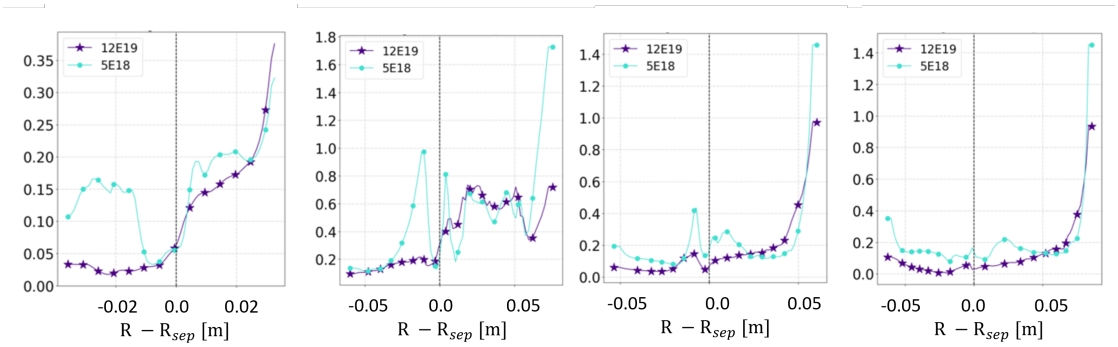

(b) $\frac{\sigma_{n_e}}{\bar{n}_e}$

Figure 4.18. – Radial profiles of the absolute (plot (a), top row, in [m^{-3}]) and relative (plot (b), bottom row) fluctuation of the density for the two density cases $n_{e,sep} = 0.5\times10^{19}$m^{-3} (•) and $n_{e,sep} = 1.2\times10^{19}$m^{-3} (⋆) at 4 poloidal locations: the outer mid-plane, outer target, mid-outer-divertor (at $Z \approx -0.4$) and inner target (from left to right). The horizontal axis corresponds to the radial distance to the separatrix after remapping along flux-surfaces to the outboard mid-plane.

Let us now turn to temperature fluctuations. In Fig. 4.19 the poloidal maps of the relative fluctuations for the electron temperature are reported as well as the map of

the difference between the 2 cases.

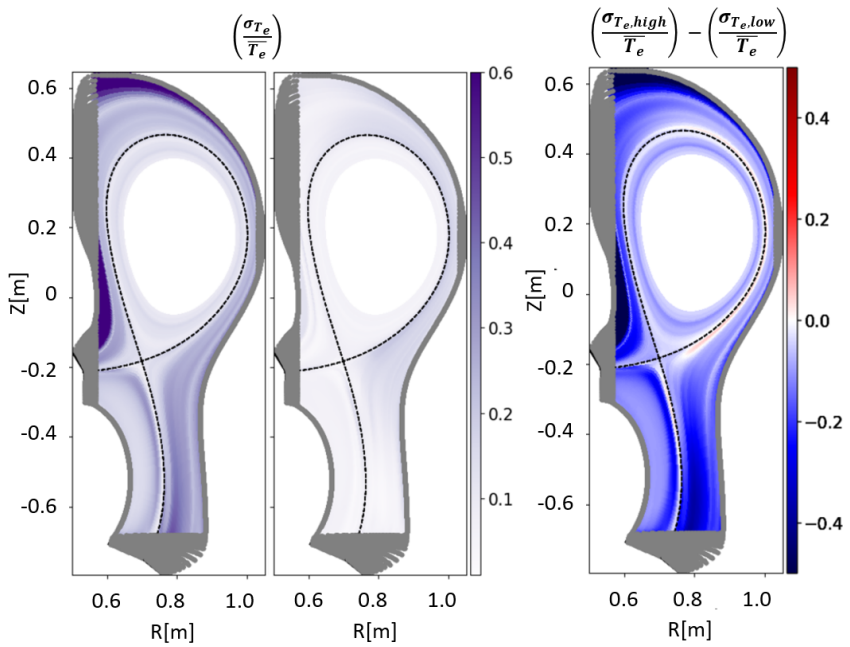

Figure 4.19. – Poloidal distribution of the relative fluctuations level for the electron temperature T_e averaged in time t and toroidal position φ, for the two density cases $n_{sep} = 0.5 \times 10^{19}\mathrm{m}^{-3}$ (left) and $n_{sep} = 1.2 \times 10^{19}\mathrm{m}^{-3}$ (center), together with the map (right) of their relative difference (high - low).

The picture that emerges is simpler than for the density. The relative fluctuation rate of the temperature decreases almost at all points in space except in the immediate vicinity of the separatrix, both in the main SOL and in the divertor. The decrease is more marked along both divertor legs than in the upstream SOL.

The radial profiles in Figure 4.20 confirm this trend. In the outboard mid-plane, the relative fluctuation rate of the electron temperature (plot (b)) is found larger in the detached case only in the first 5 mm of the SOL. Beyond this, the relative fluctuation rate decreases radially down to 15% in the far SOL while it increases up to 25% in the attached case. At the other poloidal locations in the divertor, a marked drop of the relative temperature fluctuation rate is observed at high density, typically from 30% down to 5 - 15% depending on locations. Only the immediate vicinity of the separatrix (a 1 - 2 mm wide layer) is characterized by a minor change.

Since the average temperature tends to be lower in the divertor in the high density case, the absolute temperature fluctuation level (plot (a)) exhibits an even stronger drop along the outer and inner targets and in the middle of the outer divertor leg when moving from attached to detached conditions. The profiles in the high density case are almost flat, as opposed to those in the low density case which peak at the separatrix before decreasing radially outwards. In the mid-plane, the absolute fluctuation rate

shows no significant change beyond $R-R_{sep} \approx 5$mm. In the closed flux surfaces region and by extension in the near SOL, a significant reduction is on the contrary observed in the high density case.

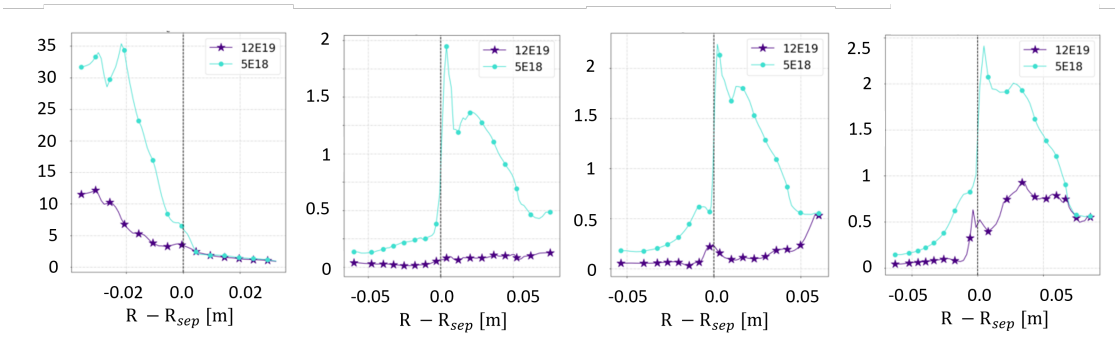

(a) σ_{T_e} [eV]

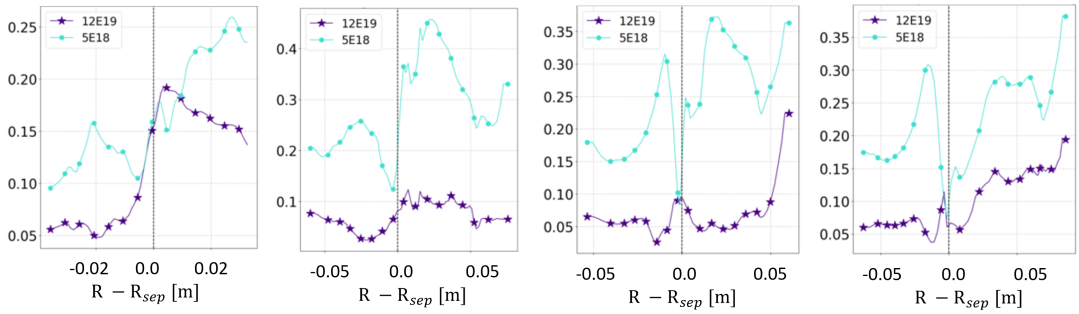

(b) $\frac{\sigma_{T_e}}{T_e}$

Figure 4.20. – Radial profiles of the absolute (plot (a), top row, in [eV]) and relative (plot (b), bottom row) fluctuation for the electron temperature for the two density cases $n_{e,sep} = 0.5 \times 10^{19}\text{m}^{-3}$ (•) and $n_{e,sep} = 1.2 \times 10^{19}\text{m}^{-3}$ (⋆) at 4 poloidal locations: the outer mid-plane, outer target, mid-outer-divertor (at Z ≈ −0.4) and inner target (from left to right). The horizontal axis corresponds to the radial distance to the separatrix after remapping along flux-surfaces to the outboard mid-plane.

No significant changes are observed between the electron and ion temperatures. The radial profiles for the ion temperature (Fig. 4.21) at the outer midplane and at the outer target are added for the sake of completeness, showing an extremely similar trend with respect to the electron temperature and they will be no longer discussed here.

Overall, the change of divertor regime is found to impact significantly absolute and relative fluctuation levels of the density and of the temperatures. The change is poloidally non symmetric, a trend already observed in the limited case in Chapter 3 following the introduction of neutrals recycling but exacerbated here by the strong

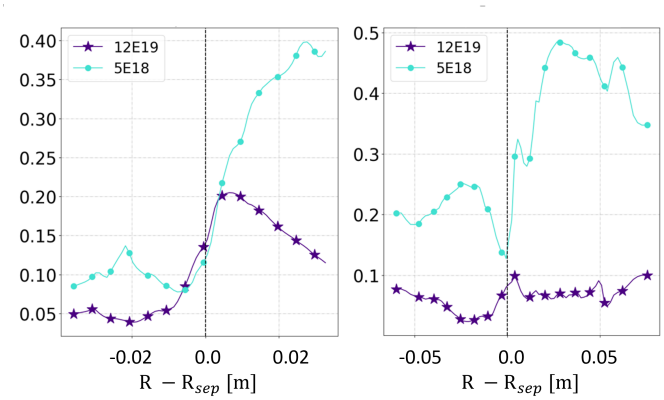

Figure 4.21. – Radial profiles of the relative fluctuation for the ion temperature $\frac{\sigma_{T_i}}{\bar{T}_i}$ for the two density cases $n_{e,sep} = 0.5\times10^{19}\mathrm{m}^{-3}$ (•) and $n_{e,sep} = 1.2\times10^{19}\mathrm{m}^{-3}$ (⋆) at the outer mid-plane (left) and outer target (right).

coupling between the plasma and neutrals, and the poloidal asymmetries driven by the magnetic geometry itself. This is important when interpreting experimental data: investigating fluctuations at the target, midplane, or X-point yields different insights, and focusing on only one location is insufficient. The initial findings from these simulations suggest examining multiple poloidal locations to determine if these trends, where distinct behaviors are observed at different positions, can be reproduced.

These changes in the fluctuations properties already hint at changes in turbulent transport mechanisms and amplitude, as will be further addressed in Section 4.7.1.

4.5.3. Intermittency

A strong positive skewness in the SOL, particularly in the far SOL, is a well-known feature of edge plasma turbulence, observed in numerous machines and regarded as a key signature of this phenomenon. Therefore, it is important, in preparation for comparison with experimental data, to examine this property in our simulations and explore whether it is influenced by the divertor density regime or not.

Hereafter, the skewness radial profiles for the density and temperature fluctuations are plotted in order to investigate the asymmetry of their probability distribution about the mean density, i.e. the intermittency of fluctuations. Depending on the skewness sign, the distribution characteristics of the quantity become evident: a positive skewness results in a longer tail on the large amplitude (right) side of the plot, whereas a negative skewness leads to a fatter tail on the low amplitude (left) side.

The radial skewness profiles for density (left figure 4.22) generally show significant poloidal asymmetry. In the low-density case, the skewness at the outboard midplane increases with radius, starting negative in the closed flux surface region and becoming positive in the scrape-off layer (SOL), which is a common characteristic of edge turbulence observed in experiments Zweben et al. 2014, Tamain, Kirk, et al. 2010, B.D. Dudson, Ayed, et al. 2008.

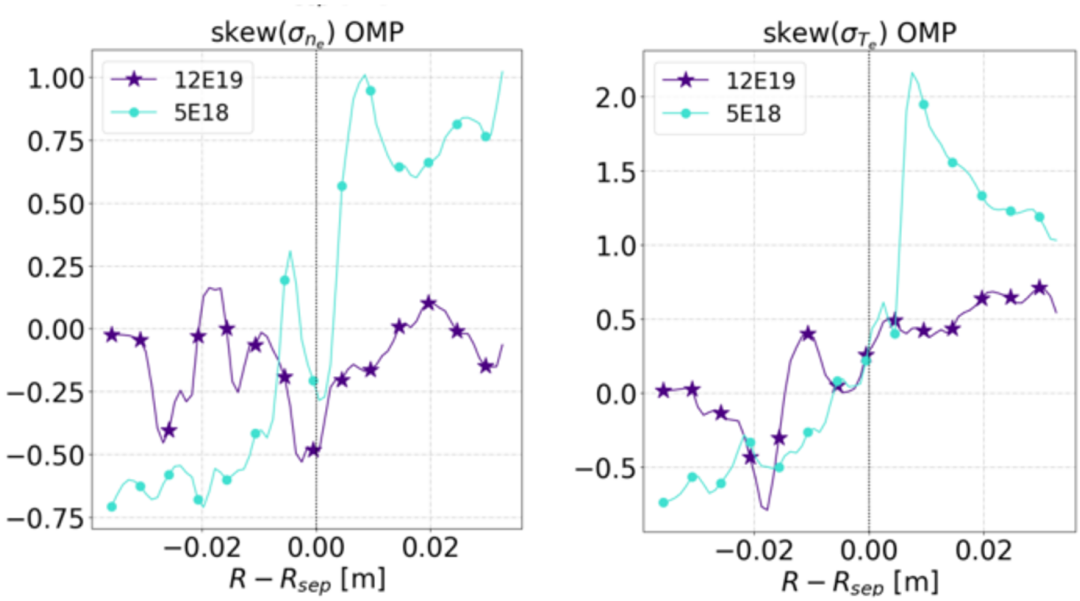

Figure 4.22. – Radial profiles of the skewness of density fluctuations (left) and electron temperature fluctuations (right) for the two density cases $n_{e,sep} = 0.5 \times 10^{19}\mathrm{m}^{-3}$ (•) and $n_{e,sep} = 1.2 \times 10^{19}\mathrm{m}^{-3}$ (⋆) at the outer mid-plane.

The main striking difference between the two density cases is observed in the mid-plane where the skewness becomes almost flat and remains around 0.

Regarding temperature skewness (right figure 4.22), the profile at the midplane follows a similar pattern to that of the density but with larger values. The skewness starts negative in the closed field line region and increases as it moves outward toward the edge, peaking at 2 just beyond the separatrix at $R - R_{sep} = 1$ cm, before decreasing to around 1 in the far SOL.

The skewness in the high-density case is generally lower in amplitude compared to the low-density case. At the OMP, it ranges between -0.5 and 0.5, remaining relatively flat in the SOL around 0.5, with a slight positive trend.

Overall, the density regime significantly impacts filament intermittency, leading to reduced skewness at the OMP for both n_e and T_e.

To summarize the previous results, the change in the divertor density regime in the 2 considered simulations leads to a significant change in turbulence properties, either in terms of fluctuation rates or intermittency. These changes strongly depend on the radial and poloidal location, with divertor turbulence evolving differently from upstream SOL turbulence. They also suggest a corresponding change in turbulent transport which should in turn impact plasma equilibrium profiles and SOL decay lengths.

4.6. Impact on equilibrium profiles

Fig. 4.23 presents the radial profiles of the time and toroidally averaged density at the four specified poloidal locations already investigated in previous figures. One can first notice on the mid-plane profiles (Fig. (a) of 4.23) that the feedback scheme on the gas-puff achieves its target of enforcing the targeted densities at the separatrix in spite of the perturbation induced by the build-up of turbulent transport when moving from the 2D mean-field to the 3D turbulent simulations. The plots confirm that the density is consistently higher at almost all location in the detached case. In the closed fluxed-surfaces (see mid-plane plot), the attached case exhibits a quasi-flat density profiles while the detached case has significant gradients. One can explain that due to the deeper penetration of the neutral ionization source in the high density case, already seen in Fig. 4.12. SOL mid-plane profiles are characterized in both cases by a narrow layer (about 5 mm thick) with of steep density just outside the separatrix, followed by a less rapid decay further out. The gradient length in the far SOL is larger in the high density case. Main SOL profiles at the inner target and in the middle of the outer divertor leg show similar flattening in the detached plasma but the narrow SOL feature is visible at these locations only in the attached case. At the outer target (Fig. (c) of 4.23), as already discussed in a section 4.4, the attached case shows higher density in the near SOL, while the profiles are relatively similar further out. The outer target PFR is much denser in the detached case.

Turning to electron temperature profiles (Fig. 4.24), the temperature at the midplane (plot (a) of Fig. 4.24) shows the attached case hotter in the closed flux surface region and near SOL $T_e \approx 30-20$ eV but cooler in the far SOL beyond $R - R_{sep} \approx 5$ mm. Similarly to the density, both the attached and detached case exhibit 2 decay lengths in the SOL, steep in the near SOL, flatter after $R - R_{sep} \approx 5$ mm. The hotter far SOL in the detached case is due to a flattening of the profiles both in the near and far SOL compared with the low density reference. At the targets and in the mid-divertor region, the detached case is systematically cooler than the attached case, except in the very far SOL, with the radius at which the crossing between the curves occurs depending on the exact poloidal locations. The outer target (plot (c) of Fig. 4.24) gives particularly low temperature in the detached case (below 1 eV at the strike-point). The shape of the profiles is also strongly impacted, with a reversal of the temperature gradient for the mid-divertor leg and the outer target (respectively plots (b) and (c) of Fig. 4.24).

Same conclusions as for T_e can be drawn for the ion temperature T_i. Ion temperature profiles are extremely similar to electron temperature profiles, highlighting effective energy equipartition by collisions between the two species. The only significant difference is that the crossover point between the low and high-density profiles (with the detached case being cooler in the near SOL and hotter in the far SOL) occurs further out for T_i than for T_e at all examined poloidal positions.

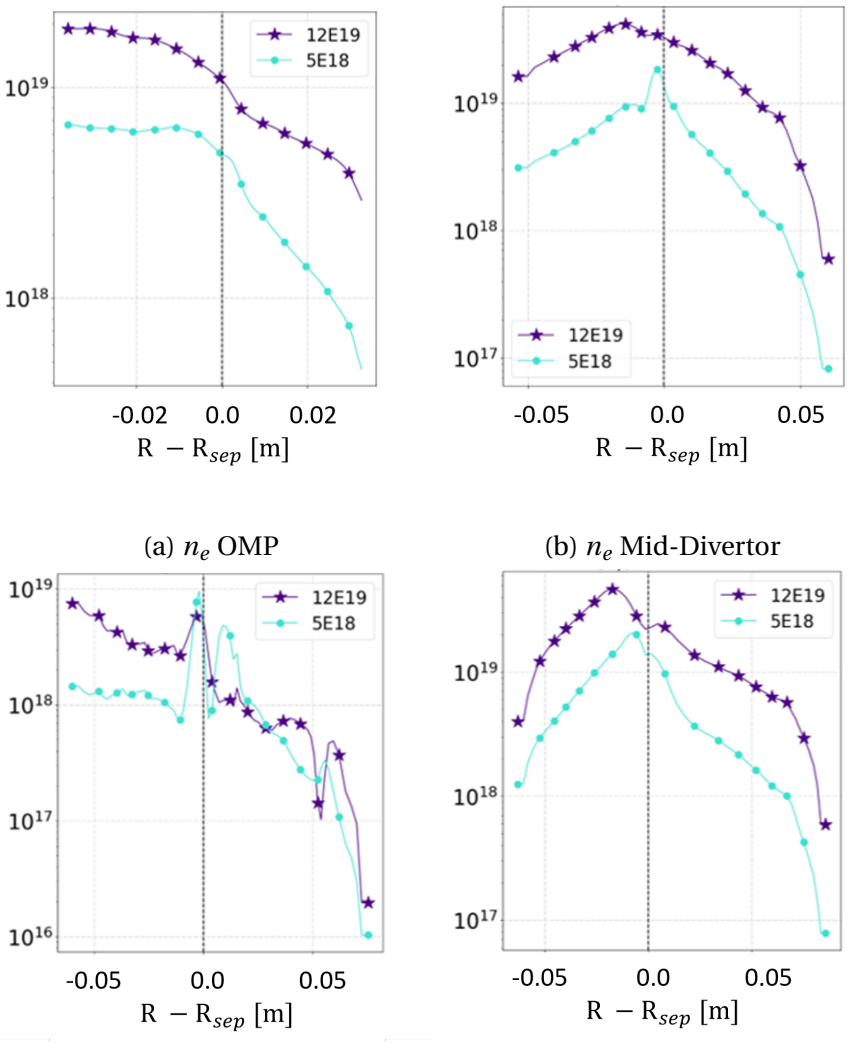

(a) n_e OMP

(b) n_e Mid-Divertor

(c) n_e Outer target

(d) n_e Inner target

Figure 4.23. – Radial profiles of the mean electron density $n_e[\mathrm{m}^{-3}]$ averaged in time t and toroidal position φ, for the two density cases $n_{e,sep} = 0.5 \times 10^{19}\mathrm{m}^{-3}$ (•) and $n_{e,sep} = 1.2 \times 10^{19}\mathrm{m}^{-3}$ (⋆) at the outer mid-plane, mid-divertor region, outer and inner targets. The horizontal axis corresponds to the radial distance to the separatrix after remapping along flux-surfaces to the outboard mid-plane.

4.6.1. SOL decay lengths

In diverted configuration, one of the standard methods to extract the heat flux decay length λ_q consists in applying the same fit as the one used to establish the Eich scaling law (Eich et al. 2020) (exponential decay in the main SOL convoluted with a gaussian for the transport to the PFR) to profiles of the heat flux reaching the outer target. In the conditions considered in our simulations however, especially the detached

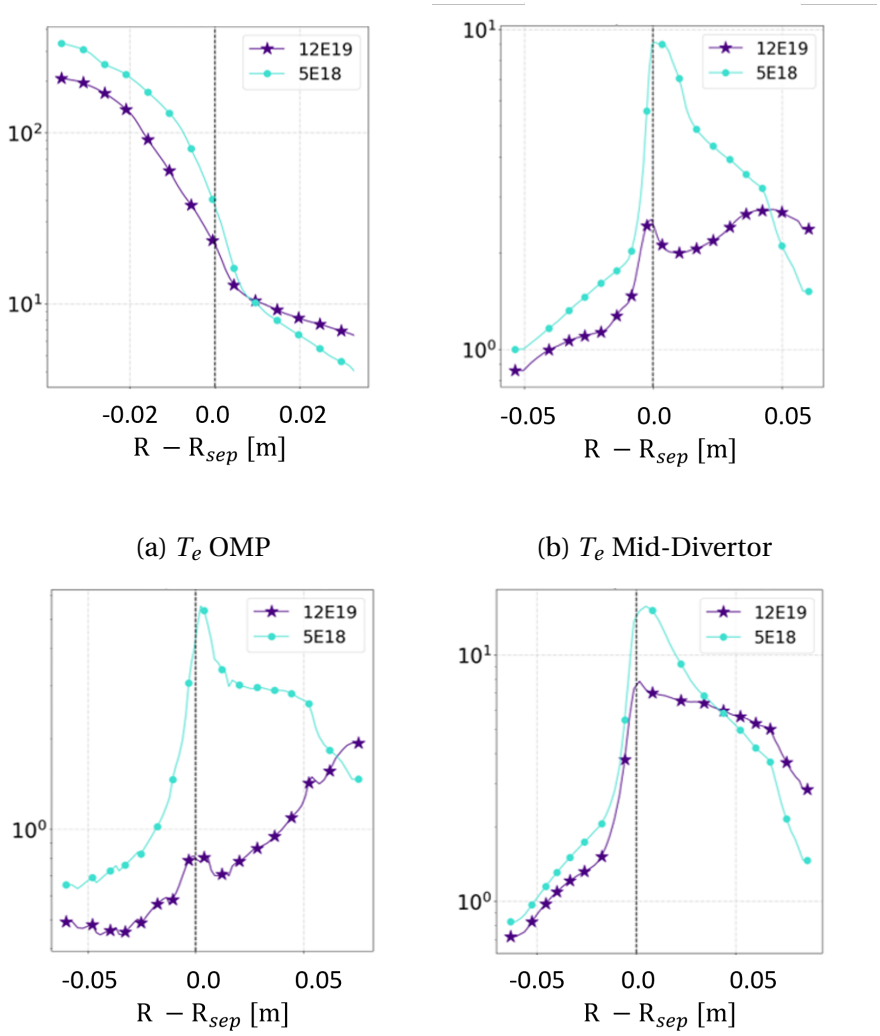

(a) T_e OMP

(b) T_e Mid-Divertor

(c) T_e Outer target

(d) T_e Inner target

Figure 4.24. – Radial profiles of the mean electron temperature T_e [eV], averaged in time t and toroidal position φ, for the two density cases $n_{e,sep} = 0.5 \times 10^{19}\mathrm{m}^{-3}$ (•) and $n_{e,sep} = 1.2 \times 10^{19}\mathrm{m}^{-3}$ (⋆) at the outer mid-plane, mid-divertor region, outer and inner targets. The horizontal axis corresponds to the radial distance to the separatrix after remapping along flux-surfaces to the outboard mid-plane.

case, the heat flux reaching the divertor has already been significantly dissipated by plasma-neutral interactions and cannot be fitted accurately with such function. Consequently, comparing the widths of the two cases based on this methodology is impractical. Therefore, as performed in Chapter 3, we will evaluate the heat flux decay length based on outboard mid-plane profiles. The flux is reconstructed via the proxy defined in Eq. 3.8 inspired from sheath boundary conditions on heat fluxes (Eq. 1.10

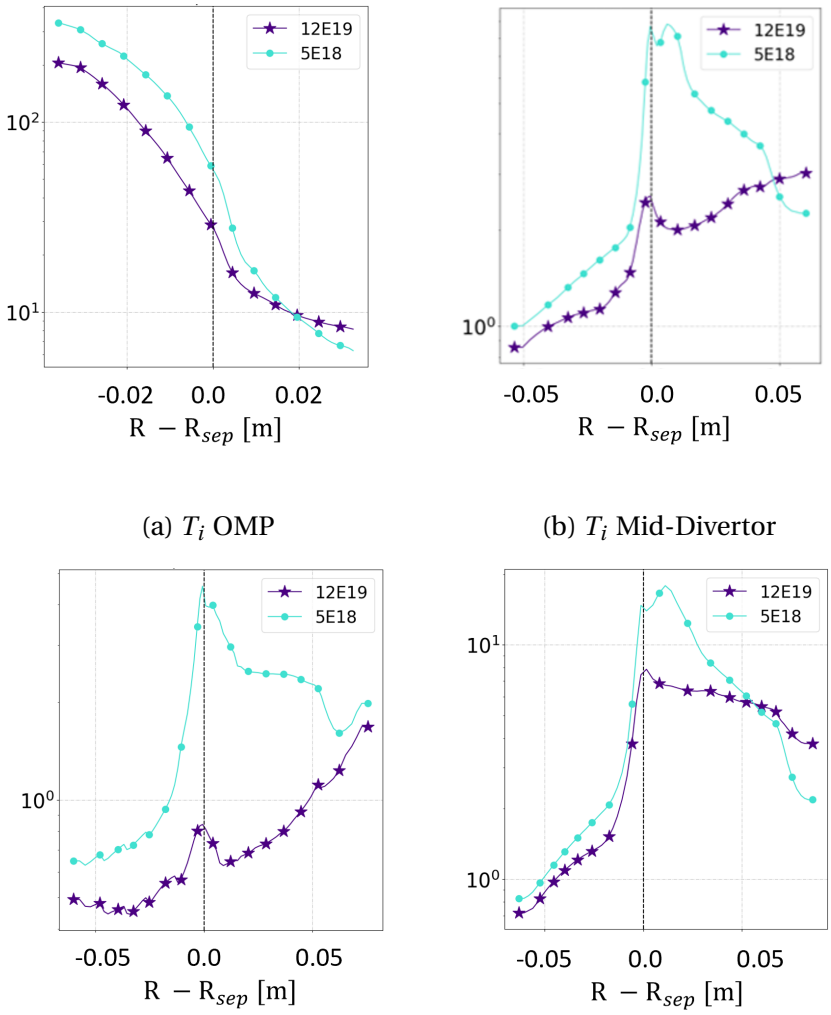

(a) T_i OMP

(b) T_i Mid-Divertor

(c) T_i Outer target

(d) T_i Inner target

Figure 4.25. – Radial profiles of the mean ion temperature T_i [eV] averaged in time t and toroidal position φ, for the two density cases $n_{e,sep} = 0.5 \times 10^{19}\text{m}^{-3}$ (•) and $n_{e,sep} = 1.2 \times 10^{19}\text{m}^{-3}$ (⋆) at the outer mid-plane, mid-divertor region, outer and inner targets. The horizontal axis corresponds to the radial distance to the separatrix after remapping along flux-surfaces to the outboard mid-plane.

and 1.11), on which we are going to apply a single- and double-exponential fits.

Before comparing the two turbulent cases, a primary investigation between the mean field simulations and the turbulent simulations has been conducted. Our goal here is to clearly separate effects related to the divertor geometry and a possible impact of neutrals on parallel transport from those related to transverse turbulent transport. Fig. 4.26 shows the radial profiles of the proxy parallel heat flux in the

outboard mid-plane. The left plot shows the output of mean-field simulations used as the initial conditions of our turbulent cases, the right plot shows the time- and toroidal-averaged data from the turbulence simulations. In both case, the low and the high density cases are compared.

There is a clear difference in the flux profiles for the turbulent cases compared to the mean field simulations. While the profiles in the mean-field simulations can be fitted accurately with a single-exponential decay, such fit are not appropriate for the 3D turbulence simulations which clearly exhibit two separate decay lengths in the near and far SOL. The latter could already be anticipated from the shape of density and temperature profiles in the mid-plane discussed above. This difference indicates that the existence of the double-decay length in turbulence simulations is not a direct effect of the parallel geometry nor of a change in the parallel transport due to plasma-neutral interactions in the divertor, but rather results from the spatial organization of turbulent transport.

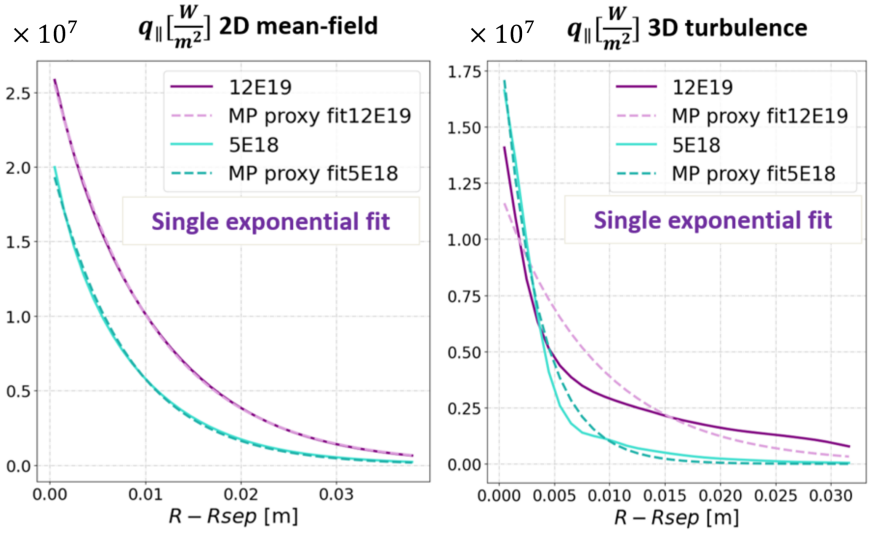

Figure 4.26. – Radial profiles of the proxy parallel heat flux (Eq. 3.8) in the outboard mid-plane. Left: from the 2D mean-field simulations used as initial conditions; right: from the time- and toroidal-averaged data from the 3D global turbulence simulations. Full lines are the actual data computed via Eq. 3.8 at the midplane while dashed lines are the result of a single exponential fit respectively for the mean-field cases and turbulent cases as defined in Eq. 3.9. Cyan lines are for the low density case $n_{sep} = 0.5 \times 10^{19}\mathrm{m}^{-3}$ and purple lines for the high density case $n_{sep} = 1.2 \times 10^{19}\mathrm{m}^{-3}$.

The fitting parameters for the single exponential fit, λ_q and q_{peak}, are given in Table 4.1 for the 2D mean-field simulations. One sees here that the change from attached to detached divertor conditions leads to a mild increase of the heat flux decay length by $\sim 30\%$. Since transverse perpendicular transport was prescribed by fixed and identical perpendicular diffusion coefficients in these simulations, this change can be interpreted as a measure of the effect the density regime has on other mechanisms at

play in setting the SOL width, in particular the parallel transport (advection flows or heat conduction). Such increase of the heat flux decay length purely due to parallel transport when moving from attached detached conditions has already been reported in mean-field ITER simulations (Rivals et al. 2022).

$n_{sep}[\mathbf{m}^{-3}]$	$\lambda_q[\mathbf{mm}]$	$q_{peak}[\frac{\mathbf{W}}{\mathbf{m}^2}]$
0.5×10^{19}	≈ 6	2.0×10^{7}
1.2×10^{19}	≈ 8	2.7×10^{7}

Table 4.1. – Single exponential fit parameters λ_q and q_{peak} for the 2D mean-field simulations at low and high separatrix density n_{sep}.

Figure 4.27 shows again the outer mid-plane profiles of the proxy heat flux obtained from the 2 turbulent simulations. This time, a double exponential fit as defined in Eq. 3.9 is used. One sees immediately that the match to the data is much better than with a single exponential decay. Table 4.2 gives the values of the fitting parameters. The first thing to note is the stark difference between the near and the far SOL width in both cases. In the low density case, the far SOL width $\lambda_{q,FAR}$ is about 2.5 times larger than the near SOL one. This ratio increases to a factor of 4 in the high density simulation. Comparing now the 2 density regimes, the detached case exhibits larger heat flux decay lengths both in the near and far SOL. The increase is moderate in the near SOL (about 65%) but reaches a factor of 2.7 for the far SOL width. One should note however that even the moderate increase in the near SOL is twice as large as the one observed in equivalent mean-field simulations, proving that a change of turbulent transport is at play. Another interesting point is the relative increase of $q_{peak,FAR}$ with respect to $q_{peak,NEAR}$. While in the attached case, $q_{peak,FAR}/q_{peak,NEAR} \approx 0.12$, this ratio increases to 0.21 in the detached case. This way, not only the far SOL decay length increases, but its relative amplitude also increases.

It is also noteworthy to point out that the transition point between the near SOL and the far SOL decay does not seem to depend significantly on the density regime. This suggests that more fundamental aspects, such as magnetic geometry, might be at play. One could for example think of the near SOL as being the characteristic width needed for SOL turbulence to develop after crossing the separatrix. The near SOL could then be interepreted as a limit layer between closed-field lines and open field-lines turbulence.

$n_{sep}[\mathbf{m}^{-3}]$	$\lambda_{q,NEAR}[\mathbf{mm}]$	$q_{peak,NEAR}[\frac{\mathbf{W}}{\mathbf{m}^2}]$	$\lambda_{q,FAR}[\mathbf{mm}]$	$q_{peak,FAR}[\frac{\mathbf{W}}{\mathbf{m}^2}]$
0.5×10^{19}	2.6	1.7×10^{7}	6.3	2×10^{6}
1.2×10^{19}	4.3	1.45×10^{7}	17	3.0×10^{6}

Table 4.2. – Values of λ_q and q_{peak} extracted from turbulent simulations via a double exponential fit

To conclude, our simulations demonstrate that moving from an attached to a detached divertor significantly increases the SOL heat flux decay lengths. This effect is

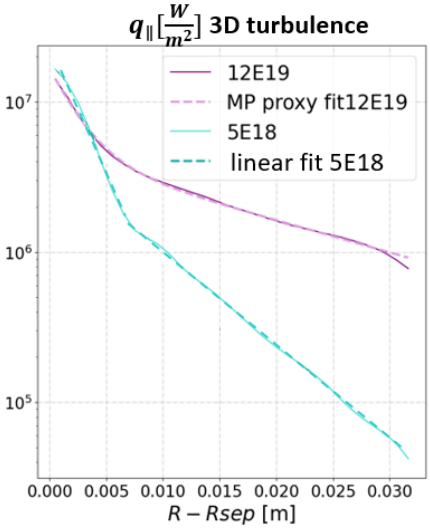

Figure 4.27. – Comparison between the proxy parallel energy flux (see Eq. 3.8) at the midplane averaged in time t and toroidal position φ for the low density case $n_{sep} = 0.5 \times 10^{19}\mathrm{m}^{-3}$ (turquoise) and for the high density case $n_{sep} = 1.2 \times 10^{19}\mathrm{m}^{-3}$ (magenta). Full lines are the actual data from the turbulent simulation while dashed lines are the result of the double-exponential fits (Eq. 3.9). Note the log scale for the y axis.

mainly due to changes reported earlier in turbulent transport since 2D mean-field simulations only recover a fraction of such increase. This way, the experimental trend of a widening of the SOL at high density regimes Wynn et al. 2018, Faitsch et al. 2021 is recovered and the fact that this can be related to turbulence confirmed.

4.6.2. Discussion: link with density shoulders

The existence of a clear inflection point in the SOL profiles of our turbulence simulations is reminiscent of the so-called shoulders reported in the literature (Carralero, Madsen, et al. 2017). In this section, we are going to take a closer look at possible analogies between our simulations and experimental results to assess to which point the phenomenology observed in the simulations can be related to the one observed in experiments.

Let us first discuss which of the density or/and temperature profiles is actually responsible for the presence of the shoulder on the parallel heat flux profiles. In the following, Fig. 4.28 and 4.29 respectively report the density and electron temperature profiles at the outboard mid-plane for the low and high density scenarios together with double-exponential fits. One can see that both the density and temperature profiles present an inflection point, in both the attached and the detached case. While the change of slope seems less marked at high density for the density, it seems to get more marked for the temperature. Table 4.3 gives the values of the near and far SOL decay lengths for both fields in the 2 simulations. All decay lengths increase when

moving from the attached to the detached plasma, by a factor ranging between 1.2 ($\lambda_{T,NEAR}$) and 2.7 ($\lambda_{N,NEAR}$). In the far SOL, the flattening of the temperature profile is the main contributor to the increase in $\lambda_{q,FAR}$, while in the near SOL it is the flattening of density profiles that is the dominant factor. The ratio of the far to near SOL decay lengths in the detached case is larger for the temperature but lower for the density. In agreement with the study conducted in Vianello, C. Tsui, et al. 2017 for TCV (L-mode), our simulations similarly exhibit that the process of shoulder formation take place in a frame where the increase of the density decay length in the near SOL is more marked than in the far SOL (in ibid., λ_N varied from 0.5 to 1 in their system of reference).

This way, the phenomenology observed in our simulations rather points to a smearing of the slope break on the density profiles and an amplification of it on the temperature profiles when increasing the density. This seems at odds with the measurements in JET that clearly indicate the formation of an inflection point at high density (Wynn et al. 2018). It is however in line with results from TCV (Stagni et al. 2022) (though in H-mode) or in ASDEX-U (Vianello, Carralero, et al. 2019) where a global flattening of the density profiles has been observed. Moreover, the fact that λ_T increases faster than λ_N is in agreement with trends observed in ASDEX-U (Grenfell, Manz, et al. 2022). One has here to point out that much less discussion can be found in the literature concerning the evolution of SOL temperature profiles in high density discharges than concerning density profiles, rendering more difficult any discussion on temperature profiles.

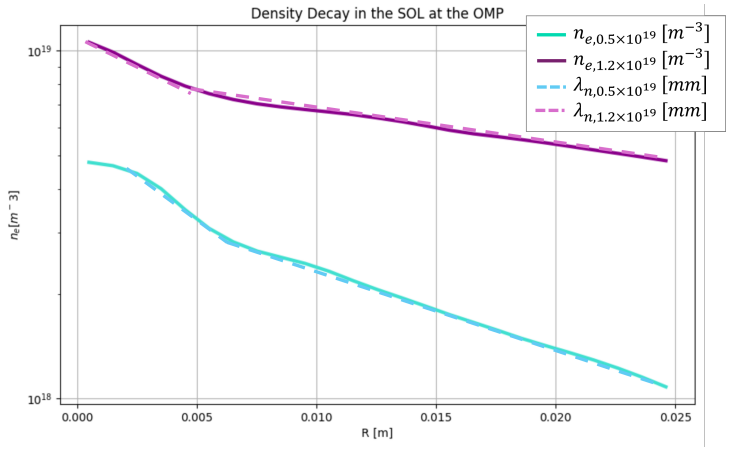

Figure 4.28. – Density decay length in the SOL at the outer midplane for the low $0.5 \times 10^{19}\mathrm{m}^{-3}$ and high $n_{sep} = 1.2 \times 10^{19}\mathrm{m}^{-3}$ density case.

$n_{sep}[\mathbf{m}^{-3}]$	$\lambda_{n,NEAR}[mm]$	$\lambda_{T,NEAR}[mm]$	$\lambda_{n,FAR}[mm]$	$\lambda_{T,FAR}[mm]$
0.5×10^{19}	4.4	6.1	14	22
1.2×10^{19}	12	7.7	26	42

Table 4.3. – Values of λ_n and λ_T for the low and high density case obtained via an exponential regression, in the near and in the far SOL at the OMP.

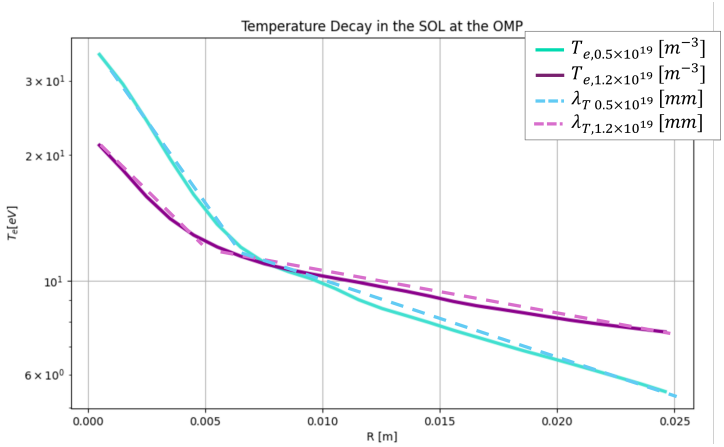

Figure 4.29. – Temperature decay length in the SOL at the outer midplane for the low $0.5\times10^{19}\mathrm{m}^{-3}$ and high $n_{sep}=1.2\times10^{19}\mathrm{m}^{-3}$ density case.

Overall, our results are qualitatively consistent with multi-machine experimental trends of the impact of high density discharges on SOL profiles and decay lengths. Since detailed phenomenology seems to be machine dependent and little published data is available on temperature profiles, it is however difficult to conclude further concerning the relevance of our simulations with respect to experiments. It is noteworthy however, that simulation point as much to the existence of a temperature shoulder as to the existence of a density shoulder. A direct comparison with the results from the TCV experiments for the pulses modelled here will shed more light on the question when the analyzed experimental data become available.

To go further into the comparison with experimental trends, we now discuss the correlation of the observed changes on profiles with the change in the SOL collisionality. Indeed, several experimental studies have highlighted a possible role of the divertor collisionality in determining SOL turbulence and eventually the formation of SOL shoulders (Carralero, Manz, et al. 2015, Vianello, Carralero, et al. 2019), even though others have suggested that other mechanisms might be at play (Wynn et al. 2018). The key control parameter identified in these studies is the effective divertor collisionality:

$$\Lambda_{div}=\frac{L_\parallel/c_s}{1/\nu_{ei}}\frac{\Omega_i}{\Omega_e}\propto n_e T_e^{-3/2}, \tag{4.3}$$

where n_e and T_e are usually measured in the divertor assuming that the divertor dominates the parallel integral of the collisionality. Since simulations offer a more detailed view of the plasma conditions along the poloidal direction than experiments, we also define a local dimensionless collisionality lineic density as follows $\frac{d}{dl}\Lambda_{div}$:

$$\frac{d}{dl}\Lambda_{div}=\frac{1/c_s}{1/\nu_{ei}}\frac{\Omega_i}{\Omega_e}\propto nT_e^{-3/2}, \tag{4.4}$$

and we will hereafter compute Λ_{div} as the parallel integral of this quantity rather than

only based on divertor values.

In Carralero, Manz, et al. 2015, a the threshold for the transition to shoulders has been identified as $\Lambda_{div} > 1$ at the midplane. In Wynn et al. 2018 however, this criterion is showed to be a necessary but not a sufficient condition for the existence of SOL shoulders. Fig. 4.30 shows the radial profiles of Λ_{div} in our simulations. Λ_{div} is larger at all radial positions in the detached case. The difference with the low density case reaches a factor of 30 at the separatrix before steadily going down to factor of 4 in the far SOL, most likely due to the flattening of the temperature profiles in the detached case. Λ_{div} is already larger than 1 in the whole SOL in the attached case so our density scan does not cover the experimentally observed threshold. One might be tempted to relate this to the fact that our simulations actually both show inflection points in SOL profiles and might both be beyond the density threshold for the appearance of shoulders. Running a lower density simulation would be necessary to explore further the role of the threshold. Finally, the curves do not exhibit specific features, such as the crossing of a specific value or a change of slope, at the position of the inflection points in the SOL profiles. This suggests that, even if the dimensionless collisionality plays a role in the widening of the SOL, its radial distribution cannot be directly related to the transition from near to far SOL profiles. One might speculate that the position of the inflection point is more related to a fundamental non-local property of edge plasma turbulence after crossing the separatrix rather than to local plasma conditions.

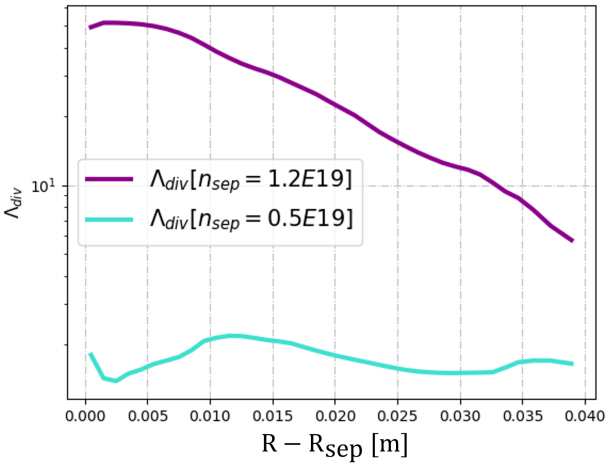

Figure 4.30. – Radial profiles of the effective collisionality $\Lambda_{div}[\mathrm{m}^{-1}]$ for $n_{sep} = 0.5 \times 10^{19}\mathrm{m}^{-3}$ and $n_{sep} = 1.2 \times 10^{19}\mathrm{m}^{-3}$.

4.7. Impact of density regime on turbulence driven transport

4.7.1. Anomalous transverse transport coefficients

Let us now evaluate the impact of the density regime on the anomalous transport coefficients, as we did in Section 3.3.6.2 for the study in circular limited configuration. For this purpose we reconstruct effective diffusion coefficients from the radial fluxes driven by the ExB velocity and fluctuations. $D_{\perp}^{\text{anom}}$ and $\chi_{\perp e}^{\text{anom}}$ are reconstructed following Eq. 3.12 and 3.13 respectively. In this chapter, we will additionally compute the ion transverse transport coefficient as follows:

$$\chi_{\perp i}^{\text{anom}} \equiv -\frac{\Gamma_{Ei}^{\psi,\text{anom}} - \frac{\epsilon_i}{n_i}\Gamma_n^{\psi,\text{anom}} - m_i u_{\parallel,i}\Gamma_{\Gamma}^{\psi,\text{anom}}}{n_i \vec{\nabla}\langle T_i\rangle_{t,\varphi}\cdot\vec{n}^{\psi}} \tag{4.5}$$

where $\Gamma_{\Gamma}^{\psi,\text{anom}}$ is the anomalous ExB radial parallel momentum flux.

Fig. 4.31 and 4.32 show the poloidal maps of the so-obtained diffusion coefficients, for the attached and the detached divertor case respectively. Fig. 4.33 and 4.34 show the same data using the same colorbars for the low and high density cases and cropped from negative values.

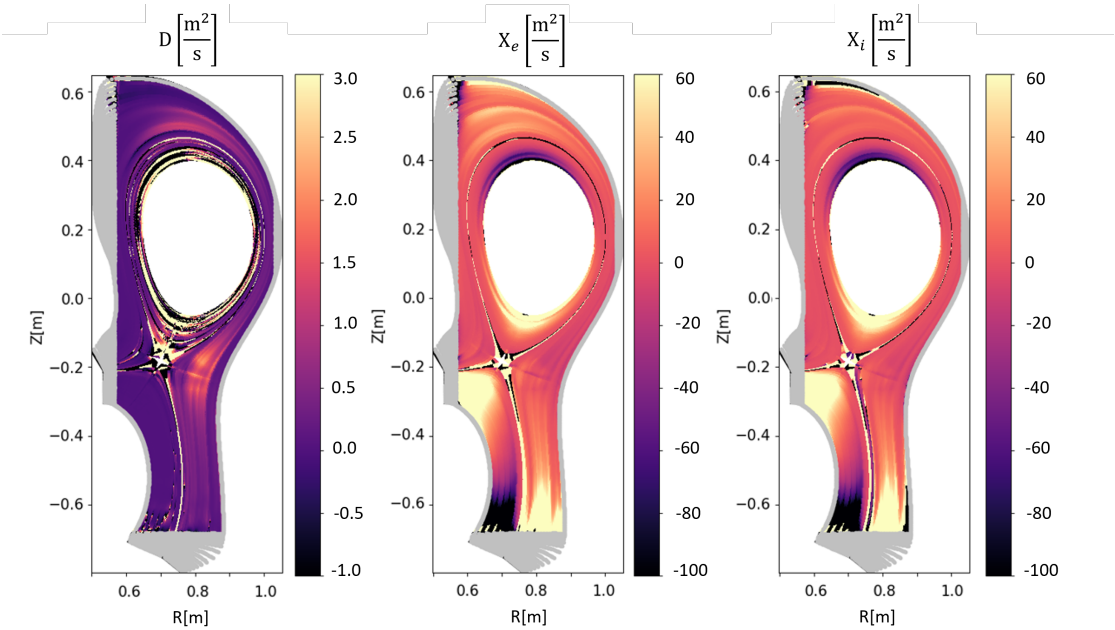

Figure 4.31. – Poloidal maps of reconstructed ExB anomalous transverse transport coefficients for particles, electron energy and ion energy (from left to right) for the attached case $n_{sep} = 0.5 \times 10^{19}\text{m}^{-3}$.

For the first analysis proposed in this thesis, we will focus solely on the transport coefficients in the main SOL. In particular, we will not focus on what happens inside

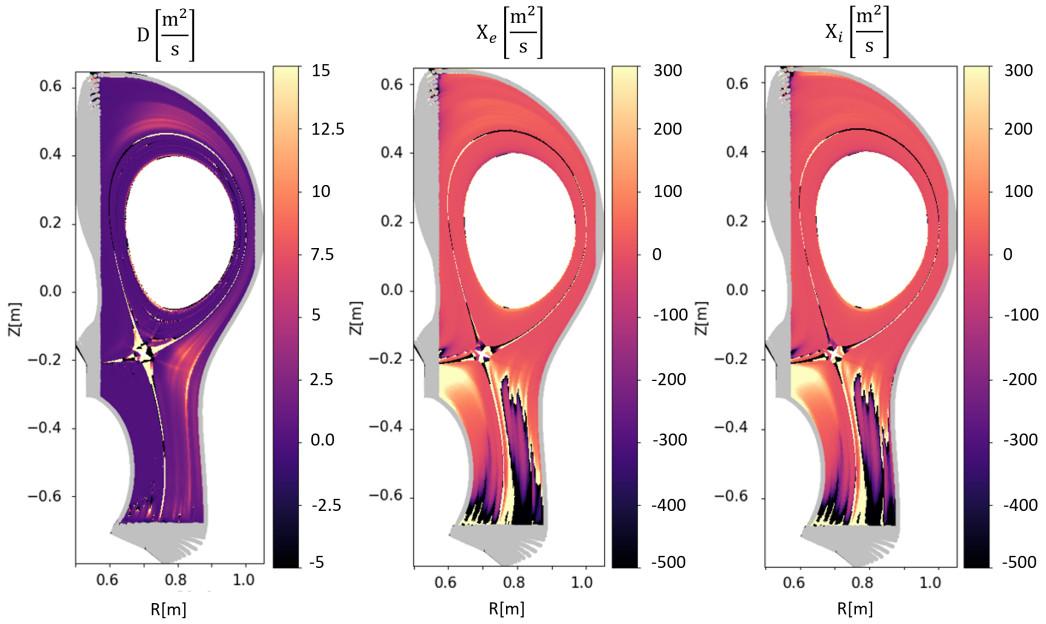

Figure 4.32. – Poloidal maps of reconstructed ExB anomalous transverse transport coefficients for particles, electron energy and ion energy (from left to right) for the detached case $n_{sep} = 1.2 \times 10^{19} \mathrm{m}^{-3}$.

the Private Flux Region nor inside the private flux region where complex structures emerge and would require dedicated analysis.

Let us first look at the particle transport coefficient. The attached and the detached cases exhibit extremely similar patterns in the SOL. In agreement with previous published studies with the TOKAM3X code (Galassi et al. 2017), the poloidal distribution is dominated by the combination of a ballooning structure (larger diffusion on the low field side of the machine) and a modulation with the local poloidal flux expansion. As suggested in Gallo et al. 2017, this leads to significant transport all along the outer divertor leg. However, the 2 cases differ strikingly concerning the amplitude of the transport coefficient, with the detached simulation showing 5 times larger particle diffusion than the attached one.

Things get more complex when looking at the heat transport coefficients. First of all, let us note that the electron and ion ones exhibit extremely similar structures and amplitudes so that we will speak indistinctively of the two. In the attached case, anomalous perpendicular heat diffusion also exhibits a ballooning pattern combined with a modulation with poloidal flux expansion. A striking difference with particle diffusion is that the heat transport coefficient increases to extremely large value when moving towards the outer target, reaching values larger than $60 m^2.s^{-1}$ at the target itself. It is common usage in mean-field simulations to adopt a particle heat diffusion coefficient twice as large as the particle diffusion coefficient. This assumption appears not valid at all from the output of our simulations. When moving to the detached case, a large amplitude structure still appears in the outer divertor leg, but this time with

negative values. This reversal of the sign is due to the fact that the anomalous ExB heat transport in the outer leg is still outwards in that region, but that temperature profiles exhibit a gradient reversal already seen in Fig. 4.24 and 4.25. This type of temperature gradient reversal is not uncommon in mean-field simulations in the presence of strong plasma-neutral interaction in the divertor, such as in ITER simulations, where plasma detaches in the near SOL while remaining attached in the far SOL (Rivals et al. 2022). What our turbulence simulations show however is that this is not accompanied by a reversal of the anomalous energy flux.

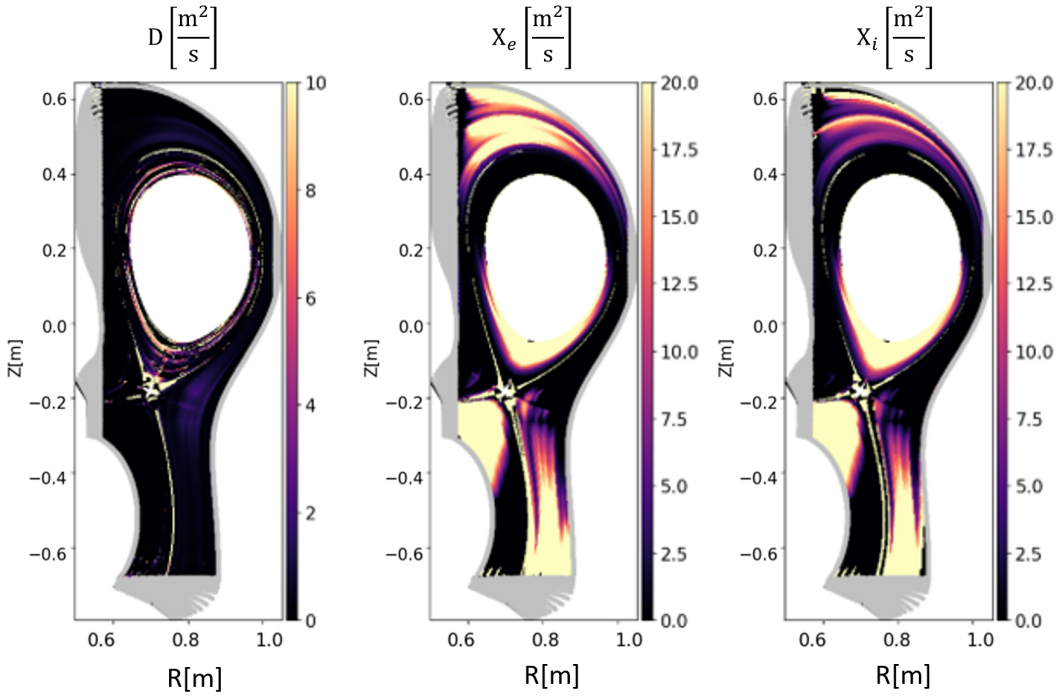

Figure 4.33. – Poloidal maps of reconstructed ExB anomalous transverse transport coefficients for particles, electron energy and ion energy (from left to right) for the attached case $n_{sep} = 0.5 \times 10^{19} \mathrm{m}^{-3}$. This figure shows the same data as Fig. 4.31 but with different colorbars shared with Fig. 4.34 to ease the comparison with the detached case.

This is an extremely problematic result for at least 3 reasons:

1. a negative diffusion coefficient is in practice impossible to implement in a mean-field code as this would lead immediately to an unstable behavior
2. more fundamentally, a negative diffusion coefficient goes against the second principle of physics, as it would lead to a local reduction of entropy
3. our result suggests a local decoupling of anomalous heat transport and temperature gradients, most likely explained by a non-local behavior of turbulent transport, contradicting the basic assumption behind the gradient-diffusion closure in mean-field codes

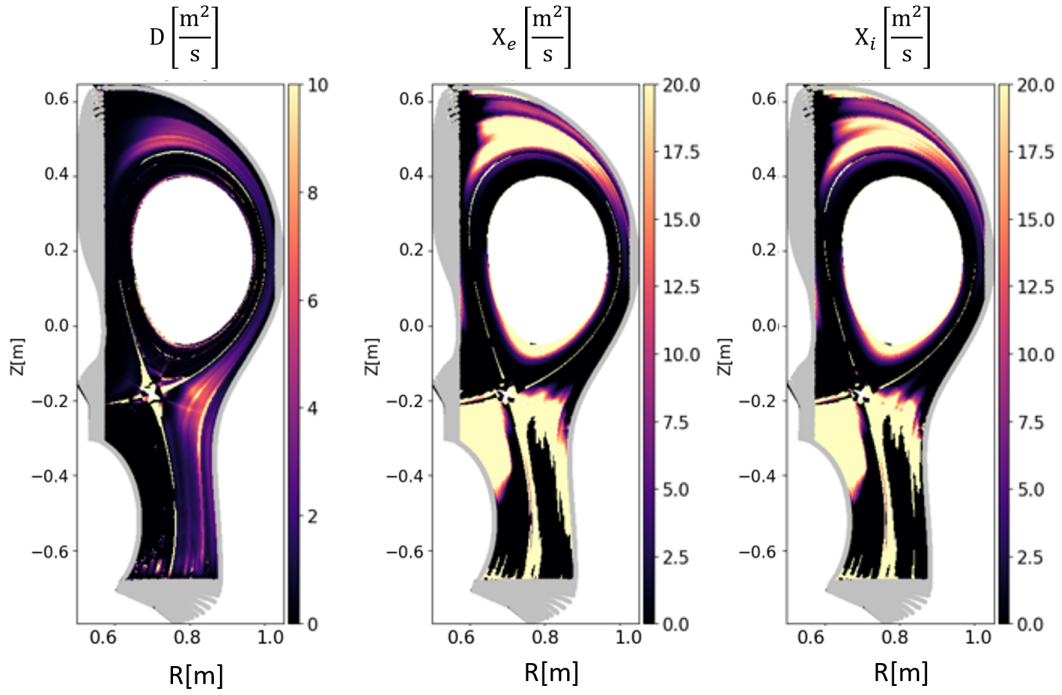

Figure 4.34. – Poloidal maps of reconstructed ExB anomalous transverse transport coefficients for particles, electron energy and ion energy (from left to right) for the detached case $n_{sep} = 1.2 \times 10^{19} \mathrm{m}^{-3}$. This figure shows the same data as Fig. 4.32 but with different colorbars shared with Fig. 4.33 to ease the comparison with the attached case.

Our simulations hence seem to highlight that the standard gradient-diffusion approach used in mean-field codes is not adapted for divertor conditions with strong localized interaction with neutrals. This result is reminiscent of the one already found in the previous chapter in the frame of circular limited plasmas, where negative transport coefficients were observed in the area of strong local interaction with the gas puff. It also raises a very fundamental question concerning the type of transport model that should be used in mean-field codes. In the next session, we open a discussion on possible alternate transport models and offer a preliminary assessment of their relevance in the conditions found in our simulations.

4.7.2. Discussion on alternate mean-field transport models

Edge turbulent transport has long been acknowledged as being of ballistic nature, with cohesive structures propagating radially over long distances in the SOL (Naulin 2007, Ghendrih, Sarazin, et al. 2003, Manz, Ribeiro, et al. 2015). It was often argued that this prevents the use of a gradient-diffusion description for transverse turbulent transport, although some studies have showed it is possible to partially reconcile both

descriptions (Manz, Hufnagel, et al. 2020).

In this section, we investigate two alternate descriptions of transverse transport for mean-field models and evaluate how well they compare to the data from our simulations. Both of the approaches we will address still rely on a local description of anomalous transport, i.e. on the idea that the flux at a given point in space is fully determined by the local values of plasmas quantities or their gradients. More complex non local models could eventually be proposed but are out of the scope of this manuscript. For each of these models, we are going to follow the same approach as above: 1- define the closure relation between anomalous transverse fluxes and plasma fields and gradients; 2- rebuild the free parameters of these closures based on our simulations data; 3- analyze the poloidal pattern of these parameters as well as their change when moving from attached to detached conditions. Our main criterion for the analysis of the results will be Ockham's razor: a simpler phenomenology void of obvious issues like negative diffusion coefficients will be considered as a hint for an improvement of the model.

4.7.2.1. Heuristic transport model

We start our discussion with a heuristic approach to the description of anomalous heat transport. The idea behind this model stems from 2 observations:

1. while the temperature gradients in the outer divertor leg get reversed in the detached case, the density gradient does not. The ratio of slopes is such that the radial pressure gradients actually remain negative, like in the attached case
2. some of the key instabilities in the SOL (interchange, drift-waves) are driven by the perpendicular pressure gradient rather than the perpendicular temperature gradient

This way, one can think of a model in which the non convective transverse anomalous transport of energy is driven locally proportional to the perpendicular pressure gradient rather than the perpendicular temperature gradient, i.e.:

$$\Gamma_n^{\psi,\text{anom}} \equiv -D_{\perp,P}^{\text{anom}} \vec{\nabla} \langle \left(p_e + p_i\right) \rangle_{t,\varphi} \cdot \vec{n}^{\psi} \tag{4.6}$$

$$\Gamma_{Ee}^{\psi,\text{anom}} - \frac{3}{2} T_e \Gamma_n^{\psi,\text{anom}} \equiv -\chi_{\perp e,P}^{\text{anom}} \vec{\nabla} \langle p_e \rangle_{t,\varphi} \cdot \vec{n}^{\psi} \tag{4.7}$$

$$\Gamma_{Ei}^{\psi,\text{anom}} - \frac{\epsilon_i}{n_i} \Gamma_n^{\psi,\text{anom}} - m_i u_{\parallel,i} \Gamma_{\Gamma}^{\psi,\text{anom}} \equiv -\chi_{\perp i,P}^{\text{anom}} \vec{\nabla} \langle p_i \rangle_{t,\varphi} \cdot \vec{n}^{\psi} \tag{4.8}$$

This model introduces 3 new parameters, $D_{\perp,P}^{\text{anom}}$, $\chi_{\perp e,P}^{\text{anom}}$ and $\chi_{\perp i,P}^{\text{anom}}$. Dimensionally-speaking, the first one is not a diffusion coefficient anymore, its unit in the SI system being $\frac{\text{m}^2}{\text{sJ}}$. The 2 latter are still diffusion coefficients.

The cross-field transport coefficients reconstructed from the turbulence data in our simulations are given in Fig. 4.35 for the attached divertor case and Fig. 4.36 for the detached case. The new transport coefficient for the density behaves relatively similarly to the one from the classic mean-field approach, with a clear ballooning

pattern combined with a modulation with the flux expansion. The main difference is the appearance of a new large amplitude structure when moving towards the target, due to the facts that the temperature is now accounted for in the gradient driving the flux and that it tends to decrease in proximity with the target. The detached case is associated with a strong increase up to 100% at the outer target in the mid SOL, in the amplitude of this transport coefficient. In the mid divertor region, the value of $D_{\perp,P}^{\text{anom}}$ for the detached case is found to be 40 times larger than the attached one. Turning to the heat transport coefficients, the key result is that none of the figures now exhibit any significant zone of negative value. Significant non convective heat transport is observed close to the targets with a pattern similar to what was observed on the perpendicular conduction coefficients of the classic gradient-diffusion model in the attached case (Fig. 4.31). The change of density regime from attached to detached outer target translates for these coefficients also into a significant increase by a factor of 3 typically.

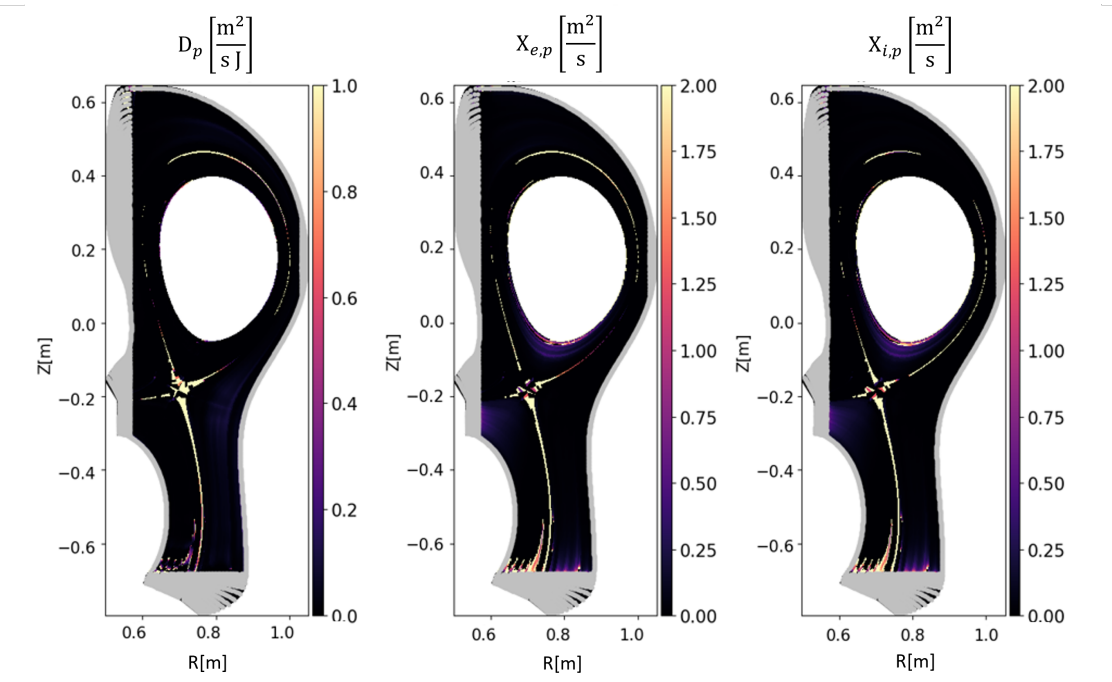

Figure 4.35. – Poloidal maps of transport coefficients for the heuristic mean-field transport model (Eq. 4.6 to 4.8), as reconstructed from turbulence data for the attached case $n_{sep} = 0.5 \times 10^{19} \text{m}^{-3}$.

The proposed heuristic mean-field transport model based on the pressure gradient as a drive for transverse anomalous transport hence seems to solve the main issue uncovered with the classic mean-field transport model in the detached case. It is also noteworthy that the poloidal pattern of transport coefficients remains similar when moving from the attached to the detached plasma, and that the main change between the 2 cases concerns the amplitude of the coefficients.

This model however suffers from a theoretical drawback. As we will discuss just

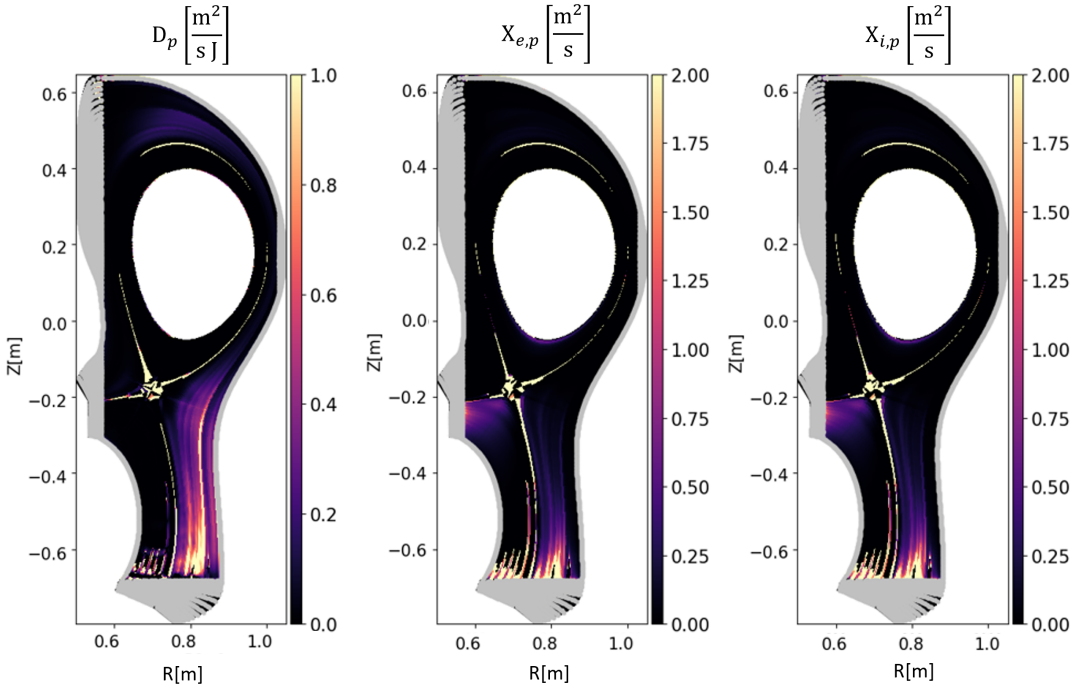

Figure 4.36. – Poloidal maps of transport coefficients for the heuristic mean-field transport model (Eq. 4.6 to 4.8), as reconstructed from turbulence data for the detached case $n_{sep} = 1.2 \times 10^{19} \mathrm{m}^{-3}$.

after, it does not respect a basic symmetry principle of turbulent transport models. For this purpose, we now inspect another alternate model inspired from core turbulent transport theory.

4.7.2.2. Model inspired from core transport modelling

It is standard in core transport modelling to assume that transverse particle and energy fluxes can be written in the following form:

$$\begin{bmatrix} \frac{\Gamma_n^{\psi,\mathrm{anom}}}{n_e} \\ \frac{\Gamma_{E\alpha}^{\psi,\mathrm{anom}}}{n_\alpha T_\alpha} \end{bmatrix} = - \begin{bmatrix} D_{nn} & D_{nT,\alpha} \\ D_{En,\alpha} & D_{ET,\alpha} \end{bmatrix} \begin{bmatrix} \frac{\vec{\nabla} n_e \cdot \vec{n}^\psi}{n_e} \\ \frac{\vec{\nabla} T_\alpha \cdot \vec{n}^\psi}{T_\alpha} \end{bmatrix} \tag{4.9}$$

where $\alpha = e$ or i is the considered particle species. In these expressions, we have omitted for simplicity the time and toroidal average operators that implicitly apply to all the plasma fields. Four transport parameters appear in the so-called transport matrix: D_{nn} and $D_{ET,\alpha}$ can be interpreted as the usual particle and heat diffusivity, while the non diagonal terms are the so-called thermodiffusion $D_{nT,\alpha}$ and the heat pinch $D_{En,\alpha}$.

Before moving further we need to insist that the model above is a simplified version of core turbulent transport models that can be found in the literature. The model

presented here can be refined further in different manners, for example by including considerations on the curvature of the magnetic field, see Angioni et al. 2009. These refinements however are out of the scope of the manuscript and would require a deeper analysis than what is proposed hereafter. Our point is only to touch upon the existence of these models and discuss their applicability to the data from our simulations in order to come up with possible recommendations for future studies.

Eq. 4.9 provides a generic framework (see Isichenko et al. 1997) in which both the classic gradient-diffusion mean-field approach and our heuristic model can be cast. The classic gradient-diffusion mean-field model corresponds to the following choices (here for electrons):

$$D_{nn} = D_{\perp}^{\text{anom}} \tag{4.10}$$
$$D_{nT,e} = 0 \tag{4.11}$$
$$D_{En,e} = \frac{3}{2} D_{\perp}^{\text{anom}} \tag{4.12}$$
$$D_{ET,e} = \chi_{\perp e}^{\text{anom}} \tag{4.13}$$

As for our heuristic model, it corresponds to the following choices:

$$D_{nn} = T_e D_{\perp,P}^{\text{anom}} \tag{4.14}$$
$$D_{nT,e} = T_e D_{\perp,P}^{\text{anom}} \tag{4.15}$$
$$D_{En,e} = D_{\perp,P}^{\text{anom}} + \chi_{\perp e,P}^{\text{anom}} \tag{4.16}$$
$$D_{ET,e} = D_{\perp,P}^{\text{anom}} + \chi_{\perp e,P}^{\text{anom}} \tag{4.17}$$

As mentioned earlier, none of these choices however respect a fundamental criterion to make the model consistent with fundamental symmetry principles. In the frame of the quasi-linear theory, and from the work of Baker et al. 2000, it can be shown that a symmetry constraint applies to the 4 transport coefficient, known as Onsager symmetry. Basically, it states that the transport matrix should be symmetric, i.e.

$$D_{nT,\alpha} = D_{En,\alpha} \tag{4.18}$$

If we impose this constraint, we are left with 3 unknown transport coefficients and 2 equations to determine them from the data. To determine uniquely the system, we are going to impose an additional constraint on the relative amplitude of some of the terms of the transport matrix. If one assumes that temperature and density fluctuations are in phase, a reasonable assumption in interchange dominated turbulence and actually consistent with fluctuations data in our simulations, it is possible in quasi-linear theory, see Samain et al. 1997, to show that $D_{ET,\alpha}/D_{nn} = \frac{3}{2}$. We are then left with only 2 unknown transport coefficients D_{nn} and $D_{nT,\alpha}$ that we can determine by solving the

following linear system:

$$\begin{bmatrix} \frac{\Gamma_n^{\psi,\text{anom}}}{n_e} \\ \frac{\Gamma_{E\alpha}^{\psi,\text{anom}}}{n_\alpha T_\alpha} \end{bmatrix} = - \begin{bmatrix} D_{nn} & D_{nT,\alpha} \\ D_{nT,\alpha} & \frac{3}{2} D_{nn} \end{bmatrix} \begin{bmatrix} \frac{\vec{\nabla} n_e \cdot \vec{n}^\psi}{n_e} \\ \frac{\vec{\nabla} T_\alpha \cdot \vec{n}^\psi}{T_\alpha} \end{bmatrix} \tag{4.19}$$

or expressed more explicitly as a function of the unknowns of interest:

$$\begin{bmatrix} \Gamma_n^{\psi,\text{anom}} \\ \Gamma_{E\alpha}^{\psi,\text{anom}} \end{bmatrix} = - \begin{bmatrix} \vec{\nabla} n_e \cdot \vec{n}^\psi & \frac{n_e}{T_\alpha} \vec{\nabla} T_\alpha \cdot \vec{n}^\psi \\ \frac{3}{2} n_e \vec{\nabla} T_\alpha \cdot \vec{n}^\psi & T_\alpha \vec{\nabla} n_e \cdot \vec{n}^\psi \end{bmatrix} \begin{bmatrix} D_{nn} \\ D_{nT,\alpha} \end{bmatrix} \tag{4.20}$$

where we assumed $n_e = n_\alpha$ for the simple plasma considered here.

For this preliminary assessment, we have focused exclusively on the electron transport. The similarity of ion temperature profiles and fluxes reported above in this chapter suggests that results apply also for ions[3].

Fig. 4.37 and 4.38 show the obtained poloidal maps for these transport coefficients in the low and high density case respectively. Like for the heuristic model driven by pressure gradients, the diffusion coefficients look better behaved than the ones obtained with the classic gradient-diffusion model: they are positive almost everywhere (except in the private flux region that we won't discuss here), and present a much smoother spatial distribution.

In the low density case, Fig. 4.37, the maps for D_{nn} and $D_{nT,e}$ show a relatively similar poloidal distribution, with enhanced transport at the top of the machine in the high flux expansion region and along the outer divertor leg where curvature is favourable. The latter tends to increase with the proximity to the target plates. $D_{nT,e}$ is typically found twice as large as D_{nn}. The presence of the poloidal cosine-like structure in the closed field lines region for D_{nn}, already seen in the reconstructed coefficients of the classic model, suggests some curvature-related contribution whose origin would need to be investigated further.

At high density, there is significant change in the two poloidal maps. $D_{nT,e}$ still exhibits the same 2 structures at the top of the machine and in the SOL of the outer divertor leg, but with increased amplitude compared with the low density case. The change in amplitude is different at the 2 locations: it reaches a factor of 5 in the divertor region while it only doubles at the top. The difference between the 2 density regimes is even more marked for D_{nn}. In particular, the enhanced transport region in the vicinity of the target plates vanishes and one is left only with transport in the high flux expansion areas at the top of the machine and on the low field side of the X-point. In these regions, the amplitude of D_{nn} is found slightly larger in the detached case,

3. The difference between the ion energy transport and the electron energy transport stems from the fact that ion energy also includes a kinetic energy component related to the flow velocity. Dealing with the later actually complexifies significantly the analysis of energy transport for ions as it requires one to take into account perpendicular transport or parallel momentum (see for example Eq. 3.13). In most of our domain however, the parallel Mach number of ions is small in front of 1. The only exception is the immediate vicinity of target plates. This way, assuming that ion energy transport and electron energy transport behave similarly is justified in the vast majority of the domain.

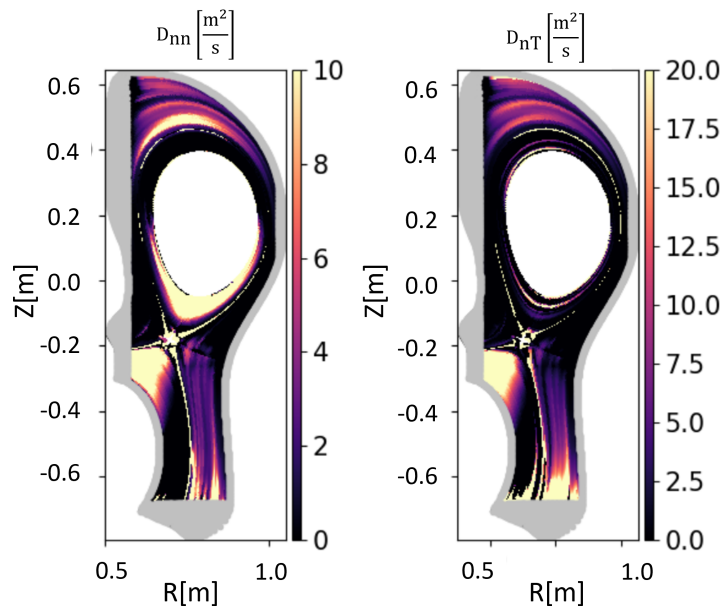

Figure 4.37. – Poloidal maps of the transport coefficients D_{nn} (left) and $D_{nT,e}$ (right) as defined in Eq. 4.20 for the attached case, $n_{sep} = 0.5 \times 10^{19}\mathrm{m}^{-3}$.

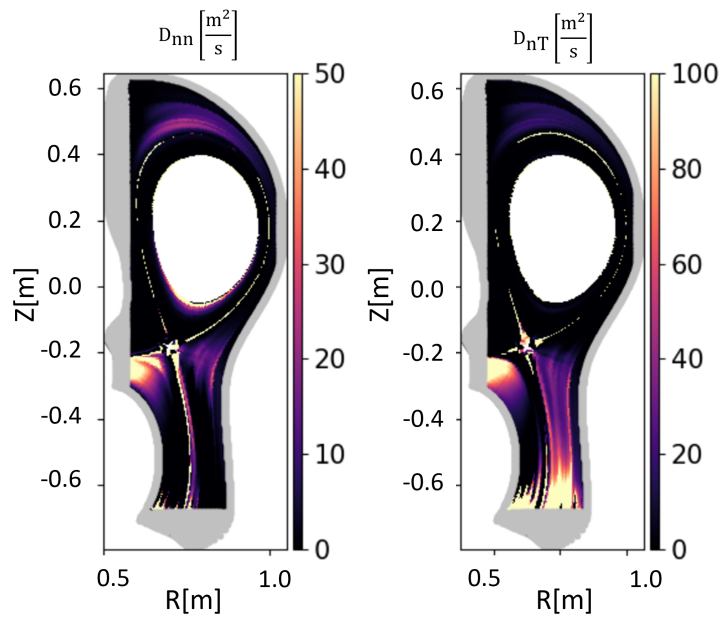

Figure 4.38. – Poloidal maps of the transport coefficients D_{nn} (left) and $D_{nT,e}$ (right) as defined in Eq. 4.20 for the detached case, $n_{sep} = 1.2 \times 10^{19}\mathrm{m}^{-3}$.

but far from the increase factors seen on $D_{nT,e}$.

This way, this alternate transport model suggests that the main effect of the change in density regime is the transition from a regime in which both diffusion and ther-

modiffusion/heat pinch play a role (at low density) to a situation where thermodiffusion/heat pinch become the dominant mechanisms. Whether this conclusion is a generic result or a specificity of the considered simulation would require deeper dedicated analysis of the turbulence phenomenology.

Overall, the preliminary analysis presented in this manuscript demonstrate a strong impact of the density regime on anomalous transport coefficients. Whatever the adopted mean-field transport model, two key trends emerge:

1. transport coefficients are far from uniform and exhibit a complex pattern combining an effect of ballooning, a modulation with flux expansion and a local effect in the divertor outer leg sometimes sensitive to the distance to the targets
2. transport coefficients tend to increase significantly (from a factor of 2 to a factor of 40) when moving from an attached to a detached regime, but the increase is not uniform in space and depends strongly on the adopted transport models

Moreover, the classic description of anomalous transport in mean-field models fails when applied to our detached case as it results in negative transverse heat conduction coefficients. The two alternate transverse anomalous transport closures that we have presented do not face the same issue and recover physically plausible transport coefficients. It is at this stage not possible to put forward one or the other as a recommendation for a better description, although the model inspired from core turbulent transport modelling has the advantage to respect fundamental symmetry principles. One would need to investigate a larger database of cases in different plasma conditions, on different machines and if possible different codes to discriminate the models.

Conclusion

The primary focus of this thesis has been to analyse and evaluate the response of turbulence in the edge plasma of tokamaks to plasma-neutrals interactions and recycling. For this purpose, we used the SOLEDGE3X drift-fluid edge turbulence code. Dedicated developments were made in the code to enable a self-consistent description of neutrals recycling in 3D turbulence simulations. Two routes were followed: an extension to 3D of the coupling to the Monte-Carlo kinetic neutrals code EIRENE and the implementation of an embedded fluid neutrals model. Due to technical limitations related to the memory usage of the EIRENE code, the first approach could eventually not be applied in production runs for 3D turbulence simulations at high resolution, in spite of being technically implemented. The fluid neutrals model however allowed us to capture qualitatively the first order physics at play in particle recycling and divertor density regimes.

Based on this numerical model, two separate studies have been performed: a first one in limited geometry discussing the primary impact of the neutrals recycling on the self-organization of edge plasma turbulence and the edge plasma equilibrium, and a second one in realistic diverted geometry offering an analysis of the impact of divertor regimes on edge turbulence transport. The latter is, to our knowledge, the first modelling of turbulence in detached conditions in real size diverted geometry with a 3D global first principle model.

This work has been centered around four key questions:

1. how does the localization of the particle source due to fuelling and recycling impact turbulent transport in the edge plasma?
2. can simulations reproduce a change in turbulent transport between low and high density regime? In particular:
   a) can one reproduce and explain the appearance of SOL shoulders?
   b) how does the SOL width respond to density regimes?
3. what recommendations can be made to mean-field codes to model this phenomenology?
4. does one need specific methodology to run turbulence simulations with self-consistent neutrals?

The results presented in this manuscript offer key insights for answering these questions, as well as perspectives for addressing them in future work.

The first question above was addressed in Chapter 3 through the analysis of 3D turbulent simulations in circular limited configuration. The choice of this idealized

academic geometry was made in order to isolate the lowest order effects related to neutrals recycling without the complexity of an X-point. Even in divertor machines, such geometry corresponds to the magnetic configuration used during the start-up phase of the plasma before the current gets ramped-up in the divertor coils to produce the X-point so the conclusions reached in that study actually apply to this phase of the plasma discharge. The study was performed by comparing a simulation without neutrals, in which the particle flux was driven from the center of the plasma, to a simulation driven by a gas puff and including self-consistent neutrals recycling.

Before analysing the impact of recycling, we first demonstrated that the presence of a toroidally localized gas puff can have a significant impact on the toroidal symmetry of the plasma and of turbulence properties. The perturbation induced by the neutral puff is mainly localized in the vicinity of the gas valve but also propagates along connected flux tubes. The distance of propagation is dependent on the considered field, being much larger for the temperature than for the density due to the difference in parallel transport mechanisms. Properties of turbulence fluctuations and the associated transport are also perturbed by the gas injection. These results raise questions concerning the analysis of gas puff imaging diagnostics which rely on the local injection of gas to increase their contrast. Answering them is however out of the scope of this manuscript and would require dedicated simulations and analysis. For what this manuscript was concerned, we further demonstrated that this loss of symmetry does not impede the aggregation of toroidal directions for the statistical analysis of fluctuation properties, as local perturbations exert only limited in toroidal averages.

The main outcome of our study is that the inclusion of self-consistent neutrals recycling in the model affects deeply both the plasma equilibrium and turbulence characteristics even in the low-recycling conditions considered in Chapter 3. In particular, one observed a reversal of density and temperature profiles in the closed flux surfaces region, with flat density and steep temperature profiles in the presence of neutrals while the opposite can be found when fuelling the discharge from the center. In the SOL, temperature profiles are little affected while density profiles present a significant flattening beyond some transition layer, reminiscent of experimental density shoulders. Fluctuation properties also exhibit profound and opposite changes, with a drop by a factor of 2 of the density relative fluctuation rate but a 3-fold increase of the electron temperature fluctuation rate in the outboard mid-plane. New poloidal asymmetries, complementary of the usual ballooning structure related to interchange turbulence, emerge due to the localized recycling source in the vicinity of the limiter plates. With or without neutrals, our simulations are characterized by different decay lengths for the heat flux in the near and in the far SOL. Neither the near SOL decay length nor the position of the inflection point were found to change significantly with neutrals recycling, but the far SOL widened by a factor of 2.4 due to the flattening of the density profiles. The reconstruction of mean-field transport coefficients from turbulence data shows that the transverse particle diffusion and heat conduction keep the same spatial distribution (mainly a ballooning structure with marked increase in the SOL) whether neutrals are included or not, but that the amplitude of the coeffi-

cients increases by 100% and 60% respectively. By the use of dedicated simulations with artificially large and fixed neutrals transport coefficients, we have demonstrate that all these effects can be explained by the change in localization of the particle source, forcing the plasma and turbulence to self-organize to decorrelate heat fluxes from particle fluxes, and not by some other effect related to the presence of neutrals themselves.

To investigate the impact of density regimes (Chapter 4) and answer questions 2 and 3, the choice was made to adopt a realistic divertor geometry that helps promoting dissipative processes due to plasma neutrals interactions. A TCV configuration was chosen in relation with on-going EUROfusion-led experiments so that these studies can be considered as a predictive modelling exercise in sight of future comparison with experimental results.

A preliminary study led with the code run in 2D mean-field mode demonstrated the possibility to access a detached divertor regime with the embedded fluid neutrals model in the density range observed in experiments. This also allowed us to assess the fidelity of the fluid neutrals model by comparing it to the results obtained with EIRENE and a much more advanced kinetic neutrals model (including for example molecules). One finds that the phenomenology captured by the fluid neutrals model is significantly different from the one observed with kinetic neutrals, especially concerning the peak particle flux at the outer target. The peak target electron temperature was also found systematically larger by a factor of 2 with the fluid neutrals than with EIRENE. One can hence conclude that the fluid neutrals model is not relevant for heat exhaust studies when prediction of the divertor state are the key issue. Nevertheless, key trends are recovered in terms of target density increase and temperature drop when the mid-plane density increases. More importantly for what concerns turbulence, the 2 models lead to very similar increases of the collisionallity and a qualitatively realistic localization of the particle source. Hence, for the purpose of the investigation of the impact of density regimes on edge turbulent transport, our fluid neutrals model provides a sufficient approximation of the effect of neutrals recycling on density regimes.

Two 3D turbulence simulations were then performed, one at low density with an attached outer divertor, one at high density in which the outer divertor target is detached. A key finding from these simulations is that the combination of the X-point configuration and of the localized presence of neutrals in the divertor leads to important poloidal asymmetries. Plasma equilibrium and turbulence properties depend strongly in both cases of the exact considered poloidal location and the impact of the divertor state is often different at different spatial positions, such as the outer mid-plane, the divertor legs or the target plates themselves. This has important implications for interpreting experimental data, as examining fluctuations at various locations (target, midplane, or X-point) yields different insights; thus, focusing solely on one location is inadequate. Our findings suggest the need for a multi-poloidal location analysis to determine whether distinct behaviors observed at different positions can be reproduced.

Overall, the transition from attached to detached regimes revealed substantial

changes in both global and local properties of plasma and turbulence. The detached case exhibits much lower temperature relative fluctuation levels almost everywhere in the domain while the density relative fluctuation level also decrease in most of the domain with the notable exception of the far SOL, particularly in the outer divertor. Intermittency of density fluctuations tends to increase in the divertor but decrease in the outer mid-plane, while it decreases at all point except in the immediate vicinity of the separatrix in the upstream SOL for the electron temperature. While the density is everywhere larger in the high density case (except at the outer target which is detached), the equilibrium temperature is lower in the closed field lines region and in the near SOL but is actually larger in the far SOL. This is due to a significant flattening of the temperature profiles beyond some inflection point in the outboard mid-plane in the detached case. The flattening is also visible on the density, here again reminiscent of experimental density shoulders. In the outer divertor leg, the equilibrium temperature profiles even reverse due to the local energy losses associated with divertor physics.

As a consequence, one finds that detachment leads to an increase of both the near SOL and far SOL heat flux decay lengths by a factor of about 1.6 in the near SOL, and of about 2.7 in the far. Hence, our simulations seem to be able to recover the main trend observed in experiments of a widening of the SOL, with larger impact on the far SOL than on the near SOL beyond some inflection point in the profiles. The link with density shoulders as they are reported in the litterature though is not so clear yet and would need to be analyzed more deeply. First, our simulations exhibit the flattening both on the density and temperature profiles, not only the density; second, no clear correlation is observed with the normalized collisionality identified by Carralero, S. Artene, et al. 2018 as a key parameter.

Coming to the third key question, we finally reconstructed mean-field transport coefficients from our turbulence simulations. Whatever the considered density regime, one finds that perpendicular diffusion coefficients are poloidally non-uniform with a marked ballooning structure combined with a modulation associated with local flux-expansion. This result is in-line with previous studies performed with the TOKAM3X code and found in the literature. Detachment leads to a large increase of the particle diffusion coefficient by up to a factor of 5 compared with the attached case. However, it also leads to the transverse heat conductivity becoming negative in the outer divertor legs region, due to the reversal of the temperature gradient there while the turbulent heat flux remains outwards. This result is consistent with what was observed on a smaller scale in the limited case in the vicinity of the gas puff: in the presence of significant local perturbations to the plasma related to neutrals, transport coefficients are significantly impacted and can even become negative. Such result actually raises fundamental questions about the validity of the standard gradient-diffusion description of anomalous transverse transport in mean-field codes as perpendicular anomalous heat transport can be locally decoupled from the gradient. A negative diffusion coefficient is both impossible to implement in a code (for stability reasons) and nonphysical as it goes against the second principle of thermodynamics. We proposed in this manuscript several routes to solve this inconsistency, one heuristic and another

one based on analogies with core plasma transport theory. Both result in transport coefficients with a more physical behavior, i.e. without spatial discontinuities nor negative values. Further studies and simulations would be necessary to discriminate between them and come up with final recommendations to the mean-field community.

Finally let us mention that the work done for this thesis has provided us with a first feedback concerning the answer to the last key question on the methodology to run turbulence simulations with self-consistent neutrals. The addition of self-consistent recycling in the model changes fundamentally the particle and energy balance of the system. It leads to the appearance of additional long time scales for the achievement of a meaningful steady-state in which energy input is balanced by radiation losses and plasma energy losses at the target, and gas puff is balanced by pumping. This additional time scale, already known in mean-field simulations, can exceed several 100 ms in large machines and is a major issue for global turbulence simulations which cannot currently cover a long enough time range to get to convergence with available computing resources. We showed in this thesis, that some key plasma quantities can still evolve on these long time scales so that one must take great care not to over-interpret the results of simulations that have not run up to full convergence. A possible option to shorten the time needed to get to steady-state was explored in this thesis by using converged 2D mean-field simulations as an initial condition for the 3D turbulence ones. This allowed us to gain a factor of 2 on the imbalance between in- and out-fluxes compared to a simulation started from a naive arbitrary initial condition. However, this was still not sufficient to push our simulations to convergence in a reasonable amount of time. The critical point with this method is the choice of the mean-field transport coefficients for the initial mean-field run. Using an iterative approach, in which the output of a previous turbulence simulation is used to define the mean-field diffusion coefficients could allow one to cut further on the convergence time scale and should be explored in the future.

Overall, the analyses presented is this thesis have allowed us to answer the 4 initial key questions asked at the beginning of this manuscript. They have also raised several questions that will need to be addressed in the near future. One should however keep in mind that the results presented here rely on a handful of global turbulence simulations only. The edge turbulence community has seen in the last few years several codes access to the capability of running simulations with self-consistent neutrals physics. In the light of the major implications this has for the physics at play and the potential consequences for the mean-field modeling of heat exhaust issues, it is necessary to construct an exhaustive database of global turbulence simulations involving neutrals physics, covering a wider range of geometries, density regimes and involving different codes to exclude possible biases due to numerical discretization or approximations in the models. Eventually, the analysis of these simulations in terms of mean-field transport coefficients should become systematic in order to come up with a consensus on the recommendations to make to the mean-field modeling community. A direct comparison to experimental results is also a mandatory step to

gain confidence in the relevance of the phenomenology uncovered by the simulations. The choice of an experimental configuration and conditions for the TCV simulations presented in this thesis is a step in this direction that will need to be completed once experimental data is becomes fully available. Similar validation exercises will also have to be carried out in other machines to disentangle machine specific results from generic trends.

Bibliography

[MD24] D. "Mancini and D. S." De Oliveira. *TCV-X23 Data*. 2024. URL: https://indico.euro-fusion.org/event/2947/contributions/12666/attachments/5972/10495/TCVX23ManciniSales_TSVV3_10Jul24.pdf (cit. on pp. 139, 141).

[Ang+09] C. Angioni, E. Fable, M. Greenwald, et al. "Particle transport in tokamak plasmas, theory and experiment". In: *Plasma Physics and Controlled Fusion* 51.12 (2009), p. 124017 (cit. on p. 181).

[ABS02] R. Aymar, P. Barabaschi, and Y. Shimomura. "The ITER design". In: *Plasma physics and controlled fusion* 44.5 (2002), p. 519 (cit. on p. 58).

[Bak+00] D.R. Baker, M.R. Wade, C.C. Petty, et al. "Particle transport phenomena in the DIII-D tokamak". In: *Nuclear Fusion* 40.5 (2000), p. 1003 (cit. on p. 181).

[Bra65] S.I. Braginskii. "Transport processes in a plasma". In: *Reviews of plasma physics* 1 (1965), p. 205 (cit. on p. 71).

[Buf23] H. Bufferand. *Global 3D full-scale turbulence simulations of TCV-X21 experiments with SOLEDGE3X*. Communication in plasma edge theory in fusion devices (PET-19). 2023 (cit. on p. 81).

[Buf+22] H. Bufferand, J. Balbin, S. Baschetti, et al. "Implementation of multi-component Zhdanov closure in SOLEDGE3X". In: *Plasma Physics and Controlled Fusion* 64.5 (2022), p. 055001 (cit. on pp. 73, 75).

[Buf+17] H. Bufferand, C. Baudoin, J. Bucalossi, et al. "Implementation of drift velocities and currents in SOLEDGE2D–EIRENE". In: *Nuclear Materials and Energy* 12 (2017), pp. 852–857 (cit. on p. 77).

[Buf+21] H. Bufferand, J. Bucalossi, G. Ciraolo, et al. "Progress in edge plasma turbulence modelling—hierarchy of models from 2D transport application to 3D fluid simulations in realistic tokamak geometry". In: *Nuclear Fusion* 61.11 (Oct. 2021), p. 116052. DOI: 10.1088/1741-4326/ac2873. URL: https://dx.doi.org/10.1088/1741-4326/ac2873 (cit. on pp. 64, 73, 74).

[Buf+15] H. Bufferand, G. Ciraolo, Y. Marandet, et al. "Numerical modelling for divertor design of the WEST device with a focus on plasma–wall interactions". In: *Nuclear Fusion* 55.5 (2015), p. 053025 (cit. on pp. 74, 78, 79).

[Car+18] D. Carralero, S. Artene, M. Bernert, et al. "On the role of filaments in perpendicular heat transport at the scrape-off layer". In: *Nuclear Fusion* 58.9 (2018), p. 096015 (cit. on pp. 16, 188).

[Car+17] D. Carralero, J. Madsen, S.A. Artene, et al. "A study on the density shoulder formation in the SOL of H-mode plasmas". In: *Nuclear Materials and Energy* 12 (2017), pp. 1189–1193 (cit. on p. 170).

[Car+15a] D. Carralero, P. Manz, L. Aho-Mantila, et al. "Experimental validation of a filament transport model in turbulent magnetized plasmas". In: *Physical review letters* 115.21 (2015), p. 215002 (cit. on pp. 62, 172, 173).

[Car+15b] D. Carralero, H.W. Müller, M. Groth, et al. "Implications of high density operation on SOL transport: A multimachine investigation". In: *Journal of Nuclear Materials* 463 (2015), pp. 123–127 (cit. on p. 62).

[CKW04] C. S. Chang, S. Ku, and H. Weitzner. "Numerical study of neoclassical plasma pedestal in a tokamak geometry". In: *Physics of Plasmas* 11.5 (May 2004), pp. 2649–2667. ISSN: 1070-664X. DOI: 10.1063/1.1707024. eprint: https://pubs.aip.org/aip/pop/article-pdf/11/5/2649/19290044/2649_1_online.pdf. URL: https://doi.org/10.1063/1.1707024 (cit. on p. 68).

[Cho05] R. Chodura. "Limiting boundary conditions of a plasma fluid at an absorbing target". In: *Physics of plasmas* 12.1 (2005) (cit. on p. 49).

[CR22a] A. Coroado and P. Ricci. "A self-consistent multi-component model of plasma turbulence and kinetic neutral dynamics for the simulation of the tokamak boundary". In: *Nuclear Fusion* 62.3 (2022), p. 036015 (cit. on p. 86).

[CR22b] A. Coroado and P. Ricci. "Numerical simulations of gas puff imaging using a multi-component model of the neutral–plasma interaction in the tokamak boundary". In: *Physics of Plasmas* 29.3 (2022) (cit. on p. 110).

[De +21] H De Oliveira, C Theiler, H Elaian, et al. "A fast-reciprocating probe array for two-dimensional measurements in the divertor region of the tokamak à configuration variable". In: *Review of Scientific Instruments* 92.4 (2021) (cit. on p. 141).

[Dif+22] G. Dif-Pradalier, Ph. Ghendrih, Y. Sarazin, et al. "Transport barrier onset and edge turbulence shortfall in fusion plasmas". In: *Communications Physics* 5.1 (2022), p. 229 (cit. on p. 68).

[Dif+11] G. Dif-Pradalier, J. Gunn, G. Ciraolo, et al. "The Mistral base case to validate kinetic and fluid turbulence transport codes of the edge and SOL plasmas". In: *Journal of nuclear materials* 415.1 (2011), S597–S600 (cit. on p. 79).

[Dud+15] B. D. Dudson, A. Allen, G. Breyiannis, et al. "BOUT++: Recent and current developments". In: *Journal of Plasma Physics* 81.1 (2015), p. 365810104. DOI: 10.1017/S0022377814000816 (cit. on p. 64).

[Dud+08] B.D. Dudson, N. B. Ayed, A. Kirk, et al. “Experiments and simulation of edge turbulence and filaments in MAST”. In: *Plasma Physics and Controlled Fusion* 50.12 (2008), p. 124012 (cit. on p. 162).

[Dud+09] B.D. Dudson, M.V. Umansky, X.Q. Xu, et al. “BOUT++: A framework for parallel plasma fluid simulations”. In: *Computer Physics Communications* 180.9 (2009), pp. 1467–1480. ISSN: 0010-4655. DOI: https://doi.org/10.1016/j.cpc.2009.03.008. URL: https://www.sciencedirect.com/science/article/pii/S0010465509001040 (cit. on p. 64).

[Dül+24] R. Düll, H. Bufferand, E. Serre, et al. “Introducing electromagnetic effects in Soledge3X”. In: *Contributions to Plasma Physics* (2024), e202300147 (cit. on p. 74).

[Duv+24] BP Duval, A Abdolmaleki, M Agostini, et al. “Experimental research on the TCV tokamak”. In: *Nuclear Fusion* 64.11 (2024), p. 112023 (cit. on p. 139).

[Edd79] A. S. Eddington. *45. The Internal Constitution of the Stars*. Ed. by Kenneth R. Lang and Owen Gingerich. Cambridge, MA and London, England: Harvard University Press, 1979, pp. 281–290. ISBN: 9780674366688. DOI: doi:10.4159/harvard.9780674366688.c50. URL: https://doi.org/10.4159/harvard.9780674366688.c50 (cit. on p. 40).

[Ede+22] K. Eder, A. Stegmeir, W. Zholobenko, et al. “Self-consistent neutral gas description in the edge turbulence fluid code GRILLIX”. In: *86. Jahrestagung der DPG und DPG-Frühjahrstagung der Sektion Materie und Kosmos (SMuK)*. DPG. 2022 (cit. on p. 150).

[Eic+20] T. Eich, P. Manz, R.J. Goldston, et al. “Turbulence driven widening of the near-SOL power width in ASDEX Upgrade H-Mode discharges”. In: *Nuclear Fusion* 60.5 (Apr. 2020), p. 056016. DOI: 10.1088/1741-4326/ab7a66. URL: https://dx.doi.org/10.1088/1741-4326/ab7a66 (cit. on pp. 51, 52, 58, 60, 61, 165).

[EPF21] EPFL/SPC. *Repository GitHub SPC Data TCV-X21*. 2021. URL: https://github.com/SPCData/TCV-X21 (cit. on p. 139).

[Fai+21] M. Faitsch, T. Eich, G.F. Harrer, et al. “Broadening of the power fall-off length in a high density, high confinement H-mode regime in ASDEX Upgrade”. In: *Nuclear Materials and Energy* 26 (2021), p. 100890 (cit. on p. 170).

[Fan+19] D.M. Fan, Y. Marandet, P. Tamain, et al. “Effect of turbulent fluctuations on neutral particles transport with the TOKAM3X-EIRENE turbulence code”. In: *Nuclear Materials and Energy* 18 (2019), pp. 105–110. ISSN: 2352-1791. DOI: https://doi.org/10.1016/j.nme.2018.12.011. URL: https://www.sciencedirect.com/science/article/pii/S2352179118301200 (cit. on pp. 84, 115).

[Fed+17] N. Fedorczak, J.P. Gunn, N. Nace, et al. "Width of turbulent SOL in circular plasmas: a theoretical model validated on experiments in Tore Supra tokamak". In: *Nuclear Materials and Energy* 12 (2017), pp. 838–843 (cit. on p. 58).

[Fed+12] N. Fedorczak, J.P. Gunn, J-Y. Pascal, et al. "Electrostatic transport in L-mode scrape-off layer plasmas of Tore Supra tokamak. II. Transport by fluctuations". In: *Physics of Plasmas* 19.7 (2012) (cit. on pp. 58, 59).

[Fév+21] O. Février, H. Reimerdes, C. Theiler, et al. "Divertor closure effects on the TCV boundary plasma". In: *Nuclear Materials and Energy* 27 (2021), p. 100977 (cit. on p. 141).

[FS03] W. Fundamenski and S. Sipilä. "Classical vs. Anomalous SOL Transport in JET ELMy H-modes". In: *30th EPS Conference on Controlled Fusion and Plasma Physics, St. Petersburg, Russia, July 7-11, 2003*. European Physical Society (EPS). 2003, O–4 (cit. on pp. 58, 59).

[Gal+17a] D. Galassi, P. Tamain, H. Bufferand, et al. "Drive of parallel flows by turbulence and large-scale E× B transverse transport in divertor geometry". In: *Nuclear Fusion* 57.3 (2017), p. 036029 (cit. on p. 175).

[Gal+17b] A. Gallo, N. Fedorczak, S. Elmore, et al. "Impact of the plasma geometry on divertor power exhaust: experimental evidence from TCV and simulations with SolEdge2D and TOKAM3X". In: *Plasma Physics and Controlled Fusion* 60.1 (2017), p. 014007 (cit. on p. 175).

[Gar+04] O.E. Garcia, V. Naulin, A.H. Nielsen, et al. "Computations of intermittent transport in scrape-off layer plasmas". In: *Physical review letters* 92.16 (2004), p. 165003 (cit. on p. 64).

[Ghe+22] Ph. Ghendrih, G. Dif-Pradalier, O. Panico, et al. "Role of avalanche transport in competing drift wave and interchange turbulence". In: *Journal of Physics: Conference Series*. Vol. 2397. 1. IOP Publishing. 2022, p. 012018 (cit. on p. 59).

[Ghe+03] Ph. Ghendrih, Y. Sarazin, G. Attuel, et al. "Theoretical analysis of the influence of external biasing on long range turbulent transport in the scrape-off layer". In: *Nuclear fusion* 43.10 (2003), p. 1013 (cit. on p. 177).

[GR20] M. Giacomin and P. Ricci. "Investigation of turbulent transport regimes in the tokamak edge by using two-fluid simulations". In: *Journal of Plasma Physics* 86.5 (2020), p. 905860502 (cit. on p. 58).

[Gia+22] M. Giacomin, P. Ricci, A. Coroado, et al. "The GBS code for the self-consistent simulation of plasma turbulence and kinetic neutral dynamics in the tokamak boundary". In: *Journal of Computational Physics* 463 (2022), p. 111294 (cit. on p. 63).

[Gol61] J. Goldstone. "Field theories with ' Superconductor ' solutions". In: *Il Nuovo Cimento (1955-1965)* 19 (1961). DOI: 10.1007/BF02812722 (cit. on pp. 58, 59).

[Gör+11] T. Görler, X. Lapillonne, S. Brunner, et al. "The global version of the gyrokinetic turbulence code GENE". In: *Journal of Computational Physics* 230.18 (2011), pp. 7053–7071. ISSN: 0021-9991. DOI: https://doi.org/10.1016/j.jcp.2011.05.034. URL: https://www.sciencedirect.com/science/article/pii/S0021999111003457 (cit. on p. 68).

[Gre+22] G. Grenfell, P. Manz, G.D. Conway, et al. "Turbulence in the near scrape-off layer towards the L-mode density limit in ASDEX-Upgrade". In: *Nuclear Materials and Energy* 33 (2022), p. 101277 (cit. on p. 171).

[Gre+20] G. Grenfell, M. Spolaore, D. Abate, et al. "Turbulent filament properties in L and H-mode regime in the RFX-mod operating as a tokamak". In: *Nuclear Fusion* 60.12 (2020), p. 126006 (cit. on p. 60).

[Hal+16] F.D. Halpern, P. Ricci, S. Jolliet, et al. "The GBS code for tokamak scrape-off layer simulations". In: *Journal of Computational Physics* 315 (2016), pp. 388–408. ISSN: 0021-9991. DOI: https://doi.org/10.1016/j.jcp.2016.03.040. URL: https://www.sciencedirect.com/science/article/pii/S0021999116001923 (cit. on p. 64).

[Har+17] J.R. Harrison, W.A.J. Vijvers, C. Theiler, et al. "Detachment evolution on the TCV tokamak". In: *Nuclear Materials and Energy* 12 (2017), pp. 1071–1076 (cit. on p. 153).

[HS21] A. Hassanein and V. Sizyuk. "Potential design problems for ITER fusion device". In: *Scientific Reports* 11.1 (2021), p. 2069 (cit. on p. 47).

[Hel12] P. Helander. "Classical and neoclassical transport in tokamaks". In: *Fusion Science and Technology* 61.2T (2012), pp. 133–141 (cit. on p. 59).

[HH76] F. L. Hinton and R. D. Hazeltine. "Theory of plasma transport in toroidal confinement systems". In: *Rev. Mod. Phys.* 48 (2 Apr. 1976), pp. 239–308. DOI: 10.1103/RevModPhys.48.239. URL: https://link.aps.org/doi/10.1103/RevModPhys.48.239 (cit. on p. 58).

[HSB17] N. Horsten, G. Samaey, and M. Baelmans. "Development and assessment of 2D fluid neutral models that include atomic databases and a microscopic reflection model". In: *Nuclear Fusion* 57.11 (Aug. 2017), p. 116043. DOI: 10.1088/1741-4326/aa8009. URL: https://dx.doi.org/10.1088/1741-4326/aa8009 (cit. on pp. 54, 85, 87, 88).

[HY22] M. Hsieh and S. Yamana. "Base change and triple product -series". In: *Representation Theory of the American Mathematical Society* 26.13 (2022), pp. 402–431 (cit. on p. 42).

[Ian+18] F. Iannone, G. Bracco, C. Cavazzoni, et al. "MARCONI-FUSION: The new high performance computing facility for European nuclear fusion modelling". In: *Fusion Engineering and Design* 129 (2018), pp. 354–358. ISSN: 0920-3796. DOI: https://doi.org/10.1016/j.fusengdes.2017.11.004. URL: https://www.sciencedirect.com/science/article/pii/S0920379617309018 (cit. on p. 65).

[IY97] M.B. Isichenko and V.V. Yankov. “Turbulent equipartitions in two-dimensional drift convection”. In: *Physics reports* 283.1-4 (1997), pp. 161–175 (cit. on p. 181).

[Jus+15] B. Justin, W. Wehner, E. Schuster, et al. “Simultaneous closed-loop control of the current profile and the electron temperature profile in the TCV tokamak”. In: *Proceedings of the American Control Conference* 2015 (July 2015), pp. 3316–3321. DOI: 10.1109/ACC.2015.7171844 (cit. on p. 45).

[Kaw+06] H. Kawashima, K. Shimizu, T. Takizuka, et al. “Development of integrated SOL/divertor code and simulation study in JAEA”. In: *Plasma and Fusion Research* 1 (2006), pp. 031–031 (cit. on p. 71).

[Kir+06] A. Kirk, N. B. Ayed, G. Counsell, et al. “Filament structures at the plasma edge on MAST”. In: *Plasma physics and controlled fusion* 48.12B (2006), B433 (cit. on p. 59).

[KK17] S.I. Krasheninnikov and A.S. Kukushkin. “Physics of ultimate detachment of a tokamak divertor plasma”. In: *Journal of Plasma Physics* 83.5 (2017), p. 155830501. DOI: 10.1017/S0022377817000654 (cit. on p. 57).

[Lip+97] M. Lipa, P. Chappuis, P. Garin, et al. “Towards long pulse high performance discharges in TORE SUPRA: Upgrading of inner vessel components (CIEL PROJECT)”. In: *17th IEEE/NPSS Symposium Fusion Engineering (Cat. No.97CH36131)* 1 (1997), 353–356 vol.1. URL: https://api.semanticscholar.org/CorpusID:110706532 (cit. on p. 47).

[LPH16] B. Lipschultz, F. Parra, and I. H. Hutchinson. “Sensitivity of detachment extent to magnetic configuration and external parameters”. In: *Nuclear Fusion* 56.5 (2016), p. 056007 (cit. on p. 58).

[Mak+21] S.O. Makarov, D.P. Coster, V.A. Rozhansky, et al. “Equations and improved coefficients for parallel transport in multicomponent collisional plasmas: Method and application for tokamak modeling”. In: *Physics of Plasmas* 28.6 (2021) (cit. on p. 71).

[Man24] D. Mancini. private communications. 2024 (cit. on p. 141).

[Man+21] D. Mancini, P. Ricci, N. Vianello, M. Giacomin, et al. “Investigation of the density shoulder formation by using self-consistent simulations of plasma turbulence and neutral kinetic dynamics”. In: *Nuclear Fusion* 61.12 (2021), p. 126029 (cit. on pp. 63, 151).

[Man+23] D. Mancini, P. Ricci, N. Vianello, G. Van Parys, et al. “Self-consistent multicomponent simulation of plasma turbulence and neutrals in detached conditions”. In: *Nuclear Fusion* 64.1 (2023), p. 016012 (cit. on p. 63).

[Man+20] P. Manz, C. Hufnagel, A. Zito, et al. “The diffusion limit of ballistic transport in the scrape-off layer”. In: *Physics of Plasmas* 27.2 (2020) (cit. on p. 178).

[Man+15] P. Manz, T.T. Ribeiro, B.D. Scott, et al. “Origin and turbulence spreading of plasma blobs”. In: *Physics of Plasmas* 22.2 (2015) (cit. on p. 177).

[McG24] B. McGibbon. *Self consistent edge turbulence neutrals simulations in reversed field*. Internship Report, CEA Cadarache - Eindhoven University of Technology. 2024 (cit. on pp. 127, 128, 131, 132).

[Mil22] Fulvio Militello. “Radiation and Detachment”. In: *Boundary Plasma Physics: An Accessible Guide to Transport, Detachment, and Divertor Design*. Springer, 2022, pp. 313–386 (cit. on p. 58).

[Nac+16] N. Nace, M. Perin, P. Tamain, et al. “Turbulence Interaction with Driven Transport Barriers in the Scrape-Off Layer of Tokamaks”. In: *Contributions to Plasma Physics* 56.6-8 (2016), pp. 581–586 (cit. on p. 96).

[Nau07] V. Naulin. “Turbulent transport and the plasma edge”. In: *Journal of nuclear materials* 363 (2007), pp. 24–31 (cit. on p. 177).

[Nol+10] B. Nold, G.D. Conway, T. Happel, et al. “Generation of blobs and holes in the edge of the ASDEX Upgrade tokamak”. In: *Plasma Physics and Controlled Fusion* 52.6 (2010), p. 065005 (cit. on p. 119).

[Oli+22] D.S. Oliveira, T. Body, D. Galassi, et al. “Validation of edge turbulence codes against the TCV-X21 diverted L-mode reference case”. In: *Nuclear Fusion* 62.9 (2022), p. 096001 (cit. on p. 139).

[Pan+06] R. Panek, O. Bilyková, V. Fuchs, et al. “Reinstallation of the COMPASS-D tokamak in IPP ASCR”. In: *Czechoslovak Journal of Physics* 56 (2006), B125–B137 (cit. on p. 95).

[Pit+19] R.A. Pitts, X. Bonnin, F. Escourbiac, et al. “Physics basis for the first ITER tungsten divertor”. In: *Nuclear Materials and Energy* 20 (2019), p. 100696. ISSN: 2352-1791. DOI: https://doi.org/10.1016/j.nme.2019.100696. URL: https://www.sciencedirect.com/science/article/pii/S2352179119300237 (cit. on pp. 57, 58).

[Pit+11] RA Pitts, S Carpentier, F Escourbiac, et al. “Physics basis and design of the ITER plasma-facing components”. In: *Journal of Nuclear Materials* 415.1 (2011), S957–S964 (cit. on p. 51).

[Rei+00] D. Reiter et al. “The data file AMJUEL: additional atomic and molecular data for EIRENE”. In: *Forschungszentrum Juelich GmbH* 52425 (2000) (cit. on p. 87).

[RBB05] D. Reiter, M. Baelmans, and P. Boerner. “The EIRENE and B2-EIRENE codes”. In: *Fusion science and technology* 47.2 (2005), pp. 172–186 (cit. on p. 82).

[Riv+22] N. Rivals, P. Tamain, Y. Marandet, et al. “SOLEDGE3X full vessel plasma simulations for computation of ITER first-wall fluxes”. In: *Contributions to Plasma Physics* 62.5-6 (2022), e202100182. DOI: https://doi.org/10.1002/ctpp.202100182. eprint: https://onlinelibrary.wiley.com/doi/pdf/10.1002/ctpp.202100182. URL: https://onlinelibrary.wiley.com/doi/abs/10.1002/ctpp.202100182 (cit. on pp. 53, 57, 81, 82, 169, 176).

[SN97] A. Samain and F. Nguyen. “Onsager relaxation of toroidal plasmas”. In: *Plasma physics and controlled fusion* 39.8 (1997), p. 1197 (cit. on p. 181).

[SG98] Y. Sarazin and Ph. Ghendrih. “Intermittent particle transport in two-dimensional edge turbulence”. In: *Physics of Plasmas* 5.12 (1998), pp. 4214–4228 (cit. on p. 64).

[Sco05] B.D. Scott. “Drift wave versus interchange turbulence in tokamak geometry: Linear versus nonlinear mode structure”. In: *Physics of Plasmas* 12.6 (2005) (cit. on p. 59).

[Sco07] B.D. Scott. “Tokamak edge turbulence: background theory and computation”. In: *Plasma Physics and Controlled Fusion* 49.7 (June 2007), S25. DOI: 10.1088/0741-3335/49/7/S02. URL: https://dx.doi.org/10.1088/0741-3335/49/7/S02 (cit. on p. 58).

[sco02] B.D. scott. “The nonlinear drift wave instability and its role in tokamak edge turbulence”. In: *New Journal of Physics* 4.1 (July 2002), p. 52. DOI: 10.1088/1367-2630/4/1/352. URL: https://dx.doi.org/10.1088/1367-2630/4/1/352 (cit. on p. 58).

[Shi+09] K. Shimizu, T. Takizuka, K. Ohya, et al. “Kinetic modelling of impurity transport in detached plasma for integrated divertor simulation with SONIC (SOLDOR/NEUT2D/IMPMC/EDDY)”. In: *Nuclear fusion* 49.6 (2009), p. 065028 (cit. on p. 71).

[Sim+94] R. Simonini, G. Corrigan, G. Radford, et al. “Models and Numerics in the Multi-Fluid 2-D Edge Plasma Code EDGE2D/U”. In: *Contributions to Plasma Physics* 34.2-3 (1994), pp. 368–373. DOI: https://doi.org/10.1002/ctpp.2150340242. eprint: https://onlinelibrary.wiley.com/doi/pdf/10.1002/ctpp.2150340242. URL: https://onlinelibrary.wiley.com/doi/abs/10.1002/ctpp.2150340242 (cit. on p. 71).

[Sta+22] A. Stagni, N. Vianello, C.K. Tsui, et al. “Dependence of scrape-off layer profiles and turbulence on gas fuelling in high density H-mode regimes in TCV”. In: *Nuclear Fusion* 62.9 (2022), p. 096031 (cit. on p. 171).

[Sta+00] P. C. Stangeby et al. *The plasma boundary of magnetic fusion devices*. Vol. 224. Institute of Physics Pub. Philadelphia, Pennsylvania, 2000 (cit. on pp. 44, 47–49, 55–57, 71, 87).

[Ste+18] A. Stegmeir, D. Coster, A. Ross, et al. "GRILLIX: a 3D turbulence code based on the flux-coordinate independent approach". In: *Plasma Physics and Controlled Fusion* 60.3 (Jan. 2018), p. 035005. DOI: 10.1088/1361-6587/aaa373. URL: https://dx.doi.org/10.1088/1361-6587/aaa373 (cit. on p. 64).

[Sur+25] S. Sureshkumar, N. Rivals, P. Tamain, et al. "First SOLEDGE3X-EIRENE simulations of the ITER Neon seeded burning plasma boundary up to the first wall". In: *Submitted to Nuclear Materials and Energy JNME-D-24-00262* (2025) (cit. on p. 92).

[Tam+18] P. Tamain, C. Baudoin, H. Bufferand, et al. "Impact of self-consistent neutrals dynamics and particle sources on edge plasma transport and turbulence in 3D first principle simulations". In: *23rd International Conference on Plasma Surface Interactions in Controlled Fusion Devices (PSI23)* (2018) (cit. on pp. 63, 112, 116, 151).

[Tam+13a] P. Tamain, G. Bonhomme, F. Brochard, et al. "Interaction of plasma transport and turbulence on particle fuelling". In: *Journal of nuclear materials* 438 (2013), S148–S154 (cit. on pp. 74, 78).

[Tam+13b] P. Tamain, G. Bonhomme, F. Brochard, et al. "Interaction of plasma transport and turbulence on particle fuelling". In: *Journal of nuclear materials* 438 (2013), S148–S154 (cit. on p. 110).

[Tam+16] P. Tamain, H. Bufferand, L. Carbajal, et al. "Interplay between plasma turbulence and particle injection in 3D global simulations". In: *Contributions to Plasma Physics* 56.6-8 (2016), pp. 569–574 (cit. on p. 110).

[Tam+14] P. Tamain, H. Bufferand, G. Ciraolo, et al. "3D Properties of Edge Turbulent Transport in Full-Torus Simulations and their Impact on Poloidal Asymmetries". In: *Contributions to Plasma Physics* 54.4-6 (2014), pp. 555–559 (cit. on pp. 84, 119).

[Tam+15] P. Tamain, Ph. Ghendrih, H. Bufferand, et al. "Multi-scale self-organisation of edge plasma turbulent transport in 3D global simulations". In: *Plasma physics and controlled fusion* 57.5 (2015), p. 054014 (cit. on p. 96).

[Tam+10a] P. Tamain, Ph. Ghendrih, E. Tsitrone, et al. "TOKAM-3D: A 3D fluid code for transport and turbulence in the edge plasma of Tokamaks". In: *Journal of Computational Physics* 229.2 (2010), pp. 361–378. ISSN: 0021-9991. DOI: https://doi.org/10.1016/j.jcp.2009.09.031. URL: https://www.sciencedirect.com/science/article/pii/S0021999109005233 (cit. on p. 64).

[Tam+10b] P. Tamain, A. Kirk, E. Nardon, et al. "Edge turbulence and flows in the presence of resonant magnetic perturbations on MAST". In: *Plasma Physics and Controlled Fusion* 52.7 (2010), p. 075017 (cit. on p. 162).

[Tat+21] R. Tatali, E. Serre, P. Tamain, et al. “Impact of collisionality on turbulence in the edge of tokamak plasma using 3D global simulations”. In: *Nuclear Fusion* 61.5 (2021), p. 056002 (cit. on pp. 126, 128).

[Van+22] W. Van Uytven, W. Dekeyser, M. Blommaert, et al. “Assessment of advanced fluid neutral models for the neutral atoms in the plasma edge and application in ITER geometry”. In: *Nuclear Fusion* 62.8 (2022), p. 086023 (cit. on pp. 85, 86).

[Via+19] N. Vianello, D. Carralero, C.K. Tsui, et al. “Scrape-off layer transport and filament characteristics in high-density tokamak regimes”. In: *Nuclear Fusion* 60.1 (2019), p. 016001 (cit. on pp. 171, 172).

[Via+17] N. Vianello, C. Tsui, C. Theiler, et al. “Modification of SOL profiles and fluctuations with line-average density and divertor flux expansion in TCV”. In: *Nuclear Fusion* 57.11 (2017), p. 116014 (cit. on p. 171).

[Wie+15] S. Wiesen, D. Reiter, V. Kotov, et al. “The new SOLPS-ITER code package”. In: *Journal of nuclear materials* 463 (2015), pp. 480–484 (cit. on pp. 71, 92).

[Wyn+18] A. Wynn, B. Lipschultz, I. Cziegler, et al. “Investigation into the formation of the scrape-off layer density shoulder in JET ITER-like wall L-mode and H-mode plasmas”. In: *Nuclear Fusion* 58.5 (Mar. 2018), p. 056001. DOI: 10.1088/1741-4326/aaad78. URL: https://dx.doi.org/10.1088/1741-4326/aaad78 (cit. on pp. 61, 170–173).

[Yan+22] H. Yang, G. Ciraolo, J. Bucalossi, et al. “Numerical modelling of the impact of leakage under divertor baffle in WEST”. In: *Nuclear Materials and Energy* 33 (2022), p. 101302 (cit. on p. 82).

[Yan+23] H. Yang, G. Ciraolo, O. Février, et al. “Numerical study of divertor detachment in TCV H-mode scenarios”. In: *Plasma Physics And Controlled Fusion* 65.12 (2023), p. 125005 (cit. on pp. 82, 142, 144).

[Yon17] N. Yong-Su. *Introduction to Nuclear Fusion*. University Lecture. 2017 (cit. on p. 46).

[Zhd02] V. M. Zhdanov. *Transport processes in multicomponent plasma*. CRC Press, 2002 (cit. on p. 71).

[Zho+21] W. Zholobenko, A. Stegmeir, M. Griener, et al. “The role of neutral gas in validated global edge turbulence simulations”. In: *Nuclear Fusion* 61.11 (2021), p. 116015 (cit. on p. 63).

[Zho+22] Y. Zhou, B. Dudson, F. Militello, et al. “Investigation of the role of hydrogen molecules in 1D simulation of divertor detachment”. In: *Plasma Physics and Controlled Fusion* 64 (Apr. 2022). DOI: 10.1088/1361-6587/ac6827 (cit. on p. 54).

[Zit+21] A. Zito, M. Wischmeier, D. Carralero, et al. “Numerical modelling of an enhanced perpendicular transport regime in the scrape-off layer of ASDEX Upgrade”. In: *Plasma Physics and Controlled Fusion* 63.7 (May 2021), p. 075003. DOI: 10.1088/1361-6587/abfcb6. URL: https://dx.doi.org/10.1088/1361-6587/abfcb6 (cit. on p. 64).

[Zwe+14] S.J. Zweben, D.P. Stotler, R.E. Bell, et al. “Effect of a deuterium gas puff on the edge plasma in NSTX”. In: *Plasma Physics and Controlled Fusion* 56.9 (2014), p. 095010 (cit. on pp. 119, 162).

ANNEXES

A. Eirene mesh generator

This appendix provides a detailed explanation of the technical aspects involved in the 3D coupling of the SOLEDGE3X - EIRENE package. The first step relies on the automatic generation of the EIRENE meshes, from the SOLEDGE3X mesh. The methodology used, along with the variables and subroutines developed within the code, will be thoroughly explained.

As addressed in Chapter 2, the necessary steps leading to the writing of the mesh files are the following:

1. The definition of the objects structure and of variables suitable for MPI/OpenMP parallelization.
2. The routine for splitting the SOLEDGE3X quadrangles mesh into EIRENE triangles mesh.
3. The routine for cutting of SOLEDGE3X quadrangles mesh to EIRENE triangles mesh for each chunk
4. The routine for checking the direction of the triangles corners (called nodes) in the cells
5. The routine for gathering the entire mesh of triangles from each chunk.
6. The routine for merging the triangles meshes owned by each MPI process into a single triangles mesh on the master MPI process
7. The routines for detecting the wall and the core inside the mesh.
8. The routines for the writing of the meshes files, both texts (soledge3x.neighbors, soledge3x.elemente, soledge3x.npco-char) and h5 file (meshEIRENE.h5)

First, FORTRAN requires the definition of objects. To create a new mesh from an existing one, it is necessary to refer to new structures for the triangles, the wall, and the core, ensuring consistency with the original quadrangular ones.

— Allocation of the structures thought to hold the mesh of triangles with the relative information. It includes general information as the number of all the triangles generated (Ntriangles), as well as the specific information for the triangle, such as the number associated to each of nodes, the radial and vertical position (R, Z) expressed in [cm], the table of the nodes composing each triangles with a dimension of [3, Ntriangles], the definition of its neighbors. This latter is made by providing the triangle number of the neighbor at each face of each triangle (size [3, Ntriangles]): here a values convention is taken, imposing 0 if at the edge of the domain where no neighbors are present, or the specific number of neighbouring triangle. Additionally, the face number inside neighbouring triangle at each face

of each triangle, following the previous values convention and with the same size. Moreover, in case of domain edge, this structure contains the definition of the type of boundary conditions (BC) applied with 0 if not domain edge, 1 if core BC, 3 if wall BC. And, as last requirements, the coordinates of the corresponding quadrangular cell in terms of zone inside the domain (first index, izone), radial coordinates (second, ipsi) and poloidal coordinates (third, itheta) for each triangle, with the usual size of [3, Ntriangles].

— Allocation of the structures thought to hold the information for each wall sequence (since the wall might be split into several portions), in specificity the array of triangles along each piece of the wall, the array for storing the value concerning the material type of each segment of the wall and the one for defining the pumping: 0 if the wall is not pumping, a given number if there is a kind of pump on it.

— Allocation of the structures thought to hold the wall with the relative information. It includes general information as the number of all the triangles along the wall (Ntriangles), with their specific information for the triangle, such as the number associated to each of them and to their faces along the wall, the number of wall pieces (Nseq), and an array for storing the information of each piece of wall, having the dimension of the triangles along the wall. In this context, some arrays for storing the number of cell whose flux should be projected on the triangle face along the wall has to be added, together with a convention on the face orientation: East = relative maximum index along the poloidal direction, West = relative minimum index along the poloidal direction, North = relative maximum index along the radial direction, South = relative minimum index along the radial direction. These arrays have the dimension of [3, Ntriangles], where the first dimension is the coordinates of the corresponding quadrangular cell (1=ipsi, 2=itheta, 3=izone) for each triangle. As complementary information to this latter, one needs to provide the arrays for storing the weight of the flux projection on the faces along the wall, with a dimension of [Ntriangles].

— Allocation of the structures thought to hold the core information, with the definition of the number of triangles along the core, an array for storing the number of each triangles and another one for the face number of each triangles along the core together with a number defining the wall pieces.

To finish with the definition of the variables suitable for MPI and OpenMP parallelization of SOLEDGE3X.

Getting into the details of the implementation of the needed routine to generate the EIRENE mesh, one may start with the first one to be called. This is a subroutine called quadMesh2triMesh, which takes several input parameters:

— split, is the domain decomposition info.

— Rcorners, the radial position of corners of cells in each chunk (size [Nchunks])

— Zcorners, the vertical position of corners of cells in each chunk (size [Nchunks])

— chi, wall mask in each chunk (size [Nchunks])

— chicore, core mask in each chunk (size [Nchunks])

This subroutine operates on the whole mesh and calls the splitting subroutine

(chunkQuad2Tri) on each chunk before assembling all of them into a single global mesh.

First, all processes work independently on their chunks and so it defines triangles mesh on each chunk. It is assumed by the code that the mesh is toroidal symmetric and that the first toroidal point of the chunk is representative of it. To respect this assumption, the computation of the triangles mesh is made only for chunks that are dealing with the first poloidal plane. If it is not the case, an empty triangular mesh will be generated.

After this step, the subroutine proceeds to assemble triangle mesh from all chunks into a single mesh of triangles and to merge all the triangle meshes from all MPI process on master MPI process, moving afterzards to the detection of th ewall and of the core in the global mesh. The final step is up to the master process which is in charge of exporting these global information to the files, calling the writing subroutines.

The nested sub-routine chunkQuad2Tri provides the cut of each quads to triangles in each chunks. For each triangle, obtained by cutting along the diagonal of the quadrangle cell, it computes the number of faces, of nodes, neighbours and their information and facetype. In particular, the boundary conditions are taken into consideration as facetype. The inputs are:

1. nodes2D, a real array giving the radial position of nodes (with size [Ntheta+1,Npsi+1], where Ntheta and Npsi are respectively the number of points along the poloidal and the radial directions.)
2. Znodes2D, a real array giving the vertical position of nodes (with size [Ntheta+1,Npsi+1])
3. chi2D, the mask of wall including ghost cells (size [Ntheta+2*Nghosts,Npsi+2*Nghosts])
4. izone (optional), index of zone to which the chunk belongs
5. ipsimin (optional), starting index of chunk in psi direction in the zone.
6. ithetamin (optional), starting index of chunk in psi direction in the zone.

The routine returns as output the triangle mesh structure for each chunks.

It operates by counting the number of triangles and nodes, generating the corresponding arrays of nodes and the mapping between coordinates and node number, and later on triangle number. Once this is done, it proceeds to generate triangles only if the triangle is outside the wall mask. It starts with the generation of the first triangle, via the definition of each faces; for face one and three, if they are on the wall mask edge, corresponding to a Bohm boundary condition, the convention imposes a face type equals to 3 and a neighbor of type 0, with a face of type 0. Else, if the triangle face sits on the edge of the chunk, the computation returns an undefined sequence for the moment and it assigns to all these values the -1 label. Face number two is by assumption the one sitting along the cut, so it is always referred to the internal one; as consequence, there is no need to check on boundaries as internal face by default. Inside the chunk, the triangle face type is taken as the default 0 and the neighbor number is consistently provided by the mapping. Then, it moves in the same fashion to the generation of the second triangle. The routine keeps also trace of the quadrangle

originates the traingles, storing the information about coordinates into a specific table called backInterp.

Once having called the chunkQuad2Tri sub-routine, the main routine proceeds in checking the direction of the nodes in the cells before merging each chunk meshes. This is performed by calling the checkTriMeshDir, that once the triangles mesh is obtained, it checks if the nodes of triangles are well ordered and if not, it reverses them. It takes as input the triangle mesh to treat, and an integer called direc, equal to +1 or -1 according to whether triangles should be oriented in the direct or indirect trigonometric direction when looking at the poloidal plane with the Low Field Side on the right. The sub-routines return the triangle mesh structured from the input, treated if it has needed.

Later, when the directional check has been done, each mesh produced by a single chunk has to be merge with all the other ones. In order to do that, it is necessary to get aware of not duplicate nodes and reorder correctly the enumeration of nodes and triangles. To do that job, the main calls the gathering routine mergeTriMeshes for generating the entire mesh from each chunks, taking the sub-meshes as input and returning the final mesh merged.

The operations involved begin from the summing all of the sub meshes to obtain the total number of triangles, allocating the triangles, the neighbors, the neighbor faces, the face types, and the backInterp arrays. Then, the mapping between old nodes and unique new nodes is built by looping several times on the nodes list to check whether they are duplicated or not. Once it is done, it goes through all the triangles to redefine the nodes and copy the neighbors, the neighbor faces, the face types arrays.

The merge into a global is attributed to the master MPI process, via the routine mergeTriMeshMPI which takes as input the triangles meshes local to each MPI process and the global triangles mesh, which is returned as defined only on the master process.

At this point the mesh should be clean. There is however one exception: in meshes that are logically periodic in some direction although the positions of mesh cells themselves are not, the mesh generator will not detect that triangles on both sides of the periodic direction should be neighbours so that the corresponding faces will have faceType = -1. An additional routine called checkTriMeshPeriodicity can be used to solve the issue by detecting triangles that are neighbours due to periodicity. Nevertheless, this solution is anyway not compatible with EIRENE that will not be able to consider these triangles as neighbours, as they are effectively not facing each other in space. This fix has to be adjusted in the later work.

As last steps, the code has to detect the zall and the core inside the mesh. Once the mesh is merged, two separate routines allow to detect the face of the triangles which are along the core and the zall. Starting from a preliminary segment and going both clockwise and counterclockwise they select the nodes owned by two sequential faces until the border of the core or of the wall are reached and no more faces are founded. At this point, a first sequence of core and of wall are created, until one covers all the sequences. The input is the global mesh, while the outputs are the structures holding the information for the core and the wall.

The ultimate task concern the writing of the files, by using the information re-

covered in the other routines to produce the structure for the H5 file and for the soledge3x.neighbors, soledge3x.elemente, soledge3x.npco-char.

Here in the table A.1, some additional details about the information they contain.

File name	Type	Data
soledge3x.neighbors	Text	Neighbouring information between triangles as well as definition of the edge faces (tells for each triangle face what is on the other side).
soledge3x.elemente	Text	Tells for each triangles the 3 nodes it is composed of.
soledge3x.npco-char	Text	Tells the (R,Z) position of each node in [cm].
meshEIRENE.h5	hdf5	— Nknots: number of knots (nodes) in triangle mesh — Ntriangles: number of triangles — knots: group for info on nodes containing R[Nknots] and Z[Nknots], respectively the radial and vertical position of knots in meters — triangles: group for info on triangle, containing the triKnots[Ntriangles,3], the typeFace[Ntriangles,3] and the backInterp[Ntriangles,3] info. The first one consists in the list of indices of the 3 nodes composing each triangle; the second one the type of face for each of the 3 faces of each triangle, while the latter provides for each triangle the coordinates of the corresponding cell (1=izone, 2=ipsi, 3=itheta). — wall: group for info on wall, containing the information about the number of triangles along the wall (Ntriangles), the number associated to each triangle along the wall (triNum), the number of the face inside each triangle along the wall (triFace), the number of disjoint walls (nseq). Moreover, the wall group contains other sub-groups providing information on the first piece of wall (triSequence1): the triangles along that piece of wall (tri), the material type for each wall segment (typemat) and whether or not there is a pump (ispump) by setting 0 in case not, or 1. Other groups are defined in case of additional pieces of wall (triSequence2, triSequence3) up to nseq. Additionally, the wall provides information about the projected flux on each triangle's faces (eastCellToUse, westCellToUse, northCellToUse and southCellToUse), as long as their weights (eastCellWeight, westCellWeight, northCellWeight and southCellWeight).

Table A.1. – EIRENE mesh files list and contents description.